

Investigation of All-Solid-State Batteries' Transition towards Large-Scale Processing with Emphasis on In Situ Gas Analysis

Untersuchung des Übergangs von Festkörperbatterien
hin zur großtechnischen Verarbeitung mit Schwerpunkt
in situ Gasanalyse

dem Fachbereich Biologie und Chemie der
Justus-Liebig-Universität Gießen

vorgelegte Dissertation zur Erlangung des akademischen Grades
Doktor der Naturwissenschaften
-Dr. rer. nat.-

von

Jun Hao Teo

Gießen 2022

Dean/Dekan
1. Reviewer/Gutachter
2. Reviewer/Gutachter

Prof. Dr. Jürgen Janek
Prof. Dr. Jürgen Janek
Prof. Dr. Bernd Smarsly

Die vorliegende Arbeit wurde im Zeitraum von Mai 2018 bis Dezember 2021 am Institut für Nanotechnologie des Karlsruher Instituts für Technologie unter Betreuung von Prof. Dr. Jürgen Janek angefertigt.

Ich erkläre:

Ich habe die vorgelegte Dissertation selbständig und ohne unerlaubte fremde Hilfe und nur mit den Hilfen angefertigt, die ich in der Dissertation angegeben habe. Alle Textstellen, die wörtlich oder sinngemäß aus veröffentlichten Schriften entnommen sind, und alle Angaben, die auf mündlich Auskünften beruhen, sind als solche kenntlich gemacht. Bei den von mir durchgeführten und in der Dissertation erwähnten Untersuchungen habe ich die Grundsätze guter wissenschaftlicher Praxis, wie sie in der "Satzung der Justus-Liebig-Universität Gießen zur Sicherung guter wissenschaftlicher Praxis" niedergelegt sind, eingehalten.

Ort, Datum, Unterschrift

Abstract

With liquid-based lithium-ion batteries approaching both its theoretical and practical limits, the progress in all-solid-state batteries (SSBs) offer an exciting improvement and future for energy storage systems. The exponential progress of SSBs on the laboratory/research-scale in the last decade has led to promising results and is currently on the cusp of large-scale implementation. The transition from lab-scale to industrial-scale is not trivial and require the considerations of several intertwined factors, for example safety, processability, performance, etc..... In the present work, the use of industrial relevant materials are crucial for a seamless transition from liquid- to solid-based lithium ion batteries. The cathode active material (CAM) is a layered lithium transition metal oxides $\text{Li}_{1+x}(\text{Ni}_{1-y-z}\text{Co}_y\text{Mn}_z)_{1-x}\text{O}_2$ (NCM or NMC). For the solid electrolyte (SE), sulfides (thiophosphate) are a popular choice largely due to both its processability and mechanical properties. The present work will address key questions on the safety aspect, specifically the gas evolution during cell operation using *in situ* gas analysis. Additionally, questions regarding the processability and performance will be addressed using a number of analysis techniques with *in situ* gas analysis in tandem.

The first section will introduce the motivations and principles behind a lithium-ion battery and elaborate upon the active materials used for our study on SSBs. In the second section, the customized cell setup used for *in situ* gas analysis for SSBs will be elaborated. Additionally, we will provide an in-depth insight into the gassing technique used in this study (Differential electrochemical mass spectrometry, DEMS). The third section will elaborate upon the large-scale processing technique employed in our lab to produce sheet-based electrodes. The process of selection and optimization along every stage of the fabrication process will be described in detail. Lastly, in the fourth section (results and discussion), a compilation of the various publications can be found.

The first publication will demonstrate the capabilities of the customized cell to investigate gas evolution in SSBs. This study was used to establish a baseline for future gassing studies on SSBs, thus the comparison between conventional liquid-based lithium-ion batteries (LIBs) and two sulfide-based SSBs ($\beta\text{-Li}_3\text{PS}_4$ and $\text{Li}_6\text{PS}_5\text{Cl}$). The measurements first illustrate the differences in the type and amount of gas evolved between LIBs and SSBs, with LIBs mostly outgassing the SSBs except for two exceptions, namely O_2 and SO_2 . The observation of toxic SO_2 gas brings to attention the hazards of using sulfide SEs in SSBs. Additionally, the main contribution of CO_2 gas evolution in SSBs was clarified to be a result of electrochemical decomposition of the coating (impurity) layer. This led to the further use of *in situ* gassing studies for the evaluation of coating chemistries in future publications.

The second publication will display the transition toward large-scale processing techniques for SSBs. First, the individual processing steps (mixing, casting, drying) were optimized for the preparation of mechanically stable, homogeneous electrode sheets (section 3). The electrode sheets exhibited highly competitive performance versus those prepared using conventional powder-based processing. The second publication highlights a design-of-experiments (DoE)-guided approach to evaluate the influence of polymeric binder and carbon additives on the overall cell performance. The results were primarily supported by *in situ* gas analysis, which showed that certain polymeric functional group and/or chains/units potentially interact with the surrounding electrode components and lead to an increased degradation during cell operation.

In the third publication, the dependence of cell performance on (chemo)mechanical effects was investigated. The combination of slurry-based processing and glassy SE was shown to improve the (chemo)mechanical properties of a cell, which allowed the cell components to maintain tight contact between each other while at the same time mitigating volume changes.

The results demonstrate that the CAM/SE interface should not only function as a self-limiting interface, preventing further (electro)chemical reactions, but also possess the necessary mechanical strength needed to maintain intimate contact after prolonged cycling.

Keywords: NCM, In Situ Gas Analysis, DEMS, Slurry-based processing, All-Solid-State battery

Contents

Abstract	V
1. Introduction	1
1.1. Motivation	1
1.2. Principles of a Lithium-Ion battery	4
1.3. Positive Electrode (Layered Transition Metal Oxides, LiTMO ₂)	8
1.4. Negative electrode (Li ₄ Ti ₅ O ₁₂)	12
2. In Situ Gas Analysis	14
2.1. Differential Electrochemical Mass Spectrometry (DEMS)	14
2.2. Mass Spectrometry	19
3. Slurry-casting of All-Solid-State batteries	23
3.1 Motivation	23
3.2. Selection of solvent and binder	23
3.2.1. Solvent-related parameters	23
3.2.2. Binder-related parameters	25
3.2.3. In-house optimization of the binder-solvent parameters	27
3.3. Sheet fabrication process	30
3.3.1. Mixing of components	30
3.3.2. Layer formation	32
3.3.3. Layer compaction	34
4. Results and Discussion	36
4.1. Gas Evolution in Lithium-Ion Batteries: Solid versus Liquid Electrolyte	36
4.2. Design-of-experiments-guided optimization of slurry-cast cathodes for solid-state batteries	49
4.3. The interplay between (electro)chemical and (chemo)mechanical effects in the cycling performance of thiophosphate-based solid-state batteries	86
Equations	109
Figures	110
Bibliography	111

1. Introduction

1.1. Motivation

Battery technology, specifically lithium-ion batteries have come a long way since its discovery in the '90s by Sony. To fully understand the importance that battery technologies play in our current day and the near future, we take a brief look at history and the many influences throughout that led to their development to this day. Although lithium-ion batteries (LIBs) were used early on in phones, cameras and other portable devices, there were no evident interest in them among the consumers apart from the devices that they were powering. The first change was seen when the Apple iPhone was unveiled in 2007. These devices changed how humans work, travel, communicate and perceive the world around them. Its functionality led to a consumer-led advancement in small, more powerful portable devices, which in turn required better and more complex energy storage systems. Thus, battery technologies and research are accelerated in the process to satisfy the needs of the consumers. The next boost to battery research came unfortunately in the form of the 2011 nuclear disaster in Fukushima, Japan. This led to a change in many countries' mindset on their reliance on nuclear energy. In 2011, Germany's energy policy changed to reduce their reliance on nuclear energy by sequentially phasing out nuclear power plants and increase their supply of alternative sources such as oil, natural gas and renewable energies. Renewable energies from off-shore wind farms and solar power rapidly replaced a large proportion of electricity generation in Germany.¹ As renewable energy generation are unreliable and depended on the weather, providing uninterrupted power to the energy grid would require the development on stationary energy storage systems. One such system is lithium-ion batteries. Today, the current boost to battery research and development originates from a car emission scandal among the world's largest car manufacturers in 2015. Towards the end of 2017, calls for banning of internal combustion engines (ICE) and a transition towards electric cars was underway.² Decrease in production costs for electric vehicles and improvements to battery technologies were demonstrated by Tesla Inc. with the Tesla Model S in 2011.^{3,4} From then on, interest in the consumer-base and a growing competitor in the form of Tesla and its charismatic leader, Elon Musk, started to encourage established car manufactures to enter the electric car market. With electric car demands expected to grow at an increasing rate, the demand for electric cars that can travel longer distances between charges in different environments propelled a new wave of battery research into new materials that can provide higher energy and power densities. The main cathode materials used in state-of-the-art LIBs are lithium transition metal oxides (LiTMO_2), olivine LiFePO_4 (LFP), layered transition metal oxides ($\text{LiNi}_{1-x-y}\text{Co}_x\text{Al}_y\text{O}_2$ (NCA) or $\text{LiNi}_{1-x-y}\text{Co}_x\text{Mn}_y\text{O}_2$ (NCM)^{5,6} Each cathode material has its own advantages and disadvantages and are tailored for different applications. Regardless of the progress, the capabilities in both energy and power densities of liquid-based LIBs are approaching its limits.^{7,8} Innovations, technologies and consumer demands are evolving at a much faster pace than advancement in battery technologies. The limitations of the LIBs are not just restricted to the cathode side, but also at the anode, where graphite instead of lithium metal has been the preferred choice of anode material

1.1 Introduction – Motivation

in commercial LIBs. The use of lithium-metal anode is still limited due to its prevalent safety issues, despite offering the highest theoretical capacity ($q_{th} = 3860 \text{ mAh/g}$)^{9,10}. Thus, the search for a battery system that can overcome these limitations is underway and all-solid-state batteries (SSBs) are a promising candidate. By replacing the liquid electrolyte by a solid electrolyte, the benefits of increased gravimetric and volumetric densities alongside the possible use of lithium-metal anodes have placed SSBs front and center as a successor to the LIB systems. In addition, SSBs can be operated within a wider temperature range, which is beneficial for applications in different environmental conditions. However, despite all the potential advantages, there are still many problems plaguing their commercial viability and must be overcome for them to be competitive with LIBs. The enabling of lithium-metal anodes is not limited to SSBs and progress has been made on the LIBs front, where electrolyte with high concentration of lithium salt enabled the use of lithium-metal anodes in a LIB¹¹. However, the focus of this study is on SSBs. Before elaborating on the challenges SSBs face, it has to be noted that solid electrolytes (SEs) can be divided into three groups, the oxides, the sulfides and the polymers. The challenges depend on the group of solid electrolytes (SE) used. In the case of oxides, the major bottleneck to its use lies in its mechanical properties. Oxides possess a high Young's modulus, making them hard and brittle, which causes them to be prone to mechanical defects during the preparation and assembling stage of cell manufacturing. Especially during the assembling stage, where favorable contact between the cathode and SE layer cannot be achieved by standard cold pressing, but has to be performed at high temperatures.¹² In the case of sulfides, their major drawback lies in its low thermodynamic stability.^{13,14} Lastly, polymers are plagued by low lithium-ion conductivity at ambient temperatures. Elevated temperatures above 80°C are required for competitive performance.¹⁵ Among the mentioned systems, sulfide-based SSBs are the closest towards a breakthrough and are on the verge of commercialization¹⁶. As mentioned, sulfide systems suffer from a small thermodynamic stability window, which meant that most of them reacts and forms an interphase when in contact with the components within the electrode. This interphase determines the long-term stability and performance of the cell. The best-case scenario would involve the formation of an interphase that possess high lithium-ion conductivities and negligible electronic conductivities.^{13,14} However, this is not often the case. In fact, it is rare and interphases with both lithium-ion and electronic conductivities are often formed. These mixed conducting interphases are non-passivating and does not prevent further reactions between the SE and the active materials (cathode and anode).¹⁷ To suppress the formation of such interphases, an artificial coating layer on the active materials can be used to protect them against degradation reactions with the SE by firstly being a poor electronic conductor and secondly bridging the Li chemical potential gap between the SE and the active materials.¹⁴ Degradation reactions at the interface can be investigated with a variety of *ex situ* and *in situ* analytical techniques. To name a few, these include X-ray diffraction (XRD), Raman spectroscopy, X-ray photoelectron spectroscopy (XPS), Time-of-Flight secondary ion mass spectrometry (ToF-SIMS) and differential electrochemical mass spectroscopy (DEMS).

This work will comprise of industrially relevant stages in the scaling up of cathode composites for SSBs, starting from investigation of lab-scale pelletized setups to industrial-scale slurry-cast electrode sheets. At every stage, DEMS will be used to

1.1 Introduction – Motivation

characterize the gas evolution, giving indications on the safety aspects, electrochemical stability of the cell components and long-term cycling stability. The aim of this study is to show the high sensitivity and versatility of DEMS in combination with other techniques. For example, the difference in gassing trend of a cathode active material (CAM) with different coating chemistries could elucidate the underlying degradation reactions during cell operation. The chemical nature and quantity of the gas evolved could also help discover reaction mechanisms previously hypothesized. Depending on the potential negative influences these evolved gases have, methods of preventing the evolution of such gases can be implemented. Another example showing the versatility of DEMS was during the screening of different chemical components for slurry-cast electrodes. Further details of the use of DEMS in the transition of powder-based setups to slurry-cast setups would be discussed in chapter 4.

The thesis will proceed in the following sequence. First, a brief introduction to the fundamental principles of a lithium-ion battery will be discussed, which applies similarly to all-solid-state lithium-ion batteries. In the following chapter, the principles and methodology of the *in situ* gas analysis technique used in our lab will be elaborated upon. The third chapter will summarize the in-house knowledge developed for large-scale fabrication of SSBs. The fourth chapter will showcase the results as journal articles and lastly, in the fifth chapter, a summary and outlook for further investigations will be provided.

1.2. Principles of a Lithium-Ion battery

In general, a battery is simply an energy storage device. Electrical energy is stored in this device through an energy conversion process involving redox reactions as chemical energy. The stored chemical energy can be converted back into electrical energy through the reverse redox reaction. A conventional liquid-based lithium-ion battery consists of two electrodes separated by a polymer separator and filled together with a liquid electrolyte (**Figure 1**). The electrodes are characterized as positive and negative respectively and maintain an ionic contact with each other through the lithium-ion conducting electrolytes, which are permeable through the polymer separator. The polymer separator allows Li-ion conduction but prevents electronic contact between the two electrodes. The liquid electrolyte consists of a concoction of lithium salts (e.g. LiClO_4 and LiPF_6), organic solvents (Ethylene carbonate, Dimethyl carbonate and additives that facilitate ionic conductivity, solid electrolyte interface (SEI) formation and improves battery life and safety.¹⁸ The concepts and principles for conventional liquid-based LIBs can be applied to all-solid-state LIBs, where the liquid electrolyte is replaced by a solid electrolyte, thus removing the need of a polymer separator. In SSBs, the solid electrolyte functions as both a separator and a Li-ion contact between the two electrodes, effectively combining the functionality of both the polymer separator and the liquid electrolyte into one (**Figure 1**). This makes the ionic conductivity of the solid electrolyte extremely important and is by far one of the largest researched topics for SSBs.^{19–21} The redox reactions for the energy conversion from electrical to chemical energy and vice versa involves both a movements of electrons and ions through a combination of oxidation and reduction reactions at the respective electrodes.

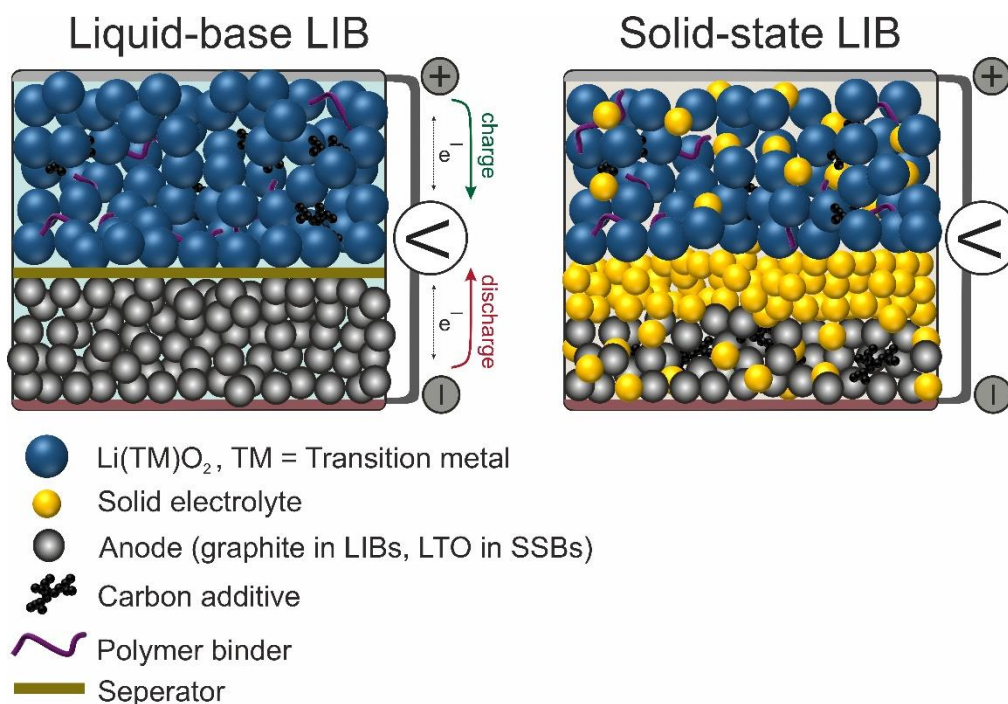
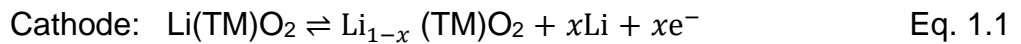


Figure 1.1 Graphical representation of a conventional liquid-base LIB (left) and a solid-state LIB (right).

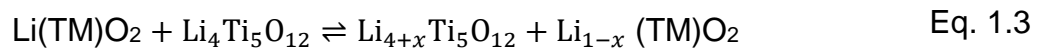
1.2 Introduction – Principles of a Lithium-Ion battery

In electrochemistry, the term cathode represents the metal electrode where reduction reactions occur, and the term anode represents the metal electrode where oxidation occurs. However, depending on the charge or discharge stage, these reactions occur on different electrodes. Therefore, in the battery community, for simplification, the positive electrode is simply called the cathode and the negative electrode the anode, regardless of the type of redox reactions taking place. Until now, only the mention of lithium-ion movements from either electrode through the medium known as the electrolyte was mentioned. However, with all redox reactions, electron movements are accompanied by lithium-ion movements, but in the opposite direction. The flow of electrons take place in the external circuit, which can be connected in series with an electric load or electric source. In the case of an electric load, the powering of the load is just a byproduct of the electron movements between electrodes through the external circuit. This byproduct enables the use of portable devices and electric vehicles.

In our studies, the positive electrode is a Ni-rich layered transition metal oxide [L(TM)O₂, TM = transition metal], while the spinel Li₄Ti₅O₁₂ is used as the negative electrode. Both are considered intercalation materials, whose crystal structure center around a redox active transition metal. A more detailed description of the materials, its crystal structure, intercalation and deintercalation process will be discussed in the following sections. The term intercalation refers to a reversible occupation of a vacant crystal interstitial lattice site (tetrahedral/octahedral) by a mobile ion species (in this case Li-ion). An advantage of an interstitial storage mechanism over its counterparts such as conversion is its minimal volume and structural changes.²² This characteristic enables very stable cycling performance. During charge, lithium ions deintercalates from the cathode and is transported with the help of the Li-ion conducting medium (liquid/solid electrolyte) to the anode, where it intercalates into the anode structure. The process is reversed in the discharge process and together with the charge process can be described with the following equations:



The total redox reaction can then be given as:



The amount of lithium ions that can be intercalated/deintercalated per mass of active material corresponds according to the same amount of electrons injected/removed, which is a measure of the cell's specific capacity. This amount depends on a variety of factors, including the host/electrode's ability to modify its valance state, the available interstitial lattice sites to accommodate the intercalated lithium ions and the reversibility of the intercalation reactions. In addition, the cell operating parameters such as the voltage window, cycling rate (C-rate) and temperature, among others have a large impact on the practical specific capacity. The term practical (specific) capacity is often used instead of theoretical (specific) capacity because cells are almost never cycled to reach their theoretical values. This is due to several reasons, one of which is that battery manufactures limit the operating parameters to increase its cycle life and long-

1.2 Introduction – Principles of a Lithium-Ion battery

term stability. Without these restrictions, the materials will be subjected to extreme degrees of intercalation/deintercalation, resulting in destabilization of the electrode structure and large volume changes. A measure of value called the state-of-charge (SOC) is defined as the ratio between the achieved (practical) capacity and the theoretical capacity and is written as such:

$$\text{SOC} \cong \frac{\text{practical capacity}}{\text{theoretical capacity}} \times 100 \% \quad \text{Eq. 1.4}$$

Another important value of measure is the Coulombic efficiency (CE), which can be defined as the ratio between the discharge and charge capacity within the same cycle:

$$\text{CE} \cong \frac{\text{discharge capacity}}{\text{charge capacity}} \times 100 \% \quad \text{Eq. 1.5}$$

The CE tells us the reversibility of the intercalation reactions (i.e., the redox reactions taking place at either electrodes). In general, these redox reactions are not fully reversible and CE values < 100% are typically measured. The irreversibility is attributed to side reactions that consumes mobile Li-ions that were meant to be intercalated/deintercalated. In a solid-state system, the side reactions that consume active mobile Li-ions typically result in the formation of a mixed conducting interface. Due to its mixed conducting characteristics (electronic and ionic conducting), the interface would grow and become thicker, increasing the interfacial resistance between the electrodes and the SE over time.¹⁷ However, in systems where a protective coating is used on the electrodes, a stable and robust interface can be formed, which prevents further degradation reactions and decelerates consumption of mobile Li-ions.^{13,14} Another important electrochemical value is the electrochemical cell voltage (U), which is a sum of contributions that includes the voltage difference between the two electrodes, the overpotentials (η) at the interfaces and the ohmic resistance of the bulk phases (IR). The total cell voltage can be written as such:

$$U = \Delta E + \eta_{\text{cathode}} + \eta_{\text{anode}} + IR \quad \text{Eq. 1.6}$$

$$U = (E_{\text{cathode}} - E_{\text{anode}}) + \eta_{\text{cathode}} + \eta_{\text{anode}} + IR \quad \text{Eq. 1.6.1}$$

With the help of the Nernst's equation, we can describe the changes in cell voltage via changes in the electrode potentials of the lithium intercalation compounds (E_{cathode} and E_{anode}). The Nernst's equation gives the electrode potentials according to the following:

$$E_i = E_0 + \frac{RT}{nF} \ln \frac{a_{\text{reduction}}}{a_{\text{oxidation}}} \quad \text{Eq. 1.7}$$

with the standard electrode potential E_0 , the gas constant R , the temperature T , the number of electrons transferred in the redox reactions n , the Faraday's constant F , the concentration/activity of the oxidized species a_{ox} and the reduced species a_{red} . It is however important to note that these individual electrode potentials (E_i , i : cathode/anode) are not the potentials of a single electrode-solution interface, but the potential difference with respect to a standardized electrode (e.g., the reversible

1.2 Introduction – Principles of a Lithium-Ion battery

hydrogen electrode). Thus, all electrode potentials are potential differences and the potential difference (or electrode potential) under standard conditions is given as E_0 . However, as described by the Nernst's equation, under non-standard conditions ($T \neq 298\text{ K}, P \neq 1\text{ atm}, c \neq 1\text{ mol/L}$), the electrode potential is dependent on the concentration/activity of the redox species. For the case of lithium intercalation compounds, the redox reactions involving lithium-ions can be described as such:²³



where the oxidizing species is the vacant interstitial sites of the host structure (Li_nH_P) and the reducing species is the occupied interstitial sites (H_P). Thus, equation 1.7 can be rewritten as such:

$$E = E_0 + \frac{RT}{nF} \ln \frac{a[\text{H}_P]}{a[\text{Li}_n\text{H}_P]} \quad \text{Eq. 1.9}$$

$$\xrightarrow{\text{activities for metal } a_i = \gamma_i x_i} \quad E = E_0 + \frac{RT}{nF} \ln \frac{\gamma_{[\text{H}_P]} x_{[\text{H}_P]}}{\gamma_{[\text{Li}_n\text{H}_P]} x_{[\text{Li}_n\text{H}_P]}} \quad \text{Eq. 1.9.1}$$

$$\Rightarrow \quad E = E_0 + \frac{RT}{nF} \ln \frac{x_{[\text{H}_P]}}{x_{[\text{Li}_n\text{H}_P]}} + \ln \frac{\gamma_{[\text{H}_P]}}{\gamma_{[\text{Li}_n\text{H}_P]}} \quad \text{Eq. 1.9.2}$$

with x_i as the molar fraction and γ_i the activity coefficient of the metal-like interstitial electrodes. The calculation of activity coefficients in a solid solution is complex and is outside the scope of this chapter. From Eq. 1.9.2, we can see how the cell voltages changes during the charging/discharging process. For example, during charging of the CAM (NCM), deintercalation of Li-ions occur, thus resulting in a simultaneous increase in vacant interstitial sites and decrease in occupied interstitial site. This leads to an increase in the second logarithmic term and thus an increase in the electrode potential of the positive electrode (E_{cathode}). Parallel to this, intercalation of the Li-ions in the anode will lead to a decrease in vacant interstitial sites and an increase in occupied interstitial site. This leads to a decrease in the second logarithmic term and thus a decrease in the electrode potential of the negative electrode (E_{anode}). Together, the processes at both cathode and anode will lead to an increase in ΔE ($E_{\text{cathode}} - E_{\text{anode}}$), which meant an increase in the voltage of the electrochemical cell. The opposite is true during the discharge stage.

1.3. Positive Electrode (Layered Transition Metal Oxides, LiTMO₂)

Before describing the layered Ni-rich transition metal oxides that are used in this study, a brief introduction to its origin will be given and how they became such a widely used CAM in state-of-the-art LIBs. The pioneering material for this category of CAMs was lithium cobalt oxide (LCO), which was jointly developed by the group of John B. Goodenough and later made commercially available by Sony.²⁴ LCO has relatively good cycling performance and is still used in commercialized LIBs. However, despite its high theoretical capacity (274 mAh/g), it only has a practical capacity of ~140 mAh/g within the voltage range of 2.5 V – 4.2 V vs Li⁺/Li.^{25,26} The limited voltage window is designed to allow ~ 50% lithium extraction and is done in order to prevent both structural and (electro)chemical instabilities. During the same period, a material possessing extremely high theoretical specific capacities like LCO was discovered, which was LiNiO₂ (LNO). At that time, it was regarded as the most promising CAM, in part due to its high specific capacities and the availability/abundance of its elements. However, after decades of research, the problems inhibiting its commercialization persists. LNO suffers from stability issues, which are both (electro)chemical and mechanical in nature. An example of an (electro)chemical instability is seen at high degrees of delithiation (i.e., high SOC), phase transition occurs forming highly reactive Ni⁴⁺ ions, which may react with surrounding electrode components such as the electrolyte to form resistive interphases. Furthermore, large volume changes from phase transitions around 4% can lead to mechanical separations within the primary particle as well as with surrounding electrode components such as the solid electrolyte in SSBs.^{27–30} In addition, thermal instabilities were also reported, which further limits its viability in a commercial LIB.³¹ Therefore, in the past few decades, substitution of Ni with other transition elements such as Co, Mn and/or Al to suppress the various instabilities has led to the discovery of the current state-of-the-art CAMs such as LiNi_{1-x-y}Co_xAl_yO₂ (NCA) or LiNi_{1-x-y}Co_xMn_yO₂ (NCM). The different substituted elements all have a role in achieving a balance between electrochemical performance and safety.^{32,33} First, the substitution of Mn or Al improves the stability and cycle life as these substituted transition elements do not undergo changes in its valence states during charge and discharge and is thus not participating in the redox process. Second, there will be less Ni²⁺ ions available in the transition-metal oxide framework, thus the phase transformation to a rock-salt structure and forming the reactive Ni⁴⁺ ion is suppressed. Another common substitution is Co, but in lower contents due to cost and political issues. However, Co substitution improves the electronic conductivity of the CAM and enables high-rate capabilities. In recent years, higher Ni-content CAMs that are relatively stable within a set voltage range are used in state-of-the-art LIBs, to the point where the next possible composition will be LNO itself. Thus, progress in high Ni-content CAMs have in a way revitalized the research in overcoming the inherent stability issues in LNO. Representative voltage profiles for different Ni-content layered transition metal oxides are depicted in **Figure 1.2** with their characteristic electrochemical properties listed in **Table 1**.

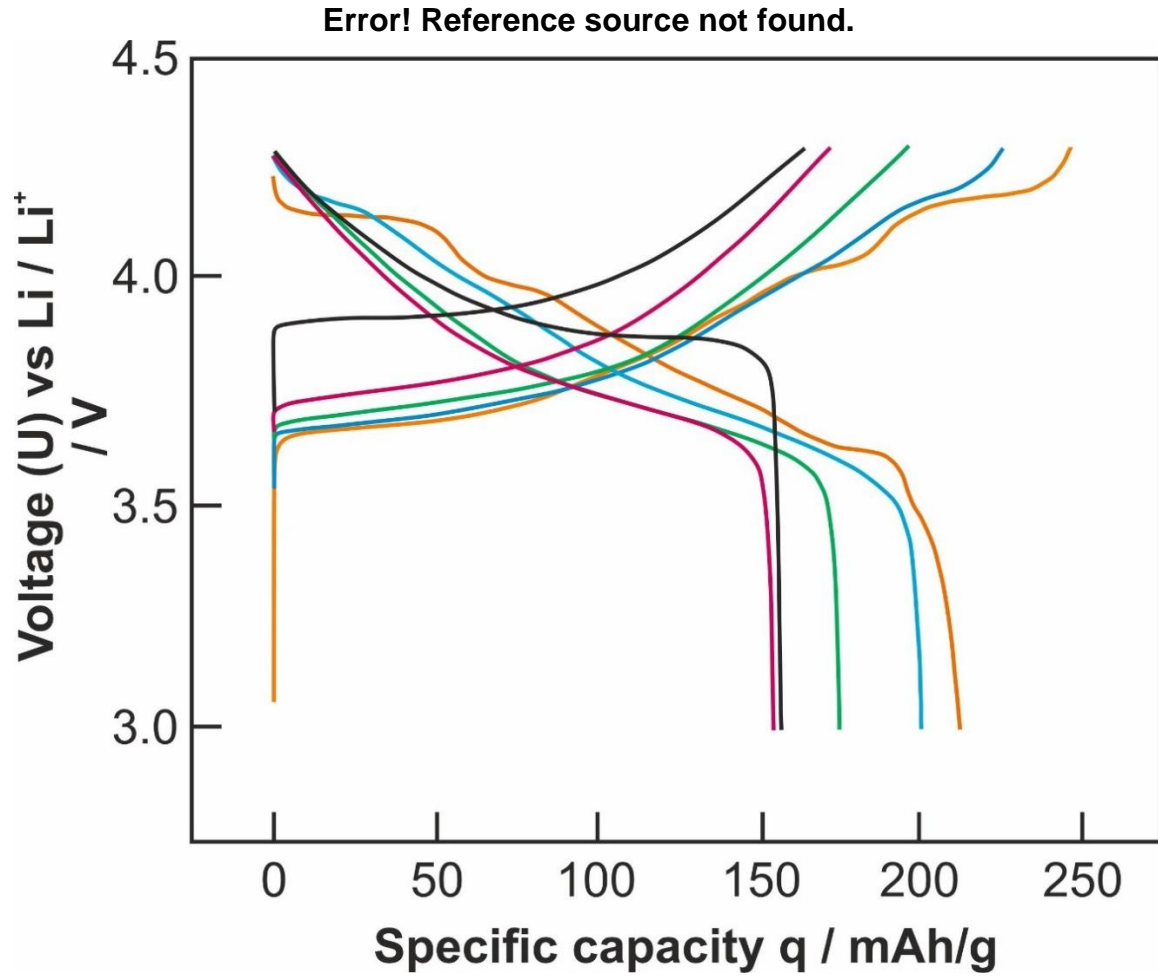


Figure 1.2 Representative 1st cycle voltage profiles for common layered transition metal oxides with LCO represented in black, NCM111 in red, NCM622 in green, NCM851005 in blue and LNO in orange. The cells are cycled in a liquid-based LIB against a Li metal anode at C/10 and 25°C in the voltage range 3.0 – 4.3 V. LP5 was used as the liquid electrolyte (Ref. Bella Group).

Table 1 Specific charge/discharge capacities (q_{ch} and q_{dis}) and their respective mean charge/discharge (\bar{U}_{ch} and \bar{U}_{dis}) of the cathode active material with compositions LiCoO_2 (LCO), $\text{LiNi}_{0.33}\text{Co}_{0.33}\text{Mn}_{0.33}\text{O}_2$ (NCM111), $\text{LiNi}_{0.6}\text{Co}_{0.2}\text{Mn}_{0.2}\text{O}_2$ (NCM622), $\text{LiNi}_{0.85}\text{Co}_{0.1}\text{Mn}_{0.05}\text{O}_2$ (NCM851005) and LiNiO_2 (LNO).

Cathode active material	$q_{\text{ch}} /$ mAh g^{-1}	$q_{\text{dis}} /$ mAh g^{-1}	$\bar{U}_{\text{ch}} /$ V	$\bar{U}_{\text{dis}} /$ V
LCO	164	157	4.00	3.96
NCM111	172	155	3.90	3.85
NCM622	196	175	3.87	3.83
NCM851005	225	200	3.88	3.85
LNO	247	212	3.90	3.86

From **Figure 1.2**, it can be seen that with increasing Ni content (NCM851005 and LNO), distinct plateaus in the high-voltage regimes could be seen. These plateaus are representative of phase transitions within the crystal structure, which lead to decreasing crystal lattice stability. The destabilizing effect increases with increasing Ni content and is a major influencing factor to capacity fading.^{27,34}

The crystal structure of all layered transition metal oxides is a layered α -NaFeO₂ structure ($R\bar{3}m$), regardless of the Ni content. While the transition metal atoms (Ni, Co, Mn and Al) occupy the Wyckoff 3a sites randomly, the Li occupies the 3b sites (**Figure 1.3**).^{35–37} Both Li and transition metal atoms are coordinated by oxygen atoms on the octahedral 6c sites and these octahedra are stacked on top of each other along the c-axis in an alternating ABC sequence, which allows the Li ions to move (intercalate/deintercalate) perpendicular to the c-axis during cycling.

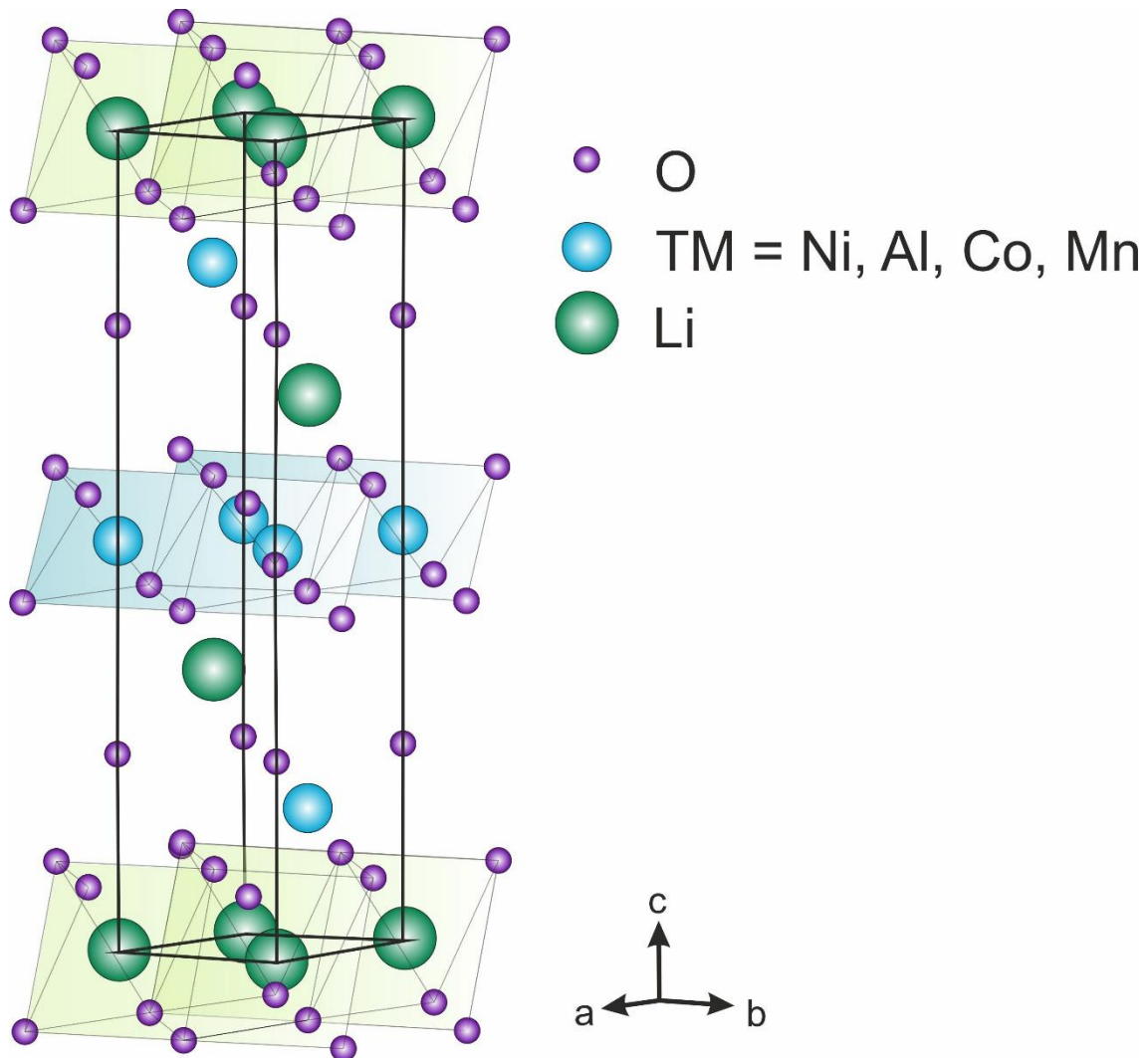


Figure 1.3 Unit cell of the layered transition metal oxide [Li(TM)O₂] with crystal structure $R\bar{3}m$.

1.3 Introduction – Positive Electrode

The cause of the stability problem is related to the phase transformation from layered to a rock-salt structure that begins near the outermost surface of the NCM. Moreover, the destabilizing transformation is associated with the formation of Ni^{4+} ions, large volume changes and the release of highly reactive oxygen molecules. These highly reactive oxygen molecules are crucial to this study as their reaction with electrode components can produce gaseous byproducts. By studying and quantifying these gaseous byproducts, we can indirectly gain an insight into the many underlying mechanisms within the electrode during cycling. In the first publication, an investigation into the gaseous byproducts of thiophosphate-based SSBs was performed and compared with that of a conventional liquid-based LIB. The study showed that sulfur-species were oxidized by the highly reactive oxygen to form toxic SO_2 gas in the process. In Publication 2, the investigation of gaseous products was used to screen electrode components such as carbon additives and polymer binder. The study showed that certain binder chemistries were more susceptible to oxidation by the highly reactive oxygen, resulting in increase CO_2 gas evolution. Furthermore, in some binder chemistries, an increase in SO_2 gas evolution was observed, which was attributed to a binder-involved destabilization of the thiophosphate solid electrolyte. Publication 3 was focused on the mitigation of the mechanical instability caused by the volume changes (i.e., phase transition) of the NCM during cycling. By using a SE with lower Young's modulus together with improved processing techniques, mechanical separations can be suppressed. These results were verified with a distinct difference in oxygen evolution and would be further elaborated in **Chapter 4**.

1.4. Negative electrode ($\text{Li}_4\text{Ti}_5\text{O}_{12}$)

$\text{Li}_4\text{Ti}_5\text{O}_{12}$ (LTO) is another interstitial electrode with very stable characteristics. Because of its high stability during prolonged cycling, it was chosen as the anode material of choice for all the bench testing of SSBs in our study. Specifically, the anode consists of a composite of LTO, carbon additives and solid electrolyte in an optimized ratio. Its popular use in SSBs is primarily due to its negligible volume change during cycling. It is widely known as a zero-strain insertion material and its lattice parameters remain almost unchanged during insertion and extraction. In addition to its stability, it also has a flat voltage profile. These characteristics make it an attractive anode material for isolating differences in electrochemical performance, crystal structure, among others, to purely the CAM. As an anode in an uncharged state, LTO crystallizes in the spinel structure with the ($\text{Fd}\bar{3}m$) space group (**Figure 1.4**). Li occupies fully the tetrahedral 8a sites and partially the octahedral 16d sites. The remaining octahedral 16d sites are then occupied by Ti^{4+} ions. The randomly distributed Li and Ti^{4+} ions in the octahedral 16d sites are coordinated with oxygen in a cubic close packed structure. Since the octahedral 16c, tetrahedral 8b and 48f sites are empty, they are capable of Li insertion/extraction. During intercalation, LTO can allow up to three lithium ions per formula unit, allowing it to achieve a theoretical specific capacity of 175 mAh/g. Alongside the insertion of Li^+ ions, the Ti^{4+} ions undergo a redox reaction which results in a phase transformation of the spinel structure to a rock-salt structure ($\text{Li}_7\text{Ti}_5\text{O}_{12}$). This transformation starts at the outermost surface and proceeds inwards, eventually transforming the entire particle from a spinel structure to a rock-salt structure (**Figure 1.5**).

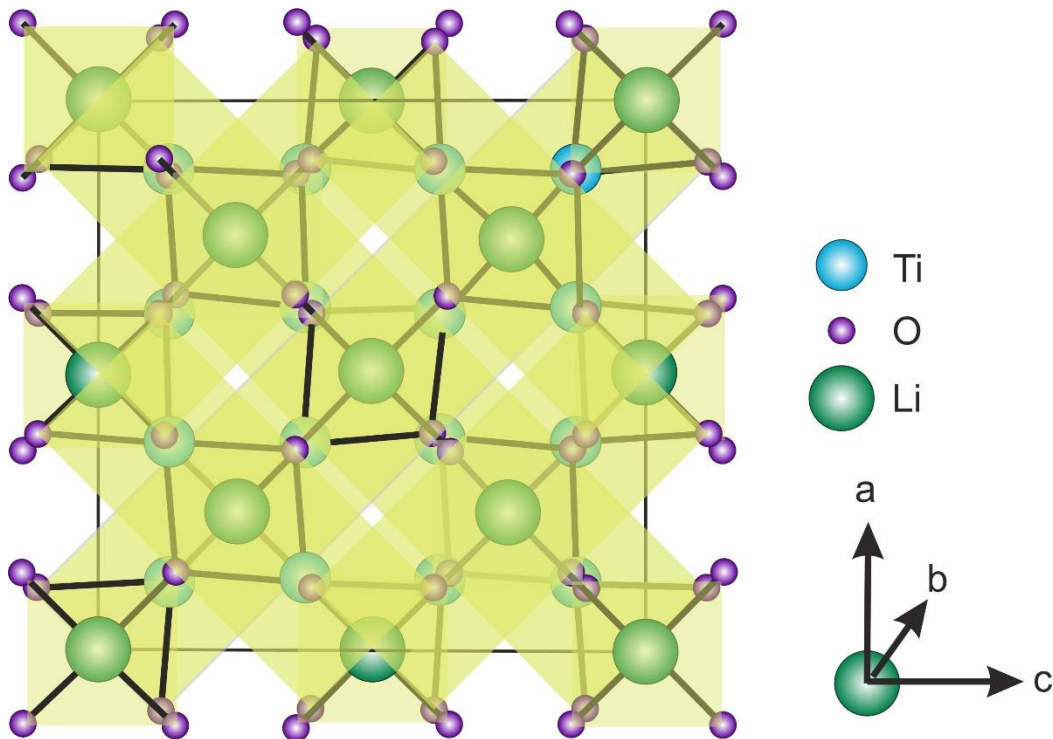


Figure 1.4 Unit cell of spinel $\text{Li}_4\text{Ti}_5\text{O}_{12}$ with crystal structure $\text{Fd}\bar{3}m$.

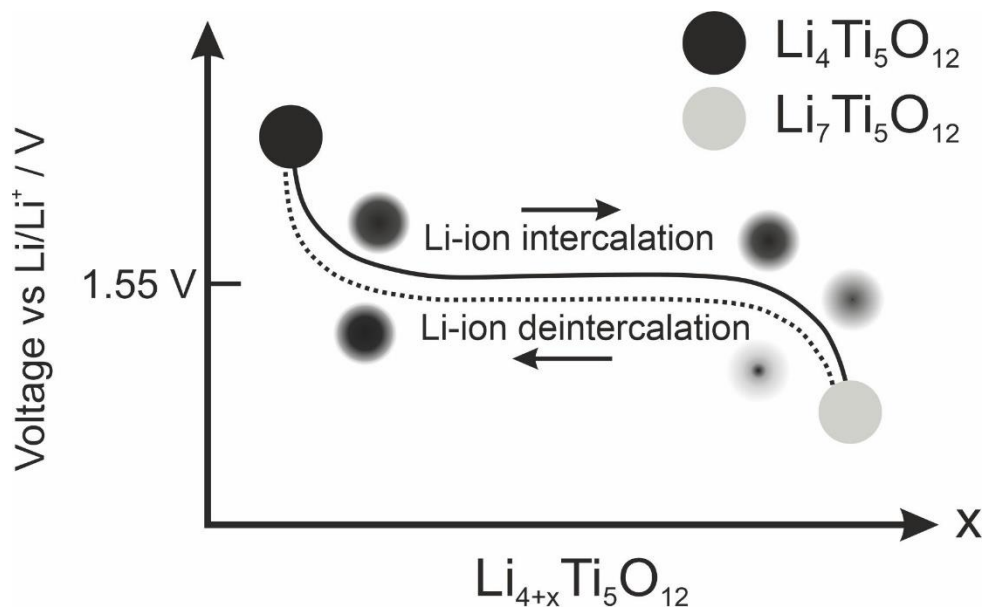


Figure 1.5 Voltage profile of $\text{Li}_{4+x}\text{Ti}_5\text{O}_{12}$ as it transitions from spinel- $\text{Li}_4\text{Ti}_5\text{O}_{12}$ to rock-salt- $\text{Li}_7\text{Ti}_5\text{O}_{12}$ with graphical representation of the transformation (starting at the outermost surface inwards).

2. In Situ Gas Analysis

2.1. Differential Electrochemical Mass Spectrometry (DEMS)

In this study, we mainly use differential electrochemical mass spectrometry (DEMS) to investigate and enable the transition of SSBs from lab- to industrial-scale. A brief history into the development of electrochemical mass spectrometry (EMS) will be provided in the following sections and will help provide an understanding of the advantages/disadvantages of the system employed in our lab.³⁸ Two system of application of mass spectrometry on electrochemical cells were developed and are still used until this day. The first system was developed by Bruckenstein and Gadde in 1971.^{39,40} The characteristic design of this system is the closed vacuum reservoir, where gaseous species are first accumulated and later transferred to the mass spectrometer (MS). Therefore, the measured ionic current is the total concentration of a gaseous species and is represented as an integral signal. Another system developed by Wolter and Heitbaum had a design difference in the form of a continuously pumping inlet system between the MS and the electrochemical cell, thus the concept of “differential”.⁴¹ This meant that the gaseous species evolved were measured as a function of time (time-resolved ion current). The continuous purging of evolved reaction gaseous products increased the sensitivity of detection and enabled the investigation of smaller quantities of gaseous products.^{42,43} Despite the improved sensitivity, the differential/continuous purging system (DEMS) is not optimal for investigating gas evolution in LIBs as the electrolyte gets depleted over time and could result in non-representative results. Moreover, a differential system requires a flow rate of at least 1 mL/min, which is considered large for a battery cell, which typically has an electrolyte volume of ~10 – 100 μ L (for a small area 1cm² cell). This has resulted in the further development of the EMS system with a closed system. To that end, McCloskey *et al.* developed a new interface system, improving upon the initial setup developed by Bruckenstein and Gadde.⁴⁴ The setup allows purging of accumulated gaseous products in defined intervals. A similar setup employed by Gasteiger *et al.* but with an addition of a crimped-capillary leak had a reported response time of ~1 s (versus DEMS ~30 s).^{45,46} Moreover, the group of Gasteiger was able to modify the setup, allowing the separate detection of gas evolution originating from both the anode and cathode side.^{46,47} Despite the various advantages of the system, there is a significant downside. These systems have a single stage pressure reduction (as opposed to DEMS), leading to mass fractioning of the evolved gaseous products.⁴⁵ The disadvantages led Berkes *et al.* to develop a differential/continuous purging system for use in our lab, which was also shown to be suitable for long-term studies of LIBs. A graphical representation of the setup is depicted in Error! Reference source not found.. This was made possible by the incorporation of an electrolyte reservoir that prevents electrolyte dry-out from the continuous purging.⁴⁸

2.1 Differential Electrochemical Mass Spectrometry (DEMS)

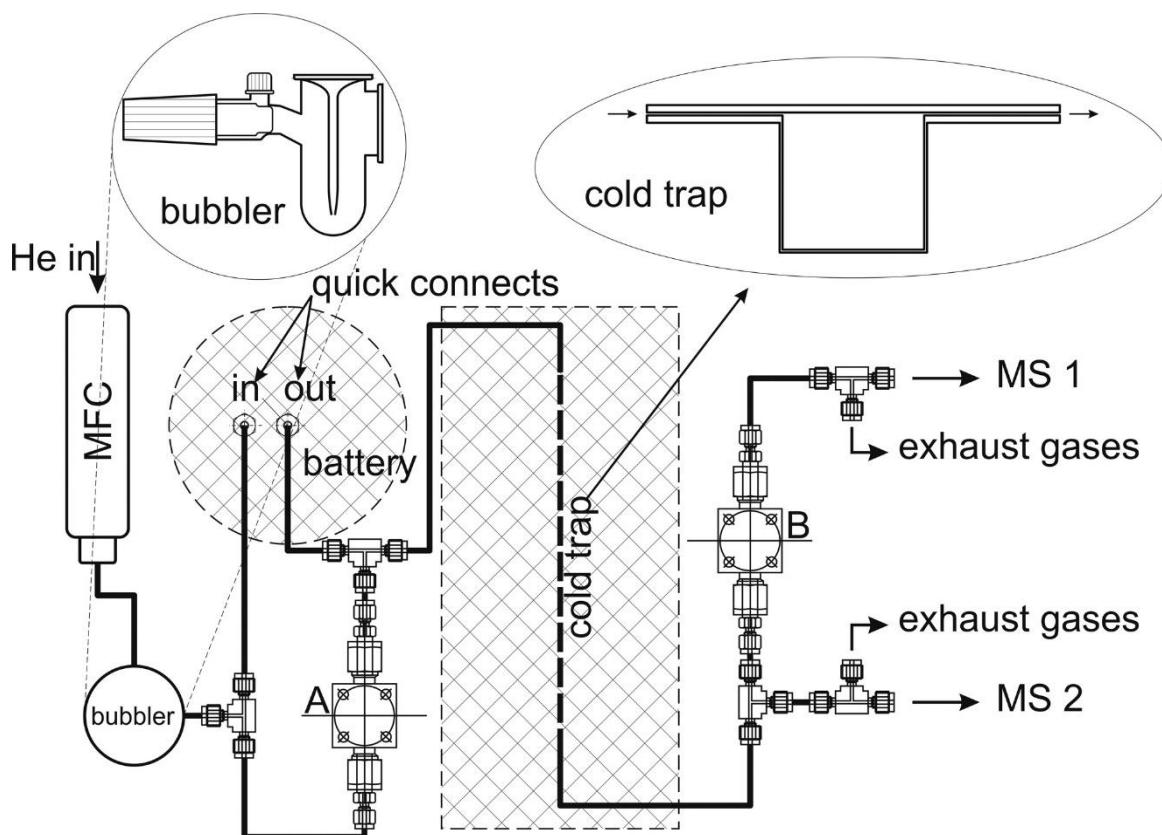


Figure 2.1 Graphical representation of the DEMS setup. The individual components are labeled accordingly.⁴⁸

The DEMS setup starts with two mass flow controllers (F-201CV-020-RAD-33-Z), each regulating the flow rate of the carrier and calibration gas respectively. The stepwise increment/decrement of the calibration/carrier gas at the end of the measurement is required to quantify the amount of gas evolved during cell operation. The calibration gas is a mixture of gaseous species (e.g., H₂, CO₂, O₂, CO, N₂) with a known amount of concentration (ppm).

In this continuous flow system, the carrier gas of choice is Helium (He) and is used to flush the cell continuously during cycling and thus sending all evolved gasses to the MS. Helium fulfills all the experimental conditions of being both inert and possessing a singular mass signal ($m/z = 4$). Despite being inert as well, Argon (Ar) was not chosen as a carrier gas. This is attributed to its high collision energy and high fragmentation. The high collision energy could cause potential damage to the detector, while the high fragmentation creates a variety of mass signals ($m/z = 18, 20, 36$ and 40), which causes an increase noise-to-signal ratio.

A series of stainless-steel tubing (1/16") connects the individual components (MFC, bubbler, battery, cold trap and mass spectrometer together). The cold trap is installed between the battery and the mass spectrometer (Pfeiffer Omnistar GSD 320 O2), which acts as a solvent trap for electrolyte vapor, preventing it from reaching the MS and damaging it. Both the cold trap and electrolyte-bubbler are not needed for the solid-state battery configuration (SSB-DEMS) as there is no liquid electrolyte present. The customized cell body for the measurement of LIB-DEMS⁴⁸ has been redesigned,

2.1 Differential Electrochemical Mass Spectrometry (DEMS)

modified and optimized for SSB-DEMS measurements and is depicted in Error! Reference source not found..

2.1 Differential Electrochemical Mass Spectrometry (DEMS)

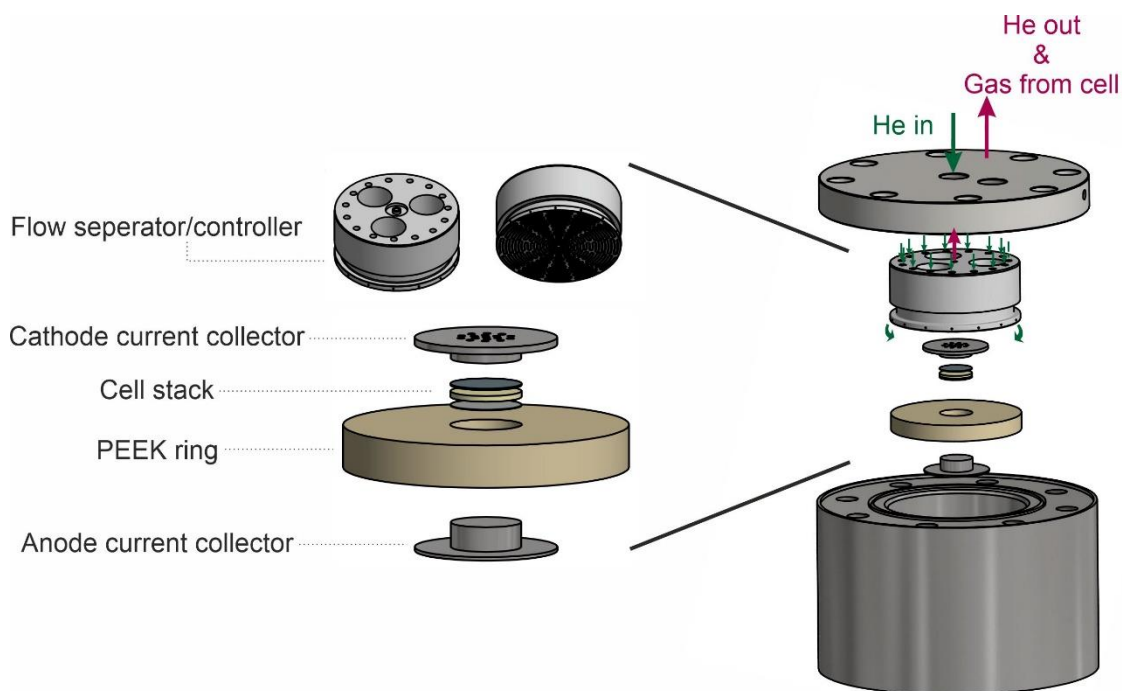


Figure 2.2 Modified design of the DEMS cell design for use in SSB-DEMS analysis. Flow of the carrier gas and the evolved gas during cycling is indicated.

The SSB-DEMS customized cell consists of a solid stainless-steel body to reduce residual moisture from potentially influencing the measurement, as moisture-susceptible materials were being investigated throughout the study. The cell stack is cold-pressed within a polyether ether ketone (PEEK) ring in a customized mold prior to assembly in the stainless steel cell body. The cell stack together with the PEEK ring is sandwiched between the cathode and anode current collector. The cathode current collector is designed with multiple holes (diameter = 1 mm) to allow for ease of gas flow. The flow separator/controller component has a set of O-rings to control and separate the stream of incoming and outgoing gas. Temperature control is regulated with the help of a Peltier element, which in the case of the SSB-DEMS is set at 45 °C.

A comparison between the old setup with a freestanding cell stack (prior to customization and optimization) showed a distinct difference in gas evolution. With the customized and optimized cell, we noticed an increase in measurement sensitivity in the form of larger quantity of gas evolution (**Figure 2.3**). The increase gaseous signals can be attributed to both a smaller dead volume within the cell body and increased electrochemical performance. The presence of a PEEK ring and current collector reduces the amount of dead volume and helps direct the released gas towards the outlet. Moreover, the encasement of the cell stack within a PEEK ring reduces mechanical defects during assembly and cycling, which contributed to an improved electrochemical performance. Unfortunately, to electrically isolate the cathode and anode from each other, the ring must be made from PEEK, which is not as moisture resistant as stainless-steel. Thus, the PEEK is dried at 80°C under vacuum over prolonged periods prior to use.

2.1 Differential Electrochemical Mass Spectrometry (DEMS)

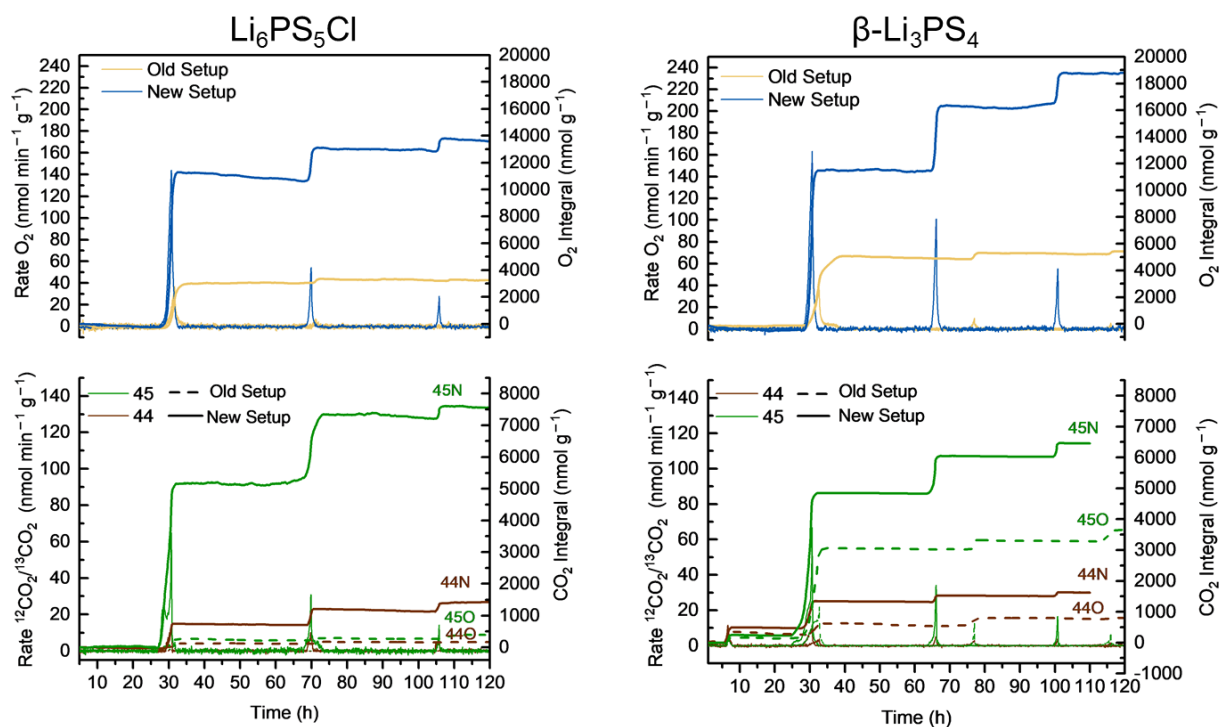


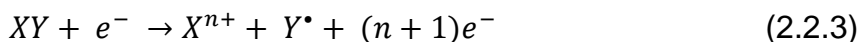
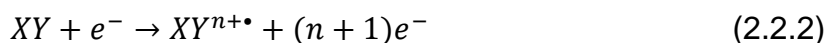
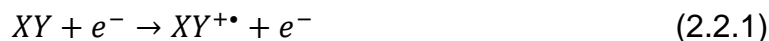
Figure 2.3 Representative O_2 , $^{13}\text{CO}_2$ and $^{12}\text{CO}_2$ gas evolution of two thiophosphate-based SSB ($\text{Li}_6\text{PS}_5\text{Cl}$ and $\beta\text{-Li}_3\text{PS}_4$) in both the old (free-standing) and new (sandwich in PEEK) setup

2.2. Mass Spectrometry

Mass spectrometry, as its name suggest is an analytical technique to separate/filter molecular fragments by their individual mass to charge (m/z) ratio. Mass spectrometers rely on different approaches to separate the fragments, ranging from use of electric force (separation based on kinetic energy) to magnetic force (separation based on momentum) and even by their time-of-flight (separation based on velocity). A mass spectrometer consists of four main components, namely the gas inlet valve, the ion source, the mass analyzer/filter and the detector. A pump system is connected to these components, most likely as a combination of a diaphragm and turbo pump. In general, a low-pressure environment is required for mass spectrometry. In the case of the Pfeiffer Omnistar GSD 320 O2 mass spectrometer, the low-pressure environment is achieved by an interstage pumping system. The pressure is incrementally lowered from the gas inlet system to the ion source, quadrupole mass analyzer and the detector.

The evolved gases enter the mass spectrometer through a heated capillary system to the gas inlet valve. As part of the gas inlet system, the heated capillary can reduce the pressure from atmospheric pressure down to $\sim 700 - 1000$ hPa ($1 \text{ hPa} = 100 \text{ Pa}$), allowing for a laminar flow into the vacuum chamber. The next pumping stage begins with a diaphragm pump reducing the pressure down to a range where the turbo pump is able to operate (< 10 hPa). After which, the turbo pump kicks in and reduces the pressure down to $\sim 10^{-8}$ hPa, which is required to prevent interactions/collisions between molecular species or ions and improve the noise-to-signal ratio.

The gaseous species then enters the ionization chamber and are ionized with the help of an ion source, which in our case is an yttrium-coated Iridium filament that has an operating temperature of 1300°C (**Figure 2.4**). As the filament gets heated, it produces an ionizing electron beam by thermionic emission, which is accelerated towards an oppositely charged electrode plate and to an electron trap. The incoming neutral gaseous molecules passes through the electron beam and is ionized in a process called electron ionization (EI) or electron impact ionization.⁴⁹ EI is a process where neutral species can generate a molecular ion by collision with an electron. In practice, the electrons emitted from the ion source are accelerated to energies much higher than the minimal energy required to ionize the gaseous species. Generally, electrons with energy in the range between $60 - 80 \text{ eV}$ are used to impact the neutral gaseous species and ionize them. The ionization leads to the formation of different type of ions, which includes single charged ion ($XY + e^- \rightarrow XY^{+\bullet} + e^-$ (2.2.1), multiply charge ions $XY + e^- \rightarrow XY^{n+\bullet} + (n+1)e^-$ (2.2.2), molecular fragments $XY + e^- \rightarrow X^{n+} + Y^\bullet + (n+1)e^-$ (2.2.3) or ion-pairs $XY + e^- \rightarrow X^+ + Y^- + e^-$ (2.2.4).⁵⁰



Ionization chamber Linear quadrupole

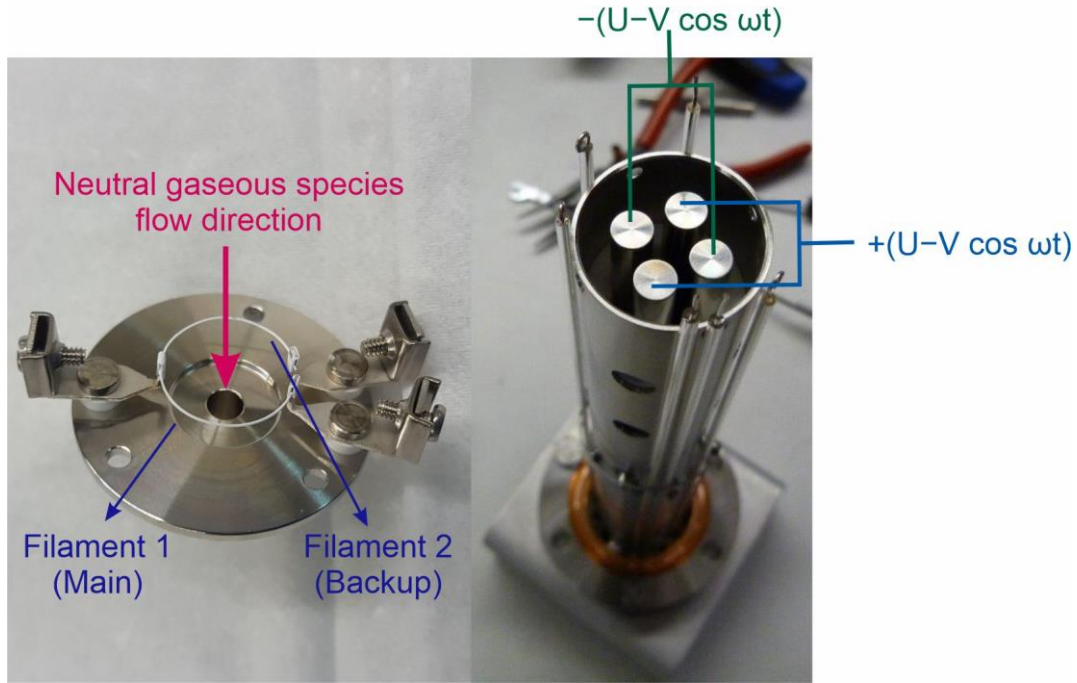


Figure 2.4 Photograph of the ionization chamber (left) and the linear quadrupole/mass filter (right) used in the mass spectrometer Omnistar GSD320

The ionized species are directed towards the linear quadrupole, where they get separated according to their (m_i/z) value. The linear quadrupole mass analyzer/filter consists of four cylindrically shaped rod electrodes positioned symmetrically in a square configuration. A voltage possessing both a DC (U) and an AC (V) component is applied to these rods, resulting in the generation of a periodically alternating electric force with angular frequency ω . A top view image of the quadrupole mass analyzer is shown in **Figure 2.4**, where two rods opposite each other have the same potential of either $-(U - V \cos \omega t)$ and $(U - V \cos \omega t)$. The alternating electric force exerts a periodic attractive and repulsive force on the ions in the x - and y -direction, which propels them to pass through the quadrupole in a sinusoidal path along the length of the rods. As long as certain parameters are maintained, the ions would pass through without touching the rods. These parameters can be mathematically represented by solving for both the equations of motions and the total potential. The total potential at a position in the x - y plane $[\Phi(x, y)]$ between the four rods is given by equation (2.2.5)(2.2.5).

$$\Phi(x, y) = \frac{(x^2 - y^2)(U - V \cos \omega t)}{r_0^2} \quad (2.2.5)$$

r_0 is the distance from the center of the square configuration to the rod. The equation of motion is given by equation (2.2.6).

$$\vec{F} = m\vec{a} = -ze\vec{V}\Phi \quad (2.2.6)$$

2.2 Mass Spectrometry

a is the acceleration of the ions. From (2.2.6), we see the relationship between the potential applied on the rods and the motion of the ionized ions. The substitution of equation (2.2.5) into (2.2.6) and solving it will result in the Paul equations ((2.2.7) and (2.2.8)).

$$m\vec{a} = -ze\vec{V}\Phi$$

$$\rightarrow F_x = m \frac{d^2x}{dt^2} = -ze \frac{\partial \Phi}{\partial x} \quad \rightarrow F_y = m \frac{d^2y}{dt^2} = -ze \frac{\partial \Phi}{\partial y} \quad (2.2.7)$$

$$\frac{d^2x}{dt^2} + \frac{2ez}{mr_0^2} (U - V \cos \omega t)x = 0 \quad (2.2.8)$$

$$\frac{d^2y}{dt^2} - \frac{2ez}{mr_0^2} (U - V \cos \omega t)y = 0$$

To solve equation (2.2.8), we make use of the Mathieu equations, whose solutions are known. To that end, equation (2.2.8) is rewritten with dimensionless parameters a and q to resemble that of the Mathieu equations giving equation (2.2.9).

$$\frac{d^2x}{d\tau^2} + (a_x - 2q_x \cos 2\tau)x = 0 \quad (2.2.9)$$

$$\frac{d^2y}{d\tau^2} - (a_y - 2q_y \cos 2\tau)y = 0$$

, with the dimensionless parameters a and q given as:

$$a_x = -a_y = \frac{8zeU}{m_i \omega^2 r_0^2} \quad q_x = -q_y = \frac{4zeV}{m_i \omega^2 r_0^2} \quad \tau = \frac{\omega t}{2} \quad (2.2.10)$$

These parameters can be plotted against one another (a vs. q), giving a graphical representation of the region of stable flight path of the ions ("stability diagram"). Since the values ω and r_0 are kept constant in an operating mass spectrometer, a and q are considered proportional multiplications of the variables U and V . Equation (2.2.10) can also be rewritten to equation (2.2.11).

$$U = a_x \left(\frac{m_i}{z} \right) \frac{\omega^2 r_0^2}{8e} \quad V = q_x \left(\frac{m_i}{z} \right) \frac{\omega^2 r_0^2}{4e} \quad (2.2.11)$$

3. Slurry-casting of All-solid-state batteries

Equation (2.2.11) shows that the parameters U and V are proportional to (m_i/z) . Thus, by varying U and V , while keeping the U/V ratio constant, the quadrupole is able to scan/filter for different masses (m_i/z) . However, this also meant that for a given U and V at a given time, only one specific (m_i/z) is allowed to pass through the quadrupoles. Thus, for a mass spectrometer that scans multiple masses, an important requirement is that the time needed for the ions to pass through the analyzer is much faster than the time it takes for the quadrupole to switch to another mass.

The ions leaving the mass analyzer in our system could be detected with either a Faraday cup or a secondary electron multiplier (SEM) (**Figure 2.5**). While the Faraday cup is located behind the quadrupole mass analyzer, the SEM is positioned 90° away from the mass analyzer axis. The ions are deflected away from the mass analyzer axis towards the SEM with a metal mesh. Neutral species, photons and electrons travel unaffected through the metal mesh along this axis and does not enter the SEM, thus preventing them from contributing to the background signal. In our studies, the detection of choice is with the SEM. The SEM consists of a conversion and a continuous dynode. The conversion dynode is an electrode and converts incoming ions into electrons to be accelerated in the continuous dynode. The continuous dynode is shaped as a curved funnel with the inner walls coated with an isolator, thus providing a uniform resistance along the length of the dynode. A voltage is applied to the dynode with values decreasing along the dynode towards the bottom (i.e., the ground potential). Electrons entering the dynode are propelled to move along the length of the dynode towards the ground potential. In doing so, the electrons travel through the funnel by colliding continuously with the inner walls and every collision causes the emission of an electron. A cascade of electrons is produced, which when added up provide an amplified electric current that is recorded.

Secondary electron multiplier

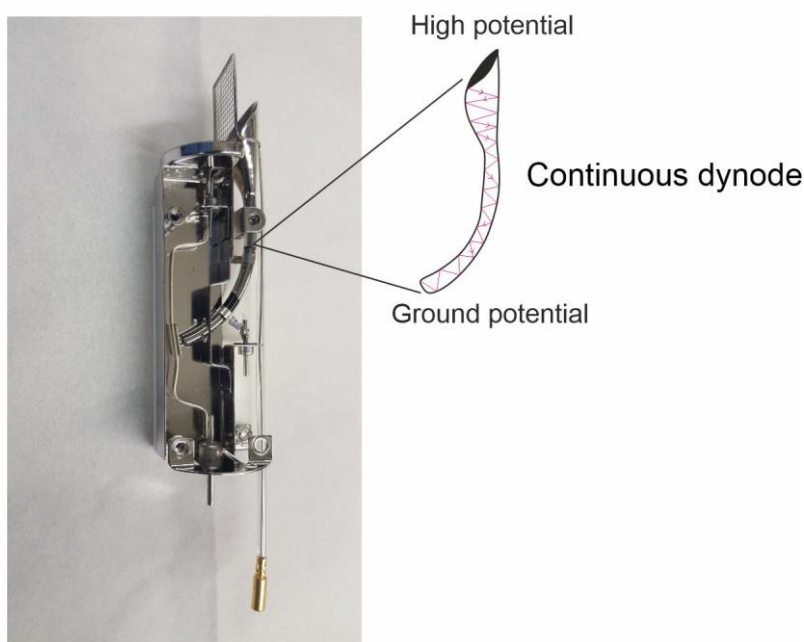


Figure 2.5 Photograph of the secondary electron multiplier (SEM) used in the mass spectrometer Omnistar GSD320

3. Slurry-casting of All-Solid-State batteries

3.1 Motivation

Within the last decade, exponential growth in the research and development of powder-based pelletized SSBs has shown increasing competitiveness in terms of performance with state-of-the-art liquid-based LIBs, while providing additional safety improvements to the cell. This has led SSBs joining the few elite LIB systems that would eventually succeed the liquid-based LIBs. This success on the laboratory scale has prompted growing interest in transitioning the technology to an industrial scale. However, the laboratory preparation techniques for SSBs involve a series of complex steps, which are not directly transferable to large volume fabrication processes on an industrial scale (e.g., roll-to-roll processing). Drawing inspiration from the processing of LIBs that has been modified and optimized over the past three decades, there have been attempts to make SSBs possess the needed mechanical stability and flexibility for roll-to-roll processing. This would require a shift towards sheet-based designs, incorporating a non-active polymer component (binder), prepared through either a wet chemical process or a high viscosity process.¹² In the wet chemical process, the electrode components including the binder is dispersed in a suitable solvent, creating a slurry. In contrast, the high viscosity process is solvent-free and involves the (mechanical) mixing of all solid components including the binder at an elevated temperature, creating a highly viscous paste. This processing method is however outside the scope of this study, and we chose to focus primarily on wet-chemical processing.

3.2. Selection of solvent and binder

In a wet-chemical process, the solid components (including the binder) are dispersed in a suitable solvent, resulting in a dispersion called a slurry. The development of a homogeneous and stable slurry suspension is not trivial and extremely challenging, considering the large number of parameters needed to be optimized. These parameters include the solvent properties (e.g., volatility, viscosity, polarity, toxicity, etc....) and the binder properties (e.g., molecular mass, reactivity, solubility, etc....).

3.2.1. Solvent-related parameters

Solvent properties such as the volatility (vapor pressure), polarity, inertness (towards the electrode components) and toxicity have to be taken into account.⁵¹ The physical and chemical properties of commonly used solvents (both in LIBs and SSBs) are compiled in **Table 1**.^{52–55} For instance, the vapor pressure of the solvent can determine the quality (homogeneity, mechanical property and electrochemical performance) of the electrode sheet. Solvents possessing a high vapor pressure ($> 7\text{ kPa}$) would be very volatile and evaporate almost immediately after casting, leaving behind uneven rough surfaces.^{51,56} For example, N-Methyl-2-pyrrolidone (NMP) is a commonly used solvent for LIBs electrode fabrication as it possesses a low vapor pressure of 0.04 kPa , albeit a high polarity index (PI) of 6.7. The polarity of the solvent is an extremely important parameter in sheet fabrication (especially for SSBs) and its consideration depends largely on the type of components used. In the case of SSBs, the type of solid

3. Slurry-casting of All-solid-state batteries

electrolyte largely determines the type of solvent that can be used. Sulfide SEs have a very high reactivity towards polar protic solvents with a high PI value, which leads to the degradation of the SE and is typically indicated visually by a change in the color of the suspension.^{51,56,57} The degradation of solvent-treated SEs have been reported experimentally by utilizing analysis techniques such as Raman spectroscopy, X-ray photoelectron spectroscopy (XPS), X-ray diffraction (XRD) and electrochemical impedance spectroscopy (EIS). After dispersion of a sulfide SE in a polar protic solvent, Raman spectroscopy showed depressed/missing PS_4^{3-} signals ($\sim 426 \text{ cm}^{-1}$) and additional signals, which indicates both the partial degradation of the sulfide SE structure and the formation of impurities, respectively.⁵⁷ The formation of impurities can be further supported with XPS spectra data. An example can be seen in the form of a widened P2p spectra for the THF-treated $\text{Li}_6\text{PS}_5\text{Cl}$, revealing the formation of PO_4^{3-} -containing impurities. XRD analysis was also reported to confirm the partial decomposition of the core SE structure into the crystal structure of the precursors, which form as impurities after solvent treatment. The mechanism of solvent-induced degradation reactions is reported to be a nucleophilic attack by the solvents on the SE.⁵⁸ Thus, for sulfide SEs, the use of non-polar solvents is a mandatory requirement for the successful fabrication of high performance sulfide SSB electrodes.

Table 2 Properties of organic solvents used in lithium-ion fabrication

Solvent	d^a (g cm^{-3})	μ^b (mPa s)	LD_{50}^c ($\text{g}_{\text{oral}}\text{Kg}_{\text{rat}}^{-1}$)	p^{*d} (kPa)	PI^e
Acetonitrile (ACN)	0.79	0.34	6.69	11.81	5.8
N-Methyl-2-pyrrolidone (NMP)	1.03	1.70	3.91	0.04	6.7
Acetone	0.78	0.30	5.80	30.72	5.1
Ethanol, absolute (EtOH)	0.78	1.08	10.47	7.85	4.3 ^f
2-Propanol	0.78	2.04	5.05	5.76	3.9
Tetrahydrofuran (THF)	0.89	0.46	2.45	21.55	4.0
Toluene	0.86	0.55	5.58	3.79	2.4
Hexane	0.65	0.29	25.00	20.12	0.1
Heptane	0.68	0.41	5.00	4.6	0.1
<i>p</i> -Xylene	0.86	0.60	4.03	1.17	2.5
<i>o</i> -Xylene	0.88	0.76	3.61	0.886	2.5

^a d : density and data from ref. 53 (Kosuke Izutsu Electrochemistry in Nonaqueous Solutions)

^b μ : viscosity and data from ref. 53 (Kosuke Izutsu Electrochemistry in Nonaqueous Solutions)

^c LD50: measure of toxicity, median lethal dose Oral (rat), data from Material Safety Data sheets of Sigma-Aldrich and Hazardous Substances Data Bank (HSDB)

^d p^* : specific vapor pressure at 25°C and data from ref. 53 (Kosuke Izutsu Electrochemistry in Nonaqueous Solutions)

^e PI : Polarity index from ref. 55 (L. R. Snyder Classification of the Solvent Properties of Common Liquids 1978)

^f One or more K values missing. No reasonable estimate possible

Unless stated otherwise, data are representative at 25 °C. Temperatures other than 25 °C are shown as subscript. (e.g. 2.5₂₀)

3.3. Slurry-casting of All-solid-state batteries - sheet fabrication process

In the case of oxide-based SEs, the choice of solvents are not limited to non-polar solvents, since they are shown to be relatively stable with respect to polar aprotic solvents.^{59,60} The reason for their stability towards polar solvents is attributed to the inherent chemical stability of oxides and at first glance is an ideal chemistry for sheet-based processing of SSBs.^{12,61} However, the bottleneck for oxide-based SSBs lie in the later part of the cell fabrication process, specifically during the layer compaction stage, where an additional sintering step at temperatures above 1000°C is required to ensure both a dense layer within the SE separator and intimate interfacial contact with the cathode composite layer. In contrast, sulfide SSBs are shown to exhibit dense ionic conducting layers and intimate contact between the separator and cathode layer just from room temperature mechanical compression.

Another solvent criterion that differentiates between oxides and sulfides is the toxicity of the solvents used for the respective chemistry. The non-polar solvents required by sulfide SSBs are in general more toxic than polar solvents and can be compared quantitatively with the use of the median lethal dose (LD₅₀) values. These values are measured via different exposure routes with oral exposure to rats being the most commonly used, thus the representation in terms of [g_{oral} Kg_{rat}⁻¹] (see **Table 2**). A lower LD₅₀ value represents a higher toxicity. In our study, we chose *o*-xylene as the solvent despite its relatively high toxicity. The toxicity was not a major consideration because the study is still performed on a laboratory scale in a glove box, thus exposure to the solvent and its vapor are minimal. However, the scaling up of such processes would require the use of a dry-room environment and exposure to the solvent and its fumes will be drastically increased. To that end, new design criteria such as ventilation and removal of toxic fumes would be an important aspect and the use of a less toxic solvent with similar physical and chemical properties to *o*-xylene would be ideal for the sheet fabrication of sulfide SSBs on an industrial scale.

3.2.2. Binder-related parameters

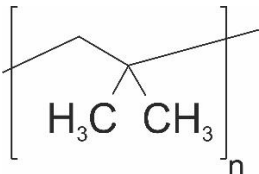
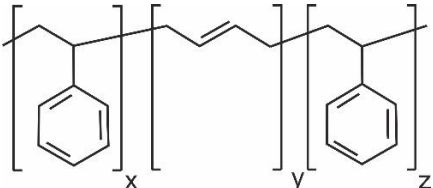
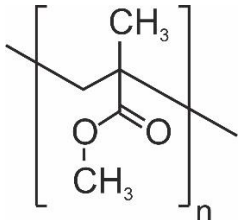
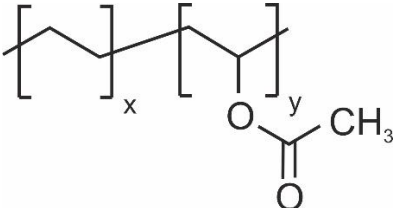
The desired binder characteristics are closely related and intertwined with the physical and chemical properties of the solvent. There are a few characteristics to look for when choosing the appropriate binders, such as their inertness, solubility in chosen solvents and adhesion strength, among others.⁵¹ Interestingly, most of the crucial properties of the binder are related to the molecular weight, chain length and the corresponding functional side groups. In a wet-chemical process, the binder is typically dissolved in the solvent of choice and used as a binder-solvent solution. Therefore, apart from the individual physical and chemical properties of both the solvent and binder themselves, the properties of the resulting binder-solvent solution are of crucial importance and have to be also taken into account. An example of which is the rheological properties of the binder-solvent solution, as it has been known to influence the mechanical integrity, homogeneity and most importantly, the electrochemical performance of the electrode sheet.⁶² One aspect of the rheology is the viscosity and is reported to have a direct correlation to the molecular weight of the binder, where a binder with higher molecular weight would result in a more viscous slurry suspension. While a high viscosity slurry suspension would be advantageous in preventing sedimentation of the solute during the drying process and maintaining a homogeneous electrode, it is not beneficial during the casting process. In fact, an ideal slurry is one having a non-newtonian fluid behavior, possessing high viscosity at low shear forces (e.g., drying

3.3. Slurry-casting of All-solid-state batteries - sheet fabrication process

stage) and low viscosity at high shear forces (e.g., casting stage). Apart from influencing the viscosity, the increase in molecular weight of the binder also results in an increase to the adhesion strength (either between the electrode and the substrate or within the electrode itself). On the topic of homogeneity, apart from relying on a viscous solution, a suitable binder and solvent combinations could also improve the distribution of the solid components within the electrode and lead to improved reaction distributions.⁶³

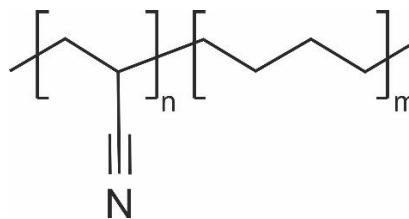
Regarding the chemical properties of the binder, it should be inert towards the components in the electrodes. The inertness of a binder is largely dependent on the functional side groups. For example, the nitrile groups ($C\equiv N$) of a nitrile butadiene rubber (NBR) was shown to interact with the Li ions in sulfide SEs via ion-dipole interactions, which contributed to an improved dispersion and adhesion strength.⁵¹ However, in our study, these interactions have shown to negatively affect the long-term electrochemical performance of the cell, at the cost of improving the homogeneity and mechanical properties of the electrode sheet. A summary of commonly reported polymer binder chemistries for SSB cell fabrication is listed together with their respective chemical structures in **Table 3**.

Table 3 Common binders for SSB cell fabrication and their chemical structures

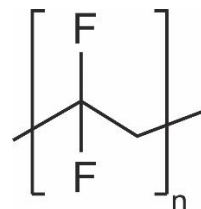
Binder	Structure
Polyisobutene (PIB)	
Styrene butadiene rubber (SBR)	
Poly(methyl methacrylate) (PMMA)	
Poly(ethylene vinyl acetate) (PEVA)	

3.3. Slurry-casting of All-solid-state batteries - sheet fabrication process

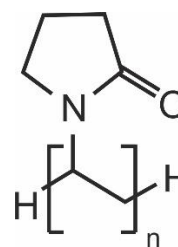
Hydrogenated nitrile butadiene rubber (hNBR)



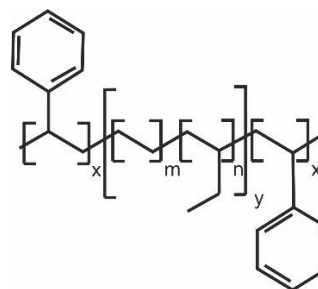
Poly(vinylidene fluoride) (PVDF)



Polyvinylpyrrolidone (PVP)



Styrene-(ethylene-butylene)-styrene (SEBS)



3.2.3. In-house optimization of the binder-solvent parameters

From the discussions in 3.2.1 and 3.2.2, we get an overview of the complex interdependency of both the solvent and binder parameters and how their individual properties and combinations together can affect the mechanical strength and the electrochemical performance of the electrode sheet.

Since the sulfide SEs ($\text{Li}_6\text{PS}_5\text{Cl}$ from NEI Corp.) are the core focus of our study, we first had to limit our choice to non-polar solvents. O-xylene (Sigma-Aldrich, anhydrous, 97 %) was our choice of solvent as it possessed a higher-than-average viscosity among the non-polar solvents and a lower-than-average vapor pressure, all of which are ideal for fabrication of electrode sheets. A preliminary study on the stability of the solvent was performed by simply observing the color change of both the suspension and the SE powder, which can indicate ongoing reactions between the solvent and the SE (**Figure 3.1**). Similar studies show a correlation between the color of polysulfide solutions and underlying degradation reactions, including their dependencies on the solvent polarity.^{51,57,58,64}

3.3. Slurry-casting of All-solid-state batteries - sheet fabrication process

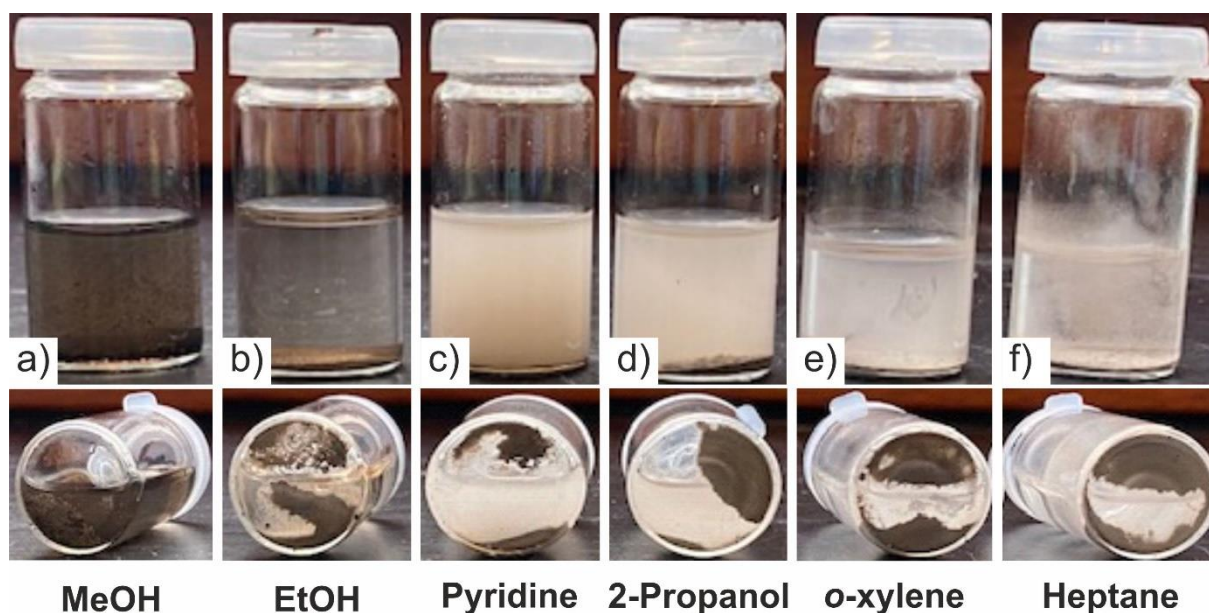


Figure 3.1 Photographs of $\text{Li}_6\text{PS}_5\text{Cl}$ SE dissolved in various solvents with decreasing polarity index (from a to f). The degree of degradation and instability of the $\text{Li}_6\text{PS}_5\text{Cl}$ SE is directly correlated to the intensity of color change of both the suspension and the SE powder. The panels show the dissolution of the SE in (a) methanol, (b) ethanol, (c) pyridine, (d) 2-propanol, (e) *o*-xylene and (f) heptane. The study was carried out under in a glovebox (Ar-atmosphere, $[\text{O}_2] < 0.1$ ppm, $[\text{H}_2\text{O}] < 0.5$ ppm).

Not surprising, the polar protic solvents such as methanol (MeOH) and ethanol (EtOH) showed an immediate color change from colorless to black after coming in contact with the sulfide SE (**Figure 3.1 a, b**). Furthermore, the color change was not restricted to the solvent but was observed for the SE powder as well, changing from greyish beige to black. In addition, minor sedimentation was observed, and the remaining undissolved powder constituted only a fraction of its original mass. Both of these observations indicate a strong reaction between the solvent and the SE. In contrast, the dispersed SE powder in a non-polar solvent such as *o*-xylene and heptane retained its original color. While the suspension was cloudy initially, it sediments very quickly, retaining most of its original mass. These observations reinforce the inertness of non-polar solvents towards sulfide SEs and is appropriate for producing sheet-based sulfide SSBs. After investigation of both ends of the polarity spectrum, we also looked at the suitability of solvents with average polarity. Examples include pyridine and 2-propanol, which had a less drastic color change to yellowish white and brown, respectively. For pyridine, the suspension remained cloudy even after a 30min rest time, while the 2-propanol was able to completely sediment. Also, within the same time, the color of the SE powder in pyridine and 2-propanol slowly changed to black and dark brown, respectively. This shows that the sulfide SE took a longer time to react with solvents of average polarity. However, no further tests were performed to ascertain if chemical changes to the SE took place for these average polarity solvents.

The chemical stability of *o*-xylene with respect to sulfide SEs was further supported with XRD data, where little to no change in the SE framework and crystal structure was observed (**Figure 3.2**). The XRD patterns of the mechanically mixed cathode composite via ball milling is represented in red and possessed both peak contributions from the CAM (green) and the SE (grey). After undergoing through the sheet fabrication

3.3. Slurry-casting of All-solid-state batteries - sheet fabrication process

process (i.e., dispersion in *o*-xylene, mixing, casting and drying), the XRD patterns remained relatively unchanged and identical to a conventional dry-mixing process (red), thus justifying *o*-xylene's chemical inertness towards the individual electrode components and its suitability as a solvent for the fabrication of sulfide SSBs.

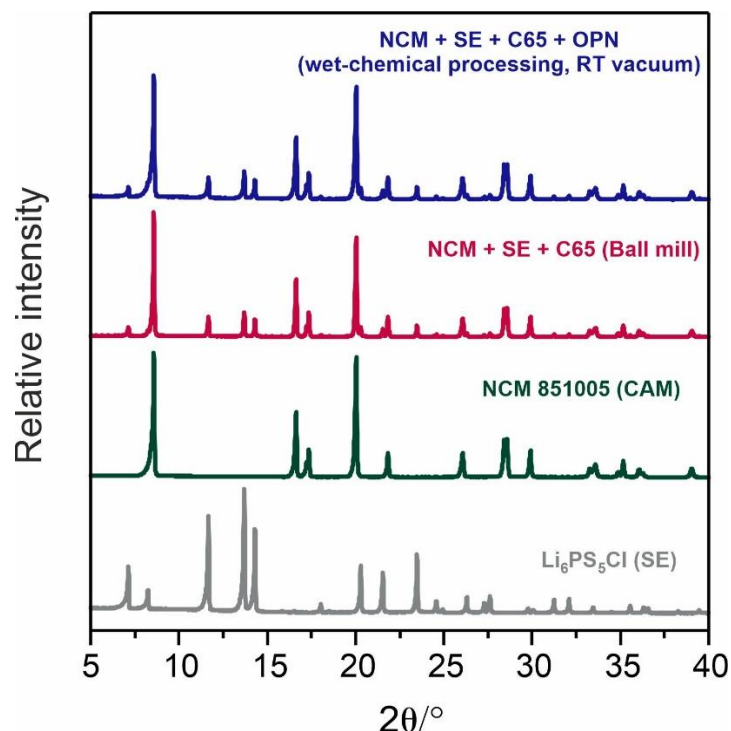


Figure 3.2 XRD patterns of the $\text{Li}_6\text{PS}_5\text{Cl}$ SE (black), CAM (NCM851005) (purple), cathode composite before solvent treatment (red) and after treatment (orange).

After choosing *o*-xylene as the solvent of choice for our study, we started to screen potential binder chemistries for our system. As mentioned above, the binder had to fulfill a couple of experimental requirements, one of which is the solubility in *o*-xylene. Three different binder chemistries were investigated, namely polyisobutene (OPN; OPPANOL N 150 from BASF SE, average molecular weight $M_w = 3.1 \cdot 10^6$ g/mol), poly(styrene-co-butadiene) (SBR; 45 wt% styrene from Sigma Aldrich, $M_w = 6 \cdot 10^5$ g/mol) and hydrogenated nitrile butadiene rubber (hNBR; THERBAN LT 1707 VP from ARLANXEO, $M_w = 5.5 \cdot 10^5$ g/mol). All the investigated binders were soluble in *o*-xylene but showed different binder-solution viscosities (μ) with the same weight fraction. The viscosities decreased in the following order: $\mu_{\text{OPN}} > \mu_{\text{SBR}} > \mu_{\text{hNBR}}$. This observed trend in viscosity correlates with their differences in average molecular weight and matches previously reported relationship between viscosities and molecular weight. The importance of the viscosity is most apparent during the optimization of the solid content, thickness and homogeneity of the electrode sheet, which will be elaborated in **Section 3.3**. After optimization and tailoring of each individual binder-solution mixtures to achieve similar viscosities, we proceeded to study the influence of different binder chemistries on the mechanical and electrochemical properties of the casted electrode. Not surprisingly, OPN-electrodes had decent mechanical stability due to its higher molecular weight. However, despite its lower molecular weight, hNBR was able to provide comparable mechanical properties with the same weight fraction. The stronger adhesion in this case was not attributed to the molecular weight but to the nitrile

3.3. Slurry-casting of All-solid-state batteries - sheet fabrication process

functional side groups along its chains, which exhibited ion-dipole interactions with the lithium ions of the sulfide SE. Provided that such interactions do not destabilize the SE framework, they can be advantageous to the homogeneity and electrochemical performance of the electrode sheet. However, our studies showed that hNBR-electrodes were more susceptible to side reactions (e.g., with reactive singlet oxygen $^1\text{O}_2$) and formed a higher fraction of oxidized species during operation. For SBR-electrodes, they showed similar mechanical properties to that of OPN-electrodes but differed slightly in their electrochemical performance. Ultimately, through a combination of *ex situ* and *in situ* analysis techniques, an optimization of electrodes with OPN binder achieved a balance between electrochemical performance and mechanical stability. A more in-depth analysis on the comparison between the three binders will be discussed later in **section 4.2**.

3.3. Sheet fabrication process

The sheet fabrication process will be primarily focused on the processing of a cathode composite electrode. In this section, we will elaborate upon the different processing stages, which starts with the mixing of the components, followed by the layer forming and lastly the layer compaction.

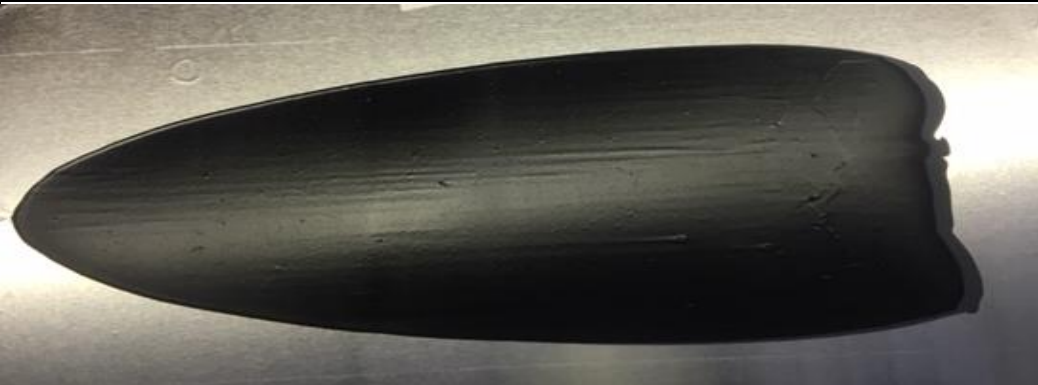
3.3.1. Mixing of components

In this stage, the components (solvent, binder, CAM, SE and conductive carbon additives) are mixed at high speeds to produce stable slurry suspensions. The high shear forces during mixing help separate and prevent agglomeration of the particles. Currently, state-of-the-art production of slurry suspension for LIBs uses a discontinuous batch process. These batch processes use batch mixers such as dissolvers and planetary mixers for both laboratory scale and series production.⁶⁵ Innovation in the mixing process have resulted in promising alternatives such as extrusion-based processing, which promises to reduce both costs and time. In our study, a discontinuous batch process with a THINKY mixer was used to produce slurry suspensions on a laboratory scale (Vol. < 5L). The components are not mixed together in one sequence, but in multiple complex optimized steps (**Table 4**). Studies have reported that the sequence of addition and mixing of the components have an impact on the resulting slurry homogeneity, electrochemical and mechanical performance.⁶⁶ In our study, we firstly mechanically dry mixed the CAM, SE and conductive carbon additives without the solvent and binder-solvent solution. This was to ensure that the main ionic and electronic conducting components have favorable contacts prior to the addition of a non-conducting polymeric binder. Second, solvents (in our case *o*-xylene) are added to the dry-mixed components together with milling balls and the resulting mixtures undergo a second mixing step. This ensures that the powders are properly wetted before the addition of the binder-solvent solution. Lastly, the binder-solvent solution is added to the mixture and mixed at high speeds. The separation of the solvent and binder-solvent solution into two stages reduces agglomeration/inhomogeneous mixing, which can be visually seen as roughness on the sheet's surface. The pre-wetting step was necessary due to the large surface areas of the particles (C65: $84 \text{ m}^2 \text{ g}^{-1}$), which readily adsorb the solvents. In the case where

3.3. Slurry-casting of All-solid-state batteries - sheet fabrication process

the binder-solvent solution is added without a pre-wetting step, precipitation of the polymeric binder from the solution could occur, causing inhomogeneous dispersion of the binder within the electrode. Lastly, the addition of the milling balls from the second mixing step is another precaution to suppress agglomeration during mixing. In our study and in the context of the components used (individual weight fractions, particle size, etc....), a solid content between 55-60 wt% was needed for producing an excellent dispersion with ideal casting viscosity, which produced sheets with state-of-the-art thickness ($d = 60 \mu\text{m}$) and homogeneity after drying and compaction. This solid content is achieved by considering the amount of solvent used in both the second mixing step (pre-wetting) and the last mixing step (binder-solvent solution).

Table 4 Recipe and mixing procedure for cathode composite electrode sheet

Cathode composite electrode sheet		
Recipe	Components	NCM622, Li ₆ PS ₅ Cl, C65, OPN
	Solvent content	42.1 wt%
	Solid content	57.9 wt%
	Binder content	1 wt%
	Slit size	240 μm
	Substrate	Aluminum
	Speed	25 mm/s
Mixing steps	Step 1	Mechanical dry mixing of NCM622, Li ₆ PS ₅ Cl, C65 at 600 rpm, 2 min
	Step 2	Added 1400 mg o-xylene (pre-wetting) and 12 mg milling balls (diameter = 1mm)
	Step 3	Mechanical wet mixing at 700 rpm, 2min
	Step 4	Added OPN binder-solvent solution
	Step 5	2x Mechanical wet mixing at 2000 rpm, 6 min
Example		

3.3.2. Layer formation

The slurry suspension from **section 3.3.1** can then be casted onto a substrate through various different techniques. One of which is tape casting, which involves the casting of the slurry with a doctor blade of defined slit size. The substrate used for the casting depends ultimately on the cell stacking design. It can be a current collector (e.g., Aluminum or Nickel foil), another electrode layer (e.g., SE separation layer) or a self-release polymer substrate. When casting onto another electrode layer, additional design requirements must be considered. For instance the choice of solvents and binders in both layers, since the solvent of one layer must not dissolve the binder of another during casting.¹² Another design difficulty would be the determination of mass loading.⁶⁷ Unless the thickness of the casted sheets can be maintained throughout the casting process, the mass loading of different electrodes cut from the same sheet will have a large variance, leading to inaccurate measurements. This is however often the case in a laboratory setup. In contrast, series productions circumvent this problem through a continuous supply of slurry to the reservoir. Regarding the current collector as a substrate, this works well for both the positive and negative electrodes, but not for the SE separator. Thus, the layer formation of the SE separator layer is often designed to be performed on either a casted layer or on a self-release polymer substrate. The self-release polymer substrate allows separation of the casted layer, making it free-standing. The concept of free-standing sheets open up more possibilities for cell assembling/stacking designs, but requires either a higher content of polymeric binder or a type of scaffold to ensure mechanical stability.⁶⁸

Another operational parameter involves the doctor blade itself. In agreement with reported studies on tape casting, we observe influences of the doctor blade's velocity, weight and design on the overall electrode properties.^{69–73} In general, there are two types of doctor-blade system, a single-blade and a double-blade system (**Figure 3.3**).^{70,74} In our study, a single-blade system is used. However, the use of a double-blade system would improve the thickness homogeneity along the length of the sheet.

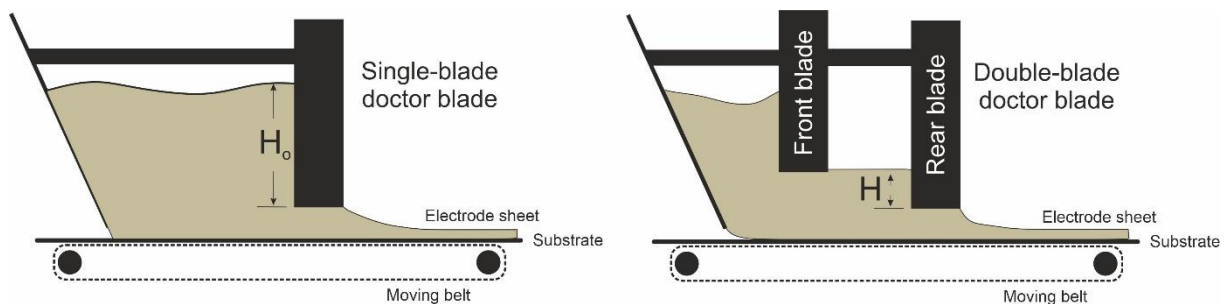


Figure 3.3 Single-blade (*left*) versus double-blade (*right*) doctor blades. (a) The height of the reservoir (H_o) decreases as the slurry gets used up, resulting in an irregular pressure-driven flow. (b) Height H is maintained even as the slurry is depleted, reducing the effect of irregular pressure-driven flow.

Thickness homogeneity is determined by three main factors: (1) the blade size, (2) the fluid flow and (3) the velocity of the blade. Logically, a larger blade size would produce thicker sheets. As for the fluid flow, there are two main types during casting, namely the shear-driven (*Couette flow*) and the pressure-driven flow (*Poiseuille flow*).⁷¹ The

3.3. Slurry-casting of All-solid-state batteries - sheet fabrication process

shear-driven flow is a result of shear stress exerted on the fluid by the relative motion of the doctor blade and the substrate, while the pressure-driven flow is a result of the pressure gradient in the direction of the slit opening. Since the pressure is directly proportional to the height of the slurry reservoir (H), a decrease will result affect the pressure-driven flow. This can be circumvented with the use of a double-blade system as H is maintained constant throughout most of the casting process, thus reducing the effect of an irregular pressure-driven flow. Unfortunately, in our studies, the use of a single-blade and a limited slurry reservoir meant that irregular pressure-driven flow is present and will affect the electrode thickness along the entire sheet. In general, as the slurry gets depleted, the hydraulic pressure will decrease (i.e., pressure-driven flow decreases) and drag-driven flow will become more dominant. As drag-driven flow becomes more dominant, the sheet thickness decreases. This increase in dominance of drag-driven flow is also apparent when the blade velocity is increased. Many parameters can affect both shear-driven and pressure-driven flow. For example, blade velocity, volume of slurry reservoir, slit size, viscosity of the slurry, among others. In our studies, we only chose to optimize the blade's velocity and slit size, while keeping the slurry volume and viscosity relatively constant, to achieve state-of-the-art electrode thickness for optimal electrochemical performance. The blade with a 240 μm slit size was moving at speeds of 25-30 mm/s and allowed the fabrication of ~ 60 μm thick electrode sheet after compaction. A last important parameter of the doctor blade is its weight. A blade with low mass was used to reduce the friction between the aluminum substrate and the blade itself. High friction impedes the movement of the blade and causes micro-jumps to occur, which results in uneven electrode surfaces.

The last step in layer formation is the drying stage of the electrodes. Drying at an inappropriate rate can cause detrimental effects to the mechanical and electrochemical properties of the sheet such as loss of adhesion and cracking.⁷⁵ In general, drying starts as the solvents is evaporated from the sheet surface and particles move closer together, reaching a final pre-compaction porosity. After which, the sheet shrinkage stops, and removal of solvents are driven by capillary transport of solvents towards the surface. The remaining trapped solvents unaffected by capillary transport evaporates and move through the pores as a gaseous phase towards the surface. Studies have shown that a high drying rate can cause accumulation of carbon additives and polymeric binder at the electrode surface, resulting in a concentration gradient along the thickness of the electrode.^{76–80} The accumulation at the electrode surface is accompanied by a depletion at the electrode/substrate interface, thus negatively affecting the adhesion of the sheet. On the other hand, a low drying rate could result in sedimentation of the components at the bottom. Therefore, optimization of the drying process is also required for fabrication of high-performance electrodes. In our studies, we dried the electrodes at room temperatures for 5h before drying under vacuum for 12h. No sedimentation was observed for the long drying time according to cross-sectional SEM images (**section 4.2**). Accordingly, the binder and carbon additive distribution along the thickness of the electrode was homogeneous.

3.3.3. Layer compaction

The final stage in the sheet fabrication process is the compaction of the sheet to reduce porosity and increase contact between the components in the electrode. Unlike LIBs, where an excessive low porosity might be detrimental to ionic conductivity, compaction for SSBs aim to be close to negligible porosity.^{12,81} The processing via calendaring should not to be confused with cold pressing, where the latter is used during the cell/stack assembly stage to increase contact between layers. On the other hand, the main objective of calendaring is to reduce porosity, bring the components closer together and improve electronic conductivity as well as the mechanical properties on a roll-to-roll process. However, on a laboratory scale, compaction can already be achieved with cold pressing during the cell/stack assembly stage, thus not needing a calendaring stage. Nevertheless, calendaring has another application on the laboratory scale, which is the preparation/compaction of an electrode layer for use as a substrate.

The calendaring of sheets can however be detrimental and lead to electrode defects such as delamination, cracks and particle pulverization.^{82–89} In our studies, we attempted to calender sheets with aluminum substrate with a relatively low line pressure to avoid any forms of defects. However, even at such low line pressures, we noticed periodic humps/waves along the electrode, which is reported to be a result on an inhomogeneous density distribution.⁸⁹ This is caused by a difference in sheet thickness, which we attribute to the use of a single-blade design and a limited slurry reservoir. Therefore, calendaring was not performed for our casted sheets and compaction of the cathode composite layer was instead performed during cell assembly via uniaxial cold pressing.

Finally, we attempted a preliminary investigation on the feasibility of processing of sulfide-based solid electrolyte in a dry-room environment ($T \sim -60^\circ\text{C}$). The bulk resistance of a Li_3PS_4 sulfide solid electrolyte was measured after different exposure time in a dry-room environment. It was found that the bulk resistance and Li-ion conductivity of the SE increases and decreases respectively with increasing exposure time. Exposure for short durations (up to 30 min) did not seem to affect the SE electrochemical properties and only after prolonged exposure (> 1 hr), did we see a distinct difference in bulk resistance and conductivity. Thus, for large-scale sulfide-based SSB production, design considerations have to be implemented to limit long-term exposure.

3.3. Slurry-casting of All-solid-state batteries - sheet fabrication process

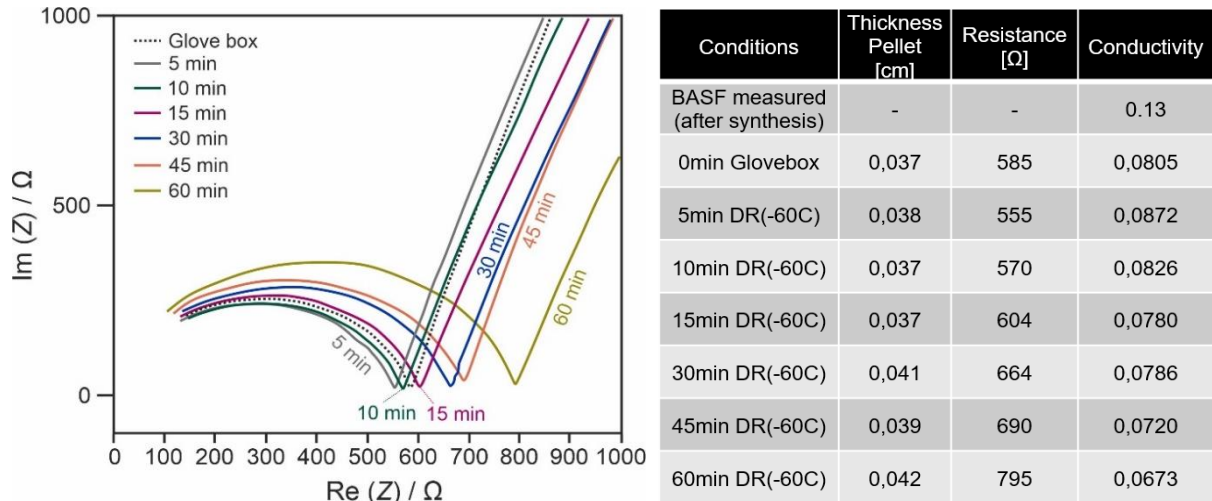


Figure 3.4 Representative Nyquist plots of Li_3PS_4 powder (BASF) exposed to dry-room conditions for different duration. The measured Li-ion conductivity provided by BASF was 0.13 mS/cm. After exposure to the glovebox environment (0 min), the conductivity was measured at 0.08 mS/cm. Only after 30 min, do we start to see a change in ionic conductivity that cannot be explained by measurement variance. The Li-ion conductivity of the SE powder was performed with a symmetric cell with stainless-steel current collectors under a stack pressure of 254 MPa (Diameter of cell = 10 mm).

4. Results and Discussion

4.1. Gas Evolution in Lithium-Ion Batteries: Solid versus Liquid Electrolyte

Differential electrochemical mass spectrometry (DEMS) measurements have been extensively used in the investigation of gas evolution behaviors in lithium-ion batteries (LIBs) and its results have contributed to further optimization and design of state-of-the-art LIBs. As all-solid-state batteries (SSBs) have progressed to the point where commercialization within the decade is increasingly possible, understanding the gas evolution trend of SSBs during cycling is of utmost importance.

Prior to this work, our group (Bartsch *et al.*) has published a preliminary study on SSB gassing, which to our knowledge was the first report of gas evolution study on SSB. There we reported the first gas evolution study for a thiophosphate-based SE, showing the evolution of H₂, CO₂, O₂ and most importantly SO₂. However, a more in-depth analysis into the mechanisms behind the gas evolution eluded us. Therefore, in an attempt to better understand the underlying mechanisms leading to gas evolution in sulfide-based SSBs, the gas evolution behavior of different thiophosphates were investigated and compared to traditional LIBs.

To begin this study, a Li₂CO₃-coated Li_{1+x}(Ni_{0.6}Co_{0.2}Mn_{0.2})_{1-x}O₂ (NCM622) with a ¹³C isotopic label was selected as the cathode active material (CAM) for both liquid and solid systems. The isotopic labeling was performed in a controlled manner as described in a previous publication (Hatsukade *et al.*). Next, the selected thiophosphate-SEs were Li₃PS₄ and Li₆PS₅Cl. We compared the gas evolution between the two SEs and noticed slight differences in the SO₂ signals. While a distinct SO₂ signal was observed for Li₃PS₄, none was seen for Li₆PS₅Cl, which we attribute to its higher chemical stability towards reactive singlet oxygen (¹O₂) that originates from the NCM lattices at high state of charges (SOCs) (> 80%). The formation of SO₂ gas from the reaction between ¹O₂ and the thiophosphates is first supported by the coincidence of the O₂ and the SO₂ peak at high SOC. A similar coincidence was also observed for the CO₂ and the SO₂ peaks and is in line with a study from Mahne *et al.*, which showed that the decomposition of Li₂CO₃ surface impurities also leads to the evolution of both CO₂ and ¹O₂.

Following which, the above gas evolution trend in SSBs was compared to that of a conventional LIB. There was a clear difference in the cumulative amount of O₂ and CO₂ (¹²C and ¹³C) recorded. The LIB system released a significantly larger amount of ^{12,13}CO₂ gas. This difference is related to the following reasons: (1) An increase in electrochemical decomposition of the Li₂¹³CO₃ coating layer and (2) the oxidation of the ¹²C-carbonate-based liquid electrolyte. The later has been extensively reported in the literature and is further supported by a considerably reduced O₂ evolution, since the released ¹O₂ is consumed through side reactions with the carbonate liquid electrolyte, leading to large amounts of ¹²CO₂ formation. In contrast, SSB cells possess less components for such oxidation processes to occur, thus a higher fraction of ¹O₂ would physically decay into molecular O₂, resulting in higher amount of O₂ measured for SSB cells. Therefore, the ¹²CO₂ and O₂ gas evolution has opposing trends in both SSB and LIB cells. As for the increase in electrochemical decomposition of the Li₂¹³CO₃, it can be attributed to a better ionic and electronic percolation within the LIB

4.1 Results and Discussion – Gas Evolution in Lithium-Ion Batteries: Solid versus Liquid Electrolyte

electrode, which results in better electrochemical addressability of the active material and therefore the $\text{Li}_2^{13}\text{CO}_3$. Hence, a higher fraction of $\text{Li}_2^{13}\text{CO}_3$ undergoes electrochemical decomposition. We further supported this argument with post-mortem analysis to find out the remaining amount of $\text{Li}_2^{13}\text{CO}_3$ on the CAMs. Cycled cathode composites were washed in N-methylformamide (NMF) to remove the SE without damaging any residual carbonates on the CAM before subjecting them to an acid titration study. The amount of remaining of $\text{Li}_2^{13}\text{CO}_3$ on a post-run CAM in a SSB cell was more than twice that in a LIB cell. This allowed us to conclude that a greater amount of Li_2CO_3 coating (^{13}C) was electrochemically decomposed during cycling in a LIB.

The equipment used in this study, especially the DEMS and acid titration setup was designed by Dr. Balázs B. Berkes and Dr. Toru Hatsukade, respectively. The customized cell used for DEMS-SSB was however redesigned and optimized by me. For its development, multiple mechanical sketches were created using CAD software "Autodesk Inventor Professional 2018" and required extensive cooperation with the mechanical workshop. The customized cell consists of a stainless-steel outer body, current collectors, a plastic polyether ether ketone (PEEK) housing and a gas-flow guiding component. The incorporation of a PEEK housing for the SSB and sandwiched between an anode and a cathode current collector was required to prevent crack and fracture during cell fabrication and cycling. The cathode current collector also has holes with 1mm diameter to enable proper flow of the evolved gases towards the exhaust. The gas-flow guiding component functions as both a connection between the cathode current collector to the external circuit and a guide for the incoming and outgoing gases. The experiments described in the manuscript were performed and evaluated by me under the scientific supervision of Prof. Dr. Jürgen Janek, Dr. Torsten Brezesinski and Dr. Florian Strauss. The manuscript was written mainly by Dr. Florian Strauss, while the experiments were performed mainly by me. The final paper was then edited by eight co-authors.

Reprinted with permission from (Strauss, F., Teo, J. H., Schiele, A., Bartsch, T., Hatsukade, T., Hartmann, P., Janek, J., Brezesinski, T.) Gas Evolution in Lithium-Ion Batteries: Solid versus Liquid Electrolyte. *ACS Appl. Mater. Interfaces* **2020**, 12, 20462-20468) Copyright © 2020 American Chemical Society.

Gas Evolution in Lithium-Ion Batteries: Solid versus Liquid Electrolyte

Florian Strauss,^{*,†} Jun Hao Teo,[†] Alexander Schiele, Timo Bartsch, Toru Hatsukade, Pascal Hartmann, Jürgen Janek, and Torsten Brezesinski^{*}

Cite This: *ACS Appl. Mater. Interfaces* 2020, 12, 20462–20468

Read Online

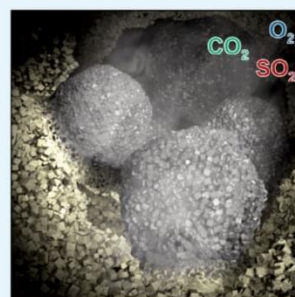
ACCESS |

Metrics & More

Article Recommendations

Supporting Information

ABSTRACT: Gas evolution in conventional lithium-ion batteries using Ni-rich layered oxide cathode materials presents a serious issue that is responsible for performance decay and safety concerns, among others. Recent findings revealed that gas evolution also occurred in bulk-type solid-state batteries. To further clarify the effect that the electrolyte has on gassing, we report in this work—to the best of our knowledge—the first study comparing gas evolution in lithium-ion batteries with NCM622 cathode material and different electrolyte types, specifically solid (β -Li₃PS₄ and Li₆PS₅Cl) versus liquid (LP57). Using isotopic labeling, acid titration, and in situ gas analysis, we show the presence of O₂ and CO₂ evolution in both systems, albeit with different cumulative amounts, and possible SO₂ evolution for the lithium thiophosphate-based cells. Our results demonstrate the importance of considering gas evolution in solid-state batteries, especially the formation and release of highly corrosive SO₂, due to side reactions with the electrolyte.



KEYWORDS: lithium-ion battery, all-solid-state battery, organic carbonate liquid electrolyte, lithium thiophosphate solid electrolyte, gas evolution, interfacial chemistry

INTRODUCTION

Lithium-ion batteries (LIBs) are an indispensable energy-storage technology nowadays, enabling the widespread use of portable electronics. In addition, and even more importantly, LIBs are key to the efforts toward transportation electrification.¹ State-of-the-art LIBs rely on layered lithium transition metal oxides as cathode, such as Li_{1+x}(Ni_{1-y-z}Co_yMn_z)_{1-x}O₂(NCM), and graphite as anode in combination with an organic carbonate-based liquid electrolyte.

Increasing the fraction of redox-active Ni in NCM-type cathode materials has been shown a viable strategy for achieving specific capacities of ≥ 200 mAh/g_{NCM} in a reasonable voltage range.² However, the operation of such NCMs in liquid electrolyte-based LIBs (referred to as liq-LIBs in the following) causes the formation of gaseous side products, such as O₂, CO, and CO₂, among others, eventually leading to performance loss and safety issues.^{3–5}

Various possible pathways of gas generation have been discussed in the literature.^{4–9} First, the electrochemical oxidation of the organic electrolyte gives rise to CO and CO₂ evolution.⁶ Second, the electrochemical decomposition of residual carbonate species, usually present on the surface of especially Ni-rich NCMs, leads to CO₂ and O₂ evolution, predominantly in the initial charge cycle.⁹ Third, the structural instability of Ni-rich NCMs at high states of charge (SOC) causes the release of lattice O₂, which chemically reacts with the liquid electrolyte, thereby producing CO and CO₂.^{5,8}

As we have shown recently for bulk-type solid-state batteries (SSBs), similar gas evolution can also occur, along with unique SO₂ formation, when using lithium thiophosphate solid electrolytes.^{10,11} Nevertheless, the effect of different thiophosphates on gas evolution is yet to be studied as well as how it compares to liq-LIBs. In this work, we present a comparative study to clarify such questions, focusing on the evolution of CO₂ and O₂ in liq-LIB and SSB cells and SO₂ in the latter using isotopic labeling combined with in situ gas analysis.

EXPERIMENTAL SECTION

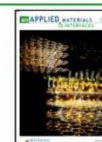
Materials Preparation. For the synthesis of β -Li₃PS₄ solid electrolyte, stoichiometric amounts of Li₂S (Sigma-Aldrich; 99+%) and P₂S₅ (Sigma-Aldrich; 99%) in a 70 mL zirconia jar with 10 mm diameter zirconia balls (~55:1 ball-to-powder ratio) were mixed under argon for 1 h at 250 rpm. The mixing speed was then increased to 650 rpm, and the milling was continued for 20 h. The resultant powder material had a conductivity of ~ 0.5 mS/cm.

For the synthesis of Li₆PS₅Cl solid electrolyte, Li₂S, P₂S₅, and LiCl (Alfa Aesar; 99+%) in a 250 mL zirconia jar with 10 mm diameter zirconia balls were milled under argon for 1 h at 250 rpm and then for 20 h at 450 rpm. Subsequently, the harvested material was heated for

Received: February 14, 2020

Accepted: April 10, 2020

Published: April 10, 2020



4.1 Results and Discussion – Gas Evolution in Lithium-Ion Batteries: Solid versus Liquid Electrolyte

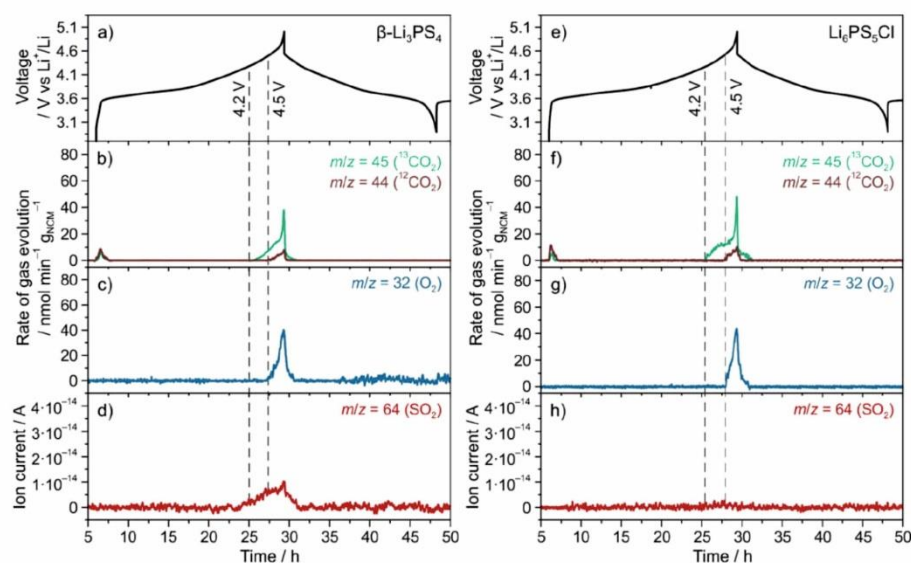


Figure 1. Electrochemical trace of SSB cells using (a) β - Li_3PS_4 and (e) $\text{Li}_6\text{PS}_5\text{Cl}$ solid electrolyte and the corresponding time-resolved (b, f) $^{12}\text{CO}_2$, $^{13}\text{CO}_2$, and (c, g) O_2 evolution rates and (d, h) ion current for SO_2 . The cells were cycled in the potential range of 2.3–4.4 V with respect to In/InLi (~ 2.9 – 5.0 V vs Li^+/Li).

5 h at 300°C in a vacuum. Note that (i) the ball-to-powder ratio was $\sim 27:1$, (ii) LiCl was predried overnight at 300°C in a vacuum, and (iii) Li_2S was used in a less than stoichiometric amount (by 10 mol %). The resultant powder material had a conductivity of ~ 2.0 mS/cm.

Regeneration of Cathode Material.

$\text{Li}_{1-x}(\text{Ni}_{0.6}\text{Co}_{0.2}\text{Mn}_{0.2})_{1-x}\text{O}_2$ (NCM622, 60% Ni) cathode material (BASF SE; $D_v^{50} = 5.19$ μm , $D_v^{90} = 9.04$ μm) was heated in an oxygen flow for 2 h at 740°C to remove both native LiOH and Li_2CO_3 surface contaminants. The resultant powder material was stored under argon for further use.^{3–5}

$\text{Li}_2^{13}\text{CO}_3$ Surface Layer Formation. For the formation of $\text{Li}_2^{13}\text{CO}_3$ on the cathode material's surface, regenerated (i.e., virtually Li_2CO_3 -free) NCM622 was placed in a custom cell under an ~ 2.5 bar ^{13}C -labeled CO_2 atmosphere (Sigma-Aldrich; 99 at. % ^{13}C).¹² The storage cell underwent purge cycles following its assembly to replace the initial argon atmosphere. In addition, 300 μL of H_2O was introduced into a cavity inside of the cell to accelerate the carbonate formation. Finally, it was placed in an oven for 2 h at 60°C .

SSB Cell Assembly and Testing. All steps were performed under argon. The cathode composite was prepared in a 70 mL zirconia jar with 10 mm diameter zirconia balls ($\sim 30:1$ ball-to-powder ratio) by mixing either β - Li_3PS_4 or $\text{Li}_6\text{PS}_5\text{Cl}$ solid electrolyte, NCM622 cathode material, and Super C65 carbon black additive (Timcal) in a 3:7:0.1 weight ratio for 30 min at 140 rpm. The SSB cells were assembled in a 10 mm diameter PEEK ring, its use ensuring relatively high pressures to be applied onto the pellet without cracking or relaxation occurring. The ring was placed on a steel mold, allowing the powder to be sequentially pressed into pellets. First, 100 mg of solid electrolyte were compacted at ~ 125 MPa. Next, 13 mg of cathode composite (11 – 12 $\text{mg}_{\text{NCM}}/\text{cm}^2$, ~ 2.1 mAh/cm^2) were pressed by hand onto the solid electrolyte layer. Then, an 8 mm diameter Al mesh was carefully placed onto the cathode composite, followed by compression at ~ 440 MPa. In addition, a 9 mm diameter stainless steel mesh was placed onto the Al mesh/cathode layer to help promote connectivity. Subsequently, the PEEK ring was removed from the steel mold along with the solid electrolyte separator and cathode composite layers. Finally, a 100 μm thick, 8 mm diameter In anode (Alfa Aesar) was attached to the pellet, and the PEEK ring containing the assembled cell (with spacers on both sides) was introduced into the differential electrochemical mass spectrometry (DEMS) setup. The cathode spacer had 1 mm diameter holes to

ensure proper outflow of released gas during cycling. All SSB cycling [after leaving the cell at open circuit voltage (OCV) for 6 h] was done at a C/20 rate, with $1\text{C} = 180$ $\text{mA}/\text{g}_{\text{NCM}}$, and at 45°C in the potential range between 2.3 and 4.4 V versus In/InLi using a BioLogic VMP potentiostat.

Separating Solid Electrolyte and Cathode Material. To determine the carbonate content of the SSB cathode composite after mixing and after the initial cycle, we had to remove the solid electrolyte, as the strong H_2S evolution when using the acid titration setup (more details below) did not allow for accurate measurement of CO_2 . Hence, ~ 30 mg of either cathode composite or cycled SSB pellet were dispersed in 3 mL of *N*-methylformamide (Sigma-Aldrich; NMF), able to dissolve the solid electrolyte while leaving Li_2CO_3 unaffected. The In anode was removed in the case of the cycled SSB pellet before dissolving in NMF. The NMF was carefully dried over activated molecular sieves (Merck KGaA); the H_2O content was determined to be ~ 2 ppm by Karl Fischer titration. After pouring of the solution and repeated washing with NMF, the powder was dried for at least 24 h in a vacuum prior to acid titration measurement. The NCM622 cathode material with an artificially grown $\text{Li}_2^{13}\text{CO}_3$ surface layer served as reference sample and was treated in the same way as described above (to ensure the carbonate is not affected by the NMF).

Liq-LIB Cell Assembly and Testing. Electrodes were prepared with a composition of 94 wt % NCM622 cathode material, 3 wt % Solef5130 polyvinylidene fluoride binder (Solvay), and 1 wt % Super C65 carbon black and 2 wt % SFG6L graphite additives (Timcal). The areal loading was ~ 8.5 $\text{mg}_{\text{NCM}}/\text{cm}^2$. For DEMS, the liq-LIB cells were assembled inside an Ar-filled glovebox by stacking 600 μm thick, 32 mm diameter Li anode (Albemarle Germany GmbH), 36 mm diameter Celgard 2500 polypropylene separator, and 30 mm diameter NCM622 cathode. The latter electrode had 4 mm diameter holes in the middle for proper gas extraction and attachment of a Li reference electrode. 260 μL of LPS7 (BASF SE; 1 M LiPF_6 in 3:7 by weight ethylene carbonate and ethyl methyl carbonate) was used as electrolyte. The cells were left at OCV for 6 h and then cycled at a C/10 rate (higher compared with the SSB cells because of the experimental constraints), with $1\text{C} = 240$ $\text{mA}/\text{g}_{\text{NCM}}$, and at 45°C with a charge capacity limitation of 240 $\text{mAh}/\text{g}_{\text{NCM}}$. The cutoff potential on discharge was set to 3.0 V versus Li^+/Li .

4.1 Results and Discussion – Gas Evolution in Lithium-Ion Batteries: Solid versus Liquid Electrolyte

Gas Characterization. The gas evolution was studied using DEMS by monitoring $m/z = 1$ –100. Helium (purity 6.0, 2.5 mL/min) served as carrier gas for both the SSB and liq-LIB cells. The extracted gas was analyzed by a mass spectrometer (Pfeiffer Vacuum GmbH; OmniStar GSD 320). Additional information is provided in the literature.^{13,14}

Carbonate Determination. Four to eleven milligrams of NCM622 powder was introduced into a vial with a septum-sealed cap. Next, 1 M H_2SO_4 (Merck KGaA), degassed for 1 h through argon bubbling, was added. The reaction between Li_2CO_3 and H_2SO_4 releases CO_2 , which was extracted from the vial using argon carrier gas (purity 6.0), controlled by a mass flow controller (Bronkhorst High-Tech BV; EL-FLOW Select) at 2.5 mL/min. The evolution of both $^{12}\text{CO}_2$ and $^{13}\text{CO}_2$ was monitored quantitatively by a mass spectrometer (Pfeiffer Vacuum GmbH; HiCube Pro with a PrismaPlus detector).

■ RESULTS AND DISCUSSION

As mentioned previously, NCM622 (60% Ni) was used in this study as cathode material. To unequivocally prove the nature of evolved gases, the native carbonate surface contaminants were first removed through 2 h treatment at 740 °C in flowing O_2 , and then they were regrown in a controlled manner using isotopically pure $^{13}\text{CO}_2$. After drying the NCM622 overnight at 300 °C in a vacuum, we carried out acid titration coupled with mass spectrometry to determine the amount of carbonate species. The resultant $\text{Li}_2^{12}\text{CO}_3$ and $\text{Li}_2^{13}\text{CO}_3$ contents were 0.07 and 0.76 wt %, respectively, corresponding to ~92% ^{13}C .

Next, SSB and liq-LIB cells were assembled, and the gas evolution in the initial cycle was monitored using DEMS (mass signals from $m/z = 1$ –100). The setup employed is described in some more detail in literature.^{10,13,14} In a first step, SSB cells with $\beta\text{-Li}_3\text{PS}_4$, NCM622, and In as solid electrolyte, cathode, and anode, respectively, were examined. They were cycled at a rate of C/20 and 45 °C between 2.3 and 4.4 V versus In/InLi, corresponding to ~2.9–5.0 V with respect to Li^+/Li . As is evident from Figure 1a, the electrochemical trace is characteristic of Ni-rich NCM, with first cycle specific charge and discharge capacities of 210 and 170 mAh/g_{NCM}. Regarding gas evolution, two signals with $m/z = 44$ and 45, referring to $^{12}\text{CO}_2$ and $^{13}\text{CO}_2$, respectively, were clearly visible near the end of the charge cycle (Figure 1b). The $^{13}\text{CO}_2$ evolution can be attributed to the electrochemical decomposition of $\text{Li}_2^{13}\text{CO}_3$ on the NCM622 surface, the onset being ~4.2 V versus Li^+/Li , in agreement with literature.^{5,9,15} However, the onset of $^{12}\text{CO}_2$ evolution was ~300 mV higher in potential compared with that of $^{13}\text{CO}_2$. An explanation might be that the native carbonate contaminants can only be partially removed from the NCM622 secondary particles during the regeneration process, especially those that are present in the interior of the material. At high potentials or SOC, the particles typically undergo some fracture, which may release $^{12}\text{CO}_2$. However, oxidation of Super C65 carbon black additive, present in the cathode composite, cannot be excluded.

Minor CO_2 formation was also observed in the beginning of the initial charge cycle, probably because of side reactions occurring at the interface of In anode and solid electrolyte separator. This hypothesis relies on the fact that the CO_2 onset potential is strongly correlated with that of H_2 ($m/z = 2$), the latter of which appears as a sharp peak (Figure S1). H_2 evolution may be related to trace H_2O reduction in the cell.^{6,10} However, we believe that it is also associated with the solid electrolyte and the released H_2 is capable of somewhat reacting with the carbonate species, thereby forming CO_2 .¹⁶ In

addition, the onset potentials of $^{12}\text{CO}_2$ and $^{13}\text{CO}_2$ evolution (in the beginning of charging) were found to be identical within the experimental error, arguing for a chemical rather than an electrochemical reaction. In this context, it should be noted that no H_2S ($m/z = 34$) evolution was detected, suggesting either complete removal of trace H_2O during the initial reduction or insensitivity of the solid electrolyte to very low levels of H_2O (Figure S1). In any case, the lack of H_2S evolution indicates that H_2O -related effects are negligible in these experiments.

Moreover, a sharp peak for $m/z = 32$, referring to O_2 , was visible at the end of charge, the onset potential being ~4.5 V versus Li^+/Li (Figure 1c). The O_2 evolution can originate from two different sources as proposed in literature, either its release from the NCM lattice or the electrochemical decomposition of Li_2CO_3 (note that for the $\text{Li}_6\text{PS}_5\text{Cl}$ -based SSB cells, the apparent molar ratio of $\text{CO}_2:\text{O}_2$ is of the order of 2:1 expected for the latter reaction).^{9,15,17} Both sources seem reasonable here. However, the release of O_2 from the NCM lattice requires the SOC to be $\geq 80\%$ (100% refers to full delithiation).¹⁷ The initial specific charge capacity was 210 mAh/g_{NCM}, which is equivalent to ~76% SOC. Hence, one would not expect to observe any O_2 evolution. Nevertheless, as demonstrated recently for SSBs, inhomogeneities in SOC may be present during cycling. In other words, occurrence of cathode material fractions possessing different SOC is possible,^{18–20} and thus some of the NCM622 particles may exceed 80% SOC, eventually leading to O_2 loss.

Lastly, a trace for $m/z = 64$ (SO_2) was observed (Figure 1d), a unique feature that has been reported so far only for SSB cells using $\beta\text{-Li}_3\text{PS}_4$ solid electrolyte.^{10,11} The most obvious route leading to SO_2 formation and release is the reaction between O_2 and the solid electrolyte, accompanied by formal sulfur oxidation, along with the formation of solid oxygenated sulfur and phosphorus species as confirmed by X-ray photoelectron spectroscopy (XPS) and time-of-flight secondary ion mass spectrometry (ToF-SIMS), among others.^{21–24} As mentioned above, two sources of O_2 are generally possible, namely O_2 released from the NCM lattice or through the electrochemical decomposition of Li_2CO_3 . Having in mind that the evolved O_2 during cycling appears to be partially or completely highly reactive $^1\text{O}_2$,^{15,25,26} a gas/solid reaction may even occur at 45 °C, despite a recent report that surface oxidation of lithium thiophosphates (by $^3\text{O}_2$) requires much higher temperatures.²⁷ The DEMS data, especially the result that the SO_2 evolution begins/stops simultaneously with the $^{13}\text{CO}_2$ evolution (during charge and discharge at ~4.2 V vs Li^+/Li), support such reaction mechanism.

Given the apparent effect of lithium thiophosphate solid electrolytes on the gassing behavior, we subsequently substituted $\beta\text{-Li}_3\text{PS}_4$ for argyrodite $\text{Li}_6\text{PS}_5\text{Cl}$ in an otherwise identical SSB. Cycling of such cells under the same conditions resulted in gas evolution characteristics of $^{12}\text{CO}_2$, $^{13}\text{CO}_2$, and O_2 (Figure 1e–g), similar to those for $\beta\text{-Li}_3\text{PS}_4$. However, a clear distinction was observed for SO_2 (Figure 1h). In contrast to $\beta\text{-Li}_3\text{PS}_4$, there was no SO_2 evolution, thereby suggesting higher chemical stability of $\text{Li}_6\text{PS}_5\text{Cl}$ toward reaction with $^1\text{O}_2$ and/or formation of only solid decomposition products. Note that its lower electrochemical stability does not necessarily affect the gas evolution.^{28,29} In all cases of $\text{Li}_6\text{PS}_5\text{Cl}$ samples, SO_2 peaks in the raw data were indistinguishable from the background. Moreover, if any peaks were observed, the ion current was usually much lower compared with the $\beta\text{-Li}_3\text{PS}_4$

4.1 Results and Discussion – Gas Evolution in Lithium-Ion Batteries: Solid versus Liquid Electrolyte

samples and they did not correspond to the time frame where other characteristic gases (CO_2 and O_2) evolved. For both types of SSB cells, the evolution of gases detected during the initial cycle was also seen for the second and third cycles, although with decreased intensity (Figures S2 and S3).

Thus far, we have shown that gas evolution related to CO_2 , O_2 , and partially SO_2 occurs in battery cells depending on the electrolyte used. To compare gassing in such systems in a more detailed manner, we assembled conventional liq-LIBs using tape-cast electrodes with the same NCM622 cathode material and LP57 electrolyte. The cells were cycled at a rate of C/10 and 45 °C with a charge capacity limitation of 240 mAh/g_{NCM} (~87% SOC). The voltage profile is displayed in Figure 2a. As

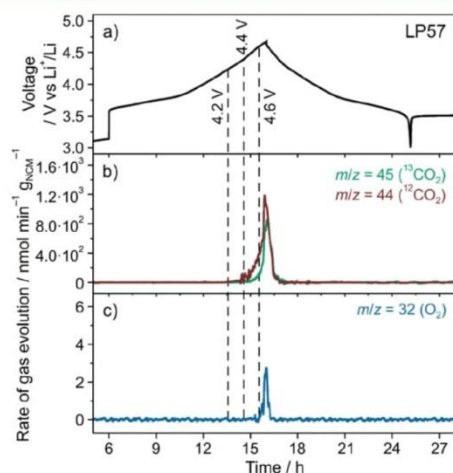


Figure 2. (a) Electrochemical trace of a liq-LIB cell cycled using a charge capacity limitation of 240 mAh/g_{NCM} and the corresponding time-resolved (b) $^{12}\text{CO}_2$, $^{13}\text{CO}_2$, and (c) O_2 evolution rates.

shown in Figure 2b, both $^{12}\text{CO}_2$ and $^{13}\text{CO}_2$ evolution at the end of charge/beginning of discharge can be spotted, with onset potentials of ~4.2 and ~4.4 V versus Li^+/Li , respectively. This result indicates that decomposition of LP57 electrolyte occurs prior to Li_2CO_3 decomposition, in agreement with literature.^{5,17} At first sight, in contrast to the SSB cells, the quantity of evolved $^{12}\text{CO}_2$ seems greater than that of $^{13}\text{CO}_2$, which can be attributed to the additional contribution from the (electro)chemical decomposition of the carbonate-based liquid electrolyte, accounting for $^{12}\text{CO}_2$ formation (note that, because of the isotopic labeling, Li_2CO_3 decomposition is mainly responsible for $^{13}\text{CO}_2$ evolution).^{5,9,30} Moreover, in line with previous literature reports, O_2 evolution arises at an onset potential of ~4.6 V versus Li^+/Li (Figure 2c), referring to ~83% SOC.¹⁷ We also observed H_2 and CO evolution (Figure S4), typically originating from the reductive decomposition of the liquid electrolyte and/or trace water.⁶ However, with their maximum amplitude occurring near the end of charge, it is more likely that these are stemming from oxidative electrolyte decomposition processes, with CO being a direct product^{12,17} and H_2 an indirect product, arising from the reduction of protic species that are formed at the positive electrode and diffuse to the negative electrode.⁶ The apparent time-shift between the peaks of CO and H_2 (with H_2 evolving slightly later than CO) supports this hypothesis.

Because the SSB and liq-LIB cells show common CO_2 and O_2 evolution, the total quantity of evolved gases in the initial cycle can be compared (Figure 3). Note that the liq-LIBs were

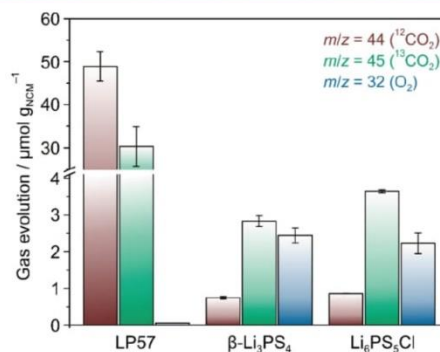


Figure 3. Total quantity of $^{12}\text{CO}_2$, $^{13}\text{CO}_2$, and O_2 evolved during the initial charge/discharge cycle at 45 °C of SSB and liq-LIB cells. Error bars indicate the standard deviation of two independent measurements.

charged using a specific capacity limitation of 240 mAh/g_{NCM} to achieve a similar SOC to the SSBs. Although the latter cells showed slightly lower specific capacities, ranging from 210 to 230 mAh/g_{NCM}, inhomogeneities in SOC of the NCM622 particles, especially for pelletized SSB cells, are inevitable,^{18–20} warranting such comparison.

First of all, in the case of the LP57 electrolyte, the $^{12}\text{CO}_2$ amount was significantly larger (~49 μmol/g_{NCM}), compared to ~1 μmol/g_{NCM} for the SSB cells. As mentioned above, this is because of decomposition of the carbonate-based liquid electrolyte, mainly contributing to $^{12}\text{CO}_2$ formation. As the carbonate surface species were labeled with ^{13}C , $^{13}\text{CO}_2$ evolution can be attributed unambiguously to the electrochemical decomposition of Li_2CO_3 . For the liq-LIB cells, about an order of magnitude more $^{13}\text{CO}_2$ evolved compared with the SSB cells (~30 vs 3–4 μmol/g_{NCM}). We suspect that this difference is due to (i) better ionic and electronic percolation in the liq-LIB electrode and/or (ii) trapping of CO_2 by the solid electrolyte (pore blocking or physisorption/chemisorption) and/or (iii) formation of solid side products in the case of the SSB cells. The fraction of $^{12}\text{CO}_2$ to the total quantity of evolved CO_2 [$^{12}\text{C}/(^{12}\text{C}+^{13}\text{C})$] was ~0.08 in the pristine ^{13}C -labeled NCM622 (from acid titration measurements). However, for the first-cycle gas evolution, it was much larger than expected at ~0.18 (from DEMS measurements). The reason is unclear at present but may be related to the unique surface structure and/or partial oxidation of Super C65 carbon black in the SSB cathode composites.

Moreover, the amount of released O_2 was similar for the different SSB cells (~2 μmol/g_{NCM}). For the liq-LIB cells, it was more than an order of magnitude lower. Nevertheless, in the case of the LP57 electrolyte, the virtually total consumption of released O_2 through side reactions with the carbonate liquid electrolyte, leading to $^{12}\text{CO}_2$ and CO formation, among others, must be taken into account.^{17,30} Note that such phenomenon is also responsible for the occasional absence of the O_2 signal (below the detection limit). Similar reactions seem to occur for the SSB cells. This means that part of the released $^{16}\text{O}_2$ undergoes follow-up reactions, leading to formation of either SO_2 or solid products as

mentioned above; however, it is not as pronounced as for the liq-LIB cells because gas/liquid reactions tend to be kinetically favored over gas/solid reactions.

Li_2CO_3 contaminants on Ni-rich and Li/Mn-rich cathode materials have been recognized lately as accounting for CO_2 evolution, especially during the initial cycle of liq-LIBs, and as being responsible for $^1\text{O}_2$ formation.^{9,12,15} Both to further clarify the role of such surface residuals in the CO_2 release and to identify unique characteristics for the SSB cells, we quantitatively determined the amount of Li_2CO_3 present on the NCM622 cathode material by acid titration measurements prior to and after cycling (Figure 4 and Table S1) and

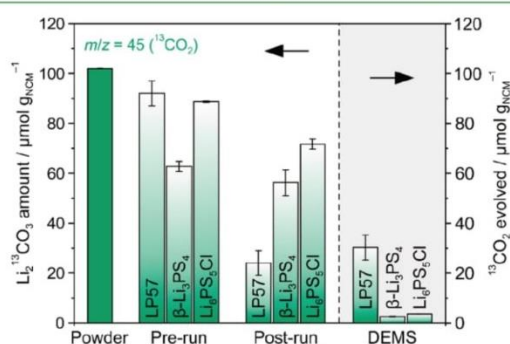


Figure 4. Amount of $\text{Li}_2^{13}\text{CO}_3$ on the NCM622 cathode material before and after cycling from acid titration measurements compared to the cumulative amount of $^{13}\text{CO}_2$ from DEMS. Error bars indicate the standard deviation of two independent measurements.

compared this with the DEMS results. We focus only on $^{13}\text{CO}_2$, as ^{13}C is the major species within the surface layer after tailored formation of $\text{Li}_2^{13}\text{CO}_3$ and thus can be considered representative for the carbonate contaminants in this case. The amount of artificially grown $\text{Li}_2^{13}\text{CO}_3$ on the NCM622 particles was determined to be $\sim 102 \mu\text{mol/g}_{\text{NCM}}$. After electrode preparation (referred to as prerun), this initial value was strongly decreased to $\sim 63 \mu\text{mol/g}_{\text{NCM}}$ for $\beta\text{-Li}_3\text{PS}_4$ and slightly decreased to ~ 89 and $\sim 92 \mu\text{mol/g}_{\text{NCM}}$ for $\text{Li}_6\text{PS}_5\text{Cl}$ and the tape-cast electrodes used in the liq-LIB cells, respectively. This implies that some of the carbonate species on the NCM622 surface react with the $\beta\text{-Li}_3\text{PS}_4$ solid electrolyte during preparation of the cathode composite, forming gaseous and/or solid side products. However, their nature remains elusive at present. After the initial cycle (referred to as postrun), a further reduction in $\text{Li}_2^{13}\text{CO}_3$ amount, because of electrochemical decomposition, was observed in all cases. Note that chemical decomposition due to reaction with HF, for example, is also feasible for the liq-LIB cells. In particular, it diminished to ~ 56 , ~ 72 , and $\sim 24 \mu\text{mol/g}_{\text{NCM}}$ for $\beta\text{-Li}_3\text{PS}_4$, $\text{Li}_6\text{PS}_5\text{Cl}$, and LP57 electrolyte, respectively. This foremost suggests higher connectivity between the NCM622 particles and the electrolyte in the liq-LIB cells (i.e., better electrochemical addressability of the active material and therefore $\text{Li}_2^{13}\text{CO}_3$), which does not come as a surprise though, as inhomogeneities pertaining to inactive (electrically isolated) cathode material in pelletized SSB cells have been reported.^{18–20} Moreover, this observation is in line with recent reports that most of the carbonate surface species are decomposed during the initial cycle for liq-LIBs.^{9,12}

Adding up the total quantity of evolved $^{13}\text{CO}_2$ from DEMS and the amount of $\text{Li}_2^{13}\text{CO}_3$ deduced from acid titration measurements after the initial cycle (postrun) should yield a similar amount of $\text{Li}_2^{13}\text{CO}_3$ to that obtained for the as-prepared cathodes (prerun). However, there are apparent discrepancies, ranging from $<15\%$ for $\beta\text{-Li}_3\text{PS}_4$ and $\text{Li}_6\text{PS}_5\text{Cl}$ to $\sim 40\%$ for the LP57 electrolyte. Such discrepancies are probably due to differences in reactivity of the electrolytes tested and/or partial solubility of CO_2 in the case of the liquid electrolyte. In addition, the altered local environment of ^{13}C in the tape-cast electrodes, resulting from the presence of graphite additive and polyvinylidene difluoride binder, may also play a role.

CONCLUSIONS

In summary, we have shown common CO_2 and O_2 evolution upon cycling of LIB cells using a Ni-rich layered oxide cathode material (NCM622) and either a liquid (LP57) or solid electrolyte ($\beta\text{-Li}_3\text{PS}_4$ or $\text{Li}_6\text{PS}_5\text{Cl}$). Both species originate from the electrochemical decomposition of Li_2CO_3 surface contaminants and/or O_2 release from the NCM lattice at high SOC. Oxidative decomposition of the liquid electrolyte also contributes to CO_2 evolution in the liq-LIB cells, amounting to a significant share of the total quantity of evolved gases. From a numbers perspective, the cumulative amount of gases released during the initial cycle is more than an order of magnitude larger for the liq-LIB than SSB cells. Moreover, we show that SO_2 evolution may occur in lithium thiophosphate-based SSBs, its origin being related to the chemical reaction between O_2 , probably $^1\text{O}_2$, and the solid electrolyte.

In a wider context, our work broadens the picture of the implications of gas evolution in LIBs. From an application perspective, gassing of SSBs appears to be less critical than for liq-LIBs, because far less gaseous species are generated during cycling. However, the effect that solid electrolytes and especially surface-modified active materials can have on the gassing behavior calls for future studies to explore the complex interplay between interface/interphase formation and impedance buildup, among others.

ASSOCIATED CONTENT

Supporting Information

The Supporting Information is available free of charge at <https://pubs.acs.org/doi/10.1021/acsami.0c02872>.

Additional results from acid titration measurements and from DEMS for the liq-LIB and SSB cells (PDF)

AUTHOR INFORMATION

Corresponding Authors

Florian Strauss – Battery and Electrochemistry Laboratory, Institute of Nanotechnology, Karlsruhe Institute of Technology (KIT), Eggenstein-Leopoldshafen 76344, Germany; orcid.org/0000-0001-5817-6349; Phone: +49 721 60828907; Email: florian.strauss@kit.edu

Torsten Brezesinski – Battery and Electrochemistry Laboratory, Institute of Nanotechnology, Karlsruhe Institute of Technology (KIT), Eggenstein-Leopoldshafen 76344, Germany; orcid.org/0000-0002-4336-263X; Phone: +49 721 60828827; Email: torsten.brezesinski@kit.edu

4.1 Results and Discussion – Gas Evolution in Lithium-Ion Batteries: Solid versus Liquid Electrolyte

Authors

Jun Hao Teo – Battery and Electrochemistry Laboratory, Institute of Nanotechnology, Karlsruhe Institute of Technology (KIT), Eggenstein-Leopoldshafen 76344, Germany;

orcid.org/0000-0002-0343-669X

Alexander Schiele – Battery and Electrochemistry Laboratory, Institute of Nanotechnology, Karlsruhe Institute of Technology (KIT), Eggenstein-Leopoldshafen 76344, Germany

Timo Bartsch – Battery and Electrochemistry Laboratory, Institute of Nanotechnology, Karlsruhe Institute of Technology (KIT), Eggenstein-Leopoldshafen 76344, Germany

Toru Hatsukade – Battery and Electrochemistry Laboratory, Institute of Nanotechnology, Karlsruhe Institute of Technology (KIT), Eggenstein-Leopoldshafen 76344, Germany;

orcid.org/0000-0001-9016-0929

Pascal Hartmann – Battery and Electrochemistry Laboratory, Institute of Nanotechnology, Karlsruhe Institute of Technology (KIT), Eggenstein-Leopoldshafen 76344, Germany; BASF SE, Ludwigshafen 67056, Germany

Jürgen Janek – Battery and Electrochemistry Laboratory, Institute of Nanotechnology, Karlsruhe Institute of Technology (KIT), Eggenstein-Leopoldshafen 76344, Germany; Institute of Physical Chemistry & Center for Materials Science, Justus-Liebig-University Giessen, Giessen 35392, Germany;

orcid.org/0000-0002-9221-4756

Complete contact information is available at:

<https://pubs.acs.org/10.1021/acsami.0c02872>

Author Contributions

[†]F.S. and J.H.T. contributed equally to this work.

Notes

The authors declare no competing financial interest.

ACKNOWLEDGMENTS

This study is part of the projects being funded within the BASF International Network for Batteries and Electrochemistry. The authors also acknowledge the Federal Ministry of Education & Research (BMBF) for funding within the project ARTEMYS (03XP0114J).

REFERENCES

- (1) Larcher, D.; Tarascon, J.-M. Towards Greener and More Sustainable Batteries for Electrical Energy Storage. *Nat. Chem.* **2015**, *7*, 19–29.
- (2) Myung, S.-T.; Maglia, F.; Park, K.-J.; Yoon, C. S.; Lamp, P.; Kim, S.-J.; Sun, Y.-K. Nickel-Rich Layered Cathode Materials for Automotive Lithium-Ion Batteries: Achievements and Perspectives. *ACS Energy Lett.* **2017**, *2*, 196–223.
- (3) Kong, W.; Li, H.; Huang, X.; Chen, L. Gas Evolution Behaviors for Several Cathode Materials in Lithium-Ion Batteries. *J. Power Sources* **2005**, *142*, 285–291.
- (4) Imhof, R.; Novak, P. Oxidative Electrolyte Solvent Degradation in Lithium-Ion Batteries: An In Situ Differential Electrochemical Mass Spectrometry Investigation. *J. Electrochem. Soc.* **1999**, *146*, 1702–1706.
- (5) Jung, R.; Metzger, M.; Maglia, F.; Stinner, C.; Gasteiger, H. Chemical vs. Electrochemical Electrolyte Oxidation on NMC111, NMC622, NMC811, LNMO, and Conductive Carbon. *J. Phys. Chem. Lett.* **2017**, *8*, 4820–4825.
- (6) Metzger, M.; Strehle, B.; Solchenbach, S.; Gasteiger, H. A. Origin of H₂ Evolution in LIBs: H₂O Reduction vs. Electrolyte Oxidation. *J. Electrochem. Soc.* **2016**, *163*, A798–A809.
- (7) Berkes, B. B.; Schiele, A.; Sommer, H.; Brezesinski, T.; Janek, J. On the Gassing Behavior of Lithium-Ion Batteries with NCM523 Cathodes. *J. Solid State Electrochem.* **2016**, *20*, 2961–2967.
- (8) Jung, R.; Metzger, M.; Maglia, F.; Stinner, C.; Gasteiger, H. A. Oxygen Release and Its Effect on the Cycling Stability of LiNi_xMn_yCo₂O₂ (NMC) Cathode Materials for Li-Ion Batteries. *J. Electrochem. Soc.* **2017**, *164*, A1361–A1377.
- (9) Renfrew, S. E.; McCloskey, B. D. Residual Lithium Carbonate Predominantly Accounts for First Cycle CO₂ and CO Outgassing of Li-Stoichiometric and Li-Rich Layered Transition Metal Oxides. *J. Am. Chem. Soc.* **2017**, *139*, 17853–17860.
- (10) Bartsch, T.; Strauss, F.; Hatsukade, T.; Schiele, A.; Kim, A.-Y.; Hartmann, P.; Janek, J.; Brezesinski, T. Gas Evolution in All-Solid-State Battery Cells. *ACS Energy Lett.* **2018**, *3*, 2539–2543.
- (11) Kim, A.-Y.; Strauss, F.; Bartsch, T.; Teo, J. H.; Hatsukade, T.; Mazilkin, A.; Janek, J.; Hartmann, P.; Brezesinski, T. Stabilizing Effect of a Hybrid Surface Coating on a Ni-Rich NCM Cathode Material in All-Solid-State Batteries. *Chem. Mater.* **2019**, *31*, 9664–9672.
- (12) Hatsukade, T.; Schiele, A.; Hartmann, P.; Brezesinski, T.; Janek, J. Origin of Carbon Dioxide Evolved during Cycling of Nickel-Rich Layered NCM Cathodes. *ACS Appl. Mater. Interfaces* **2018**, *10*, 38892–38899.
- (13) Berkes, B. B.; Jozwiuk, A.; Sommer, H.; Brezesinski, T.; Janek, J. Simultaneous Acquisition of Differential Electrochemical Mass Spectrometry and Infrared Spectroscopy Data for In Situ Characterization of Gas Evolution Reactions in Lithium-Ion Batteries. *Electrochem. Commun.* **2015**, *60*, 64–69.
- (14) Berkes, B. B.; Jozwiuk, A.; Vračar, M.; Sommer, H.; Brezesinski, T.; Janek, J. Online Continuous Flow Differential Electrochemical Mass Spectrometry with a Realistic Battery Setup for High-Precision, Long-Term Cycling Tests. *Anal. Chem.* **2015**, *87*, 5878–5883.
- (15) Mahne, N.; Renfrew, S. E.; McCloskey, B. D.; Freunberger, S. A. Electrochemical Oxidation of Lithium Carbonate Generates Singlet Oxygen. *Angew. Chem., Int. Ed.* **2018**, *57*, 5529–5533.
- (16) Lux, S.; Baldauf-Sommerbauer, G.; Siebenhofer, M. Hydrogenation of Inorganic Metal Carbonates: A Review on Its Potential for Carbon Dioxide Utilization and Emission Reduction. *ChemSusChem* **2018**, *11*, 3357–3375.
- (17) Jung, R.; Metzger, M.; Maglia, F.; Stinner, C.; Gasteiger, H. A. Oxygen Release and Its Effect on the Cycling Stability of LiNi_xMn_yCo₂O₂ (NMC) Cathode Materials for Li-Ion Batteries. *J. Electrochem. Soc.* **2017**, *164*, A1361–A1377.
- (18) Bartsch, T.; Kim, A.-Y.; Strauss, F.; de Biasi, L.; Teo, J. H.; Janek, J.; Hartmann, P.; Brezesinski, T. Indirect State-of-Charge Determination of All-Solid-State Battery Cells by X-Ray Diffraction. *Chem. Commun.* **2019**, *55*, 11223–11226.
- (19) Strauss, F.; Bartsch, T.; de Biasi, L.; Kim, A.-Y.; Janek, J.; Hartmann, P.; Brezesinski, T. Impact of Cathode Material Particle Size on the Capacity of Bulk-Type All-Solid-State Batteries. *ACS Energy Lett.* **2018**, *3*, 992–996.
- (20) Chen, K.; Shinjo, S.; Sakuda, A.; Yamamoto, K.; Uchiyama, T.; Kuratani, K.; Takeuchi, T.; Orikasa, Y.; Hayashi, A.; Tatsumisago, M.; Kimura, Y.; Nakamura, T.; Amezawa, K.; Uchimoto, Y. Morphological Effect on Reaction Distribution Influenced by Binder Materials in Composite Electrodes for Sheet-Type All-Solid-State Lithium-Ion Batteries with the Sulfide-Based Solid Electrolyte. *J. Phys. Chem. C* **2019**, *123*, 3292–3298.
- (21) Koerver, R.; Aygün, I.; Leichtweiß, T.; Dietrich, C.; Zhang, W.; Binder, J. O.; Hartmann, P.; Zeier, W. G.; Janek, J. Capacity Fade in Solid-State Batteries: Interphase Formation and Chemomechanical Processes in Nickel-Rich Layered Oxide Cathodes and Lithium Thiophosphate Solid Electrolytes. *Chem. Mater.* **2017**, *29*, 5574–5582.
- (22) Strauss, F.; Stepien, D.; Maibach, J.; Pfaffmann, L.; Indris, S.; Hartmann, P.; Brezesinski, T. Influence of Electronically Conductive Additives on the Cycling Performance of Argrodite-Based All-Solid-State Batteries. *RSC Adv.* **2020**, *10*, 1114–1119.
- (23) Auvergniot, J.; Cassel, A.; Ledeuil, J.-B.; Viallet, V.; Seznec, V.; Dedryvère, R. Interface Stability of Argrodite Li₆PS₃Cl toward

4.1 Results and Discussion – Gas Evolution in Lithium-Ion Batteries: Solid versus Liquid Electrolyte

LiCoO₂, LiNi_{1/3}Co_{1/3}Mn_{1/3}O₂, and LiMn₂O₄ in Bulk All-Solid-State Batteries. *Chem. Mater.* **2017**, *29*, 3883–3890.

(24) Walther, F.; Koerver, R.; Fuchs, T.; Ohno, S.; Sann, J.; Rohnke, M.; Zeier, W. G.; Janek, J. Visualization of the Interfacial Decomposition of Composite Cathodes in Argyrodite-Based All-Solid-State Batteries Using Time-of-Flight Secondary-Ion Mass Spectrometry. *Chem. Mater.* **2019**, *31*, 3745–3755.

(25) Freiberg, A. T.; Roos, M. K.; Wandt, J.; de Vivie-Riedle, R.; Gasteiger, H. A. Singlet Oxygen Reactivity with Carbonate Solvents Used for Li-Ion Battery Electrolytes. *J. Phys. Chem. A* **2018**, *122*, 8828–8839.

(26) Wandt, J.; Freiberg, A. T. S.; Ogrodnik, A.; Gasteiger, H. A. Singlet Oxygen Evolution from Layered Transition Metal Oxide Cathode Materials and Its Implications for Lithium-Ion Batteries. *Mater. Today* **2018**, *21*, 825–833.

(27) Sasaki, I.; Komori, T.; Honda, K.; Hibino, J. Enhancement of Rate Capability for All-Solid-State Batteries Using Surface Oxidized Sulfide Solid Electrolyte. *AiMES 2018 Meeting*; Cancun, Mexico; The Electrochemical Society: Pennington, NJ, 2018.

(28) Richards, W. D.; Miara, L. J.; Wang, Y.; Kim, J. C.; Ceder, G. Interface Stability in Solid-State Batteries. *Chem. Mater.* **2016**, *28*, 266–273.

(29) Zhu, Y.; He, X.; Mo, Y. Origin of Outstanding Stability in the Lithium Solid Electrolyte Materials: Insights from Thermodynamic Analyses Based on First-Principles Calculations. *ACS Appl. Mater. Interfaces* **2015**, *7*, 23685–23693.

(30) Jung, R.; Strobl, P.; Maglia, F.; Stinner, C.; Gasteiger, H. A. Temperature Dependence of Oxygen Release from Li-Ni_{0.6}Mn_{0.2}Co_{0.2}O₂ (NMC622) Cathode Materials for Li-Ion Batteries. *J. Electrochem. Soc.* **2018**, *165*, A2869–A2879.

Supporting Information

Gas Evolution in Lithium-Ion Batteries: Solid versus Liquid Electrolyte

Florian Strauss,^{†,*} Jun Hao Teo,[†] Alexander Schiele,[†] Timo Bartsch,[†] Toru Hatsukade,[†] Pascal Hartmann,^{†,‡} Jürgen Janek,^{†,§} and Torsten Brezesinski^{†,*}

[†] Battery and Electrochemistry Laboratory, Institute of Nanotechnology, Karlsruhe Institute of Technology (KIT), Hermann-von-Helmholtz-Platz 1, 76344 Eggenstein-Leopoldshafen, Germany.

[‡] BASF SE, Carl-Bosch-Strasse 38, 67056 Ludwigshafen, Germany.

[§] Institute of Physical Chemistry & Center for Materials Science, Justus-Liebig-University Giessen, Heinrich-Buff-Ring 17, 35392 Giessen, Germany.

E-mail: florian.strauss@kit.edu, torsten.brezesinski@kit.edu

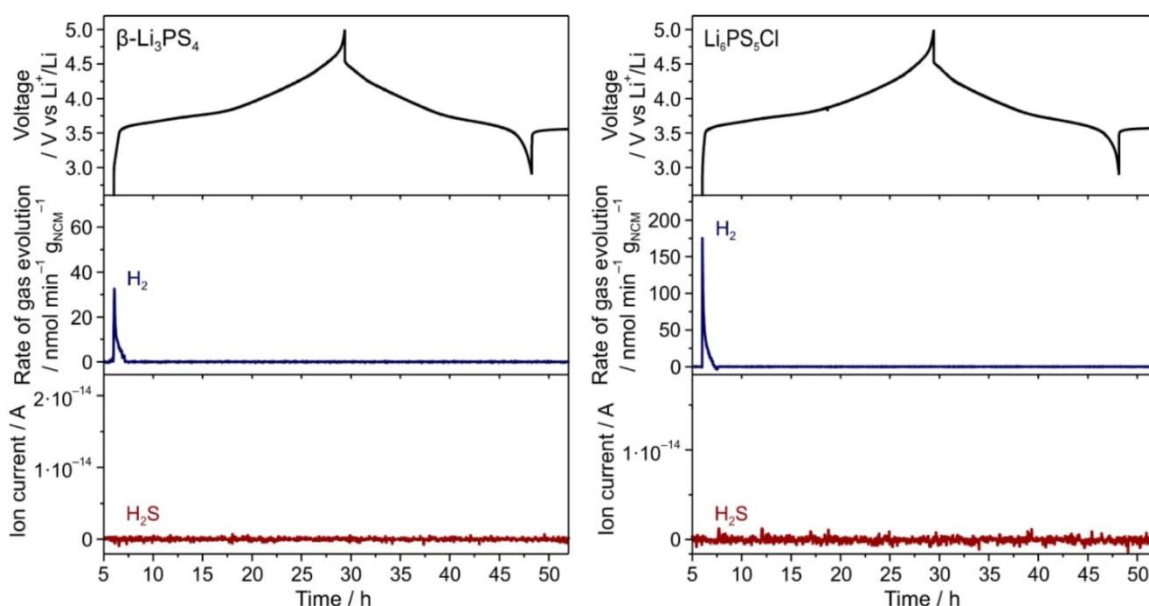


Figure S1. Electrochemical trace of SSB cells using (left) β - Li_3PS_4 and (right) $\text{Li}_6\text{PS}_5\text{Cl}$ solid electrolyte and the corresponding time-resolved H_2 evolution rate and ion current for H_2S . The cells were cycled in the potential range of 2.3–4.4 V with respect to In/InLi (~ 2.9 –5.0 V vs Li^+/Li).

4.1 Results and Discussion – Gas Evolution in Lithium-Ion Batteries: Solid versus Liquid Electrolyte

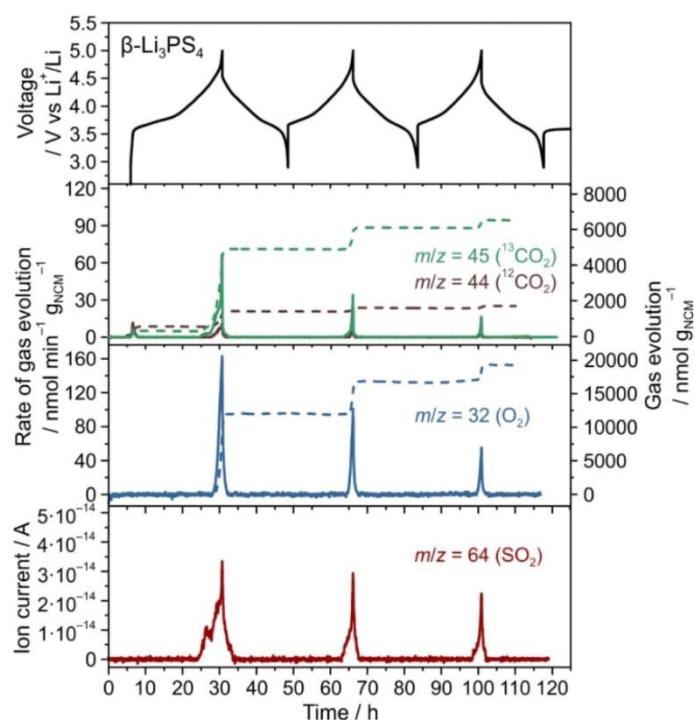


Figure S2. Electrochemical trace of a SSB cell using β - Li_3PS_4 solid electrolyte and the corresponding time-resolved $^{12}\text{CO}_2$, $^{13}\text{CO}_2$, and O_2 evolution rates and ion current for SO_2 . The cell was cycled in the potential range of 2.3–4.4 V with respect to In/InLi (~ 2.9 – 5.0 V vs Li^+/Li). Note that there are some deviations in accumulated gas amount per cycle (especially for O_2) among otherwise similar SSB cells. Such discrepancy may originate from subtle differences in cathode morphology (gas permeability) and/or reactivity.

4.1 Results and Discussion – Gas Evolution in Lithium-Ion Batteries: Solid versus Liquid Electrolyte

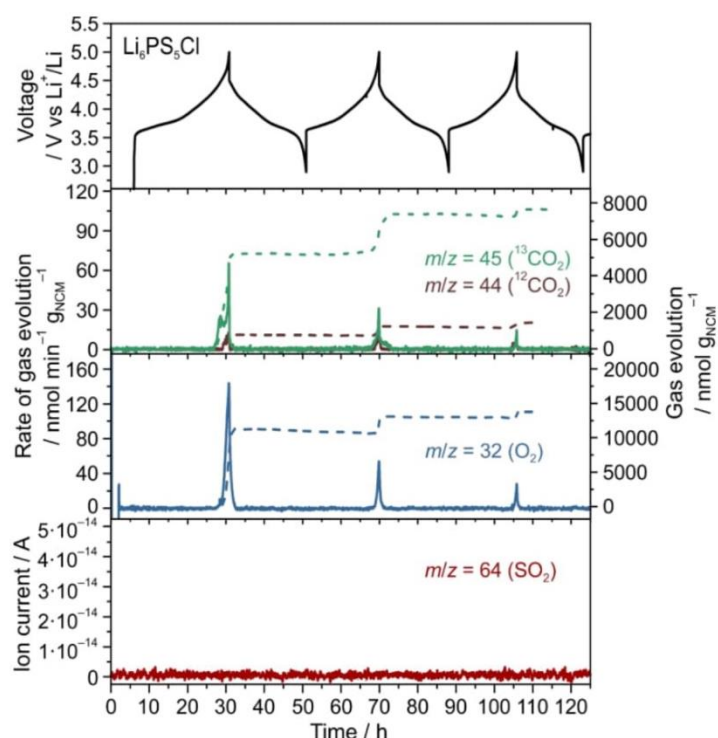


Figure S3. Electrochemical trace of a SSB cell using $\text{Li}_6\text{PS}_5\text{Cl}$ solid electrolyte and the corresponding time-resolved $^{12}\text{CO}_2$, $^{13}\text{CO}_2$, and O_2 evolution rates and ion current for SO_2 . The cell was cycled in the potential range of 2.3–4.4 V with respect to In/InLi (~ 2.9 – 5.0 V vs Li^+/Li). Note that there are some deviations in accumulated gas amount per cycle (especially for O_2) among otherwise similar SSB cells. Such discrepancy may originate from subtle differences in cathode morphology (gas permeability) and/or reactivity.

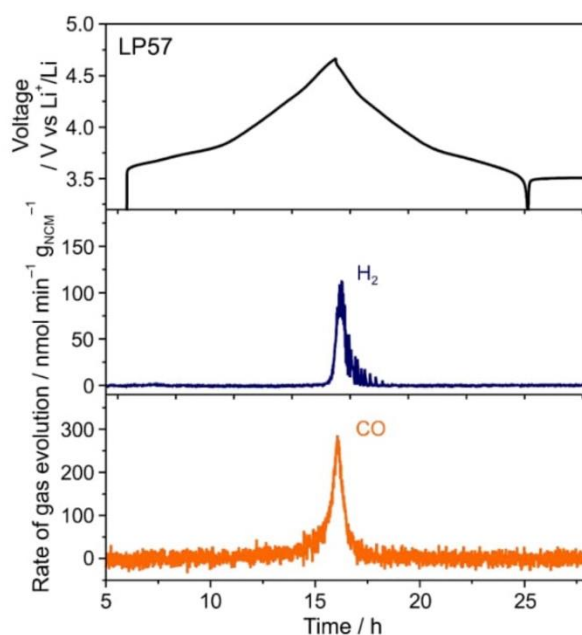


Figure S4. Electrochemical trace of a liq-LIB cell cycled with a specific charge capacity limitation of $240 \text{ mAh/g}_{\text{NCM}}$ and the corresponding time-resolved H_2 and CO (detected via IR absorption) evolution rates.

4.1 Results and Discussion – Gas Evolution in Lithium-Ion Batteries: Solid versus Liquid Electrolyte

Table S1. Amount of $^{13}\text{CO}_2$ evolved from the pristine and cycled NCM622 (in SSB and liq-LIB cells) as determined from acid titration and the respective calculated amount of $\text{Li}_2^{13}\text{CO}_3$ present on the different samples.

Sample	$m/z = 45 / \mu\text{mol}$	Gas evolution / $\mu\text{mol/g}_{\text{NCM}}$	$\text{Li}_2^{13}\text{CO}_3 / \text{wt.}\%$
Powder	0.905	102.2	0.76
$\text{Li}_6\text{PS}_5\text{Cl}_{\text{pre-run}}$	0.504	88.9	0.66
$\text{Li}_6\text{PS}_5\text{Cl}_{\text{post-run}}$	0.479	71.8	0.54
$\beta\text{-Li}_3\text{PS}_4_{\text{pre-run}}$	0.360	62.9	0.47
$\beta\text{-Li}_3\text{PS}_4_{\text{post-run}}$	0.370	56.3	0.42
$\text{Liq}_{\text{pre-run}}$	0.279	92.0	0.69
$\text{Liq}_{\text{post-run}}$	0.078	24.1	0.18

4.2. Design-of-experiments-guided optimization of slurry-cast cathodes for solid-state batteries

As mentioned in our previous publication on the importance of understanding all-solid-state batteries (SSBs) from an industrial-scale perspective, we attempt to further expand our lab's expertise and know-how in an extremely crucial stage of the scaling up of SSBs. This stage overlooks the transition of bulk-type SSBs from lab-scale powder-based pelletized cells to industrial-scale slurry-cast electrodes. Publication 2 reports an approach guided by design-of-experiments (DoE) to evaluate the influence of the type/content of polymer binder and conductive additive on both the electrochemistry and mechanical properties of the electrode sheet. The advantage of a DoE-approach is the reduction of experimental sets without compromising the information quality. Furthermore, the extrapolated results from the DoE in this study was supported by a combination of *ex situ* and *in situ* experimental analysis techniques. Unsurprisingly, given our expertise in gas analysis, *in situ* DEMS was also one of the techniques employed in the evaluation of the DoE results.

The designed set of experiments was able to screen three different types of binder, two different conductive carbon additives and their respective contents: OPN (Oppanol N 150 from BASF), SBR (45wt% styrene from Sigma Aldrich), hNBR (Therban LT 1707 VP from Arlanxeo), Super C65 carbon black (Timcal) and VGCF. Electrode sheets with $\text{Li}_{1+x}(\text{Ni}_{0.6}\text{Co}_{0.2}\text{Mn}_{0.2})_{1-x}\text{O}_2$ (NCM622), Li_3PS_4 solid electrolyte (SE), binder and carbon additive were prepared according to the designed experimental sets and underwent mechanical and electrochemical tests. The results of these tests were then input back into the statistical software JMP14 (SAS Institute Inc.), which allowed us to build a simple linear model that enables the prediction and optimization of our materials' combination. Depending on the optimization goal, the results will differ. Our study showed that when optimizing with regards to just electrochemical performance, the combination of 1 wt% OPN binder with 0.5 wt% VGCF conductive additive yielded the highest discharge capacities. In contrast, when optimizing to both mechanical and electrochemical performance, the best combination is composed of 2.7 wt% OPN with 0.5 wt% VGCF. These results reflect that the bottleneck of electrode fabrication lies in the minimum required amount of polymeric binder in order to achieve mechanical stability.

In order to support the extrapolated combination from the statistical model, a combination of *ex situ* and *in situ* experimental techniques were employed. First, galvanostatic cycling data showed an obvious difference in discharge capacities, with OPN-electrodes outperforming both SBR- and hNBR-electrodes. In addition, the first cycle Coulombic efficiency (CE) decreased in the following order OPN>SBR>hNBR, which indicated an improved electrochemical stability for the OPN-electrode. Second, electrochemical impedance spectroscopy (EIS) conducted on cycled cells showed an increase in both the cathode interfacial resistance ($R_{\text{CAM/SE}}$) and the solid electrolyte grain boundary resistance (R_{gb}) in the following order OPN>SBR>hNBR. The reduced $R_{\text{CAM/SE}}$ further support the argument of an improve electrochemical stability and that the addition of SBR or hNBR to the electrode contributed to a destabilization of the components. Such destabilization could be supported by the high R_{gb} for the hNBR-electrode and can be explained by a stronger coverage of the non-ionically conducting hNBR polymer via ion dipole interactions between the lithium ions of the SE and the nitrile functional side group of hNBR. Ultimately, the limited chemical/physical interactions of the OPN binder with the SE is believed to play a crucial role in its excellent electrochemical performance. Third, through a combination of scanning

4.2 Results and Discussion – Design-of-experiments-guided optimization of slurry-cast cathodes for solid-state batteries

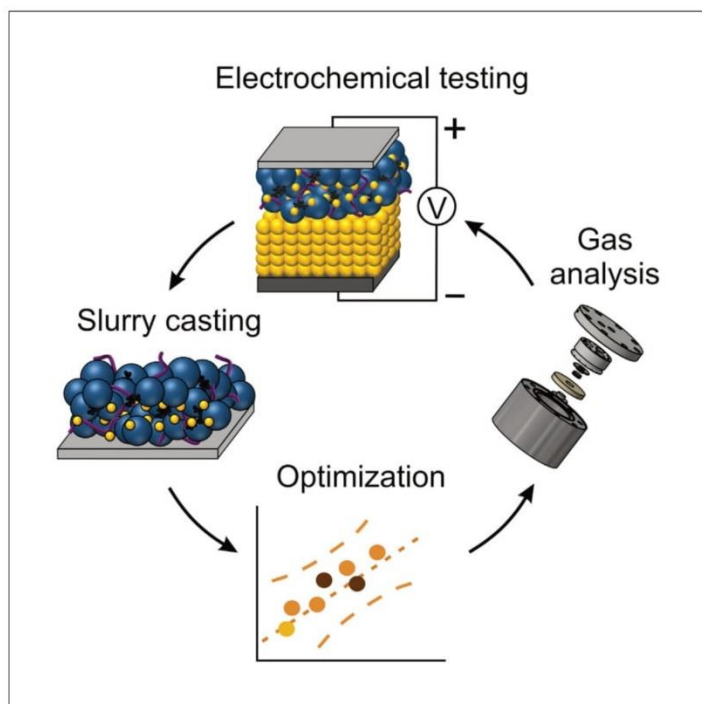
electron microscopy (SEM)/ energy-dispersive X-ray spectroscopy (EDS) and post-mortem X-ray diffraction (XRD), inhomogeneities were confirmed to play only a minor role in the electrochemical performance and should not account for the large discrepancy in electrochemical performance among the three binders. Lastly, differential electrochemical mass spectrometry (DEMS) was used to evaluate the binder stability by analyzing released gases that originate from side reactions (specifically with the reactive singlet oxygen, $^1\text{O}_2$). With the incorporation of an additional carbon-containing component (binder) to the system, we will be looking at both the CO_2 and SO_2 evolution behavior. Interestingly, SBR-electrodes show a depressed SO_2 signal coupled with a larger CO_2 signal peak at the highest state of charge (SOC). This observation indicates to us a preferential reaction of the reactive oxygen on the SBR binder, which among the three is the only one who possesses an alkene chain (units). The negative influences of hNBR on the electrode was further seen with DEMS, where a very distinct SO_2 signal was measured for hNBR-electrodes, despite a non-proportional release of O_2 . Despite having a lower SOC and lesser $^1\text{O}_2$ evolution, it showed a comparable SO_2 signal intensity to that of OPN-electrodes, which again suggests a more chemically active thiophosphates with respect to $^1\text{O}_2$. In conclusion, the various analysis techniques used corroborated the robustness of the model.

All the measurements, evaluation and writing for Publication 2 were conducted by me. The work was supervised by Prof. Dr. Jürgen Janek, Dr. Pascal Hartmann, Dr. Matteo Bianchini and Dr. Torsten Brezesinski. The final paper was then edited by eight co-authors.

Reprinted by permission from (Teo, J. H., Strauss, F., Tripković, Đ., Schweidler, S., Ma, Y., Bianchini, M., Janek, J., Brezesinski, T.) Design-of-experiments-guided optimization of slurry-cast cathodes for solid-state batteries. *Cell Rep. Phys. Sci.* **2021**, 2, 100465) Copyright © 2021 The Authors.

Article

Design-of-experiments-guided optimization of slurry-cast cathodes for solid-state batteries



Teo et al. apply a statistical approach, DoE, to facilitate the transition from pelletized to slurry-cast cathodes for solid-state batteries. Datasets from electrochemical and mechanical tests are used to build a model that allows effective tailoring of the slurry recipe. The DoE predictions/results are evaluated using various analytical techniques.

Jun Hao Teo, Florian Strauss, Đorđije Tripković, ..., Matteo Bianchini, Jürgen Janek, Torsten Brezesinski

jun.teo@kit.edu (J.H.T.)
juergen.janek@kit.edu (J.J.)
torsten.brezesinski@kit.edu (T.B.)

Highlights

Statistical optimization of slurry-cast NCM cathodes for solid-state batteries

Cycling performance and processability correlate with binder chemistry and content

Design of experiments (DoE) results are corroborated experimentally

Operando gas analysis reveals (electro-)chemical binder instability

Teo et al., Cell Reports Physical Science 2, 100465

June 23, 2021 © 2021 The Authors.

<https://doi.org/10.1016/j.xcrp.2021.100465>



Article

Design-of-experiments-guided optimization of slurry-cast cathodes for solid-state batteries

Jun Hao Teo,^{1,6,*} Florian Strauss,¹ Đorđije Tripković,² Simon Schweidler,¹ Yuan Ma,¹ Matteo Bianchini,^{1,2} Jürgen Janek,^{1,3,4,*} and Torsten Brezesinski^{1,5,*}

SUMMARY

Laboratory research into bulk-type solid-state batteries (SSBs) has been focused predominantly on powder-based, pelletized cells and has been sufficient to evaluate fundamental limitations and tailor the constituents to some degree. However, to improve experimental reliability and for commercial implementation of this technology, competitive slurry-cast electrodes are required. Here, we report on the application of an approach guided by design of experiments (DoE) to evaluate the influence of the type/content of polymer binder and conductive carbon additive on the cyclability and processability of $\text{Li}_{1+x}(\text{Ni}_{0.6}\text{Co}_{0.2}\text{Mn}_{0.2})_{1-x}\text{O}_2$ (NCM622) cathodes in SSB cells using lithium thiophosphate solid electrolytes. The predictions are verified by charge-discharge and impedance spectroscopy measurements. Furthermore, structural changes and gas evolution are monitored via X-ray diffraction and differential electrochemical mass spectrometry, respectively, in an attempt to rationalize and support the DoE results. In summary, the optimized combination of polymer binder and conductive carbon additive leads to high electrochemical performance and good processability.

INTRODUCTION

Advances in electrochemical energy storage have been going at breakneck pace in recent years. This is largely attributed to progress in mobile devices. Conventional Li-ion batteries (LIBs) have played a major role in improving connectivity in a globalized world. As battery technologies progressed, novel concepts of integrating them into existing systems have emerged, ranging from solving environmental problems to revolutionizing the century-old automobile industry. State-of-the-art LIBs remain the first choice for energy-storage systems. However, LIBs have limitations. First, they do not yet possess the desired energy and power densities for mobility and transportation applications. Second, they possess an inherent safety concern because of the flammable components in the system, which have led to well-documented spontaneous combustion and explosions.¹

Solid-state batteries (SSBs) are widely seen as the next generation of lithium batteries that could potentially overcome the previously mentioned limitations.² SSBs may possess increased power and energy densities, improved safety conditions, and a larger operating temperature window. These advantages would allow them to be used in a wider range of applications. The main components of SSBs are the cathode composite, the solid-electrolyte separator layer, and the anode composite (or Li metal). The cathode composite is a solid dispersion of solid electrolyte, active material, and additives. The separator layer is a densely packed solid electrolyte with sufficient mechanical stability and high tolerance against dendrite growth, in the

¹Battery and Electrochemistry Laboratory, Institute of Nanotechnology, Karlsruhe Institute of Technology (KIT), Hermann-von-Helmholtz-Platz 1, 76344 Eggenstein-Leopoldshafen, Germany

²BASF SE, Carl-Bosch-Str. 38, 67056 Ludwigshafen, Germany

³Institute of Physical Chemistry & Center for Materials Science, Justus-Liebig-University Giessen, Heinrich-Buff-Ring 17, 35392 Giessen, Germany

⁴Twitter: @Janek_Lab_JLU

⁵Twitter: @TBrezesinski

⁶Lead contact

*Correspondence: jun.teo@kit.edu (J.H.T.), juergen.janek@kit.edu (J.J.), torsten.brezesinski@kit.edu (T.B.)

<https://doi.org/10.1016/j.xcrp.2021.100465>



4.2 Results and Discussion – Design-of-experiments-guided optimization of slurry-cast cathodes for solid-state batteries



CellPress
OPEN ACCESS

Cell Reports
Physical Science
Article

case of a Li metal anode.³ In contrast, LIBs have a porous separator filled with flammable organic electrolyte.

There are two main groups of solid electrolytes under consideration for next-generation SSBs, namely, sulfides/oxides (glasses, ceramics, and glass-ceramics) and polymers. Each has advantages and disadvantages. The sulfide (thiophosphate) solid electrolytes have high room-temperature ionic conductivities² and low elasticity moduli and shear strengths,^{4,5} and they possess good processability at low temperatures. However, they are highly reactive under ambient conditions, requiring them to be processed in a dry environment. In addition, the reaction with water (atmospheric conditions) generates toxic gases such as H₂S, thus contributing to a potentially new safety issue. Moreover, sulfide solid electrolytes have narrow electrochemical stability windows and show significant interfacial reactivity at both low and high voltages.⁶ In contrast, the oxide ceramic electrolytes are relatively more stable under ambient conditions and do not generate toxic gases when exposed to humidity. Their electrochemical stability windows are also larger compared with those of sulfides. However, they possess lower room-temperature ionic conductivities, are brittle, and typically synthesized at high temperatures. Furthermore, processing of oxide solid-electrolyte SSBs is extremely challenging. Oxides are true ceramic materials with high elasticity moduli and shear strengths, making the formation of low-impedance interfaces between the solid electrolyte and the cathode active material (CAM) achievable only at high temperatures.⁷ Lastly, the polymers are often considered ideal solid electrolytes, possessing strong dendrite growth resistance and improved safety and reliability, but they still show too low conductivity.^{8,9}

In the last few years, there has been an exponential growth in the research and development of predominantly powder-based, pelletized SSBs, ranging from the tailored composition of the cathode composite,^{10,11} particle size,¹² cell-fabrication pressure,¹³ and stack pressure applied during electrochemical cycling^{14–17} to the operation temperature.¹⁸ Such cells often show good electrochemical performance. However, those that are typically used on a laboratory level are not scalable. Furthermore, variances between assembled SSBs are commonly observed for pelletized cells, resulting in discrepancies of experimental results. To be cost competitive with LIBs and exhibit improved reliability, SSBs have to transition toward sheet-based designs.

The concept of sheet-based (sulfide) SSBs has been thoroughly discussed and is regarded as feasible.^{19,20} However, although there are almost three decades of experience in processing of porous electrode sheets for LIB applications, there is little experience in processing of compact solid-state electrode sheets. And there are still numerous challenges for the production of sheet-based SSBs, the first of which is the formulation of a slurry recipe (choice of solvent, cathode components, etc.). For example, the application of sulfide solid electrolytes requires solvents to be nonpolar to avoid unwanted side reactions. Consequently, the polymer binders have to be nonreactive, are preferably soluble in nonpolar solvents, and should provide sufficient mechanical stability to the fabricated electrode sheets and not severely affect the ionic conductivity of the solid electrolyte.²¹ Furthermore, binders have different functional groups, and it is crucial to understand their interaction with the different components in the cathode composite and how that influences the SSB operation.

The combinations of solvent and binder alone highlight the considerable number of parameters (viscosity, adhesion force, etc.) contributing to the electrode quality and

4.2 Results and Discussion – Design-of-experiments-guided optimization of slurry-cast cathodes for solid-state batteries



ultimately the electrochemical performance. Under normal circumstances, the number of experiments required increases on a factorial scale with the number of parameters under consideration. In addition, when dealing with a large dataset, with large numbers of possible combinations between parameters, important correlations among them may be missed. Here we use a design of experiments (DoE) approach to tailor the cathode-composite-sheet preparation process for improved electrochemical performance. DoE is a well-established method for optimizing experimental sets with the goal of maximizing statistical power and/or minimizing the number of trials. We exploit DoE to reduce the number of experiments without compromising information quality (statistical power) due to the relatively cost- and labor-intensive process of electrode-sheet preparation.

In this work, we describe the screening of different types of polymer binders and carbon additives and their respective contents with the help of a DoE approach (we have several fixed parameters for the slurry recipe, such as the choice of solvent and cathode active material). Three candidates for binders and two candidates for additives are selected, and the design is evaluated using the statistical software JMP 14 (SAS Institute Inc.). A set number of electrode sheets are created with various combinations of the binder type/content and carbon type/content, which are subjected to electrochemical and mechanical tests in SSB full cells with a carbon-coated $\text{Li}_4\text{Ti}_5\text{O}_{12}$ (LTO) anode. We then feed this data back into the software to build a simple linear model that allows the prediction and optimization of the materials' combination. Finally, we use a combination of ex situ and operando techniques to better understand the cell cyclability and justify the predictions.

RESULTS AND DISCUSSION

DoE approach

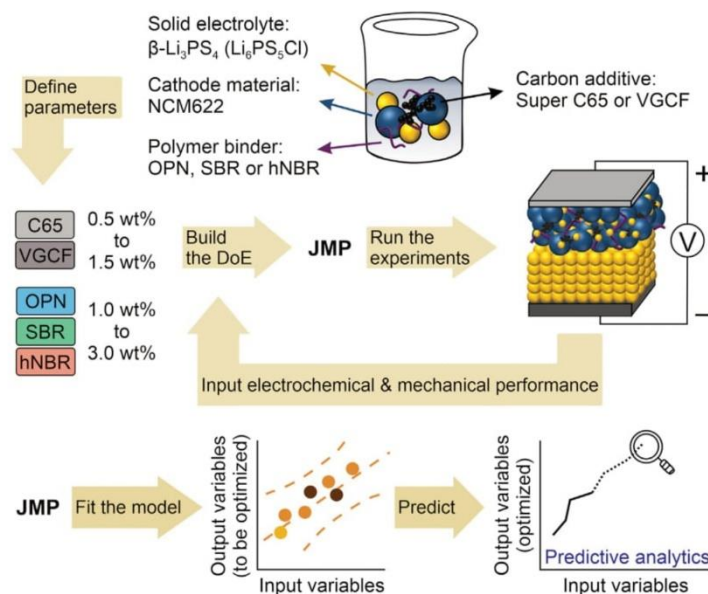
The goal of the present DoE-guided approach was the optimization of slurry-cast cathodes for application in SSBs with regard to the type and content of polymer binder and carbon additive (Scheme 1). The first step involved defining the experimental conditions. As mentioned, we focused mainly on the variation of the material-related parameters and therefore fixed the process-related ones. The material-related parameters were defined as follows: (1) carbon type (Super C65 carbon black or vapor-grown carbon fibers [VGCF]) in categorical roles, (2) carbon content (0.5–1.5 wt %) in continuous roles, (3) binder type (polyisobutene [OPN], poly(styrene-co-butadiene) rubber [SBR], or hydrogenated nitrile butadiene rubber [hNBR]) in categorical roles, and (4) binder content (1.0–3.0 wt %) in continuous roles, with “categorical” implying that the variables are represented as they are and “continuous” implying that the variables can be set to any value between the lower and the upper limits. These made up the first input variables needed for the program to design a set of experiments. The required number of runs in this study was 23 (Table S1). Then, all experiments were carried out, and the results were evaluated in terms of capacity retention and specific discharge capacity after 20 cycles and mechanical properties (bendability and punchability of the cathode sheet). These formed the second set of input variables. After preparing all 23 electrodes (details in the Supplemental Experimental Procedures) and performing the necessary tests, the results were analyzed in JMP 14. To probe the possible interactions among variables, we used the response surface model (RSM) to fit the data. While evaluating the model, it is crucial to avoid overfitting. Overfitted models are unnecessarily complex. They fit better to the dataset but produce poorer predictions. A way to avoid overfitting is to remove variables of small significance, resulting in a more robust model while maintaining a high adjusted R^2 value. The p value represents the probability of an outcome under the assumption that the null hypothesis is true. In this study, the

4.2 Results and Discussion – Design-of-experiments-guided optimization of slurry-cast cathodes for solid-state batteries



CellPress
OPEN ACCESS

Cell Reports
Physical Science
Article



Scheme 1. Schematic overview of the DoE-guided approach for tailoring of slurry-cast cathodes in SSBs

null hypothesis was defined as “The input variables (with/without their interactions) do not influence the electrochemical performance and processability of the cathode sheet.” A high p value for an input variable would mean that it does not strongly affect the electrochemical performance and processability of the cathode sheet. Hence, variables with $p > 0.05$ were removed from consideration when building the model. An advantage of using the adjusted R^2 value over the R^2 value is that it takes interactions among variables into account and is a better representation of a model that has multiple variables. The closer the adjusted R^2 value is to 100%, the better the model is at predicting the output variables.

For high prediction power, the number of parameters was reduced to eight and six for the capacity retention and specific discharge capacity, respectively. When considering both electrochemistry and mechanical outputs, the minimum number of parameters required was six (Table S2).

Optimizing for electrochemical performance

Monitoring capacity retention helps to quantify the cell degradation, whereas the specific discharge capacity is an indication of the practical energy storage capability of the cell. In general, the large scattering of the electrochemical performance among cells of different binder/carbon combinations already indicates the strong dependence on the material type and content (Figure S1). To gain more insight on how each parameter affects the electrochemical performance, the selected parameters from all 23 cells were fed into the statistical program to create prediction profiles independent from one another.

The plots in Figure 1 show the corresponding combinations of material parameters and their influence on the specific discharge capacity and capacity retention. The

4.2 Results and Discussion – Design-of-experiments-guided optimization of slurry-cast cathodes for solid-state batteries

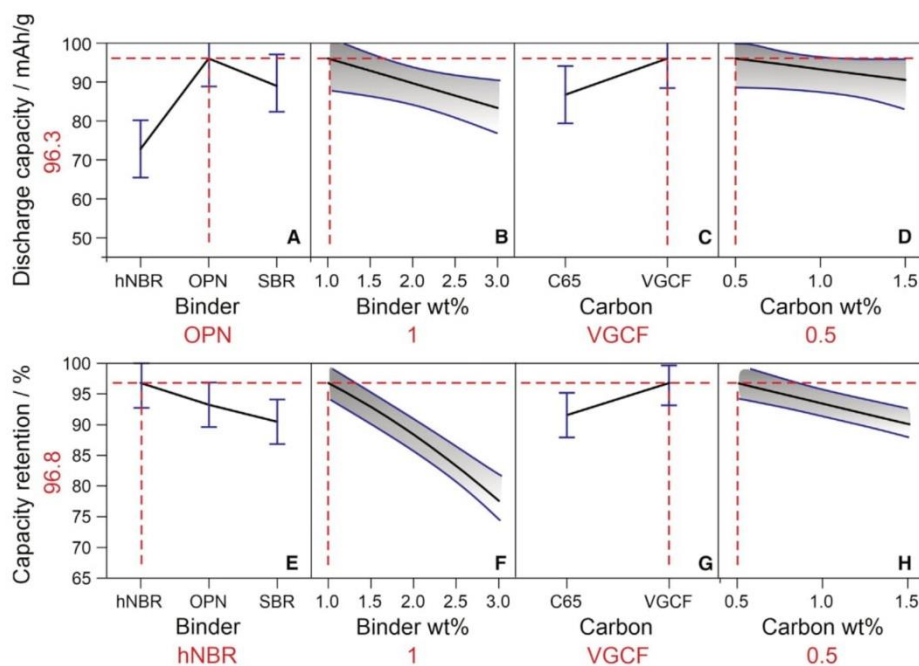


Figure 1. Prediction profiles generated for the optimization of electrochemical performance

The optimum combinations for (A–D) 20th-cycle specific discharge capacity and (E–H) capacity retention after 20 cycles are extrapolated to be OPN (1.0 wt %)/VGCF (0.5 wt %) and hNBR (1.0 wt %)/VGCF (0.5 wt %), respectively.

steeper the slope of the line, the larger the influence of the parameter. The intersection with the dashed red lines represents the optimal value for the respective variable. The blue lines for the binder and carbon type represent the 95% confidence interval for each categorical value. For the binder and carbon content, the gray areas encompassed by the blue curves represent the 95% confidence band on a continuous level. Looking at the generated profiles, the magnitude of influence of the input variables on both the specific discharge capacity and the capacity retention decreases from binder type to binder content, to carbon type, and lastly to carbon content. The optimal recipe shown in Figures 1A–1D to maximize the specific discharge capacity predicted achieving ~96 mAh/g_{NCM622} after 20 cycles. This recipe would require OPN as the polymer binder and VGCF as the conductive additive, with contents of 1.0 and 0.5 wt %, respectively. In comparison, when optimizing for capacity retention (Figures 1E–1H), a recipe resulting in ~97% would require a combination of 1.0 wt % hNBR and 0.5 wt % VGCF.

In summary, the only difference in the independent optimization of these two electrochemical parameters was the binder material (Figures 1A and 1E). For optimized capacity retention, apparently hNBR yielded the best result. However, the main reason for this is that the initial specific discharge capacity was the lowest among the three binder types (~30 mAh/g_{NCM622} lower than for OPN). In both cases, the optimal value for binder was 1.0 wt % (Figures 1B and 1F). The need for low binder content can be attributed to the employed polymers being insulating in nature, and high content increases the resistance by impeding charge transfer.^{22,23} However, in comparing the slope for binder content, a larger influence on capacity retention than

4.2 Results and Discussion – Design-of-experiments-guided optimization of slurry-cast cathodes for solid-state batteries



CellPress
OPEN ACCESS

Cell Reports
Physical Science
Article

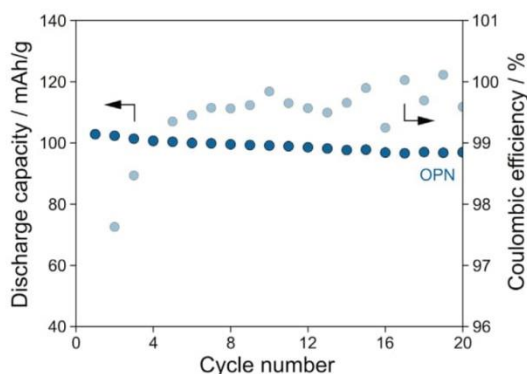


Figure 2. Cycling performance of electrochemically optimized cathodes

Specific discharge capacity (dark blue) over 20 cycles and corresponding Coulombic efficiency (light blue) of a slurry-cast cathode (uncoated NCM622, β -Li₃PS₄) with OPN binder (1.0 wt %) and VGCF conductive additive (0.5 wt %). LTO and β -Li₃PS₄ served as the pellet anode and solid-electrolyte separator, respectively, in the SSB cell. The electrochemical data represent the optimal recipe for maximum capacity and correspond to DoE run 1 (see Table S1).

on specific discharge capacity is apparent. The profiles (along the x axis) are interdependent, and the steeper slope could result from its dependence on hNBR as the choice of binder. As for carbon-related parameters, VGCF was chosen as the optimal choice in both cases (Figures 1C and 1G). This can be explained, at least partly, by its lower specific surface area compared with Super C65 (by a factor of ~6). It has been reported recently that the presence of carbon additives may potentially activate and accelerate the formation of decomposition products,^{24–26} which leads to impedance buildup. A lower specific surface area may reduce the number of contact points between the electronically conductive carbon and the thiophosphate solid-electrolyte particles, thereby reducing the probability of side reactions.^{27,28} Lastly, carbon content of 0.5 wt % was found to be optimal in both cases (Figures 1D and 1H). The more gradual slope compared with the other parameters reveals that it has a minor influence on the overall electrochemical performance of the cell.

In the present work, the specific discharge capacity was chosen to represent the electrochemical performance, because the capacity retention was not an accurate starting indicator. This is because a low-capacity cell would show inherently higher capacity retention. However, capacity retention could work as a second indicator for cells delivering similar discharge capacities. Hence, in this study, the SSB cell optimized for electrochemical performance is based on the specific discharge capacity and is represented by a slurry-cast cathode with 1.0 wt % OPN and 0.5 wt % VGCF. This recipe has been investigated in one of the 23 experimental runs (DoE run 1, see Table S1). The cyclability at a rate of C/10 and 25°C of the cell using uncoated Li_{1+x}(Ni_{0.6}Co_{0.2}Mn_{0.2})_{1–x}O₂ (NCM622) CAM (~12 mg_{NCM622}/cm² areal loading) is shown in Figure 2, in which the initial specific charge and discharge capacities amounted to ~157 and 103 mAh/g_{NCM622}, respectively, corresponding to ~66% Coulombic efficiency. The Coulombic efficiency stabilized above 99% after four cycles. After 20 cycles, the capacity decayed to ~96 mAh/g_{NCM622}. This correlates with a fade rate per cycle of ~0.36%.

Optimizing for electrochemical performance and processability

Optimization for electrochemical performance established that low binder content is necessary for optimum cyclability. However, slurry-cast cathodes with low binder

4.2 Results and Discussion – Design-of-experiments-guided optimization of slurry-cast cathodes for solid-state batteries

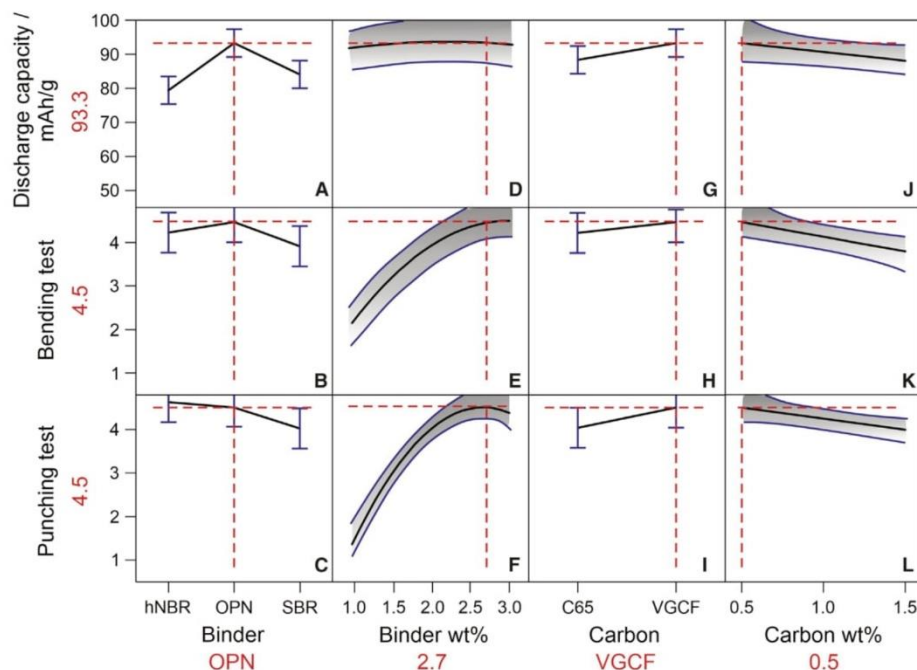


Figure 3. Prediction profiles generated for the optimization of electrochemical performance and processability

The optimum combination for the (A, D, G, and J) 20th-cycle specific discharge capacity, (B, E, H, and K) bending test, and (C, F, I, and L) punching test is OPN (2.7 wt %)/VGCF (0.5 wt %). The scale used for the bending and punching tests is detailed in the [Experimental Procedures](#) and [Figure S2](#).

content are usually prone to delamination and cracking during cell preparation. For practical applications, the electrodes have to be mechanically stable to fulfill the requirements for roll-to-roll processing. The mechanical stability was probed via two in-house mechanical tests ([Figure S2](#)), which simulated common stages in an industrial fabrication process.¹⁹ The scaling values from 1 to 4 were defined as being continuous and should be considered goodness values (they do not represent the theoretical upper and lower limits). In fact, JMP 14 extrapolated a system with processability above our set limit, which meant a slurry-cast cathode with mechanical properties better than what was observed during testing. For electrochemical performance, the 20th-cycle specific discharge capacity was chosen as the only input variable for the reasons explained earlier. Bending and punching tests were used as input variables to represent the processability of the electrode sheets. The generated profiles in [Figure 3](#) show that there are certain trade-offs to be expected among the material-related variables. OPN binder was found to be the preferred choice for achieving slurry-cast cathodes with both good electrochemical performance and good processability. The profiles indicate that the choice of binder is the bottleneck for electrochemical performance ([Figure 3A](#)) but only plays a minor role in processability ([Figures 3B](#) and [3C](#)). However, the profiles for binder content display a small influence on electrochemical performance ([Figure 3D](#)), whereas the content is a significant bottleneck for processability ([Figures 3E](#) and [3F](#)). Both bending and punching tests indicated that higher binder content is necessary for optimum processability. A larger fraction of polymer binder leads to a more compliant and processable system. However, in exchange for improved processability, the electrochemical performance would be negatively affected. To optimize for both

4.2 Results and Discussion – Design-of-experiments-guided optimization of slurry-cast cathodes for solid-state batteries



CellPress
OPEN ACCESS

Cell Reports
Physical Science
Article

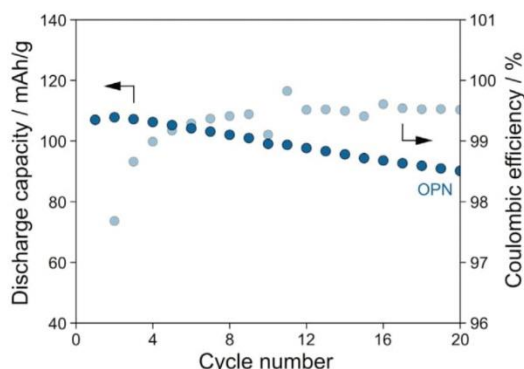


Figure 4. Cycling performance of electrochemically and processability optimized cathodes
Specific discharge capacity (dark blue) over 20 cycles and corresponding Coulombic efficiency (light blue) of a slurry-cast cathode (uncoated NCM622, β -Li₃PS₄) with OPN binder (2.7 wt %) and VGCF conductive additive (0.5 wt %). LTO and β -Li₃PS₄ served as the pellet anode and solid-electrolyte separator, respectively, in the SSB cell. The electrochemical data represent the extrapolated optimum combination for maximum electrochemical performance and processability.

electrochemical performance and processability, a recipe with 2.7 wt % binder content would be required. This trade-off between electrochemical performance and mechanical stability is also in agreement with modeling studies performed on composite cathodes in SSBs.²⁹ As for carbon-related parameters (Figures 3G–3L), the slope in the prediction profiles is generally flatter than that of the binder-related parameters, suggesting a smaller degree of influence on both the electrochemical performance and the processability of the cathode sheets. Nevertheless, VGCF with content of 0.5 wt % was chosen as the optimized fraction of conductive additive.

In summary, the optimized recipe regarding electrochemical performance and cathode processability was equally composed of 2.7 wt % OPN and 0.5 wt % VGCF. This is somewhat different from the recipe that was solely optimized with regard to electrochemical performance, in which only 1.0 wt % OPN was included. The VGCF content was similar for both recipes.

Representative cycling data at a rate of C/10 and 25°C of the SSB cell using uncoated NCM622 CAM (optimized for both electrochemistry and processability) are shown in Figure 4. The initial specific charge and discharge capacities were ~147 and 107 mAh/g_{NCM622}, respectively, corresponding to ~73% Coulombic efficiency. We hypothesize that the higher Coulombic efficiency (by ~7%) results from more extensive coverage of the NCM622 secondary particles with polymer binder, i.e., fewer solid electrolyte/CAM contact points for performance-decreasing (electro-)chemical reactions to occur. After 20 cycles, the capacity decayed to ~90 mAh/g_{NCM622}. This corresponds to a fade rate per cycle of ~0.84%, which is about twice that of the cell optimized for electrochemical performance only. With a measured 20th-cycle specific discharge capacity of ~90 mAh/g_{NCM622}, compared with the extrapolated value of 93 mAh/g_{NCM622}, this suggests that the model built in JMP 14 from the DoE approach is quite robust. The long-term cycling performance is shown in Figure S3.

Investigating binder limitations

Applying the DoE approach led us to an optimized recipe for the fabrication of slurry-cast NCM622 cathodes. As we have shown, both binder type and content

4.2 Results and Discussion – Design-of-experiments-guided optimization of slurry-cast cathodes for solid-state batteries

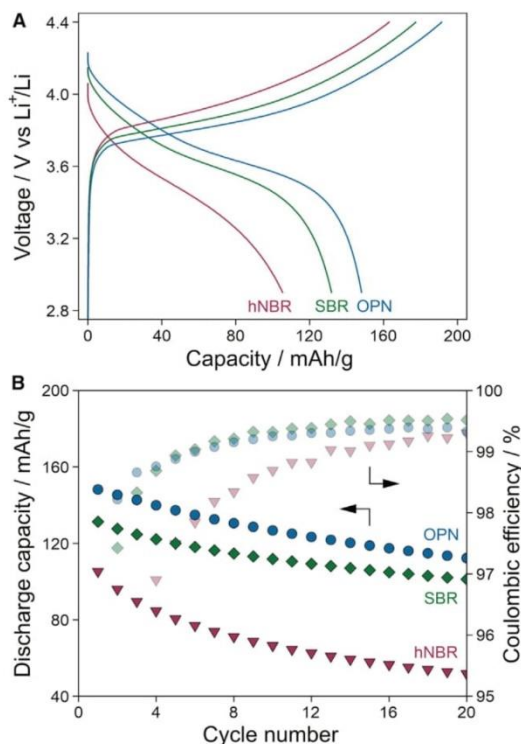


Figure 5. Cycling performance of SSB cells using different polymer binders

(A) First-cycle charge/discharge curves of slurry-cast cathodes (uncoated NCM622, β - Li_3PS_4) with 2.0 wt % polymer binder (blue, OPN; green, SBR; pink, hNBR) and 1.0 wt % VGCF conductive additive. LTO and $\text{Li}_6\text{PS}_5\text{Cl}$ served as the pellet anode and solid-electrolyte separator, respectively, in the SSB cells.

(B) Specific discharge capacities (dark blue/green/pink) over 20 cycles and corresponding Coulombic efficiencies (light blue/green/pink).

have the strongest influence on electrochemical performance and sheet processability (carbon additives exert a minor influence in both cases). To understand the differences in cyclability and the role of the polymer binder, we subsequently probed the respective SSB cells by means of electrochemical impedance spectroscopy (EIS), electron microscopy, X-ray diffraction (XRD), and differential electrochemical mass spectrometry (DEMS), see details in the Supplemental Experimental Procedures. To this end, slurry-cast cathode/ $\text{Li}_6\text{PS}_5\text{Cl}$ /LTO cells were investigated, with the positive electrode consisting of uncoated NCM622, β - Li_3PS_4 , 1.0 wt % VGCF, and 2.0 wt % OPN, SBR, or hNBR binder. This carbon/binder combination was chosen to maximize the electrochemical performance while remaining mechanically stable and reproducible on the laboratory level. Hence, instead of the recommended 2.7 wt % content, a 2.0 wt % binder sheet was used. Moreover, $\text{Li}_6\text{PS}_5\text{Cl}$ was used in the solid-electrolyte separator layer to minimize detrimental effects from low room-temperature ionic conductivity.

Figure 5A depicts the initial charge/discharge curves at a rate of $C/10$ and 25°C for the different polymer binders. As is evident, the cell containing OPN was capable of

4.2 Results and Discussion – Design-of-experiments-guided optimization of slurry-cast cathodes for solid-state batteries



CellPress
OPEN ACCESS

Cell Reports
Physical Science
Article

delivering the largest specific charge and discharge capacities of ~191 and 148 mAh/g_{NCM622}, respectively, resulting in a first-cycle Coulombic efficiency of ~77%. For SBR, slightly lower specific capacities of ~177 and 132 mAh/g_{NCM622} (~75% Coulombic efficiency) were achieved, and hNBR showed the lowest values of ~163 and 105 mAh/g_{NCM622} (~64% Coulombic efficiency), respectively. Apart from the binder, all other SSB constituents were the same. Hence, one can assign differences in specific capacity and Coulombic efficiency to the effect of the polymer binder. This implies an improved electrochemical stability in the order of OPN > SBR > hNBR, because the initial Coulombic efficiency decreased in a similar manner. On subsequent cycling, all cells underwent a rather linear capacity fade, in which those comprising OPN or SBR lost 23%–24% of their initial specific discharge capacity in the course of 20 cycles. The Coulombic efficiency stabilized above 99% after six cycles (Figure 5B). In contrast, for the cell with hNBR, the specific discharge capacity was already reduced by ~50% after 20 cycles, and the Coulombic efficiency barely exceeded 99%.

To gain more insight into the factors leading to the differences in capacity retention, EIS measurements were conducted at 25°C on the SSB cells after 20 cycles. The Nyquist plots of the electrochemical impedance and the corresponding fits to the data are shown in Figure S4. Except for OPN, the EIS data were fitted assuming an $R_1 + (R_2/Q_2)(R_3/Q_3)$ equivalent circuit. In the former case, an additional Q_4 element was included. R_1 is the resistance of the bulk solid electrolyte, R_2 is the grain-boundary resistance of the solid electrolyte, and R_3 represents the cathode interfacial resistance.³⁰ The resistances were determined by fitting semicircles to the frequency range of the respective circuit elements and taking the values of the intersection with the x axis. As expected, the bulk solid-electrolyte (separator) resistance was similar in all cases, ranging from 43–54 Ω. The calculated values for the cathode interfacial resistance were ~1,250, 1,850, and 4,200 Ω for OPN-, SBR-, and hNBR-based cathodes (0.64 cm² electrode area), respectively, confirming the results from galvanostatic cycling. Because the tested electrodes differed solely in their polymer-binder component, the EIS data further suggest the electrochemical stability is in the order of OPN > SBR > hNBR. Regarding the solid-electrolyte grain-boundary resistance, values of ~250, 550, and 1,450 Ω were calculated for OPN, SBR, and hNBR, respectively. The latter resistance has been attributed in the literature to particle fracture and/or (chemo-)mechanical-driven separation.^{25,30} Hence, we suspect that these differences may be related to the different binder material's inherent capabilities to mitigate such mechanical degradation/deformation. However, the coverage of the solid-electrolyte particle surface with polymer binder, which negatively affects the ion conduction (at the grain boundaries), must also be taken into account and may have a large impact on the resistance. For instance, the acrylonitrile groups of hNBR have been reported to exhibit ion-dipole interactions with the lithium ions of thiophosphate solid electrolytes. This interaction thus could hypothetically lead to stronger coverage, resulting in larger cathode interfacial resistance.²¹ However, SBR contains aromatic units as functional groups, exhibiting weaker intermolecular forces with the solid electrolyte. OPN, which solely contains an aliphatic hydrocarbon polymer chain without functional groups, is believed to have the least chemical/physical interactions with the solid electrolyte.

Investigating inhomogeneities

Finally, we addressed the possibility of the different polymer binders of having an effect on the distribution of the electrode constituents, thereby indirectly affecting the electrochemical performance. Specifically, combined scanning electron microscopy (SEM)/energy-dispersive X-ray spectroscopy (EDS) analysis was performed on cathode cross sections. The corresponding SEM images and elemental maps are shown in Figure S5. The cross sections revealed partial occurrence of VGCF

4.2 Results and Discussion – Design-of-experiments-guided optimization of slurry-cast cathodes for solid-state batteries

agglomerates. Such agglomerates were more visible in the cathodes containing SBR or hNBR. Overall, the SEM imaging and EDS mapping indicated that in terms of homogeneity, the carbon additive in particular is seemingly better distributed in the cathodes using OPN. This may help in achieving improved electronic conduction, which is especially important for sheet-based electrodes, in which insulating polymer binder reduces the ionic and electronic partial conductivities. Regarding porosity, we found no apparent difference among the three binders.

Inhomogeneity in the cathode composite may lead to the appearance of inactive CAM fractions, causing decreased capacities.^{31,32} The occurrence of inactive NCM622 can be observed from the remaining 003 reflection at the initial 2 θ position (as seen for the pristine CAM). To eliminate the possibility that the differences in electrochemical performance among polymer binders are related to inactive fractions of CAM, ex situ XRD measurements were carried out. The XRD patterns for all three slurry-cast cathodes showed a similar 003 peak shape (in charged state), with the reflection shifted to lower 2 θ values (Figure S6). This confirms the absence of inactive NCM622. However, the asymmetric shape suggested differences in the state-of-charge (SOC) homogeneity, as usually observed for SSBs.³¹ The unit-cell volume after the first charge cycle was examined by means of Rietveld-refinement analysis. This allowed comparison of the lattice parameters with those of NCM622 in a liquid-electrolyte-based cell (used as a reference), in which conclusions can be drawn about the degree of delithiation (Figure S7). NCM622 CAM (reference) was cycled in a half-cell configuration under identical conditions to the SSB cells. The initial specific charge capacities calculated from the $x(\text{Li})$ were ~ 187 , 176, and 171 mAh/g_{NCM622} for OPN, SBR, and hNBR, respectively. This is in good agreement with the measured values (~ 196 , 183, and 165 mAh/g_{NCM622}). Differences can be attributed to errors in the estimation of $x(\text{Li})$. In addition, these estimations rely on direct comparisons between solid-electrolyte cells (ex situ) and liquid-electrolyte cells (operando) with the same CAM, which could be unreliable because of the SSB disassembling process. Hence, an attempt on operando XRD was made. The specialized cell setup used is shown in Figure S8, and the analysis of the operando synchrotron data can be found in Figure S9. Regardless, the operando XRD measurements were able to verify the ex situ data and the SEM/EDS investigations: inactive CAM plays a minor or no role.

Investigating binder stability via gas evolution

Gas evolution during electrochemical cycling has been reported to adversely affect the state of health of batteries. Although it is not as apparent as in liquid-electrolyte-based cells, gassing occurs for SSBs in the first few cycles. Overall, material degradation from the reaction of released gases with the electrode constituents appears to be less significant for the latter cells. Nevertheless, the sulfide solid electrolytes are degrading over time as a result of outgassing of the active material.

Together with the results from EIS, XRD, and SEM, we assume that differences in the chemical/electrochemical stability of the polymer binder in the system have a significant influence on the overall performance of the SSB cells. Operando gassing studies via DEMS were thus performed to determine the stability of the different binders based on the resulting gas evolution. To this end, NCM622 was cycled at a rate of C/20 and 45°C in the voltage range of 2.9–5.0 V versus Li⁺/Li. The higher charge cutoff voltage (5.0 versus 4.4 V) and temperature (45°C versus 25°C) were chosen with the intention of increasing the evolution of highly reactive singlet oxygen (¹O₂) from the CAM lattice and observing its potential influence on the components in the cathode sheets, especially the binder material. The respective cells were cycled for three cycles, and gas evolution was observed with decreasing amounts in

4.2 Results and Discussion – Design-of-experiments-guided optimization of slurry-cast cathodes for solid-state batteries

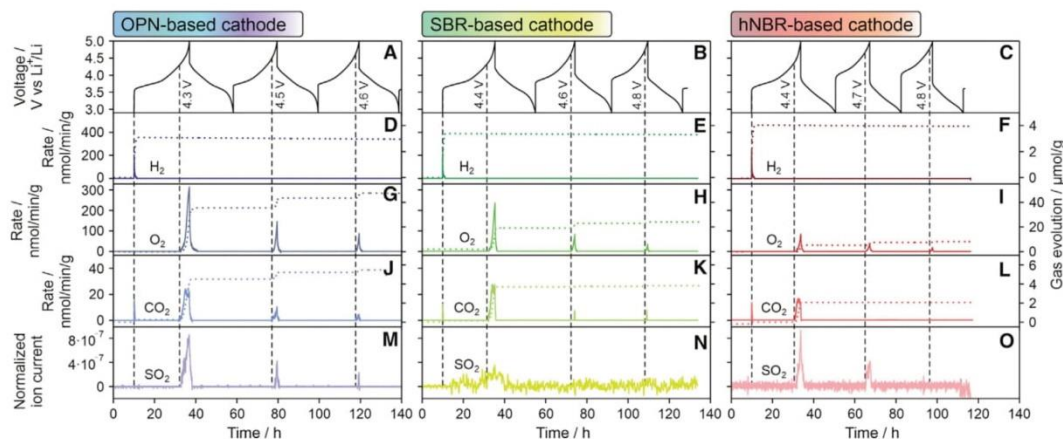


Figure 6. Gassing behavior of SSB cells using different polymer binders
(A–C) Voltage profiles and corresponding time-resolved evolution rates (left y axis) and cumulative amounts (right y axis) for (D–F) H_2 , (G–I) O_2 , and (J–L) CO_2 , as well as the normalized ion currents for (M–O) SO_2 . The SSB cells consisted of a slurry-cast cathode (uncoated NCM622, β - Li_3PS_4) with 2.0 wt % OPN, SBR, or hNBR binder and 1.0 wt % VGCF conductive additive, a Li_6PS_5Cl solid-electrolyte pellet separator, and an indium anode.

consecutive cycles at increasing onset voltages (from ~ 4.3 to $4.6/4.8$ V) (Figures 6A–6C). Four gases were detected: H_2 , O_2 , CO_2 , and SO_2 . The evolution of H_2 ($m/z = 2$) only occurred at the beginning of the first charge cycle and could be attributed to the reduction of trace water at the anode (Figures 6D–6F).³³ For O_2 evolution, the cells are required to achieve $>80\%$ SOC.^{34,35} This condition was met for all cells, and the mass signal ($m/z = 32$) showed a sharp peak (Figures 6G–6I) with onset voltages of ~ 4.3 V for OPN-based cathodes and ~ 4.4 V for SBR- and hNBR-based cathodes in the initial cycle. The origin of O_2 evolution has been proposed in the literature to be a consequence of the destabilization of the layered Ni-rich oxide lattice at high voltages (>4.5 V versus Li^+/Li).^{34,35} Although the OPN-based cell was able to reach $\sim 89\%$ SOC (243 mAh/g_{NCM622}), the SBR- and hNBR-based cells only achieved $\sim 86\%$ (235 mAh/g_{NCM622}) and $\sim 80\%$ (220 mAh/g_{NCM622}), respectively. The cumulative amount of O_2 evolved in the first cycle was ~ 36 , 18, and 5 $\mu\text{mol/g}_{\text{NCM622}}$ for OPN, SBR, and hNBR, respectively. This difference in O_2 evolution is due to the difference in SOC, because the amount follows an exponential-like relationship with SOC after reaching the 80% threshold. As seen in Figure S10, the SBR-based cathode followed a similar evolution progression to the OPN-based cathode, despite showing about 50% lower O_2 evolution.

The CO_2 mass signal ($m/z = 44$) for SSB cells predominantly stems from electrochemical decomposition of residual surface carbonates on the CAM particles, which is typically indicated by a sharp peak with an onset voltage > 4.2 V (Figures 6J–6L).^{36–38} However, a peak was also observed at the beginning of charging. In conventional liquid-electrolyte cells, CO_2 evolution at the start would be associated with an electrochemical reduction of the organic carbonate electrolyte. However, this is not applicable to SSBs. It could be postulated that the CO_2 evolution is correlated with side reactions at the anode, given that both H_2 evolution and CO_2 evolution occur almost simultaneously.³⁹ In general, we hypothesize that there are three possible sources for CO_2 evolution above 4.2 V: (1) electrochemical decomposition of residual surface carbonates, (2) chemical oxidation of the polymer binder, and (3) oxidation of the carbon additive. However, it has been shown in the literature that carbon additives are relatively stable

4.2 Results and Discussion – Design-of-experiments-guided optimization of slurry-cast cathodes for solid-state batteries

against the released oxygen from the NCM lattice⁴⁰ and therefore should not contribute to the observed CO₂ evolution. This leaves us with scenarios 1 and 2, which we elaborate upon when discussing about SO₂ evolution, because the two mass signals are believed to be correlated. Interestingly, when zooming into the gas evolution of both O₂ and CO₂ during the first cycle, we noticed a double peak for CO₂ for the OPN- and SBR-based cathodes (Figure S11). For the hNBR-based cathode, no distinct double peak was observed due to the lower SOC.

As is typical for SSB cells containing lithium thiophosphate solid electrolytes, a sharp peak corresponding to the mass signal $m/z = 64$ (SO₂) was detected (Figures 6M–6O). The mass signal of SO₂ is normalized with respect to the carrier-gas mass signal $m/z = 4$ (He) and represents at best a semiquantitative comparison. The formation of SO₂ could be attributed to the reaction between the solid electrolyte and the reactive oxygen released from the CAM at high voltages and from the electrochemical decomposition of residual surface carbonates.^{36–38,41} This is in agreement with the observed onset of SO₂ evolution, coinciding with both the O₂ and CO₂ signals. For hNBR-based cathodes, the SO₂ ion current exhibited an intensity similar to that of OPN-based cathodes, despite only showing ~14% of the O₂ evolution compared with the latter during the first cycle. The higher intensity of the SO₂ ion current in the hNBR-based cathode suggests that the solid electrolyte in these electrodes is less stable, supporting the arguments used in the discussion of the EIS data. The acrylonitrile groups of hNBR apparently exhibit ion-dipole interactions with the lithium ions of sulfide solid electrolytes, making it more vulnerable to side reactions. In contrast, SBR-based cathodes showed a more damped signal, indicating reduced SO₂ evolution, which cannot be simply explained by the lower amount of evolved O₂.

In an attempt to explain the damped SO₂ signal for the SBR-based cathodes, we hypothesize several possibilities: (1) coverage of the solid electrolyte and/or active material particles with polymer binder, preventing short-lived ¹O₂ from reaching the solid electrolyte; (2) reaction of evolved SO₂ with functional groups of the binder; and (3) preferential reaction of reactive oxygen with the binder instead of the solid electrolyte. For this discussion, a more in-depth analysis of the mass signal $m/z = 44$ was required. Specifically, both OPN- and SBR-based cathodes with a near identical SOC were needed for quantitative comparison, because CO₂ evolution, like O₂ evolution, shows an exponential-like relationship with the SOC (Figure S10). To this end, slurry-cast electrodes with LiNbO₃-coated NCM622 CAM were prepared and electrochemically tested. Representative first-cycle voltage profiles at a rate of C/10 and 25°C and the specific discharge capacities and Coulombic efficiencies over 20 cycles are shown in Figures 7A and 7B. Evidently, SSB cells with the LiNbO₃-coated NCM622 clearly outperformed those using uncoated CAM (Figure 5). This result was not unexpected and further indicates the effectiveness of the protective coating to mitigate decomposition reactions at the interfaces. OPN was capable of delivering the largest initial specific charge and discharge capacities of ~199 and 170 mAh/g_{NCM622} (~2 mAh/cm²), respectively (~85% versus ~77% Coulombic efficiency for uncoated NCM622). For SBR, lower specific capacities of ~192 and 164 mAh/g_{NCM622} were achieved (~85% versus ~75% Coulombic efficiency for uncoated NCM622). The protective surface coating was most beneficial for the hNBR-based cathode, improving both first-cycle specific discharge capacity and Coulombic efficiency by ~55% and 33%, respectively. Despite the similar initial irreversibility among the three polymer binders, the Coulombic efficiency of the hNBR-based cathode required four more cycles to stabilize above 99.5%, compared with two cycles for the OPN- and SBR-based cathodes. This suggests that more side reactions are occurring, especially in the initial cycles. However, an in-depth analysis would require

4.2 Results and Discussion – Design-of-experiments-guided optimization of slurry-cast cathodes for solid-state batteries



CellPress
OPEN ACCESS

Cell Reports
Physical Science
Article

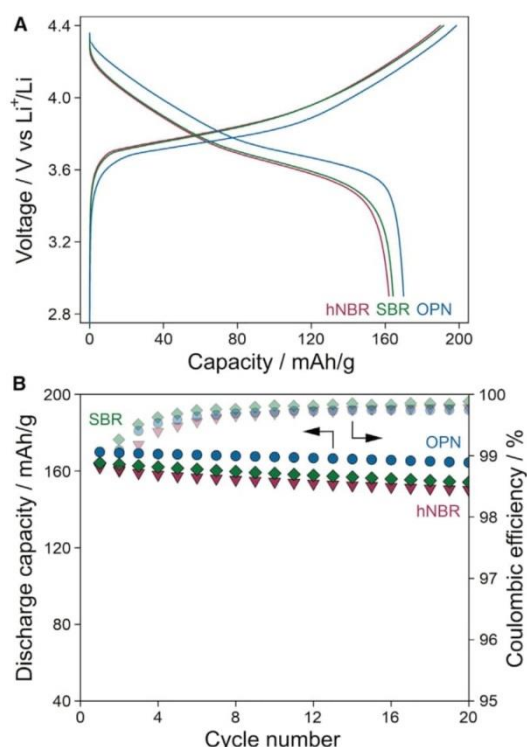


Figure 7. Cycling performance of SSB cells using different polymer binders

(A) First-cycle charge/discharge curves of slurry-cast cathodes (LiNbO₃-coated NCM622, β -Li₃PS₄) with 2.0 wt % polymer binder (blue, OPN; green, SBR; pink, hNBR) and 1.0 wt % VGCF conductive additive. LTO and Li₆PS₅Cl served as the pellet anode and solid-electrolyte separator, respectively, in the SSB cells.

(B) Specific discharge capacities (dark blue/green/pink) over 20 cycles and corresponding Coulombic efficiencies (light blue/green/pink).

further investigations. After 20 cycles, the specific discharge capacities decayed, as expected, corresponding to fade rates per cycle of ~0.17%, 0.32%, and 0.39% for OPN, SBR, and hNBR, respectively. This result marks a significant improvement over the SSB cells using uncoated NCM622 CAM.

Such slurry-cast LiNbO₃-coated NCM622 cathodes were then used in operando DEMS studies, and the gassing behavior of the corresponding SSB cells is shown in Figure 8 (for OPN and SBR) and Figure S12 (for hNBR). With a near-identical SOC for both OPN- and SBR-based cathodes (~250 versus 249 mAh/g_{NCM622}), we analyzed the evolution of O₂, CO₂, and SO₂. The total amounts of O₂ detected after the first cycle were ~205 and 161 μ mol/g_{NCM622} for OPN and SBR, respectively, thus about an order of magnitude larger than what was observed for the uncoated NCM622 cathodes. The increased amounts help with the analysis of the gas evolution trends. The higher SOC also led to the appearance of an additional redox peak at ~4.6 V versus Li⁺/Li (see differential capacity plots in Figure S13), which might be indicative of oxygen redox.^{34,42,43} In addition, we did not observe a damped signal for the SBR-based cathode with regard to the SO₂. This was to be expected because the larger amount of

4.2 Results and Discussion – Design-of-experiments-guided optimization of slurry-cast cathodes for solid-state batteries

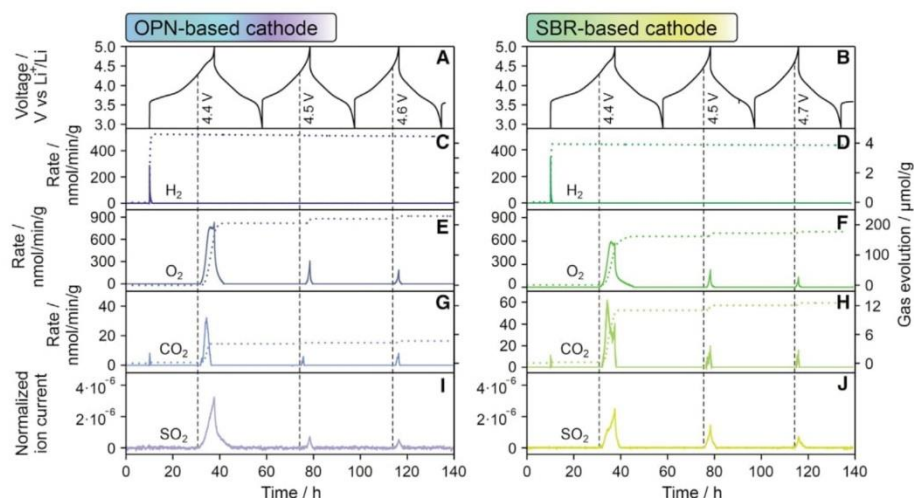


Figure 8. Gassing behavior of SSB cells using different polymer binders

(A and B) Voltage profiles and corresponding time-resolved evolution rates (left y axis) and cumulative amounts (right y axis) for (C and D) H_2 , (E and F) O_2 , and (G and H) CO_2 , as well as the normalized ion currents for (I and J) SO_2 . The SSB cells consisted of a slurry-cast cathode ($LiNbO_3$ -coated NCM622, β - Li_3PS_4) with 2.0 wt % OPN or SBR binder and 1.0 wt % VGCF conductive additive, a Li_6PS_5Cl solid-electrolyte pellet separator, and an indium anode.

evolved O_2 would mean that there are plenty of reacting agents (1O_2) available to both the polymer binder and the solid electrolyte. Nevertheless, the CO_2 evolution was more significant in the SBR-based cell. Because of the different gassing behavior of the uncoated and coated NCM622 cathodes, we are able to draw some conclusions here. We hypothesize that the first CO_2 peak (of the double peak at high voltages) is a result of the electrochemical decomposition of surface carbonates, whereas the second one results from possible reactions between the reactive oxygen and the binder material. Given that chemical oxidation of liquid electrolytes has been proposed in the literature,³⁴ it would be possible for 1O_2 to attack the carbon chains/functional groups of the binder to produce CO_2 .^{44,45} The double peak seen for CO_2 supports the hypothesis of a chemical oxidation of the binder. Moreover, the CO_2 evolution (second peak) was most pronounced in the SBR-based cathode. Reactive oxygen has been shown to be capable of reacting with polymers possessing an alkene chain (units),⁴⁴ and among the three materials, SBR is the only binder possessing one.

Finally, we try to explain the depressed SO_2 evolution seen for the SBR-based cathode using uncoated NCM622. We postulate that O_2 (probably 1O_2) reacts with both the SBR binder and the solid electrolyte. To justify this, we bring some values into context. First, the $LiNbO_3$ -coated NCM622 cathodes showed a (maximum) first-cycle normalized SO_2 ion current of 3.2×10^{-6} and 2.5×10^{-6} for OPN and SBR, respectively. The overall increase in ion current, compared with SSB cells using uncoated NCM622 (Figure 6), is due to the larger amounts of evolved O_2 . As a result, the depressed SO_2 signal is not observed, because there is enough 1O_2 to react with both the binder and the solid electrolyte. Second, despite showing less O_2 evolution, the SBR-based cathode exhibited 2–3 times more CO_2 evolution than the OPN-based electrode. Third, comparing the total amount of CO_2 evolution for both the uncoated and the $LiNbO_3$ -coated NCM622 cathodes, we noticed that it remained similar for the OPN-based electrode at 4–5 $\mu mol/g_{NCM622}$, whereas that of the SBR-based electrode increased by a factor of about three (~ 11.0 versus 3.7 $\mu mol/g_{NCM622}$). The NCM622 particles used were all from the

4.2 Results and Discussion – Design-of-experiments-guided optimization of slurry-cast cathodes for solid-state batteries



same batch and therefore should have a similar amount of residual surface carbonates. Consequently, the additional CO_2 evolved from the SBR-based LiNbO_3 -coated NCM622 cathode originated from a different source. In conclusion, these observations agree with our hypothesis that the alkene chain in SBR binder reacts with O_2 through a pathway that entails the formation of CO_2 .

In conclusion, slurry-cast cathodes with electrochemical performance on par with powder-based, pelletized SSBs were produced with the help of DoE (Table S3). In addition, the optimization obtained for unprotected NCM622 CAM was transferable to LiNbO_3 -coated NCM622, delivering high discharge capacities and showing good capacity retention and thus providing a methodology for the production of slurry-cast cathodes with different types of CAMs. Most importantly, the slurry-cast cathodes displayed similar cyclability but with increased reproducibility, which is necessary for use in future studies. When optimizing for electrochemical performance, slurry-cast cathodes with OPN binder and VGCF conductive additive were found to outperform other binder/carbon combinations. The type of binder and carbon additive and their respective content did affect the cycling performance to varying degrees. Not surprisingly, the well-performing electrode sheets all contained a low fraction of binder. JMP 14 extrapolated an optimum combination of 1.0 wt % OPN binder and 0.5 wt % VGCF conductive additive. However, slurry-cast cathodes with low binder content (<2.0 wt %) were susceptible to crack formation and delamination during cell preparation. For SSB sheet-based electrodes to be commercially viable, they have to be fabricated via continuous processing methods, in which they are usually subjected to strong mechanical forces during bending and shearing. Hence, in this study, the mechanical stability of the cathode sheet was also taken into consideration. The overall mechanical stability was found to largely depend on the binder content, with the other parameters, such as the type of binder and carbon additive, having a low degree of influence. A compromise between electrochemical performance and processability was achieved at 2.7 wt % OPN and 0.5 wt % VGCF. The measured cycling performance of SSB cells using a slurry-cast cathode with the optimal parameters corroborated the robustness of the model. Further understanding of the results from the DoE approach and the model built was provided by EIS, SEM/EDS, and XRD measurements. Lastly, operando gas analysis confirmed the (electro-)chemical stability of OPN. In addition, the correlation among O_2 evolution, CO_2 evolution, and SO_2 evolution allowed for hypotheses of reaction pathways, suggesting that polymer binders possessing alkene chains/units or functional groups that could potentially destabilize the solid electrolyte are unfavorable, especially at high voltages when in use with a layered Ni-rich oxide cathode material.

EXPERIMENTAL PROCEDURES

Resource availability

Lead contact

Further information and requests for resources should be directed to and will be fulfilled by the lead contact, Jun Hao Teo (jun.teo@kit.edu).

Materials availability

This study did not generate new reagents.

Data and code availability

The authors declare that the data supporting the findings are available within the article and the supporting information. All other data are available from the lead contact upon reasonable request.

4.2 Results and Discussion – Design-of-experiments-guided optimization of slurry-cast cathodes for solid-state batteries

Materials

Electrode sheets were prepared using pristine (unprotected) NCM622 (60% Ni, BASF)¹² powder as the CAM. The solid electrolytes, β -Li₃PS₄ (BASF) and argyrodite Li₆PS₅Cl (NEI), with room-temperature ionic conductivities of ~0.2 and 2 mS/cm, respectively, were applied as received. Three polymer binder materials were used for the study: OPN (Oppanol N 150 from BASF, average molecular weight [M_w] = 3.1×10^6 g/mol), hNBR (Therban LT 1707 VP from Arlanxco, M_w = 5.5×10^5 g/mol), and SBR (45 wt % styrene from Sigma Aldrich, M_w $\approx 6 \times 10^5$ g/mol).^{27,46,47} Super C65 carbon black (Timcal) and VGCF as electronically conductive additives were both dried at 300°C in a vacuum overnight before use. The LiNbO₃-coated NCM622 was prepared by coating a 1 wt % sol-gel-derived LiNbO₃ surface layer onto the pristine CAM.^{48–50} All materials were handled and stored in an argon glovebox from MBraun ([O₂] < 0.1 ppm, [H₂O] < 0.5 ppm).

DoE

The mass fractions of the two carbon additives, Super C65 and VGCF, were chosen to vary between 0.5 and 1.5 wt % (with a 0.5 wt % increment), whereas the content of the three polymer binders was chosen to vary between 1.0 and 3.0 wt % (with a 1.0 wt % increment). In other words, there were three variables with three levels and one variable with two levels. A classical, full factorial design of the cathode composite would thus require 54 ($3 \cdot 3 \cdot 3 \cdot 2$) experiments. Our customized experimental design reduced the number of required experiments to 23 (Table S1). The optimization was done with response variables quantifying the electrochemical and mechanical performance. Mechanical properties (processability) are represented by the results of two in-house mechanical tests, namely, bending and punching tests. To simplify the analysis, we assigned an arbitrary numerical scale to assess qualitative observations, so the higher number represents better processability. For the punching tests, round electrodes were punched from the cathode sheet with a circular geometry (9 mm diameter). They are rated according to the following scale: 4 = no mechanical deformation, 3 = edge delamination, 2 = delamination and cracking, and 1 = unprocessable (Figure S2). In case of the bending tests, the electrodes were tensioned at both ends and subjected to a rolling motion along a metal pipe (1 mm diameter) at varying bending angles. They are rated as follows: 4 = no mechanical deformation, 3 = delamination, 2 = delamination and cracking, and 1 = unprocessable. Several process-related parameters were fixed and excluded from the experimental design based on prior knowledge.

Cell assembly and electrochemical measurements

For the 23 DoE experimental runs, the SSB cells consisted of a slurry-cast cathode (9 mm diameter), a solid-electrolyte pellet separator (10 mm diameter), and a pellet anode (10 mm diameter). A specialized cell setup containing two stainless-steel dies and a plastic (polyether ether ketone, PEEK) ring was used. First, 65 mg of β -Li₃PS₄ was compressed at a pressure of ~125 MPa. The cathode was then punched into a circular geometry (2.0–2.4 mAh/cm² areal capacity), placed on top of the solid-electrolyte separator layer, and subsequently compressed at ~375 MPa. Lastly, 60 mg of anode composite was pressed onto the other side of the solid-electrolyte pellet at ~125 MPa. The anode composite was prepared by mixing 300 mg of carbon-coated LTO (NEI) with 100 mg of Super C65 carbon black and 600 mg of β -Li₃PS₄ at 140 rpm for 30 min in a 70 mL milling jar (Fritsch) with 10 zirconia balls (10 mm diameter) under an argon atmosphere using a planetary ball mill. For all subsequent electrochemical testing, SSB cells consisting of a slurry-cast cathode, a Li₆PS₅Cl pellet separator (100 mg), and a pellet anode (60 mg) were used. The anode composite was prepared in a fashion similar to that described earlier but with Li₆PS₅Cl as the solid electrolyte. During electrochemical testing, a stack pressure of ~80 MPa was maintained.

4.2 Results and Discussion – Design-of-experiments-guided optimization of slurry-cast cathodes for solid-state batteries



CellPress
OPEN ACCESS

Cell Reports
Physical Science
Article

Galvanostatic charge/discharge measurements were performed at 25°C and at a rate of C/10 (1C = 180 mA/g_{Ni_{0.8}Co_{0.15}Al_{0.05}O₂}) in the voltage range between 1.35 and 2.85 V versus Li₄Ti₅O₁₂/Li₇Ti₅O₁₂ (equal to ~2.9–4.4 V versus Li⁺/Li) using a Maccor battery cycler.

SUPPLEMENTAL INFORMATION

Supplemental information can be found online at <https://doi.org/10.1016/j.xcrp.2021.100465>.

ACKNOWLEDGMENTS

This study was supported by BASF SE. J.H.T. is grateful to the Federal Ministry of Education and Research (Bundesministerium für Bildung und Forschung, BMBF) for funding within the project ARTEMYS (03XP0114J). F.S. acknowledges financial support from Fonds der Chemischen Industrie (FCI) through a Liebig scholarship. The authors thank P. Hartmann (BASF SE), J. Kulisch (BASF SE), and X. Wu (BASF SE) for fruitful project discussions. Parts of this research were carried out at the light source PETRA III at DESY, a member of the Helmholtz Association (HGF). We thank M. Tolkiehn for assistance in using beamline P24 (EH2).

AUTHOR CONTRIBUTIONS

Conceptualization, J.H.T. and T.B.; methodology, J.H.T. and D.T.; software, D.T.; validation, J.H.T.; formal analysis, J.H.T., F.S., D.T., S.S., and Y.M.; investigation, J.H.T.; resources, M.B., J.J., and T.B.; writing – original draft, J.H.T. and T.B.; writing – review & editing, J.H.T., F.S., D.T., S.S., M.B., J.J., and T.B.; supervision, M.B., J.J., and T.B.; project administration, J.H.T. and T.B.; funding acquisition, J.J. and T.B.

DECLARATION OF INTERESTS

The authors declare no competing interests.

Received: February 18, 2021

Revised: April 14, 2021

Accepted: May 20, 2021

Published: June 15, 2021

REFERENCES

- Wang, Q., Ping, P., Zhao, X., Chu, G., Sun, J., and Chen, C. (2012). Thermal runaway caused fire and explosion of lithium ion battery. *J. Power Sources* 208, 210–224.
- Janek, J., and Zeier, W.G. (2016). A solid future for battery development. *Nat. Energy* 1, 16141.
- Kerman, K., Luntz, A., Viswanathan, V., Chiang, Y.-M., and Chen, Z. (2017). Review—practical challenges hindering the development of solid state Li ion batteries. *J. Electrochem. Soc.* 164, A1731–A1744.
- Sakuda, A., Hayashi, A., and Tatsumisago, M. (2013). Sulfide solid electrolyte with favorable mechanical property for all-solid-state lithium battery. *Sci. Rep.* 3, 2261.
- McGrogan, F.P., Swamy, T., Bishop, S.R., Eggleston, E., Porz, L., Chen, X., Chiang, Y.-M., and Van Vliet, K.J. (2017). Compliant yet brittle mechanical behavior of Li₂S-P₂S₅ lithium-ion-conducting solid electrolyte. *Adv. Energy Mater.* 7, 1602011.
- Richards, W.D., Miara, L.J., Wang, Y., Kim, J.C., and Ceder, G. (2016). Interface stability in solid-state batteries. *Chem. Mater.* 28, 266–273.
- Wolfenstine, J., Allen, J.L., Sakamoto, J., Siegel, D.J., and Choe, H. (2018). Mechanical behavior of Li-ion-conducting crystalline oxide-based solid electrolytes: a brief review. *Ionics* 24, 1271–1276.
- Wan, J., Xie, J., Kong, X., Liu, Z., Liu, K., Shi, F., Pei, A., Chen, H., Chen, W., Chen, J., et al. (2019). Ultrathin, flexible, solid polymer composite electrolyte enabled with aligned nanoporous host for lithium batteries. *Nat. Nanotechnol.* 14, 705–711.
- Zhou, J., Qian, T., Liu, J., Wang, M., Zhang, L., and Yan, C. (2019). High-safety all-solid-state lithium-metal battery with high-ionic-conductivity thermoresponsive solid polymer electrolyte. *Nano Lett.* 19, 3066–3073.
- Ito, S., Fujiki, S., Yamada, T., Aihara, Y., Park, Y., Kim, T.Y., Baek, S.-W., Lee, J.-M., Doo, S., and Machida, N. (2014). A rocking chair type all-solid-state lithium ion battery adopting Li₂O-ZrO₂ coated LiNi_{0.8}Co_{0.15}Al_{0.05}O₂ and a sulfide based electrolyte. *J. Power Sources* 248, 943–950.
- Aihara, Y., Ito, S., Omoda, R., Yamada, T., Fujiki, S., Watanabe, T., Park, Y., and Doo, S. (2016). The electrochemical characteristics and applicability of an amorphous sulfide-based solid ion conductor for the next-generation solid-state lithium secondary batteries. *Front. Energy Res.* 4, 18.
- Strauss, F., Bartsch, T., de Biasi, L., Kim, A.-Y., Janek, J., Hartmann, P., and Brezesinski, T. (2018). Impact of cathode material particle size on the capacity of bulk-type all-solid-state batteries. *ACS Energy Lett.* 3, 992–996.
- Doux, J.-M., Yang, Y., Tan, D.H.S., Nguyen, H., Wu, E.A., Wang, X., Banerjee, A., and Meng, Y.S. (2020). Pressure effects on sulfide electrolytes for all solid-state batteries. *J. Mater. Chem. A Mater. Energy Sustain.* 8, 5049–5055.
- Piper, D.M., Yersak, T.A., and Lee, S.-H. (2013). Effect of compressive stress on electrochemical

4.2 Results and Discussion – Design-of-experiments-guided optimization of slurry-cast cathodes for solid-state batteries

- performance of silicon anodes. *J. Electrochem. Soc.* 160, A77–A81.
15. Fitzhugh, W., Ye, L., and Li, X. (2019). The Effects of Mechanical Constriction on the Operation of Sulfide Based Solid-State Batteries. *J. Mater. Chem. A Mater. Energy Sustain.* 7, 23604–23627.
 16. Doux, J.-M., Nguyen, H., Tan, D.H.S., Banerjee, A., Wang, X., Wu, E.A., Jo, C., Yang, H., and Meng, Y.S. (2020). Stack pressure considerations for room-temperature all-solid-state lithium metal batteries. *Adv. Energy Mater.* 10, 1903253.
 17. Wang, M.J., Choudhury, R., and Sakamoto, J. (2019). Characterizing the Li-solid-electrolyte interface dynamics as a function of stack pressure and current density. *Joule* 3, 2165–2178.
 18. Fergus, J.W. (2010). Ceramic and polymeric solid electrolytes for lithium-ion batteries. *J. Power Sources* 195, 4554–4569.
 19. Schnell, J., Günther, T., Knoche, T., Vieider, C., Kohler, L., Just, A., Keller, M., Passerini, S., and Reinhart, G. (2018). All-solid-state lithium-ion and lithium metal batteries—paving the way to large-scale production. *J. Power Sources* 382, 160–175.
 20. Schnell, J., Knörzer, H., Imbsweiler, A.J., and Reinhart, G. (2020). Solid versus liquid—a bottom-up calculation model to analyze the manufacturing cost of future high-energy batteries. *Energy Technol. (Weinheim)* 8, 1901237.
 21. Lee, K., Kim, S., Park, J., Park, S.H., Coskun, A., Jung, D.S., Cho, W., and Choi, J.W. (2017). Selection of binder and solvent for solution-processed all-solid-state battery. *J. Electrochem. Soc.* 164, A2075–A2081.
 22. Yamamoto, M., Terauchi, Y., Sakuda, A., and Takahashi, M. (2018). Binder-free sheet-type all-solid-state batteries with enhanced rate capabilities and high energy densities. *Sci. Rep.* 8, 1212.
 23. Rosero-Navarro, N.C., Kinoshita, T., Miura, A., Higuchi, M., and Tadanaga, K. (2017). Effect of the binder content on the electrochemical performance of composite cathode using $\text{Li}_x\text{PS}_2\text{Cl}$ precursor solution in an all-solid-state lithium battery. *Ionics* 23, 1619–1624.
 24. Zhang, W., Leichtweiß, T., Culver, S.P., Koerver, R., Das, D., Weber, D.A., Zeier, W.G., and Janek, J. (2017). The detrimental effects of carbon additives in $\text{Li}_{10}\text{GeP}_2\text{S}_{12}$ -based solid-state batteries. *ACS Appl. Mater. Interfaces* 9, 35888–35896.
 25. Koerver, R., Aygün, I., Leichtweiß, T., Dietrich, C., Zhang, W., Binder, J.O., Hartmann, P., Zeier, W.G., and Janek, J. (2017). Capacity fade in solid-state batteries: interphase formation and chemomechanical processes in nickel-rich layered oxide cathodes and lithium thiophosphate solid electrolytes. *Chem. Mater.* 29, 5574–5582.
 26. Walther, F., Randau, S., Schneider, Y., Sann, J., Rohnke, M., Richter, F.H., Zeier, W.G., and Janek, J. (2020). Influence of carbon additives on the decomposition pathways in cathodes of lithium thiophosphate-based all-solid-state batteries. *Chem. Mater.* 32, 6123–6136.
 27. Ates, T., Keller, M., Kulisch, J., Adermann, T., and Passerini, S. (2019). Development of an all-solid-state lithium battery by slurry-coating procedures using a sulfidic electrolyte. *Energy Storage Mater.* 17, 204–210.
 28. Strauss, F., Stepien, D., Maibach, J., Pfaffmann, L., Indris, S., Hartmann, P., and Brezesinski, T. (2020). Influence of electronically conductive additives on the cycling performance of argyrodite-based all-solid-state batteries. *RSC Advances* 10, 1114–1119.
 29. Bielefeld, A., Weber, D.A., and Janek, J. (2020). Modeling effective ionic conductivity and binder influence in composite cathodes for all-solid-state batteries. *ACS Appl. Mater. Interfaces* 12, 12821–12833.
 30. Koerver, R., Zhang, W., de Biasi, L., Schweidler, S., Kondrakov, A.O., Kolling, S., Brezesinski, T., Hartmann, P., Zeier, W.G., and Janek, J. (2018). Chemo-mechanical expansion of lithium electrode materials—on the route to mechanically optimized all-solid-state batteries. *Energy Environ. Sci.* 11, 2142–2158.
 31. Bartsch, T., Kim, A.-Y., Strauss, F., de Biasi, L., Teo, J.H., Janek, J., Hartmann, P., and Brezesinski, T. (2019). Indirect state-of-charge determination of all-solid-state battery cells by X-ray diffraction. *Chem. Commun. (Camb.)* 55, 11223–11226.
 32. Chen, K., Shinjo, S., Sakuda, A., Yamamoto, K., Uchiyama, T., Kuratani, K., Takeuchi, T., Orikasa, Y., Hayashi, A., Tatsumisago, M., et al. (2019). Morphological effect on reaction distribution influenced by binder materials in composite electrodes for sheet-type all-solid-state lithium-ion batteries with the sulfide-based solid electrolyte. *J. Phys. Chem. C* 123, 3292–3298.
 33. Bernhard, R., Meini, S., and Gasteiger, H.A. (2014). On-line electrochemical mass spectrometry investigations on the gassing behavior of $\text{Li}_4\text{Ti}_5\text{O}_{12}$ electrodes and its origins. *J. Electrochem. Soc.* 161, A497–A505.
 34. Jung, R., Metzger, M., Maglia, F., Stinner, C., and Gasteiger, H.A. (2017). Oxygen release and its effect on the cycling stability of $\text{LiNi}_x\text{Mn}_y\text{Co}_z\text{O}_2$ (NMC) cathode materials for Li-ion batteries. *J. Electrochem. Soc.* 164, A1361–A1377.
 35. Jung, R., Strobl, P., Maglia, F., Stinner, C., and Gasteiger, H.A. (2018). Temperature dependence of oxygen release from $\text{LiNi}_{0.4}\text{Mn}_{0.2}\text{Co}_{0.2}\text{O}_2$ (NMC622) cathode materials for Li-ion batteries. *J. Electrochem. Soc.* 165, A2869–A2879.
 36. Bartsch, T., Strauss, F., Hatsukade, T., Schiele, A., Kim, A.-Y., Hartmann, P., Janek, J., and Brezesinski, T. (2018). Gas evolution in all-solid-state battery cells. *ACS Energy Lett.* 3, 2539–2543.
 37. Strauss, F., Teo, J.H., Schiele, A., Bartsch, T., Hatsukade, T., Hartmann, P., Janek, J., and Brezesinski, T. (2020). Gas evolution in lithium-ion batteries: solid versus liquid electrolyte. *ACS Appl. Mater. Interfaces* 12, 20462–20468.
 38. Strauss, F., Teo, J.H., Maibach, J., Kim, A.-Y., Mazilkin, A., Janek, J., and Brezesinski, T. (2020). Li_2ZrO_3 -coated NCM622 for application in inorganic solid-state batteries: role of surface carbonates in the cycling performance. *ACS Appl. Mater. Interfaces* 12, 57146–57154.
 39. Lux, S., Baldauf-Sommerbauer, G., and Siebenhofer, M. (2018). Hydrogenation of inorganic metal carbonates: a review on its potential for carbon dioxide utilization and emission reduction. *ChemSusChem* 11, 3357–3375.
 40. Jung, R., Metzger, M., Maglia, F., Stinner, C., and Gasteiger, H.A. (2017). Chemical versus electrochemical electrolyte oxidation on NMC111, NMC622, NMC811, LNMO, and conductive carbon. *J. Phys. Chem. Lett.* 8, 4820–4825.
 41. Mahne, N., Renfrew, S.E., McCloskey, B.D., and Freunberger, S.A. (2018). Electrochemical oxidation of lithium carbonate generates singlet oxygen. *Angew. Chem. Int. Ed. Engl.* 57, 5529–5533.
 42. Sathya, M., Rousse, G., Ramesha, K., Laiss, C.P., Vezin, H., Sougrati, M.T., Doublet, M.-L., Foix, D., Gonbeau, D., Walker, W., et al. (2013). Reversible anionic redox chemistry in high-capacity layered-oxide electrodes. *Nat. Mater.* 12, 827–835.
 43. McCalla, E., Abakumov, A.M., Saubanière, M., Foix, D., Berg, E.J., Rousse, G., Doublet, M.-L., Gonbeau, D., Novák, P., Van Tendeloo, G., et al. (2015). Visualization of O-O peroxo-like dimers in high-capacity layered oxides for Li-ion batteries. *Science* 350, 1516–1521.
 44. Clennan, E.L., and Pace, A. (2005). Advances in singlet oxygen chemistry. *Tetrahedron* 61, 6665–6691.
 45. Ogilby, P.R. (2010). Singlet oxygen: there is indeed something new under the sun. *Chem. Soc. Rev.* 39, 3181–3209.
 46. Rippa, N., Strobl, P., Stiasny, B., Zinkevich, T., Yavuz, M., Schnell, J., Indris, S., Gasteiger, H.A., and Sedlmaier, S.J. (2018). Slurry-based processing of solid electrolytes: a comparative binder study. *J. Electrochem. Soc.* 165, A3993–A3999.
 47. Strauss, F., Teo, J.H., Janek, J., and Brezesinski, T. (2020). Investigations into the superionic glass phase of Li_4PS_4 for improving the stability of high-loading all-solid-state batteries. *Inorg. Chem. Front.* 7, 3953–3960.
 48. Takada, K., Ohta, N., Zhang, L., Fukuda, K., Sakaguchi, I., Ma, R., Osada, M., and Sasaki, T. (2008). Interfacial modification for high-power solid-state lithium batteries. *Solid State Ion.* 179, 1333–1337.
 49. Ohta, N., Takada, K., Sakaguchi, I., Zhang, L., Ma, R., Fukuda, K., Osada, M., and Sasaki, T. (2007). LiNbO_3 -coated LiCoO_2 as cathode material for all solid-state lithium secondary batteries. *Electrochem. Commun.* 9, 1486–1490.
 50. Kim, A.-Y., Strauss, F., Bartsch, T., Teo, J.H., Hatsukade, T., Mazilkin, A., Janek, J., Hartmann, P., and Brezesinski, T. (2019). Stabilizing effect of a hybrid surface coating on a Ni-rich NCM cathode material in all-solid-state batteries. *Chem. Mater.* 31, 9664–9672.

Cell Reports Physical Science, Volume 2

Supplemental information

Design-of-experiments-guided optimization of slurry-cast cathodes for solid-state batteries

Jun Hao Teo, Florian Strauss, Đordije Tripković, Simon Schweidler, Yuan Ma, Matteo Bianchini, Jürgen Janek, and Torsten Brezesinski

4.2 Results and Discussion – Design-of-experiments-guided optimization of slurry-cast cathodes for solid-state batteries

1 Figures

1.1 Electrochemical Performance of All 23 DoE-Derived SSB Cells

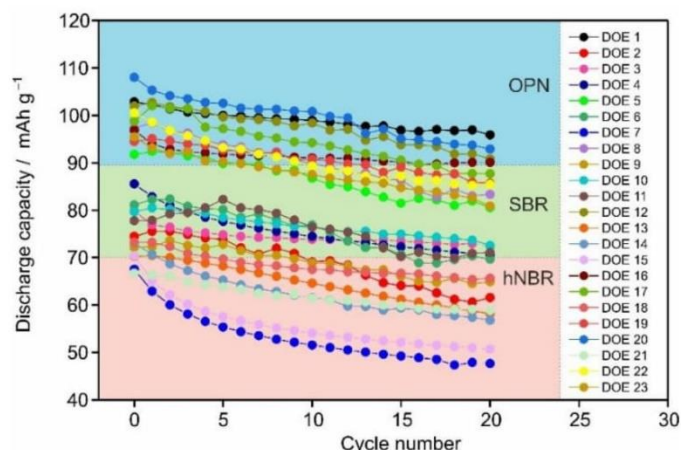


Figure S1. Cycling performance at C/10 rate and 25 °C of the 23 slurry-cast cathodes as required for the statistical approach (see **Table S1** for the carbon/binder type and composition).

The SSB cells consisted of a slurry-cast cathode (uncoated NCM622, β -Li₃PS₄, Super C65 or VGCF conductive additive, and with OPN, SBR, or hNBR binder), a β -Li₃PS₄ solid-electrolyte pellet separator, and a pelletized LTO anode.

1.2 Mechanical Tests and In-House Scaling of Processability

Mechanical tests	Description			
Scale	1	2	3	4
Punch test (P)	Unprocessable	Delamination & cracking	Edge delamination	No mechanical deformation
Bending test (B)	Unprocessable	Delamination & cracking	Delamination	No mechanical deformation

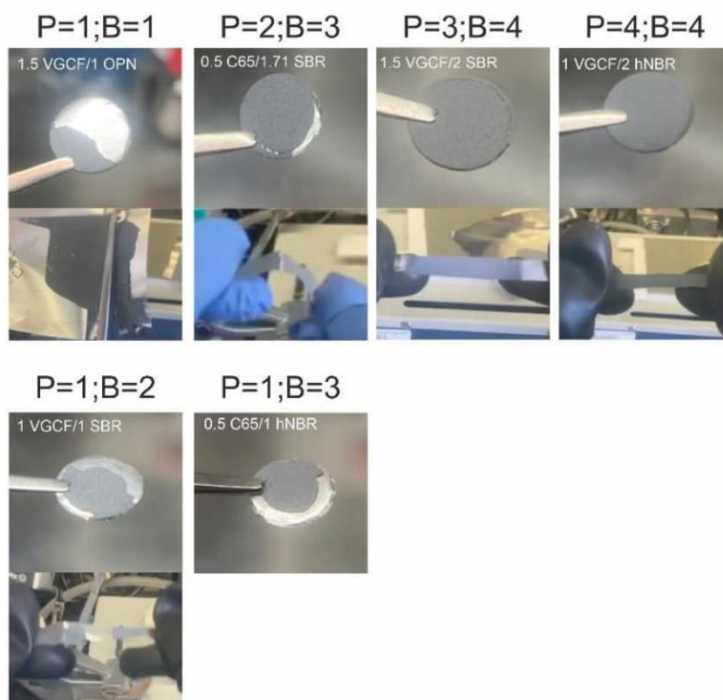


Figure S2. Mechanical tests performed on the slurry-cast cathodes with varying binder type and content.

1.3 Long-Term Performance of SSB Cells

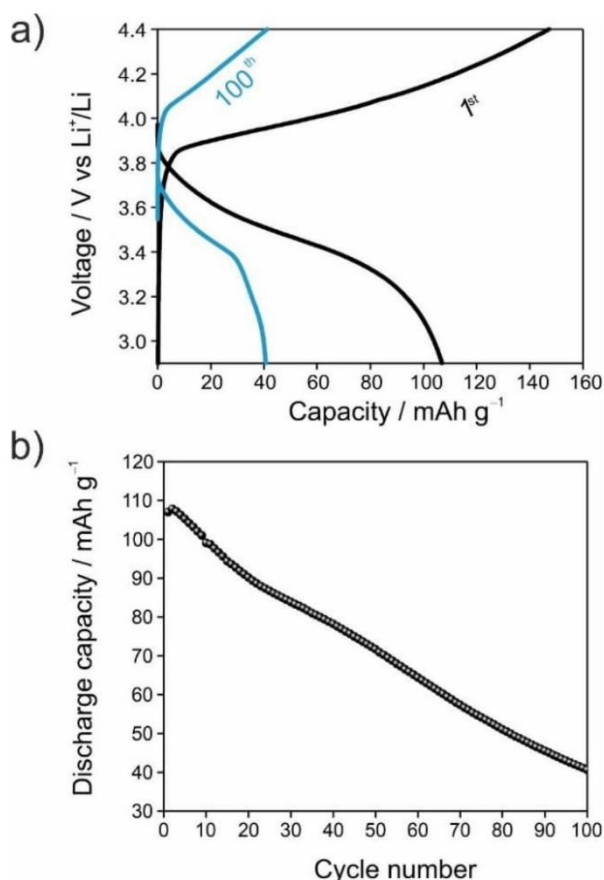


Figure S3. Long-term cycling of electrochemically optimized cathodes.

(a) First- and 100th cycle charge/discharge curves at C/10 rate and 25 °C of a slurry-cast cathode (uncoated NCM622, $\beta\text{-Li}_3\text{PS}_4$) with OPN binder (2.7 wt%) and VGCF conductive additive (0.5 wt%). LTO and $\beta\text{-Li}_3\text{PS}_4$ served as pellet anode and solid-electrolyte separator, respectively, in the SSB cell. (b) Specific discharge capacity over 100 cycles.

1.4 EIS of SSB Cells Using Different Polymer Binders

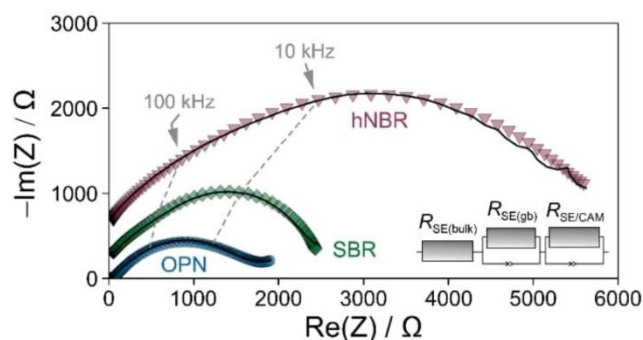


Figure S4. Nyquist plots of the electrochemical impedance of SSB cells (black lines: raw data, solid symbols: z-fits) using a slurry-cast cathode (uncoated NCM622, $\beta\text{-Li}_3\text{PS}_4$) with 2.0 wt% polymer binder (blue: OPN, green: SBR, pink: hNBR) and 1.0 wt% VGCF conductive additive. LTO and $\text{Li}_6\text{PS}_5\text{Cl}$ served as pellet anode and solid-electrolyte separator, respectively. Experimental spectra are offset relative to one another on the y-axis.

4.2 Results and Discussion – Design-of-experiments-guided optimization of slurry-cast cathodes for solid-state batteries

1.5 SEM Imaging and EDS Mapping of Pristine Composite Cathodes

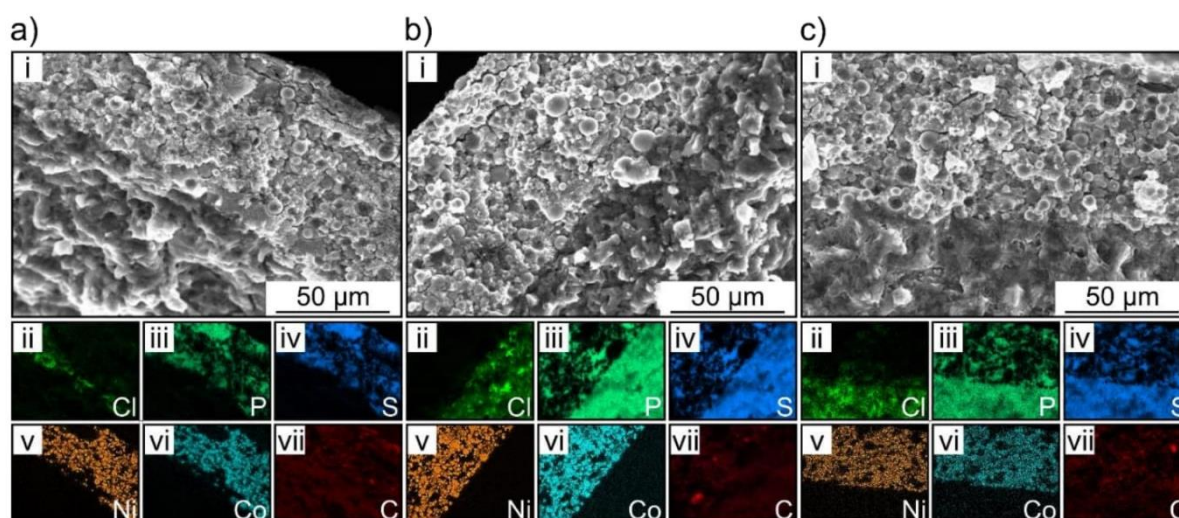


Figure S5. Cross-sectional view of cathodes and elemental mapping results.

(i) SEM images and (ii-vii) the corresponding elemental maps from EDS of slurry-cast cathodes (uncoated NCM622, β - Li_3PS_4 , VGCF) with OPN (a), SBR (b) or hNBR binder (c). Note that the $\text{Li}_6\text{PS}_5\text{Cl}$ solid-electrolyte pellet separator is also visible to some degree. Scale bars represent 50 μm .

1.6 XRD Patterns for Slurry-Cast Cathodes Using Different Polymer Binders

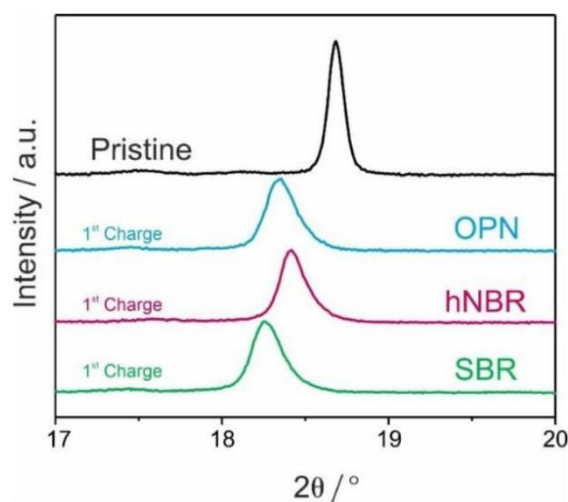


Figure S6. Comparison of the 003 reflection of NCM622 in slurry-cast cathodes (uncoated NCM622, β - Li_3PS_4) with 2.0 wt% polymer binder (blue: OPN, green: SBR, pink: hNBR) and 1.0 wt% VGCF conductive additive after the first charge cycle (4.4 V vs Li^+/Li). LTO and $\text{Li}_6\text{PS}_5\text{Cl}$ served as pellet anode and solid-electrolyte separator, respectively, in the SSB cells.

4.2 Results and Discussion – Design-of-experiments-guided optimization of slurry-cast cathodes for solid-state batteries

1.7 Rietveld-Refinement Analysis and Estimation of Specific Capacity

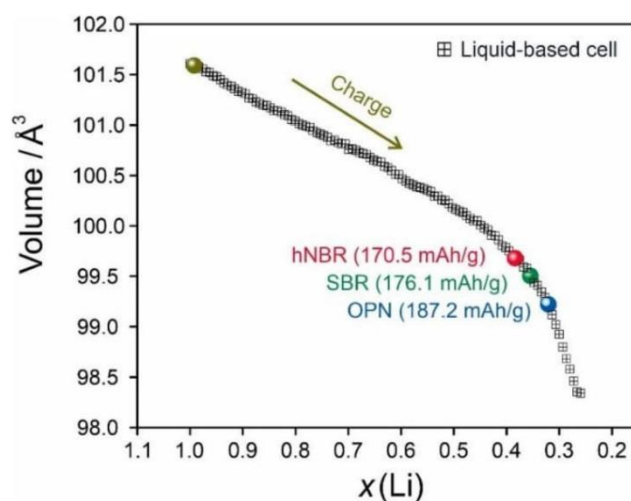


Figure S7. Evolution of unit-cell volume with the $x(\text{Li})$ from Rietveld-refinement analysis of XRD data during the first charge cycle.

The black curve represents the volume change of NCM622 in a liquid-electrolyte-based LIB pouch cell (from Rietveld analysis of *operando* XRD data). Unit-cell volumes of NCM622 in SSB cells (from Rietveld analysis of *ex situ* XRD data) at the end of the first charge cycle (4.4 V vs Li^+/Li) are denoted by circles (blue: OPN, green: SBR, pink: hNBR). The golden circle represents the pristine (non-charged) NCM622 for comparison. By reading off the respective $x(\text{Li})$ value utilizing the LIB (black curve) as a reference, the specific charge capacity can be estimated.

1.8 Customized Setup for Synchrotron-Based *Operando* XRD

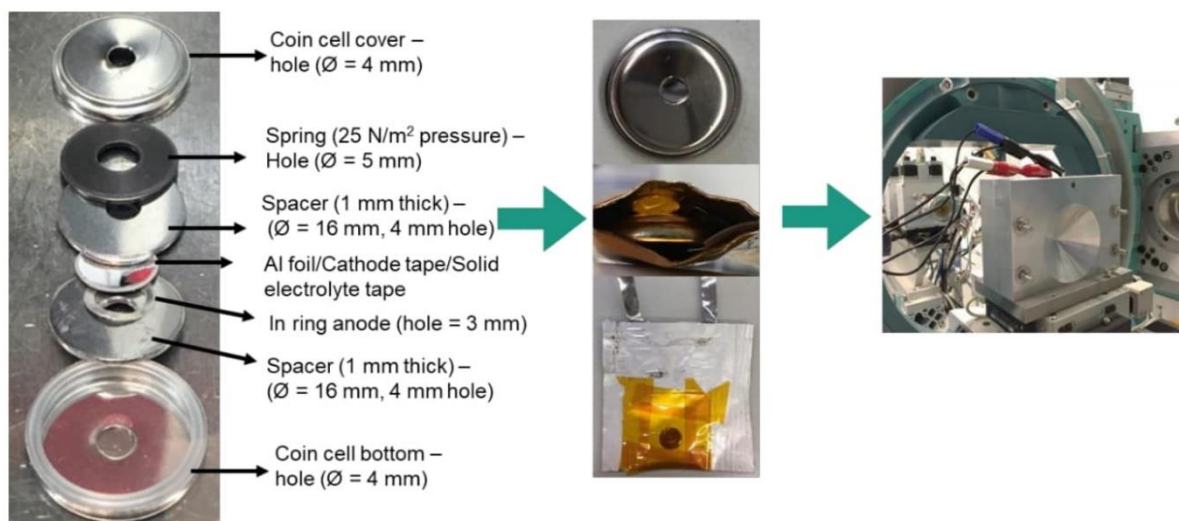


Figure S8. Synchrotron-based XRD setup.

The SSB cell consisted of a slurry-cast cathode (uncoated NCM622, $\beta\text{-Li}_3\text{PS}_4$) with OPN binder (2.0 wt%) and VGCF conductive additive (1.0 wt%), a slurry-cast solid-electrolyte ($\text{Li}_6\text{PS}_5\text{Cl}$) separator with OPN binder (2.0 wt%), and an indium-ring anode.

1.9 Synchrotron-Based *Operando* XRD Patterns

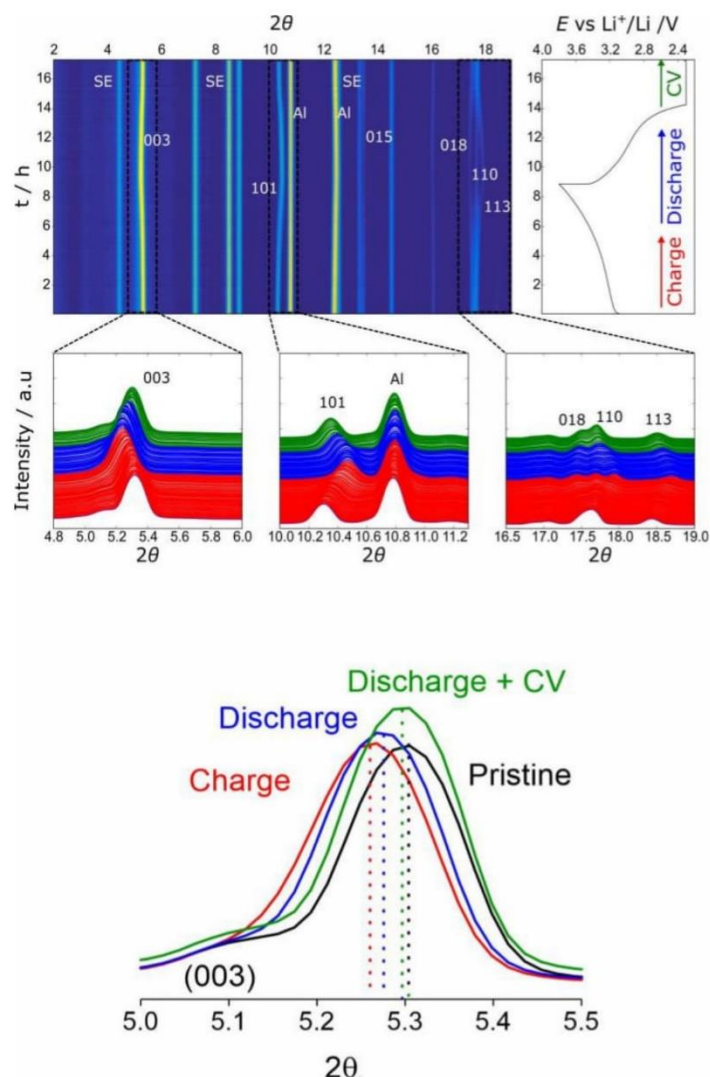


Figure S9. Contour plot of synchrotron-based *operando* XRD patterns obtained on a sheet-based SSB cell ($\lambda = 0.4428 \text{ \AA}$).

The cell consisted of a slurry-cast cathode (uncoated NCM622, β -Li₃PS₄) with 2.0 wt% OPN binder and 1.0 wt% VGCF conductive additive, a slurry-cast solid-electrolyte (Li₆PS₅Cl) separator with 2.0 wt% OPN binder, and an indium-ring anode. It was cycled in a specialized setup (**Figure S8**) at C/10 rate and 25 °C in the voltage range between 2.3 and 3.8 V versus In/InLi. An additional constant voltage (CV) step was programmed at the end of the discharge cycle.

Previously, Bartsch *et al.*¹ reported about *operando* XRD on pelletized SSB cells. In the present work, we performed a similar synchrotron-based study using a specialized (coin-type) cell with slurry-cast sheets in both the cathode and solid-electrolyte separator. The study demonstrated similar observations seen in the *operando* XRD on pelletized cells. During charge and discharge, changes in reflection positions were observed. The typical evolution of the 003 reflection of NCM622 was apparent. Initially, it shifted to lower 2θ values during the charge process, before the subsequent discharge process led to the opposite development. However, a fully reversible lithiation process did not occur in the discharge cycle. Only during the following CV step, further continuous shift to a higher 2θ value occurred, which in the end was comparable to the initial starting value. The electrochemical data of the *operando* cell did not show any abnormalities and delivered comparable first-cycle specific capacities to the same setup tested in our laboratory ($q_{\text{ch}} \approx 164 \text{ mAh/g}_{\text{NCM622}}$, $q_{\text{dis}} \approx 115 \text{ mAh/g}_{\text{NCM622}}$). However, with the CV step, both the additional shift of the 003 reflection and specific capacity achieved indicate that there is a kinetic limitation. We attribute this limitation to the lack of pressure in the beam spot area. Nevertheless, in contrast to the earlier *operando* study, we are able to demonstrate that cells produced by the slurry-casting method do not show signs of the presence of inactive CAM.

4.2 Results and Discussion – Design-of-experiments-guided optimization of slurry-cast cathodes for solid-state batteries

1.10 Gas-Evolution Trends after Reaching 80 % SOC

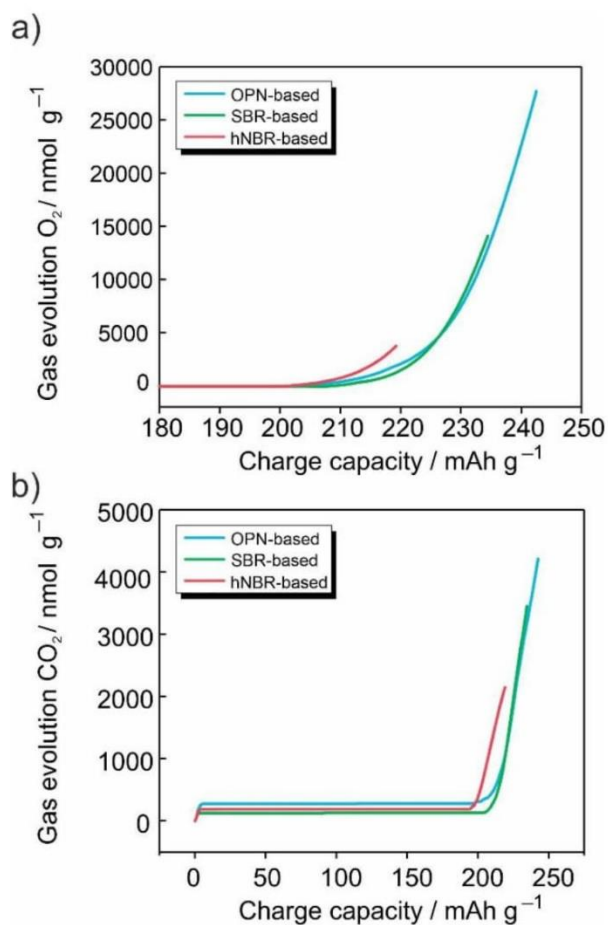


Figure S10. Exponential relationship of gas evolution with the SOC.

(a) O₂ evolution and (b) CO₂ evolution with respect to the specific charge capacity. The SSB cells consisted of a slurry-cast cathode (uncoated NCM622, β -Li₃PS₄) with 2.0 wt% OPN, SBR, or hNBR binder and 1.0 wt% VGCF conductive additive. Indium foil and Li₆PS₅Cl served as anode and pellet solid-electrolyte separator, respectively.

4.2 Results and Discussion – Design-of-experiments-guided optimization of slurry-cast cathodes for solid-state batteries

1.11 Enlarged View of Gas-Evolution Rates

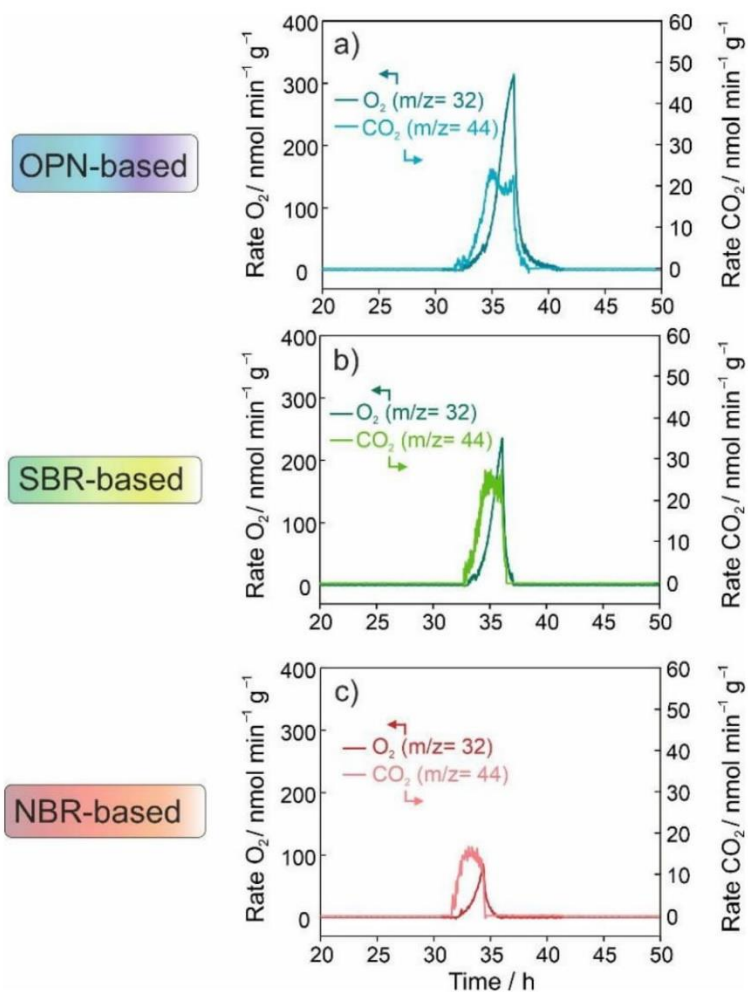


Figure S11. Time-resolved evolution rates of O_2 and CO_2 for SSB cells using a slurry-cast cathode (uncoated NCM622, β - Li_3PS_4) with 2.0 wt% polymer binder [(a) OPN, (b) SBR, (c) hNBR] and 1.0 wt% VGCF conductive additive. Indium foil and Li_6PS_5Cl served as anode and pellet solid-electrolyte separator, respectively.

4.2 Results and Discussion – Design-of-experiments-guided optimization of slurry-cast cathodes for solid-state batteries

1.12 Electrochemical and Gassing Profiles for hNBR-Based SSB Cells

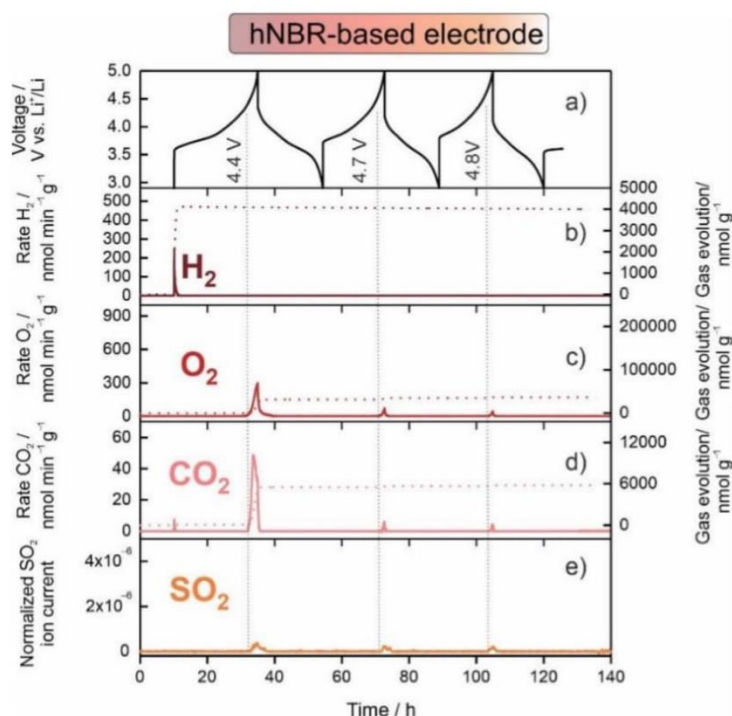


Figure S12. Gassing behavior of cathodes using hNBR binder.

(a) Electrochemical profile of a SSB cell cycled at C/20 rate and 45 °C and the corresponding time-resolved evolution rates (left y-axis) and cumulative amounts (right y-axis) for H₂ (b), O₂ (c), and CO₂ (d) and the normalized ion current for SO₂ (e). The cell consisted of a slurry-cast cathode (LiNbO₃-coated NCM622, β-Li₃PS₄) with 2.0 wt% hNBR binder and 1.0 wt% VGCF conductive additive, a Li₆PS₅Cl solid-electrolyte pellet separator, and an indium anode.

1.13 Differential Capacity Plots and Gassing Profiles

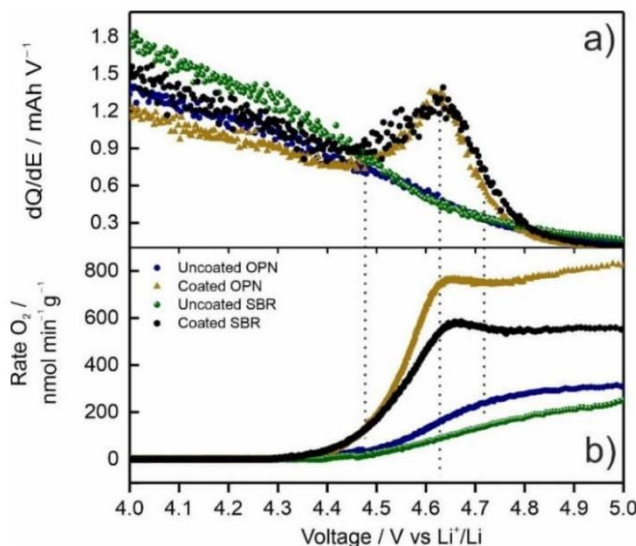


Figure S13. Differential capacity and oxygen evolution profiles.

(a) Differential capacity plots for the first charge cycle of SSB cells at C/20 rate and 45 °C using a slurry-cast cathode (uncoated or LiNbO₃-coated NCM622, β-Li₃PS₄) with 2.0 wt% OPN or SBR binder and 1.0 wt% VGCF conductive additive.

(b) The corresponding evolution rates of O₂ are plotted with respect to the voltage. Only cathodes using the LiNbO₃-coated NCM622 showed a distinct peak at ~4.6 V versus Li⁺/Li accompanied by an evident increase in O₂ evolution.

4.2 Results and Discussion – Design-of-experiments-guided optimization of slurry-cast cathodes for solid-state batteries

2 Tables

2.1 DoE Table

Table S1. Required set of experiments generated from the statistical software JMP 14 for the screening/optimization of parameters (carbon type/weight percentage and polymer type/weight percentage). The output parameters to be considered are electrochemical parameters (specific discharge capacity and capacity retention after 20 cycles) and processing parameters (mechanical stability through in-house bending and punching tests).

DoE run	Carbon / wt%	Binder / wt%	Specific discharge capacity / mAh/g	Capacity retention / %	Punching test	Bending test
1	0.5 VGCF	1 OPN	95.9	93.2	1	1
2	0.5 VGCF	3 SBR	61.5	82.6	4	4
3	1.5 C65	1 SBR	72.4	90.6	1	2
4	1.5 C65	2 hNBR	70.5	80.6	4	4
5	1 C65	2 OPN	80.5	87.7	4	4
6	1.5 C65	3 SBR	69.7	85.8	4	4
7	1.5 VGCF	3 hNBR	47.7	70.5	4	4
8	1 C65	1 OPN	83.3	85.6	1	1
9	1.5 VGCF	1 hNBR	64.9	89.9	1	3
10	0.5 C65	1 hNBR	72.5	91.1	1	3
11	1.5 VGCF	2 SBR	71.1	91.3	3	4
12	1 VGCF	2 OPN	90.8	89.1	4	4
13	1 C65	3 SBR	58.2	82.8	4	4
14	1 C65	2 hNBR	56.8	77.7	4	4
15	0.5 C65	3 hNBR	50.7	72.0	4	4
16	1 VGCF	1 SBR	90.1	93.0	1	2
17	1 VGCF	3 OPN	87.7	88.8	4	4
18	0.5 VGCF	2 hNBR	65.6	89.6	4	4
19	0.5 C65	3 OPN	85.7	90.7	4	4
20	1.5 VGCF	1 OPN	92.9	86.0	1	1
21	1 VGCF	2 hNBR	58.8	88.2	4	4
22	1.5 C65	3 OPN	85.4	85.0	4	4
23	0.5 C65	1.71 SBR	80.8	84.7	2	3

4.2 Results and Discussion – Design-of-experiments-guided optimization of slurry-cast cathodes for solid-state batteries

2.2 Chosen Set of Variables Used in Building the Models for DoE

Table S2. Minimal set of variables required to build a model with high predictability with respect to the electrochemical performance (specific discharge capacity and capacity retention after 20 cycles), as well as the electrochemical performance and processability (20th cycle specific discharge capacity and mechanical tests). Those with the largest log worth/lowest *P*-value (high significance) were chosen while maintaining large adjusted *R*-square.

Output	Variable(s)	Log worth	<i>P</i> -value
Specific discharge capacity	Binder type	6.128	< 0.00001
	Binder wt%	3.799	0.00016
	Carbon type × binder type	1.586	0.02594
	Carbon type × binder wt%	0.977	0.10533
	Carbon wt% × binder wt%	0.865	0.13649
	Binder type × binder wt%	0.790	0.16204
Capacity retention	Binder wt %	5.121	< 0.00001
	Binder type × binder wt%	4.609	0.00002
	Binder type	3.599	0.00025
	Carbon type	2.913	0.00122
	Carbon wt% × binder type	2.674	0.00212
	Carbon wt%	1.282	0.05223
	Carbon type × carbon wt%	0.782	0.16533
	Binder wt% × binder wt%	0.700	0.19950
Electrochemistry & processability	Binder wt%	11.461	< 0.00001
	Binder wt% × binder wt%	6.614	< 0.00001
	Binder type	5.402	< 0.00001
	Carbon type × carbon wt%	2.018	0.00960
	Binder type × binder wt%	1.985	0.01035
	Carbon type	0.339	0.45774

4.2 Results and Discussion – Design-of-experiments-guided optimization of slurry-cast cathodes for solid-state batteries

2.3 Electrochemical Performance of Reported NCM Composite Cathodes (Pelletized and Slurry-Cast) in SSB Cells

Table S3. The electrochemical performance of pelletized and slurry-cast NCM cathodes with sulfide solid electrolytes. Note that there are also other factors than the coating material, binder content, C-rate, and temperature affecting the cyclability of SSB cells that are not displayed such as the active material loading, stack pressure or binder type, to name a few.

Cathode active material	Ni content	Coating material	Solid electrolyte	Separator	Anode	Binder / wt%	1 st cycle discharge capacity / mAh/g	Initial Coulombic efficiency / %	Temp. / °C	Voltage range / V vs. Li ⁺ /Li	C-rate	Ref.
<i>Powder-based, pelletized SSB cells</i>												
NCM271	0.20	LiNbO ₃	Li ₆ PS ₅ Cl	Li ₆ PS ₅ Cl	Li ₄ Ti ₅ O ₁₂	—	140	82	25	2.9–4.4	C/10	2
NCM361	0.30	LiNbO ₃	Li ₆ PS ₅ Cl	Li ₆ PS ₅ Cl	Li ₄ Ti ₅ O ₁₂	—	140	82	25	2.9–4.4	C/10	2
NCM111	0.33	—	Li ₆ PS ₅ Cl	Li ₆ PS ₅ Cl	Li-In	—	80	—	—	3.4–4.0	C/10	3
NCM111	0.33	LiNbO ₃	75Li ₂ S·25 P ₂ S ₅	75Li ₂ S·25 P ₂ S ₅	Li-In	—	99	71	25	2.5–4.4	—	4
NCM523	0.50	Li ₃ B ₁₁ O ₁₈	Li ₃ PS ₄	Li ₃ PS ₄	graphite	—	147	—	r.t.	2.5–4.3	—	5
NCM523	0.50	LiNb _{0.5} Ta _{0.5} O ₃	Li ₁₀ GeP ₂ S ₁₂	Li ₁₀ GeP ₂ S ₁₂	Li-In	—	112	—	r.t.	—	C/10	6
NCM622	0.60	—	β-Li ₃ PS ₄	β-Li ₃ PS ₄	Li ₄ Ti ₅ O ₁₂	—	106	78	25	2.9–4.4	C/10	7
NCM622	0.60	Li ₂ CO ₃ /LiNbO ₃	β-Li ₃ PS ₄	β-Li ₃ PS ₄	Li ₄ Ti ₅ O ₁₂	—	136	87	25	2.9–4.4	C/10	7
NCM7511 01148	0.751	—	Li ₆ PS ₅ Cl	Li ₆ PS ₅ Cl	Li-In	—	194	85	30	3.0–4.3	C/10	8
NCM811	0.80	LiNbO ₃	Li ₁₀ GeP ₂ S ₁₂	Li ₁₀ GeP ₂ S ₁₂	Li-In	—	162	86	35	2.7–4.4	C/10	9
NCM811	0.80	Li ₃ PO ₄	Li ₁₀ GeP ₂ S ₁₂	Li ₁₀ GeP ₂ S ₁₂	In	—	171	75	r.t.	2.7–4.5	C/10	10
NCM811	0.80	—	β-Li ₃ PS ₄	β-Li ₃ PS ₄	Li-In	—	124	71	25	2.7–4.3	C/10	11
<i>Slurry-cast SSB cells</i>												
NCM111	0.33	LiNbO ₃	75Li ₂ S·25 P ₂ S ₅	75Li ₂ S·25 P ₂ S ₅	graphite	3	116	—	r.t.	3.0–4.2	0.13C	12
NCM111	0.33	LiNbO ₃	75Li ₂ S·25 P ₂ S ₅	75Li ₂ S·25 P ₂ S ₅	graphite	~2.8	114	72	30	—	C/24	13
NCM622	0.60	—	β-Li ₃ PS ₄	β-Li ₃ PS ₄	Li	2	140	79	60	3.0–4.2	C/20	14
NCM622	0.60	LiNbO ₃	β-Li ₃ PS ₄	Li ₆ PS ₅ Cl	graphite	1.5	131	—	30	2.5–4.15	C/10	15
NCM622	0.60	LiNbO ₃	Li ₂ S·P ₂ S ₅ ·LiI	Li ₂ S·P ₂ S ₅ ·LiI	Li	2.5	117	—	55	2.5–4.25	C/50	16
NCM622	0.60	LiNbO ₃	Li ₆ PS ₅ Cl	Li ₆ PS ₅ Cl	graphite	1.4	112	—	25	2.5–4.2	C/40	17
NCM622	0.60	—	β-Li ₃ PS ₄	Li ₆ PS ₅ Cl	Li ₄ Ti ₅ O ₁₂	2	148	77	25	2.9–4.4	C/10	*
NCM622	0.60	LiNbO ₃	β-Li ₃ PS ₄	Li ₆ PS ₅ Cl	Li ₄ Ti ₅ O ₁₂	2	170	85	25	2.9–4.4	C/10	*
NCM7015 15	0.70	LiNbO ₃	Li ₆ PS ₅ Cl _{0.5} Br _{0.5}	Li ₆ PS ₅ Cl _{0.5} Br _{0.5}	Li-In	1.5	163	79	30	3.0–4.3	C/10	18
NCM711	0.70	—	Li ₆ PS ₅ Cl	Li ₆ PS ₅ Cl	graphite	2	153	—	25	2.5–4.3	C/10	19
NCM711	0.70	LiNbO ₃	Li ₆ PS ₅ Cl	Li ₆ PS ₅ Cl	Li-In	2	130	—	25	2.5–4.2	C/10	20
NCM811	0.80	LiNbO ₃	Li ₆ PS ₅ Cl	Li ₆ PS ₅ Cl	Li	1	112	67	30	2.5–4.0	C/20	21
NCM811	0.80	—	75Li ₂ S·25 P ₂ S ₅	75Li ₂ S·25 P ₂ S ₅	Li-In	2	139	—	—	2.5–4.2	C/10	22

*This work.

3 Supplemental Experimental Procedures

3.1 Preparation of Cathode Sheets

The cathode composite contained β-Li₃PS₄, uncoated or LiNbO₃-coated NCM622, carbon additive (Super C65 or VGCF), and polymer binder (OPN, SBR, or hNBR). The CAM and solid electrolyte masses were fixed at 1050 and 450 mg, respectively, while the mass of the carbon additive and polymer binder varied according to the weight percentage required. The method of preparation of the cathode composite slurry varied with the carbon additive used. VGCF specifically was dispersed in o-xylene (Sigma-Aldrich, anhydrous, 97 %) with a vortex mixer for 5 min under an argon atmosphere prior to use. Super C65 carbon black, on the other hand, did not require a pre-dispersion process.

Preparation of the cathode-composite sheet involved a series of mixing steps. For the cathode having Super C65 as the carbon additive, the first mixing step was a dry-mixing of the NCM622, β-Li₃PS₄, and Super C65 as powders at 600 rpm for 2 min using a Thinky mixer. The resulting powder was then wetted dropwise with the solvent (o-xylene). The amount of solvent added was calculated to achieve a final solid content of ~45 wt%. The second mixing step was a wet-mixing at 600 rpm for 2 min, after which the binder solution (4 wt% in o-xylene) was added. The mixture was mixed twice at 2000 rpm for 6 min. The slurry obtained was then coated onto an aluminum foil with a mini-tape casting coater from MTI (300 μm doctor-blade slit size). Finally, the film was dried at room temperature in a two-step drying process, where it was first dried until no visible wet spots were seen anymore and lastly in a vacuum for 12 h.

For the cathode with VGCF, both NCM622 and β-Li₃PS₄ were first dry-mixed in a Thinky mixer at 600 rpm for 2 min. Second, VGCF/o-xylene dispersion was added dropwise to the mixed powders. Subsequently, additional o-xylene was added to achieve a final solid content of ~45 wt%. The mixture

4.2 Results and Discussion – Design-of-experiments-guided optimization of slurry-cast cathodes for solid-state batteries

was then wet-mixed at 600 rpm for 2 min. Next, the binder solution was added and the slurry subjected to the final mixing step (2000 rpm for 6 min).

All chemicals and processing steps were handled in an argon environment (Jacomex glovebox with $[O_2] < 1.0$ ppm and $[H_2O] < 1.0$ ppm).

3.2 Preparation of Separator Sheets

The solid-electrolyte sheet consisted of 98 wt% Li_6PS_5Cl and 2 wt% OPN. Prior to the slurry preparation process, the solid electrolyte was ground in a mortar to crush larger agglomerates. The preparation involved a series of mixing steps. The first step was a dry-mixing at 600 rpm for 2 min with 1 min cool-down time in between (twice). The resulting powder was then wetted dropwise with the solvent (o-xylene) to achieve a final solid content of ~45 wt%. The second mixing step was a wet-mixing at 600 rpm for 2 min, after which the binder solution (4 wt% in o-xylene) was added. The mixture was mixed twice with the Thinky mixer at 2000 rpm for 6 min, with a 5 min ultrasonication step in between. The slurry was coated with a doctor blade having a slit size of 350 μm onto an aluminum foil. The film was then dried in a similar two-step drying process as described above. Lastly, it was calendared at 1 N/mm in a dry room with -55 °C dew point.

3.3 Differential Electrochemical Mass Spectrometry (DEMS)

The SSB cells consisted of a slurry-cast cathode (uncoated or $LiNbO_3$ -coated NCM622, β - Li_3PS_4 , VGCF, and with OPN, SBR, or hNBR), a Li_6PS_5Cl pellet separator, and an indium-foil anode. They were assembled in a PEEK ring, allowing relatively high pressure to be applied to them without any cracking occurring during the preparation/cycling process. The PEEK ring was placed on a hardened steel mold, allowing the components to be sequentially pressed into pellets. To start the assembly process, an amount of 100 mg of Li_6PS_5Cl was pressed at ~113 MPa. Following this, the cathode sheet was placed on top of the solid-electrolyte layer. It was then pressed at ~113 MPa to remove the underlying aluminum foil. Subsequently, an aluminum mesh (8 mm diameter), facilitating both conductivity and airflow, was placed on top of the cathode sheet carefully, and together they were compacted at ~440 MPa. The PEEK ring was then removed from the steel mold. Furthermore, a stainless-steel mesh (9 mm diameter) to help promote connectivity was placed on top of the aluminum mesh/cathode layer. Lastly, the indium foil (100 mm thick, 8 mm diameter) was attached to the pellet. The PEEK ring containing the cell was then enclosed with the cathode and anode spacers before placing into the DEMS setup.^{23,24} The cathode spacer had 1 mm diameter holes to ensure that the gas released during cycling can effectively exit towards the outflow. Electrochemical cycling was performed at 45 °C and at a rate of C/20 in the voltage range of 2.3-4.4 V versus In/InLi (equal to ~2.9-5.0 V vs Li^+/Li) using a Biologic VSP-300 potentiostat. A 10 h open-circuit voltage period was included in the beginning to allow the cell to stabilize at the temperature and establish a proper background for the mass spectrometer. The flow of carrier gas (2.5 mL/min, 6.0 helium) was controlled by a mass flow controller (F-201CV-020-RAD-33-Z, Bronkhorst). For gas analysis, a mass spectrometer (Omnistar GSD 320 O2, Pfeiffer Vacuum GmbH) was used. After each DEMS measurement, a calibration gas was introduced to convert the measured ion currents into mol/g values.

3.4 Electrochemical Impedance Spectroscopy (EIS)

EIS was performed on the SSB cells after 20 cycles at a rate of C/10 and 25 °C using an SP-200 potentiostat (BioLogic). They consisted of a slurry-cast cathode, a Li_6PS_5Cl pellet solid-electrolyte separator, and a pellet anode-composite layer. The spectra were collected in the range of 100 mHz to 7.0 MHz with an AC voltage amplitude of 10 mV and fitted using the EC-lab software (BioLogic) assuming $R_1 + (R_2/Q_2)(R_3/Q_3)$ or $R_1 + (R_2/Q_2)(R_3/Q_3)Q_4$ equivalent circuits.

3.5 Scanning Electron Microscopy (SEM)

Cathode sheets containing 1.0 wt% VGCF additive and 2.0 wt% OPN, SBR, or hNBR binder were harvested from the SSB cells in an argon glovebox. The samples were then mounted onto a holder using conductive carbon tape and subjected to cross-sectional SEM imaging and energy-dispersive X-ray spectroscopy (EDS) mapping at 10 and 20 kV, respectively.

3.6 Ex-Situ X-Ray Diffraction (XRD)

The SSB cells were disassembled and placed with the cathode side up in an airtight dome cell (under an argon atmosphere) with a knife-edge in the middle to improve the diffraction quality. XRD patterns were collected in the range of 10-90° 2 θ with a step size of 0.01° and an exposure time of 2.3 s per step on a D8 ADVANCE diffractometer (Bruker AXS) with a $Cu-K\alpha_{1,2}$ radiation source at 40 kV and 40 mA, focusing Bragg-Brentano geometry (280 mm goniometer radius), and a LYNXEYE 1D detector.

4.2 Results and Discussion – Design-of-experiments-guided optimization of slurry-cast cathodes for solid-state batteries

3.7 Synchrotron-Based *Operando* XRD

For *operando* XRD, both the cathode sheet (uncoated NCM622, β -Li₃PS₄, VGCF, and OPN) and the slurry-cast Li₆PS₅Cl solid-electrolyte separator sheet were cold pressed at ~440 MPa on top of each other, which allowed the removal of the aluminum foil of the solid-electrolyte layer. The foil on the cathode-composite sheet remains attached and serves as a mechanical support preventing the sheets from cracking during the subsequent assembling steps. A ring-like indium foil with 7 mm outer diameter and 4 mm inner diameter was attached to the solid-electrolyte sheet. The assembled layers were then sandwiched between two stainless-steel spacers (16 mm diameter, 4 mm diameter hole in the middle) and crimped together in a specialized CR2032 coin cell having a ring-like spring (0.5 t). Both the top and bottom of the coin cell had a 4 mm diameter hole in the middle to allow for X-ray penetration. Afterwards, the coin cell was packed into a pouch with polyimide windows (8 mm diameter). Finally, the pouch-enclosed coin cell was placed in a setup described elsewhere, suitable for *operando* XRD at beamline P24 of PETRA III at DESY (Hamburg, Germany).¹ The beamline had an operating energy of 28 keV ($\lambda = 0.4428$ Å), thereby ensuring a high-flux beam (up to 1012 photons/s). The spot size was roughly (400-400) μm^2 . The patterns were collected in the range of 3-17° 2 θ in 30 s intervals while cycling at a rate of C/10 between 2.3 and 3.8 V versus In/InLi (equal to ~2.9-4.4 V vs Li⁺/Li) using a BioLogic VMP3 multi-channel potentiostat.

4 Supplemental References

1. Bartsch, T., Kim, A.-Y., Strauss, F., de Biasi, L., Teo, J.H., Janek, J., Hartmann, P., and Brezesinski, T. (2019). Indirect State-of-Charge Determination of All-Solid-State Battery Cells by X-Ray Diffraction. *Chem. Commun.* 55, 11223-11226.
2. Strauss, F., de Biasi, L., Kim, A.-Y., Hertle, J., Schweidler, S., Janek, J., Hartmann, P., and Brezesinski, T. (2020). Rational Design of Quasi-Zero-Strain NCM Cathode Materials for Minimizing Volume Change Effects in All-Solid-State Batteries. *ACS Mater. Lett.* 2, 84-88.
3. Auvergniot, J., Cassel, A., Ledeuil, J.-B., Viallet, V., Seznec, V., and Dedryvère, R. (2017). Interface stability of Argyrodite Li₆PS₅Cl toward LiCoO₂, LiNi_{1/3}Co_{1/3}Mn_{1/3}O₂, and LiMn₂O₄ in Bulk All-Solid-State Batteries. *Chem. Mater.* 29, 3883-3890.
4. Tsukasaki, H., Mori, Y., Otoyama, M., Yubuchi, S., Asano, T., Tanaka, Y., Ohno, T., Mori, S., Hayashi, A., and Tatsumisago, M. (2018). Crystallization Behavior of the Li₂S-P₂S₅ Glass Electrolyte in the LiNi_{1/3}Co_{1/3}Mn_{1/3}O₂ Positive Electrode Layer. *Sci. Rep.* 8, 6214.
5. Zhang, Y.-Q., Tian, Y., Xiao, Y., Miara, L.J., Aihara, Y., Tsujimura, T., Shi, T., Scott, M.C., and Ceder, G. (2020). Direct Visualization of the Interfacial Degradation of Cathode Coatings in Solid State batteries: A Combined Experimental and Computational Study. *Adv. Energy Mater.* 10, 1903778.
6. Wang, C., Yu, R., Hwang, S., Liang, J., Li, X., Zhao, C., Sun, Y., Wang, J., Holmes, N., Li, R., Huang, H., Zhao, S., Zhang, L., Lu, S., Su, D., and Sun, X. (2020). Single Crystal Cathodes Enabling High-Performance All-Solid-State Lithium-Ion Batteries. *Energy Storage Mater.* 30, 98-103.
7. Kim, A.-Y., Strauss, F., Bartsch, T., Teo, J.H., Hatsukade, T., Mazilkin, A., Janek, J., Hartmann, P., and Brezesinski, T. (2019). Stabilizing Effect of a Hybrid Surface Coating on a Ni-Rich NCM Cathode Material in All-Solid-State Batteries. *Chem. Mater.* 31, 9664-9672.
8. Jung, S.H., Kim, U.-H., Kim, J.-H., Jun, S., Yoon, C.S., Jung, Y.S., and Sun, Y.-K. (2020). Ni-Rich Layered Cathode Materials with Electrochemo-Mechanically Compliant Microstructures for All-Solid-State Li Batteries. *Adv. Energy Mater.* 10, 1903360.
9. Li, X., Jin, L., Song, D., Zhang, H., Shi, X., Wang, Z., Zhang, L., and Zhu, L. (2020). LiNbO₃-Coated LiNi_{0.8}Co_{0.1}Mn_{0.1}O₂ Cathode with High Discharge Capacity and Rate Performance for All-Solid-State Lithium Battery. *J. Energy Chem.* 40, 39-45.
10. Deng, S., Li, X., Ren, Z., Li, W., Luo, J., Liang, J., Liang, J., Banis, M.N., Li, M., Zhao, Y., Li, X., Wang, C., Sun, Y., Li, R., Hu, Y., Huang, H., Zhang, L., Lu, S., Luo, J., and Sun, X. (2020). Dual-Functional Interfaces for Highly Stable Ni-Rich Layered Cathodes in Sulfide All-Solid-State Batteries. *Energy Storage Mater.* 27, 117-123.
11. Koerver, R., Aygün, I., Leichtweiß, T., Dietrich, C., Zhang, W., Binder, J.O., Hartmann, P., Zeier, W.G., and Janek, J. (2017). Capacity Fade in Solid-State Batteries: Interphase Formation and Chemomechanical Processes in Nickel-Rich Layered Oxide Cathodes and Lithium Thiophosphate Solid Electrolytes. *Chem. Mater.* 29, 5574-5582.
12. Yamamoto, M., Terauchi, Y., Sakunda, A., and Takahashi, M. (2018). Binder-Free Sheet-Type All-Solid-State Batteries with Enhanced Rate Capabilities and High Energy Densities. *Sci. Rep.* 8, 1212.
13. Sakuda, A., Kuratani, K., Yamamoto, M., Takahashi, M., Takeuchi, T., and Kobayashi, H. (2017). All-Solid-State Battery Electrode Sheets Prepared by a Slurry Coating Process. *J. Electrochem. Soc.* 164, A2474-A2478.

4.2 Results and Discussion – Design-of-experiments-guided optimization of slurry-cast cathodes for solid-state batteries

14. Ates, T., Keller, M., Kulisch, J., Adermann, T., and Passerini, S. (2019). Development of an All-Solid-State Lithium Battery by Slurry-Coating Procedures Using a Sulfidic Electrolyte. *Energy Storage Materials* 17, 204-210.
15. Oh, D.Y., Kim, D.H., Jung, S.H., Han, J.-G., Choi, N.-S., and Jung, Y.S. (2017). Single-Step Wet-Chemical Fabrication of Sheet-Type Electrodes from Solid-Electrolyte Precursors for All-Solid-State Lithium-Ion Batteries. *J. Mater. Chem. A* 5, 20771-20779.
16. Choi, S.J., Lee, S.H., Yu, J.H., Doh, C.H., and Ha, Y.C. (2017). Slurry-Processed Glass-Ceramic $\text{Li}_2\text{S-P}_2\text{S}_5\text{-LiI}$ Electrolyte for All-Solid-State Li-Ion Batteries. *ECS Trans.* 77, 65-70.
17. Nam, Y.J., Oh, D.Y., Jung, S.H., and Jung, Y. S. (2018). Toward Practical All-Solid-State Lithium-Ion Batteries with High Energy Density and Safety: Comparative Study for Electrodes Fabricated by Dry- and Slurry-Mixing Processes. *J. Power Sources* 375, 93-101.
18. Kim, K.T., Oh, D.Y., Jun, S., Song, Y.B., Kwon, T.Y., Han, Y., and Jung, Y.S. (2021). Tailoring Slurries Using Cosolvents and Li Salt Targeting Practical All-Solid-State Batteries Employing Sulfide Solid Electrolytes. *Adv. Energy Mater.* <https://doi.org/10.1002/aenm.202003766>.
19. Lee, J., Lee, K., Lee, T., Kim, H., Kim, K., Cho, W., Coskun, A., Char, K., and Choi, J.W. (2020). In Situ Deprotection of Polymeric Binders for Solution-Processible Sulfide-Based All-Solid-State Batteries. *Adv. Mater.* 32, 2001702.
20. Lee, K., Lee, J., Choi, S., Char, K., and Choi, J.W. (2019). Thiol-Ene Click Reaction for Fine Polarity Tuning of Polymeric Binders in Solution-Processed All-Solid-State Batteries. *ACS Energy Lett.* 4, 94-101.
21. Zhang, J., Zhong, H., Zheng, C., Xia, Y., Liang, C., Huang, H., Gan, Y., Tao, X., and Zhang, W. (2018). All-Solid-State Batteries with Slurry Coated $\text{LiNi}_{0.8}\text{Co}_{0.1}\text{Mn}_{0.1}\text{O}_2$ Composite Cathode and $\text{Li}_6\text{PS}_5\text{Cl}$ Electrolyte: Effect of Binder Content. *J. Power Sources* 391, 73-79.
22. Lee, K., Kim, S., Park, J., Park, S.H., Coskun, A., Jung, D.S., Cho, W., and Choi, J.W. (2017). Selection of Binder and Solvent for Solution-Processed All-Solid-State Battery. *J. Electrochem. Soc.* 164, A2075-A2081.
23. Strauss, F., Teo, J.H., Schiele, A., Bartsch, T., Hatsukade, T., Hartmann, P., Janek, J., and Brezesinski, T. (2020). Gas evolution in lithium-ion batteries: solid versus liquid electrolyte. *ACS Appl. Mater. Interfaces* 12, 20462-20468.
24. Berkes, B.B., Jozwiuk, A., Vračar, M., Sommer, H., Brezesinski, T., and Janek, J. (2015). Online continuous flow differential electrochemical mass spectrometry with a realistic battery setup for high-precision, long-term cycling tests. *Anal. Chem.* 87, 5878-5883.

4.3. The interplay between (electro)chemical and (chemo)mechanical effects in the cycling performance of thiophosphate-based solid-state batteries

In Publication 2, we optimized the recipe for fabrication of electrode sheets, achieving electrochemical performance competitive with powder-based pelletized setups. However, long-term capacity fading was still prevalent. In order for all-solid-state batteries (SSBs) to be successful commercially, it has to be competitive with state-of-the-art lithium-ion batteries (LIBs) in terms of electrochemical performance. Therefore, the next step is to understand the underlying contributions to capacity fade and provide potential solutions for it. The two main contributions to capacity fading in SSBs are electrochemical and mechanical degradation of the cell components after prolonged cycling. While electrochemical degradation between the cathode active materials (CAM) and the solid electrolyte (SE) have been thoroughly investigated, the underlying contribution of mechanical degradation to capacity fading is not yet fully understood. In order to study mechanical degradation and its impact on electrochemical performance, we applied a protective LiNbO_3 protective coating on the CAM, thus effectively reducing the contribution of electrochemical degradation to our capacity fade. Following which, we varied the SE of the cathode composite electrode, while keeping everything else constant. The two different SE (glassy $1.5\text{Li}_2\text{S}-0.5\text{P}_2\text{S}_5\text{-LiI}$ and Argyrodite $\text{Li}_6\text{PS}_5\text{Cl}$) possess above all else different mechanical properties and their impact on the electrochemical performance could be observed through a combination of *ex situ* and *in situ* analytical techniques. From this study, we reveal the benefits of using a SE with a low Young's modulus and how the complex interplay between (electro)chemical and (chemo)mechanical effects has to be considered for optimal cell performance.

Remarkably, the slurry-cast cathodes outperform their powder-based pelletized counterparts. This is due to the use of a wet-chemical mixing process, which reduces voids and increases particle-particle contact. When comparing just the slurry-cast cathodes, the glassy SE outperforms the crystalline SE, showing excellent cycling performance with 87% capacity retention after 200 cycles. We associated the improved electrochemical performance with the improved particle-particle contact between the CAM and the SE after prolonged cycling, which was made possible by a lower Young's modulus of the glassy SE. Both cross-sectional and top-view secondary electron microscopy (SEM) images show larger fraction of void formation for the crystalline SE, thus suggesting that a SE with a high degree of crystallinity and hence a higher Young's modulus was not able to accommodate the large volume changes of the CAM during cycling. Additionally, electrochemical impedance spectroscopy (EIS) showed that the largest contribution to the overall resistance for the glassy SE originates from electrochemical degradation, while for the crystalline SE from mechanical separations and a loss of contact area between the SE and the CAM. A model experiment by measuring the *in situ* pressure changes of solid electrolyte/conductive carbon electrodes showed a more muted pressure response for the glassy SE, which together with previous Coulombic efficiency data indicated the formation of redox inactive degradation products. The formation of such robust and stable interface ("self-limiting" interphases) for the glassy SE is believed to be the reason for a more intimate particle-particle contact even after prolonged cycling. Realizing the importance of the interfacial (degradation) products on long-term cycling performance, we attempted to characterize the chemical nature via differential electrochemical mass spectrometry

4.3 Results and Discussion – The interplay between (electro)chemical and (chemo)mechanical effects in the cycling performance of thiophosphate-based solid-state batteries

(DEMS), X-ray photoelectron spectroscopy (XPS) and Time-of-Flight secondary ion mass spectrometry (ToF-SIMS). In general, all three analytical techniques indicated a higher degree of degradation of the glassy SE, with a higher signal intensity of SO₂ gas detected in DEMS and a higher degree of oxidized sulfur species for both XPS and ToF-SIMS. In contrast, no SO₂ signal was detected for the crystalline SE alongside weaker signals for phosphorus- and sulfur-based degradation products in both XPS and ToF-SIMS. The higher degree of degradation could be attributed to a closer proximity of electrode components in the glassy SE, which was indicated as well in both SEM and EIS measurements. Looking at the DEMS data in more details revealed a difference in O₂ and SO₂ trend for both SE. While low amounts of O₂ and high amounts of SO₂ was detected for the glassy SE, the opposite was seen for the crystalline SE. This suggests that reaction of released highly reactive singlet oxygen (¹O₂) with sulfur-containing species (either the SE or the degradation products) that are in close proximity to the CAM occurs more readily for the glassy SE. In contrast, mechanical separations in the crystalline SE allowed sufficient time for the physical decay of the excited oxygen state back to its ground state, which justifies its much larger O₂ signal compared to the glassy SE. However, there remains the possibility that the reduced oxidation of sulfur-containing species seen for the crystalline SE is due to its difference in (electro)chemical nature and should be investigated in future studies.

All the measurements, evaluation and writing for Publication 3 were conducted by me. The work was supervised by Prof. Dr. Jürgen Janek, Dr. Matteo Bianchini and Dr. Torsten Brezesinski. The final paper was then edited by nine co-authors.

Reprinted by permission from (Teo, J. H., Strauss, F., Walther F., Ma, Y., Payandeh, S., Scherer T., Bianchini, M., Janek, J., Brezesinski, T.) The interplay between (electro)chemical and (chemo)mechanical effects in the cycling performance of thiophosphate-based solid-state batteries. *Mat. Futures.* **2021**, © Copyright 2021 The Authors. Published by IOP Publishing Ltd on behalf of the Songshan Lake Materials Laboratory.

OPEN ACCESS

IOP Publishing | Songshan Lake Materials Laboratory

Materials Futures

Mater. Futures 0 (2021) xxxxxx (13pp)

<https://doi.org/10.1088/2752-5724/ac3897>

The interplay between (electro)chemical and (chemo)mechanical effects in the cycling performance of thiophosphate-based solid-state batteries

Jun Hao Teo¹, Florian Strauss¹, Felix Walther², Yuan Ma¹, Seyedhosein Payandeh¹, Torsten Scherer³, Matteo Bianchini^{1,4}, Jürgen Janek^{1,2,*} and Torsten Brezesinski^{1,*} 

¹ Battery and Electrochemistry Laboratory, Institute of Nanotechnology, Karlsruhe Institute of Technology (KIT), Hermann-von-Helmholtz-Platz 1, 76344 Eggenstein-Leopoldshafen, Germany

² Institute of Physical Chemistry & Center for Materials Research, Justus-Liebig-University Giessen, Heinrich-Buff-Ring 17, 35392 Giessen, Germany

³ KNMF Laboratory for Micro- and Nanostructuring, Institute of Nanotechnology, Karlsruhe Institute of Technology (KIT), Hermann-von-Helmholtz-Platz 1, 76344 Eggenstein-Leopoldshafen, Germany

⁴ BASF SE, Carl-Bosch-Str. 38, 67056 Ludwigshafen, Germany

E-mail: juergen.janek@kit.edu and torsten.brezesinski@kit.edu

Received 7 October 2021, revised 10 November 2021

Accepted for publication 10 November 2021

Published xx xx xxxx



Abstract

Solid-state batteries (SSBs) are a promising next step in electrochemical energy storage but are plagued by a number of problems. In this study, we demonstrate the recurring issue of mechanical degradation because of volume changes in layered Ni-rich oxide cathode materials in thiophosphate-based SSBs. Specifically, we explore superionic solid electrolytes (SEs) of different crystallinity, namely glassy $1.5\text{Li}_2\text{S}-0.5\text{P}_2\text{S}_5-\text{LiI}$ and argyrodite $\text{Li}_6\text{PS}_5\text{Cl}$, with emphasis on how they affect the cyclability of slurry-cast cathodes with NCM622 (60% Ni) or NCM851005 (85% Ni). The application of a combination of *ex situ* and *in situ* analytical techniques helped to reveal the benefits of using a SE with a low Young's modulus. Through a synergistic interplay of (electro)chemical and (chemo)mechanical effects, the glassy SE employed in this work was able to achieve robust and stable interfaces, enabling intimate contact with the cathode material while at the same time mitigating volume changes. Our results emphasize the importance of considering chemical, electrochemical, and mechanical properties to realize long-term cycling performance in high-loading SSBs.

* Authors to whom any correspondence should be addressed.



Original content from this work may be used under the terms of the Creative Commons Attribution 4.0 licence. Any further distribution of this work must maintain attribution to the author(s) and the title of the work, journal citation and DOI.

4.3 Results and Discussion – The interplay between (electro)chemical and (chemo)mechanical effects in the cycling performance of thiophosphate-based solid-state batteries

Supplementary material for this article is available [online](#)

Keywords: solid-state battery, slurry casting, lithium thiophosphate electrolyte, Ni-rich NCM cathode, degradation

(Some figures may appear in colour only in the online journal)

Future perspectives

The increasing demand for energy-dense CAMs has been a driving force toward layered Ni-rich oxides. This inevitably leads to modifications in cathode composite design, requiring solutions that can mitigate the volumetric changes during electrochemical cycling. Looking from the materials perspective, a viable approach, as demonstrated herein, is the use of a ‘soft’ SE that is capable of producing robust and stable interfaces, especially with the CAM, and maintaining tight contact even upon severe volume changes. Nevertheless, future studies are required to ascertain the properties of the degradation products as well as their formation mechanism(s), since this study indicated the large influence the composition of the CAM/SE interface has on the overall cell cyclability. Another approach would be the design of low-strain or single-crystalline CAMs, the latter of which have been reported to show increased resistance to cracking both during preparation and cycling. On the other hand, optimizing the electrode formulation and cycling conditions may help accommodate for the volume expansion/contraction, thus enabling the use of Ni-rich NCM CAMs with a larger variety of SEs. Apart from that, newly established analytical techniques in LIB research, such as acoustic emission monitoring, could be employed to probe the void/crack formation in SSBs. Lastly, it should be noted that all of the above considerations have not yet taken into account the (chemo)mechanical and (electro)chemical effects at the negative electrode side. With silicon (Si), a material that is known for undergoing extremely large relative volume changes during cycling, becoming attractive for SSB applications, an already optimized cathode would be beneficial when developing solutions for the anode.

1. Introduction

With the advance in technology ranging from mobile devices to electric vehicles and a global push toward renewable resources (away from fossil fuels), research in electrochemical energy storage has been catapulted to a position front and center. The past three decades have seen rapid adoption in the use of liquid-based lithium-ion batteries (LIBs) [1–3]. However, LIBs have limitations, such as the inherent safety problems caused by flammable components in the system and the limited temperature window for operation [2, 4, 5]. Moreover, they are approaching their theoretical energy densities. These limitations could be theoretically overcome with the inception of solid-state batteries (SSBs), i.e. replacing the liquid electrolyte by a solid electrolyte (SE). With their promise of increased gravimetric and volumetric energy densities by allowing the use of lithium-metal anodes as well as offering improved safety conditions and larger operating temperature windows, SSBs could be applied in a wider range

of applications [6]. However, they possess their own inherent problems. One persisting problem is the rapid capacity fade usually observed for SSBs, which can be attributed to an interplay between (electro)chemical and (chemo)mechanical processes [7–9]. The net effect of either process on the capacity retention depends primarily on the choice of materials and their mutual interactions.

In this study, we focus on industrially relevant materials, with the cathode active material (CAM) being a layered Ni-rich oxide, $\text{Li}_{1+x}(\text{Ni}_{0.6}\text{Co}_{0.2}\text{Mn}_{0.2})_{1-x}\text{O}_2$ (NCM622) or $\text{Li}_{1+x}(\text{Ni}_{0.85}\text{Co}_{0.10}\text{Mn}_{0.05})_{1-x}\text{O}_2$ (NCM851005), and the SEs being lithium thiophosphates. Layered oxide CAMs are well established in LIBs and are also very attractive for use in SSBs. However, they undergo distinct volume changes upon (de)lithiation, making the selection of the other components of the composite even more important [10–12]. Regarding the SE, sulfides (thiophosphates) are a popular choice for SSBs. Their low Young’s moduli enable an increased mechanical integrity of the cell [13–16]. In addition, they are easy to be processed and exhibit highly competitive ionic conductivities, with some reaching values as high as $10^{-2} \text{ S cm}^{-1}$ at room temperature [17]. Nevertheless, sulfide SEs exhibit poor (electro)chemical stability, often featuring significant interfacial decomposition at both low and high voltages [18]. This (electro)chemical instability has been studied to a great extent and addressed in various publications [19–21]. A widely adopted solution to overcome stability issues, for example, is the application of surface coating strategies to the electrode materials [22–27]. The mechanical degradation, on the other hand, and its underlying mechanism(s) and contribution to capacity fading have not been fully understood and are subject of recent works [28–32]. One approach to alleviate the capacity fading caused by such effects is to tailor the material’s mechanical properties, such as the use of a glassy SE phase instead of a crystalline one. Another possibility is to optimize the cycling conditions (e.g. cutoff voltage, anode/cathode ratio, etc) to mitigate volume changes of the active material, especially during the initial cycles [33, 34]. Herein, we chose to focus on the former, which has shown promise in the past. For example, Wang *et al* recently investigated the impact of crystallinity on the (chemo)mechanics and showed that the higher ionic conductivity that comes with it does not necessarily guarantee improved capacity retention [28]. Moreover, Minnmann *et al* demonstrated that the effective ionic conductivity of crystalline sulfide SEs in NCM-based cathode composites decreases up to an order of magnitude compared to

4.3 Results and Discussion – The interplay between (electro)chemical and (chemo)mechanical effects in the cycling performance of thiophosphate-based solid-state batteries

the bulk SE [35]. Similarly, we have recently reported electrochemical data for pelletized SSBs with two different thiophosphate SEs, namely glassy $1.5\text{Li}_2\text{S}-0.5\text{P}_2\text{S}_5\text{-LiI}$ (referred to as g-SE) and argyrodite $\text{Li}_6\text{PS}_5\text{Cl}$ (referred to as c-SE), with the former showing superior cycling stability [29].

The capacity retention after 200 cycles was found to be ~ 58 and 39% for the g-SE and c-SE cells, respectively (figure S1 (available online at stacks.iop.org/MF/00/00000/mmedia)). Interestingly, the capacity delivered by the c-SE cell continued to decline strongly even after 200 cycles. We also noticed a difference in the Coulombic efficiency. While it increased steadily for the g-SE cell, reaching a value above 99.5% after 50 cycles, the c-SE cell exhibited a different trend. It was able to achieve 99.4% within 20 cycles, then the Coulombic efficiency decreased in the subsequent cycling until a local minimum around 40 cycles was reached, followed by a new increase beyond 99.5% only after 150 cycles. It should be noted that the crystalline $\text{Li}_4\text{PS}_4\text{I}$ counterpart was not used for comparison because of its relatively poor room-temperature ionic conductivity. Instead, argyrodite $\text{Li}_6\text{PS}_5\text{Cl}$ was chosen as SE. In this work, we aim to build upon our results by utilizing different *ex situ* and *in situ* analytical techniques to better understand the interplay between (electro)chemical and (chemo)mechanical effects and their influence on the long-term cyclability of SSB cells using a slurry-cast cathode.

2. Results

2.1. Cell performance

With our previous data in mind, we attempted a similar electrochemical analysis for slurry-cast cathodes (figure 1). The components included LiNbO_3 -coated NCM622 CAM, glassy $1.5\text{Li}_2\text{S}-0.5\text{P}_2\text{S}_5\text{-LiI}$ or argyrodite $\text{Li}_6\text{PS}_5\text{Cl}$ as SE, Super C65 carbon black additive, and a polyisobutene (Oppanol) binder. The SSB cells were cycled with a similar protocol as the pelletized (powder-based) cells in the voltage range of $1.35\text{--}2.85\text{ V}$ vs $\text{Li}_4\text{Ti}_5\text{O}_{12}/\text{Li}_7\text{Ti}_5\text{O}_{12}$ (approximately $2.9\text{--}4.4\text{ V}$ vs Li^+/Li) at a C/5 rate and 45°C for 200 cycles (see section 4 for more details). Interestingly, the g-SE cell exhibited excellent cycling performance and stability (figure 1(a)). The first-cycle specific charge and discharge capacities were 190 and $162\text{ mAh/g}_{\text{NCM622}}$, respectively. Despite the slightly lower values at the beginning of the cycling experiment compared to the corresponding pelletized cell, the slurry-cast cell showed a much improved capacity retention of ~ 87 vs 58% after 200 cycles, corresponding to a fade rate per cycle of only 0.065% (~ 3.3 times lower than for the pelletized cell). Especially the Coulombic efficiency data indicated a strong stabilization from the 4th cycle onward ($>99\%$). However, this kind of improved electrochemical performance was not observed for the slurry-cast c-SE cell (figure 1(b)). The first-cycle specific charge and discharge capacities were 200 and $171\text{ mAh/g}_{\text{NCM622}}$, respectively. The capacity retention after 200 cycles was $\sim 49\%$, which is only moderately higher compared to the pelletized cell with $\sim 39\%$. In this case, the margin of 10% improvement in capacity

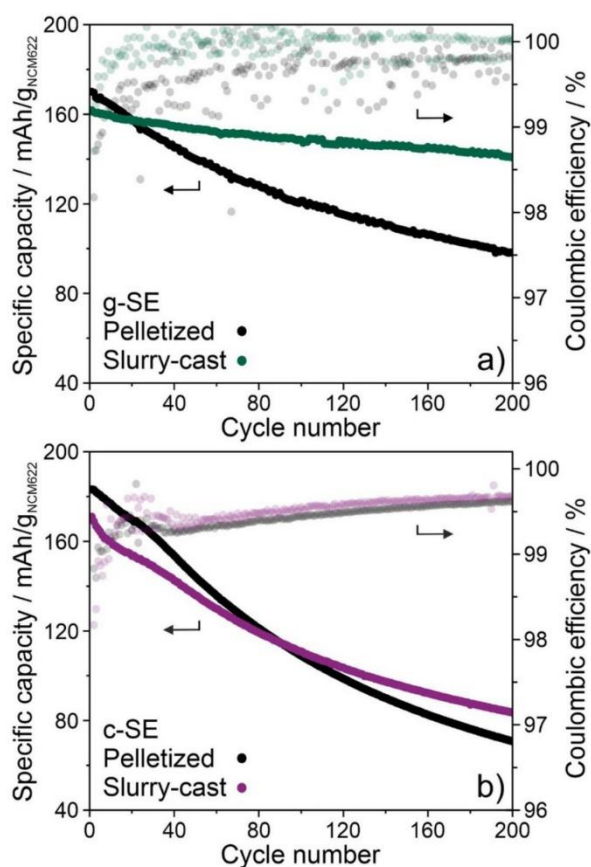


Figure 1. Cycling performance of SSB cells with (a) glassy SE ($1.5\text{Li}_2\text{S}-0.5\text{P}_2\text{S}_5\text{-LiI}$) and (b) crystalline SE ($\text{Li}_6\text{PS}_5\text{Cl}$) in both pelletized and slurry-cast cathodes and corresponding Coulombic efficiencies. Cells tested at 45°C , C/5, $2.9\text{--}4.4\text{ V}$ vs Li^+/Li .

retention is too small to conclude that a slurry-cast cathode performs better than a pelletized one when using the argyrodite SE.

2.2. Cross-sectional scanning electron microscopy (SEM) imaging

Transitioning to the slurry-cast cathodes, we noticed a much larger improvement for the g-SE cell over the crystalline one. The g-SE cell exhibited a $\sim 29\%$ increase in capacity retention (over 200 cycles), compared to a $\sim 10\%$ improvement in the c-SE cell. It has been reported that slurry-based casting processes improve the homogeneity of distribution within the cathode composite and the interfacial contact between CAM and SE [36, 37]. A morphological comparison between the pelletized and slurry-cast cathodes for the argyrodite SE using SEM showed that the use of a wet-chemical process (solvent-based mixing) reduces voids and increases the particle-particle contact (figure S2). However, even with better interfacial contact at the beginning of cycling, the capacity

4.3 Results and Discussion – The interplay between (electro)chemical and (chemo)mechanical effects in the cycling performance of thiophosphate-based solid-state batteries

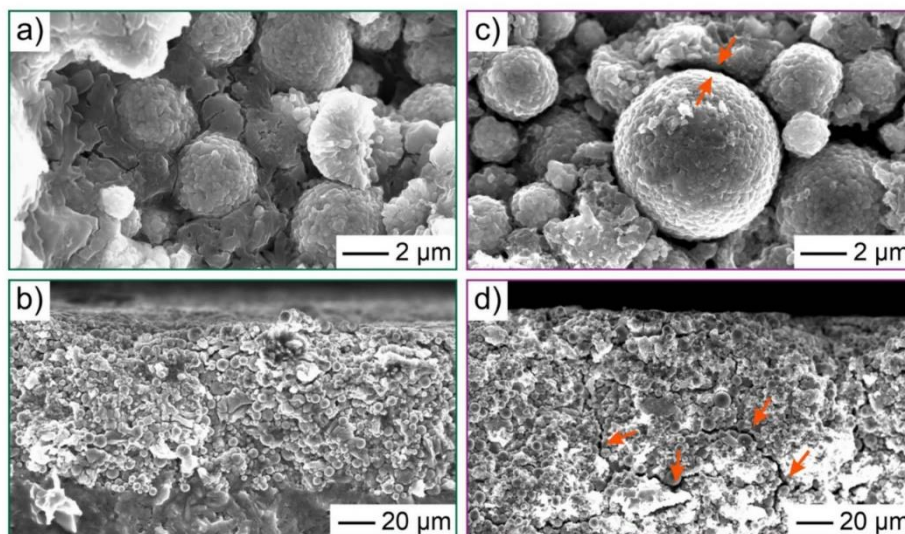


Figure 2. Cross-sectional SEM images of the slurry-cast cathode of SSB cells using (a), (b) glassy SE ($1.5\text{Li}_2\text{S}-0.5\text{P}_2\text{S}_5\text{-LiI}$) and (c), (d) crystalline SE ($\text{Li}_6\text{PS}_5\text{Cl}$) after 200 cycles at a rate of $\text{C}/5$ and 45°C . The arrows denote void formation and cracking.

fading was still prominent in the c-SE cell. To that end, cross-sectional SEM was performed on the slurry-cast cathodes after 200 cycles (figures 2(a)–(d)). From the images, it is apparent that the c-SE electrode exhibited a larger fraction of void space around the CAM secondary particles and intergranular cracks compared to the g-SE electrode. The voids (prevalent in the c-SE cell) have been reported in literature to result from the mechanical separation between CAM and SE [18, 30, 38]. (Chemo)mechanically-driven separations and possible cracking, typically due to volume changes during cycling, with $\Delta V/V \approx -3\%$ at 4.4 V vs Li^+/Li for NCM622 in LIBs [10, 32], would lead to less electrochemically active contact area (material), thereby adversely affecting the reversibility and capacity retention. The images suggest that even with improved interfacial contact, mechanical separation occurs if the SE does not possess the necessary mechanical properties required for mitigation of void formation/cracking. On a side note, the protective coating (LiNbO_3) plays a minor or no direct role in contributing to mitigating (chemo)mechanically-driven separations. In a recent publication, Ma *et al* showed that there are no major differences in CAM/SE contact between (cycled) cathodes using uncoated and LiNbO_3 -coated LiNiO_2 [9]. However, indirectly, the coating plays a role in the formation of interfacial degradation products, which possess their own inherent (electro)chemical and (chemo)mechanical properties. While the (electro)chemical aspect can be examined by observing the cycling behavior, the (chemo)mechanical aspect remains elusive. Nevertheless, the objective of this study was the comparison of (electro)chemical and (chemo)mechanical properties from the SE point of view, thus the role of the coating will not be elaborated upon any further.

In the following sections, a more in-depth analysis into the ability of the glassy SE to alleviate (chemo)mechanical effects in slurry-cast cathodes will be conducted. This encompasses

study of the interfacial degradation via electrochemical impedance spectroscopy (EIS), differential electrochemical mass spectrometry (DEMS), x-ray photoelectron spectroscopy (XPS), and time-of-flight secondary ion mass spectrometry (ToF-SIMS).

2.3. EIS

EIS was performed to better understand the correlation between void/crack formation and electrochemical performance. The Nyquist plots of the electrochemical impedance after cycling and corresponding fits to the data are shown in figure 3. Fitting was done assuming an $R_1(R_2/Q_2)(R_3/Q_3)(R_4/Q_4)$ equivalent circuit. R_1 is the resistance of the bulk (separator) SE, R_2 the SE grain boundary (gb) resistance, R_3 the cathode (CAM/SE) interfacial resistance, and R_4 represents the anode (anode active material (AAM)/SE) interfacial resistance [18, 39, 40]. The SE bulk (area specific) resistance was ~ 38.2 and $15.9 \Omega \text{ cm}^2$ for the g-SE and c-SE cells, respectively. This difference can be explained by a more than doubled room-temperature ionic conductivity for the crystalline SE compared to the glassy SE (~ 2.0 vs 0.8 mS cm^{-1}). Moreover, we found that the cathode interfacial resistance exhibited a larger value for the g-SE cell ($\sim 8.3 \Omega \text{ cm}^2$) than for the c-SE cell ($\sim 2.5 \Omega \text{ cm}^2$). The major factors contributing to the latter resistance are electrochemical decomposition of the SE (interfacial reaction between CAM and SE) and void/crack formation [28]. We assume that in case of the g-SE cell, the largest contribution to the $R_{\text{CAM/SE}}$ is the formation of a relatively thick layer of degradation products at this interface. The contribution of void formation and/or cracking is probably small, since no visible (chemo)mechanically-driven separation between CAM and SE was apparent from SEM imaging (figures 2(a) and (b)). On the other hand, the major contribution to the $R_{\text{CAM/SE}}$ for the c-SE cell can most

4.3 Results and Discussion – The interplay between (electro)chemical and (chemo)mechanical effects in the cycling performance of thiophosphate-based solid-state batteries

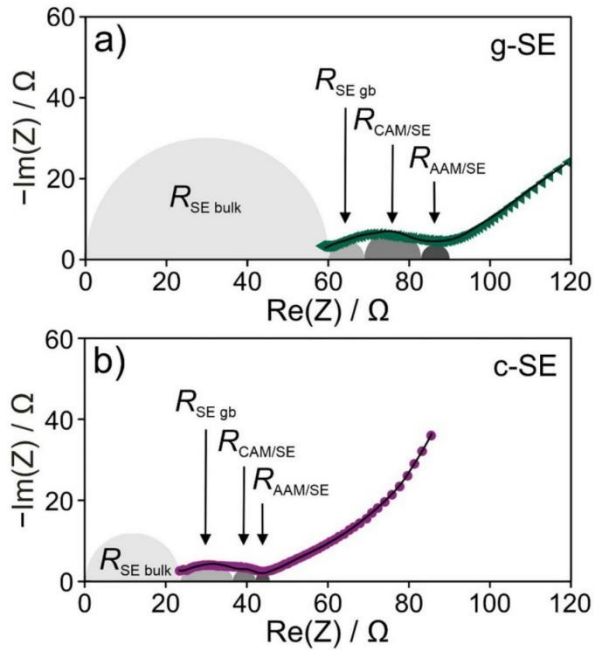


Figure 3. Nyquist plots of the electrochemical impedance of SSB cells (black lines: measured data; solid symbols: fitted data) using a slurry-cast cathode with (a) glassy SE ($1.5\text{Li}_2\text{S}-0.5\text{P}_2\text{S}_5\text{-LiI}$) and (b) crystalline SE ($\text{Li}_6\text{PS}_5\text{Cl}$) after 200 cycles at a rate of C/5 and 45°C . Semicircles provide eye guidance for the individual resistance contributions.

likely be attributed to (chemo)mechanically-driven separation effects, as evidenced by the void/crack formation (figures 2(c) and (d)). To support this argument, we will incorporate solid-state diffusion into the analysis. The total cell impedance consists of the SE bulk resistance, the charge-transfer resistance, and the low-frequency Warburg component (equation S1). The Warburg coefficient having an inverse relationship with the contact area between CAM and SE can be represented as shown in equation S2 (see also figure S3 and accompanying explanation). While electrochemical degradation only affects the charge-transfer resistance, mechanical separation increases both the charge-transfer and Warburg resistances; both contributions can be distinguished. Overall, a larger Warburg coefficient (assuming that the lithium-diffusion coefficient is constant) means a smaller contact area and therefore a higher degree of mechanical separation. In fact, the Warburg coefficient for the c-SE cell was larger by a factor of about two compared to the g-SE cell, suggesting a lower contact area between CAM and SE after 200 cycles. Lastly, we observed a lower SE grain boundary resistance in the g-SE cell (~ 5.7 vs $8.3 \Omega \text{ cm}^2$), which could be explained by the reduced degree of crystallinity. SE particle fracturing resulting from (chemo)mechanically-induced stress during cycling may also contribute to this difference, as indicated by the larger void fraction observed within the argyrodite SE in 3D reconstructions of focused ion beam (FIB)-SEM slice images of the electrodes (figure S4) [29].

Despite the lower cathode interfacial resistance of the c-SE cell, its electrochemical performance was drastically worse than the g-SE cell, indicating that mechanical separation more strongly affects the long-term cycling performance than electrochemical decomposition reactions do. In addition, the data suggest that the formation of ‘self-limiting interphases’ for the g-SE cell ($>99\%$ Coulombic efficiency after three cycles) might not be as detrimental to the cyclability as originally thought.

2.4. In situ pressure monitoring

Next, we attempted to elucidate the differences in void/crack formation via *in situ* pressure monitoring of the respective SSB cells [28, 30, 38]. The as-measured force response is shown in figure S5. The force response was corrected for its baseline and converted to pressure change (uniaxial stress, σ_{11}). To focus on the changes in stress in the slurry-cast composite cathodes, $\text{Li}_4\text{Ti}_5\text{O}_{12}$ (LTO) was used as AAM. LTO is a zero-strain electrode material, i.e. its relative volume changes upon cycling are negligible [41–43]. Among the various contributors to the changes in stress within the cathode, the expansion/contraction of the CAM dominated the pressure signal. During delithiation (charge cycle), a negative net pressure change (Δp) was recorded because of the volume contraction of the NCM622 [10]. Upon lithiation (discharge cycle), the volume change was reversed, leading to a positive net pressure change, at first sight independent of the SE. Following several cycles, a sudden decrease in Coulombic efficiency was seen, which was unique to the c-SE cell (figure S6). This confirms the non-monotonous nature of the Coulombic efficiency versus cycle number curve shown in figure 1(b) and could be an indication of (chemo)mechanically-driven separations between cathode constituents reaching a critical point [31, 44]. However, in the pressure measurements, probing primarily the CAM breathing, no distinct changes in stress response were observed. In fact, the pressure response was similar for both SEs, despite the g-SE cell using one with a lower Young’s modulus ($<14 \text{ GPa}$) [15, 45] compared to the c-SE cell ($>22 \text{ GPa}$) [13]. This was to be expected because of the large fraction of CAM in the composite ($>68 \text{ wt.}\%$). The equipment used and the measuring conditions did not allow for resolving the subtle changes (to the pressure response) originating from (chemo)mechanical interactions involving the SE.

Therefore, model experiments attempting to remove the CAM contribution by using SE/carbon black electrodes were conducted. Specifically, cyclic voltammetric (CV) measurements were carried out for the different SE-based cells, and the corresponding pressure response during the first two cycles was recorded (figures 4(a)–(c) and (e)–(g)). A net pressure change was observed in both cases. The data showed a relatively large negative pressure response for the crystalline SE/Super C65 as opposed to a minor positive pressure response for the glassy SE/Super C65. Taking the current response into account, these pressure changes seem to be due to a more prominent electrochemical oxidation of the crystalline SE [46]. The increased electrochemical stability window of $\text{Li}_2\text{S-P}_2\text{S}_5$ SEs with LiI incorporation has also

4.3 Results and Discussion – The interplay between (electro)chemical and (chemo)mechanical effects in the cycling performance of thiophosphate-based solid-state batteries

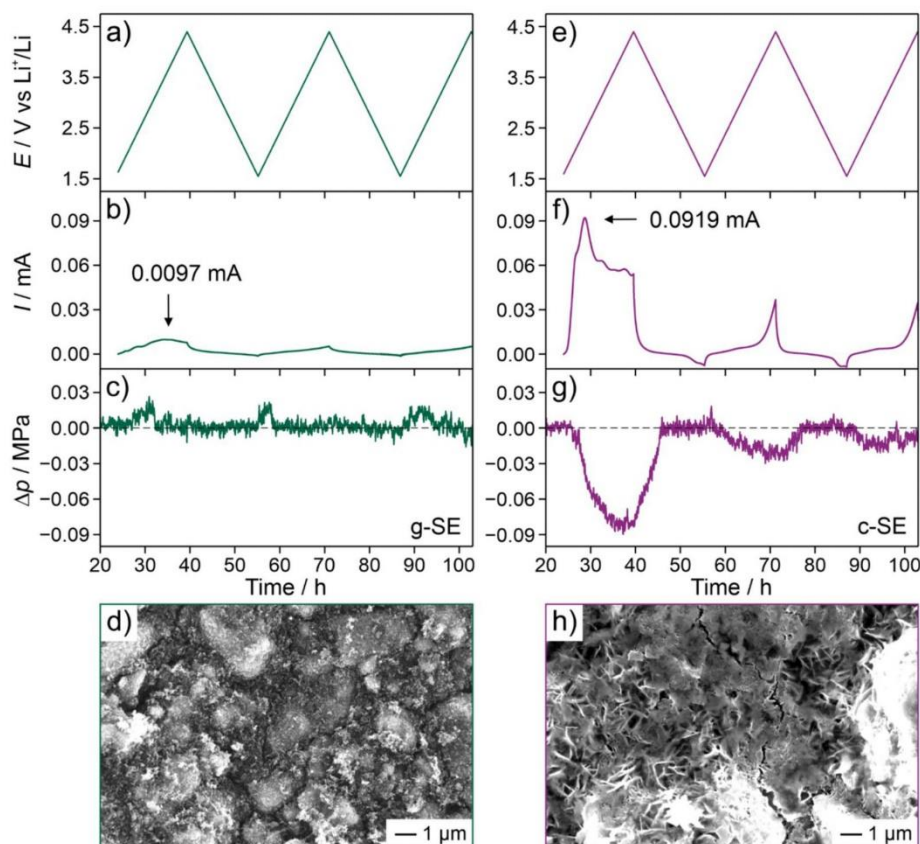


Figure 4. *In situ* pressure monitoring of Super C65 electrodes with (a)–(c) glassy SE ($1.5\text{Li}_2\text{S}-0.5\text{P}_2\text{S}_5\text{-LiI}$) and (e)–(g) crystalline SE ($\text{Li}_6\text{PS}_5\text{Cl}$). (a), (e) CV profiles, (b), (f) current response, and (c), (g) pressure response. Cells tested at 45°C , 0.05 mV s^{-1} , OCV- $4.4\text{ V vs Li}^+/\text{Li}$ in the first cycle and $1.55\text{--}4.4\text{ V vs Li}^+/\text{Li}$ in the following cycles. Top-view SEM images of the (d) glassy SE/Super C65 and (h) crystalline SE/Super C65 electrodes after cycling.

been reported in literature [47, 48]. This is further supported by the crack/void formation observed by SEM primarily for the crystalline SE/Super C65 electrode (figures 4(d) and (h)), a result of the shrinkage (volume contraction) of the SE. Additionally, in case of the crystalline SE/Super C65 electrode, the initial decrease in pressure was recovered during the cathodic sweep (reduction), indicating partial reversibility of the degradation processes [49]. On the other hand, the glassy SE/Super C65 electrode did not show a change in pressure in the cathodic sweep, suggesting that the degradation products formed are either redox inactive or do not lead to significant pressure changes. These findings help explain the observation of a quicker stabilization of the Coulombic efficiency above 99.5% [formation of robust/stable interfaces and ('self-limiting') interphases] and the good interfacial contact (no voids/cracks) for the glassy SE. Because the major part of side product formation occurs in the initial cycle, we noticed an opposing trend to the EIS measurements. However, it has to be noted that EIS was performed after 200 cycles and does not take into account the fast stabilization of the g-SE cell. Besides, the CAM is not present in this simple model experiment, and the (electro)chemical reaction between

NCM622 and SE must also be considered in case of the EIS measurements.

2.5. *In situ* gas analysis

Building upon the observations from *in situ* pressure monitoring and reports on the impact of side product formation on the pressure evolution, a series of *ex situ* and *in situ* analytical techniques (DEMS, XPS, and ToF-SIMS) were used to characterize the chemical nature of the gaseous and solid degradation products for both SEs [28].

First, *in situ* gassing studies via DEMS were performed on the slurry-cast cathodes (figure 5). To this end, the SSB cells were cycled at a C/20 rate and 45°C in the voltage range of $2.9\text{--}5.0\text{ V vs Li}^+/\text{Li}$. The higher charge cutoff voltage was chosen with the intention of increasing the evolution of reactive oxygen from the NCM622 CAM and observing its reaction with the surrounding SE. The cells underwent three cycles and the gas evolution was monitored for $m/z = 1\text{--}100$. While four gases were detected for the g-SE cell (H_2 , O_2 , CO_2 , and SO_2 ; see figure 5(a)), only three were detected for the c-SE cell (H_2 , O_2 , and CO_2 ; see figure 5(b)).

4.3 Results and Discussion – The interplay between (electro)chemical and (chemo)mechanical effects in the cycling performance of thiophosphate-based solid-state batteries

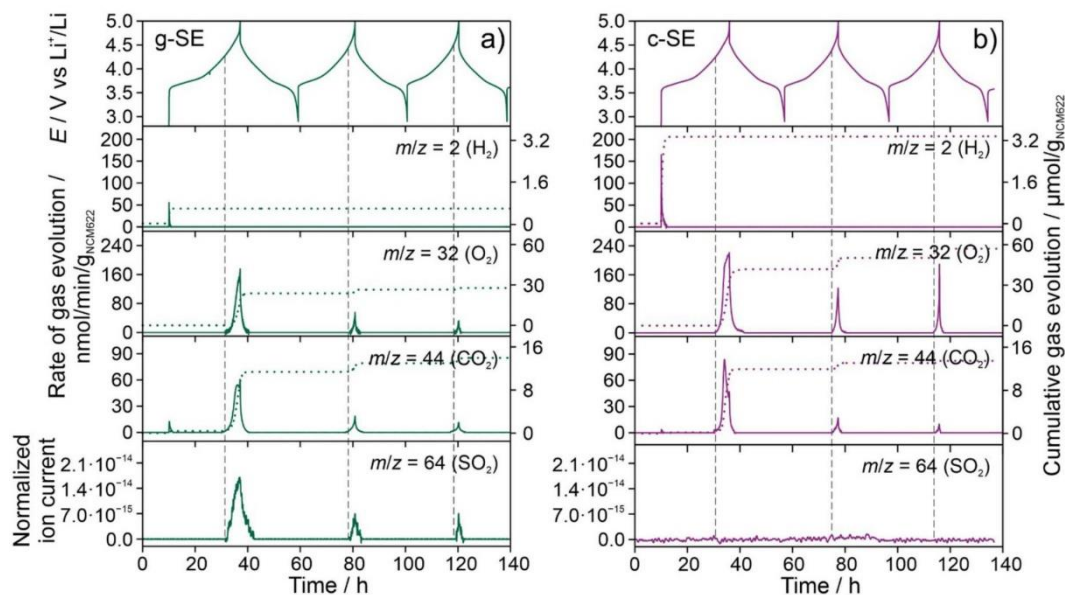


Figure 5. Electrochemical profile of SSB cells using a slurry-cast cathode with (a) glassy SE ($1.5\text{Li}_2\text{S}-0.5\text{P}_2\text{S}_5\text{-LiI}$) and (b) crystalline SE ($\text{Li}_6\text{PS}_5\text{Cl}$) and corresponding time-resolved evolution rates (left y-axis) and cumulative amounts (right y-axis) for H_2 , O_2 , and CO_2 , as well as normalized ion currents for SO_2 . Cells tested at 45°C , $\text{C}/20$, $2.9\text{--}5.0\text{ V vs Li}^+/\text{Li}$.

H_2 evolution ($m/z = 2$) occurred at the onset of the initial charge cycle and can most likely be related to the reduction of trace H_2O at the anode. For example, it has been reported that a charged $\text{Li}_4\text{Ti}_5\text{O}_{12}$ ($\text{Li}_7\text{Ti}_5\text{O}_{12}$) anode in LIBs undergoes redox reactions with H_2O , thereby producing H_2 [50]. The lithiated indium anode should follow a similar reaction pathway creating 0.5 mol of H_2 for every mol of H_2O . Interestingly, the cumulative amount of H_2 evolution was lower by a factor of around four for the g-SE cell compared to the c-SE cell (~ 0.6 vs $3.4\text{ }\mu\text{mol/g}_{\text{NCM622}}$). Given that both cathode composites were fabricated and processed identically with the only difference being the type of SE used, this result suggests that the reduction of residual H_2O is mitigated in the g-SE cell. Recently, it has been reported that $\text{Li}_4\text{PS}_4\text{I}$ exhibits a high stability toward H_2O , partially routed in the formation of an $\text{LiI}\cdot\text{H}_2\text{O}$ adduct. The formation of such a phase might take place as well here, competing with the electrochemical reduction of H_2O and therefore H_2 release [51]. Nevertheless, in case of the c-SE cell, solely electrochemical reduction of H_2O traces occurs, being responsible for the increased amount of evolved H_2 .

Regarding O_2 evolution, cells containing an NCM622 CAM are typically required to achieve a state of charge (SOC) $\geq 80\%$. This condition was met with $\sim 89\%$ ($244\text{ mAh/g}_{\text{NCM622}}$) and $\sim 85\%$ ($234\text{ mAh/g}_{\text{NCM622}}$) for the g-SE and c-SE cells, respectively. Mass signals characteristic of O_2 ($m/z = 32$) with onset voltages of $\sim 4.3\text{ V vs Li}^+/\text{Li}$ were observed, in agreement with reports available in literature [37, 52–55]. The origin of O_2 (presumably at least partly in the form of $^1\text{O}_2$) evolution in layered Ni-rich oxide CAMs has been extensively studied in the past and shown to be a consequence of the destabilization of the

crystal lattice at high SOC (due to either layered-to-spinel or layered-to-rocksalt transformation) [52, 53]. Prior to the physical decay of the highly reactive $^1\text{O}_2$ toward its triplet ground state [56], there is a possibility of the singlet oxygen reacting with the different components present in the cathode composite. Moreover, the amount of O_2 evolving should scale exponentially with the SOC [37]. Despite showing a lower SOC, the cumulative amount of molecular O_2 in the first cycle was $\sim 42\text{ }\mu\text{mol/g}_{\text{NCM622}}$ for the c-SE cell versus $\sim 23\text{ }\mu\text{mol/g}_{\text{NCM622}}$ for the g-SE cell. This difference seems explainable by the consumption of reactive oxygen through follow-up reactions with the thiophosphate SE, which appears to be facilitated for the g-SE cell because of the more intimate CAM/SE contact. In contrast, the c-SE cell showed increased particle distances from mechanical separations, apparently reducing the extent of oxidation reactions. Apart from that, the formation of voids is believed to affect the gas release from the bulk of the cathode to the surface.

We also monitored the evolution of SO_2 , which is a common phenomenon for SSB cells containing sulfide SEs and is of utmost interest in this study. SO_2 formation and release is a clear indication of chemical oxidation of the thiophosphate SE. In case of the g-SE cell, a sharp peak corresponding to the mass signal $m/z = 64$ [normalized with respect to the carrier-gas signal $m/z = 4$ (He)] was detected at high SOC. SO_2 evolution has been reported to be a result of the chemical reaction between SE and reactive oxygen that is released from the CAM or the electrochemical decomposition of residual surface carbonates [55, 57, 58]. However, the exact reaction mechanism (degradation route) is unclear at present. While SO_2 was clearly detected in the g-SE cell, no SO_2 evolution was observed for the c-SE cell. This result strengthens the argument above, where

4.3 Results and Discussion – The interplay between (electro)chemical and (chemo)mechanical effects in the cycling performance of thiophosphate-based solid-state batteries

in case of the g-SE cell, the amount of released O_2 is decreased in favor of SO_2 formation because of the better CAM/SE contact. However, there remains the possibility that the increased SO_2 evolution is instead due to differences in composition and chemical stability/reactivity. The lower cumulative amount of O_2 for the g-SE cell could be attributed to the formation of non-gaseous, oxidized sulfur species, resulting in the consumption of reactive oxygen through side reactions (see section on XPS/ToF-SIMS characterization below).

Lastly, we monitored the CO_2 mass signal ($m/z = 44$). CO_2 evolution in SSB cells is typically indicated by sharp peaks with onset voltages ≥ 4.2 V. However, CO_2 release has also been observed at the beginning of the first charge cycle and postulated to be due to side reactions at the anode [37, 54, 55]. At high voltages, CO_2 evolution could stem from three possible sources: (a) electrochemical decomposition of residual surface carbonates present on the CAM particles, (b) chemical oxidation of the polymer binder, and (c) chemical oxidation of the carbon additive [37, 57]. The electrochemical decomposition of surface carbonates is reported to proceed by the process shown in equation S3 [58, 59]. While the mechanisms for sources (b) and (c) are largely unknown, they are indirectly observed by the coincidence of $m/z = 44$ and 32 signals at the highest SOC [37]. This suggests that beyond 4.8 V vs Li^+/Li , reactions between the carbon-related components (binder and additive) and the reactive oxygen are possible. Unsurprisingly, the cumulative CO_2 evolution was similar with ~ 13.9 and $13.4 \mu\text{mol/g}_{\text{NCM622}}$ for the g-SE and c-SE cells, respectively. This is because CO_2 evolution is largely independent of the type of SE used and rather dependent on the CAM surface chemistry (carbonate impurities).

2.6. Interfacial degradation

Taken together, the gas analysis via DEMS revealed an increased formation of SO_2 in the g-SE cell because of chemical oxidation of the SE with reactive oxygen species released by the CAM. To further investigate the interfacial reactions occurring in the slurry-cast cathodes, we utilized a combination of post-mortem XPS and ToF-SIMS and studied the formation of solid side products after 200 cycles.

Typical of thiophosphate-based SSBs, analysis of the S 2p and P 2p core-level spectra before and after cycling was conducted to probe the degradation products at the CAM/SE interface. The XPS data in figure 6 were taken after 480 s sputtering to mitigate any detrimental effects from the current collector [27, 60]. The S 2p signals for the uncycled g-SE and c-SE cells were fitted with three doublets (figure 6(a)). The first doublet with binding energies of 160.1/161.4 eV (gray component) represents the ‘free’ S^{2-} ions from the SE crystal structure and/or Li_2S impurities [27, 46, 49, 60–63]. The relative signal intensity of this doublet decreased upon cycling because of oxidation reactions occurring during charge, with the decrease being more prominent in the g-SE cell. While the doublet was still present after 200 cycles for the c-SE cell, it was not detectable anymore for the g-SE cell. The second doublet at 161.7/162.7 eV corresponds to the PS_4^{3-} tetrahedra (red component). The third doublet at 162.9/164.1 eV (blue component)

can be attributed to various compounds. On the one hand, this includes anionic frameworks that thiophosphate SE phases can pass through toward the formation of P_2S_5 [46, 62]. On the other hand, the doublet may arise from oxidized sulfur species (polysulfides) [61, 63]. Note that the signal position of polysulfides depends on the chain length and gradually approaches the theoretical binding energy of elemental sulfur [27]. The pronounced signal intensity and broadening of this doublet for the g-SE cell may either indicate stronger degradation reactions or the presence of thiophosphate anions, i.e. $P_2S_7^{4-}$ and $P_2S_6^{2-}$, in agreement with Raman spectroscopy data obtained on related $xLi_2S-yP_2S_5-zLiI$ phases [16, 48, 62–64]. After cycling, the g-SE cell showed a more severe degradation of the sulfur species, apparent by an increase in signal contributions at higher binding energies. The electrochemical decomposition reactions of the SE can, in principle, occur at all interfaces allowing electron transfer in the cathode, i.e. towards the current collector, the carbon additive, and the CAM, assuming the polymer binder to be electronically insulating [27]. Hence, this observation cannot be directly attributed to a specific interface and/or differences in the thermodynamic stability window of the SE. However, the S 2p spectrum for the g-SE cell showed an additional weak component around 170 eV, not observed for the c-SE cell. This signal is typically related to oxygenated sulfur species in thiophosphate-based SSBs [49]. Because the NCM622 is the only oxygen source in the cathode, it can be directly attributed to CAM/SE interfacial degradation reactions. This result thus indicates either an increased oxygen-involving degradation because of the tight contact between CAM and SE for the g-SE cell or a poorer chemical stability of the glassy SE against reactive oxygen. Nevertheless, the stronger signal of oxygenated sulfur species agrees with the more significant SO_2 evolution discussed above.

For the interpretation of P 2p data, the spectrum is usually deconvoluted into three contributions (figure 6(b)). The main contribution was fitted with a doublet having binding energies of 131.9/133 eV (red component) and can be assigned to the PS_4^{3-} tetrahedra [49, 61, 63]. The c-SE cell did not show additional signal contributions prior to cycling. However, a shoulder evolved at higher binding energies upon cycling, which we relate to the overlapping of newly formed doublets, analogous to the S 2p spectra [doublet at 133.2/133.9 eV (blue component), anionic framework transitions and phosphorus-containing polysulfide species; doublet at 134.4/135.4 eV (orange component), oxygenated phosphorus species, such as Li_3PO_4 and/or transition-metal phosphates). Especially the latter degradation products are believed to cause impedance buildup at the cathode side [63, 65]. Again, because the only oxygen source is the NCM622, the appearance of the doublet at 134.4/135.4 eV is indicative of adverse oxygen-involving side reactions at the CAM/SE interface. As somewhat expected, the higher binding-energy signals were more distinct for the g-SE cell than for the c-SE cell.

Finally, ToF-SIMS analysis was used to gain further insights into the interfacial degradation reactions. The high sensitivity of ToF-SIMS allows to investigate side products below the detection limit of XPS. However, ToF-SIMS is a semi-quantitative method and direct comparison of secondary

4.3 Results and Discussion – The interplay between (electro)chemical and (chemo)mechanical effects in the cycling performance of thiophosphate-based solid-state batteries

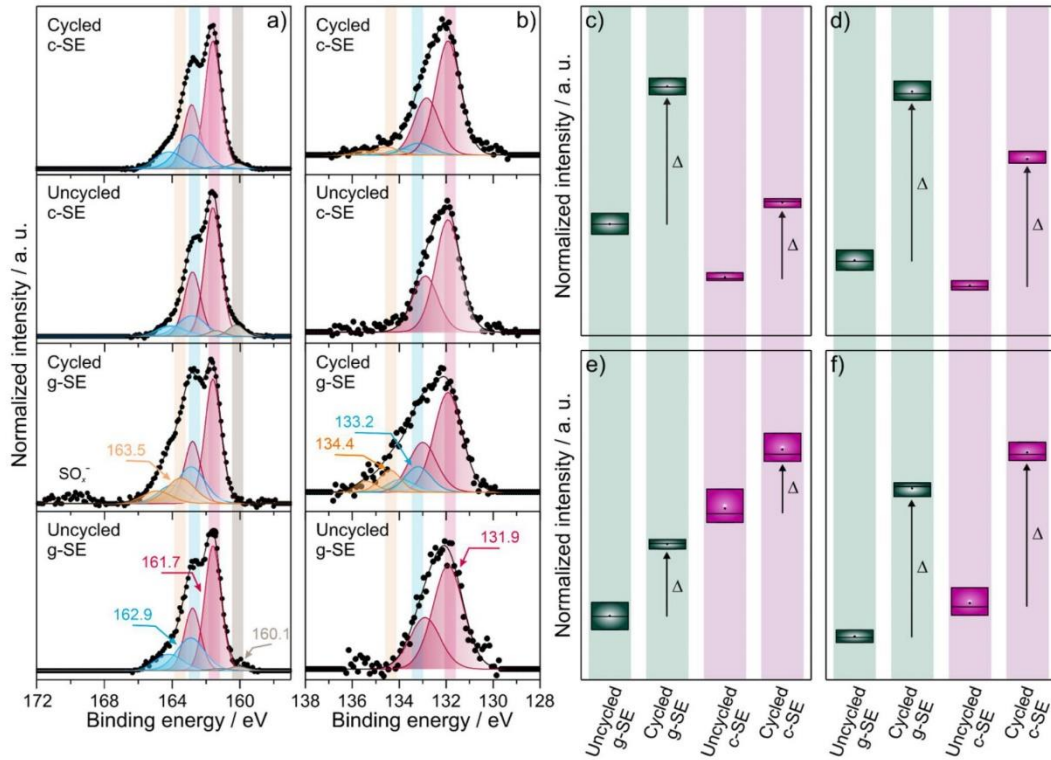


Figure 6. XP spectra of the (a) S 2p and (b) P 2p core levels of slurry-cast cathodes with glassy SE ($1.5\text{Li}_2\text{S}-0.5\text{P}_2\text{S}_5\text{-LiI}$) and crystalline SE ($\text{Li}_6\text{PS}_5\text{Cl}$) collected before and after 200 cycles at a rate of C/5 and 45°C . Box plots of the normalized intensity of (c) PO_2^- , (d) PO_3^- , (e) SO_2^- , and (f) SO_3^- fragments for the uncycled and cycled g-SE and c-SE cells from ToF-SIMS depth-profiling analysis.

ion intensities presupposes an identical chemical matrix. The matrix strongly determines the ionization probability and therefore the signal intensity of the charged fragments. Because SEs with a slightly different chemical composition were used in this study, a direct comparison of normalized intensities is not possible. For this reason, we considered the two systems independently, without comparing absolute values. Instead, the relative signal changes from uncycled to cycled cells were compared to assess differences in the degree of degradation. Figures 6(c)–(f) shows results from ToF-SIMS depth-profiling experiments. The first ten scans of the profiles were excluded in the evaluation to minimize detrimental effects of the current collector. The PO_x^- and SO_x^- fragments ($2 \leq x \leq 3$) increased in both cases upon cycling. A comparison of the relative signal increase (Δ) between the g-SE and c-SE cells revealed an increased oxygen-involving degradation for the cathode using the glassy SE. This is in line with the XPS and DEMS results. However, keeping in mind the Coulombic efficiency of the g-SE cell, the majority of the interfacial degradation products should have formed within the first few cycles. Moreover, they appear to be stable over the course of cycling.

Overall, the experimental data agree well with each other and point toward the fact that there is a more intimate contact between CAM and SE for the g-SE cell. Although interfacial reactions (as seen in the initial cycles for the g-SE cell)

are known to adversely affect the cell impedance, the contact loss (in the c-SE cell) apparently has a stronger effect on the battery performance. The favorable formation of stable ('self-limiting') interphases adds to the (chemo)mechanical stability in the g-SE cell by ensuring tight CAM/SE contact. Coupled with the already improved mechanical properties from the lower Young's modulus, this leads to a well-performing cell. In conclusion, the present work shows that (chemo)mechanical and (electro)chemical effects are mutually dependent and superimposed in the cycling data. If not considered carefully, this may lead to misleading interpretations.

2.7. Pushing the (Chemo)mechanical limit

The beneficial properties of the glassy SE can also provide similar stability to NCM CAMs with an even higher Ni content (exemplified here for NCM851005), which naturally experience larger relative volume changes during cycling ($\Delta V/V \approx -6.5\%$ at 4.4 V vs Li^+/Li for NCM851005 in LIBs) [10, 32]. The slurry-cast NCM851005 cell was cycled under identical conditions (C/5, 45°C) and in the same voltage range of 1.35–2.85 V vs $\text{Li}_4\text{Ti}_5\text{O}_{12}/\text{Li}_7\text{Ti}_5\text{O}_{12}$ (approximately 2.9–4.4 V vs Li^+/Li) as the slurry-cast NCM622 g-SE cell described above (figure 7). The first-cycle specific charge and discharge capacities were 210 and 177 mAh/g_{NCM851005} ($\sim 2.7 \text{ mAh cm}^{-2}$), respectively, corresponding to an initial

4.3 Results and Discussion – The interplay between (electro)chemical and (chemo)mechanical effects in the cycling performance of thiophosphate-based solid-state batteries

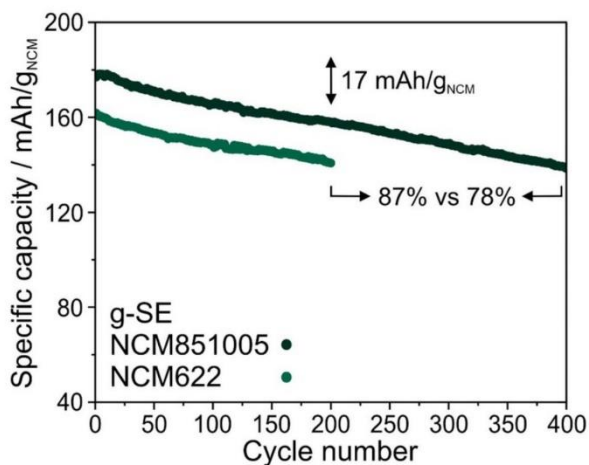


Figure 7. Cycling performance of SSB cells using a slurry-cast cathode with NCM622 (see also figure 1(a)) or NCM851005 and with glassy SE (1.5Li₂S-0.5P₂S₅-LiI). Cells tested at 45 °C, C/5, 2.9–4.4 V vs Li⁺/Li.

Coulombic efficiency of 84%. The cell was able to show an extremely competitive capacity retention of ~78% after 400 cycles (~2.1 mAh cm⁻²) with a fade rate per cycle of only 0.054%, compared to 0.065% for the NCM622 (over 200 cycles).

3. Conclusion

Herein, we have investigated the influence of a glassy (1.5Li₂S-0.5P₂S₅-LiI) and crystalline (Li₆PS₅Cl) thiophosphate SE on the cyclability of pelletized and slurry-cast SSB cells. We demonstrate that (chemo)mechanical and (electro)chemical effects contribute to the overall better performance for the glassy SE. These effects are interconnected and were elucidated by *ex situ* and *in situ* analytical techniques. The (chemo)mechanical effects were probed using pressure monitoring, for example, revealing an alternating increase/decrease in pressure during cycling (breathing of CAM), thus causing void/crack formation in case of the c-SE cell. In contrast, the g-SE cell exhibited signs of accommodating for such pressure changes, which seems highly beneficial to the cycling stability. Finally, gaseous and solid degradation products evolving at the CAM/SE interface were analyzed via DEMS, EIS, XPS, and ToF-SIMS. From these results, we conclude that the g-SE cell is more prone to interfacial degradation. However, given the excellent electrochemical performance, it is clear that the degradation products must be stable and sufficiently (ionically) conductive to allow for reversible battery operation [66].

Ultimately, considering all research data presented in this work, we state that for the studied compositions, the (chemo)mechanical benefits of a using a glassy SE outweigh the increased decomposition for the good of the SSB performance. The sacrifice in capacity over the first few cycles for

improved capacity retention shows that the composition of the as-formed CAM/SE interface is of prime importance and strongly dictates the cyclability.

4. Methods

4.1. Materials and synthesis

Cells were prepared using LiNbO₃-coated Li_{1+x}(Ni_{0.6}Co_{0.2}Mn_{0.2})_{1-x}O₂ (NCM622, BASF SE) or LiNbO₃-coated Li_{1+x}(Ni_{0.85}Co_{0.10}Mn_{0.05})_{1-x}O₂ (NCM851005, BASF SE) powder as CAM [25]. Two SEs, glassy 1.5Li₂S-0.5P₂S₅-LiI and argyrodite Li₆PS₅Cl (NEI Corp.), with room-temperature ionic conductivities of ~0.8 and 2 mS cm⁻¹, respectively, were used. Glassy 1.5Li₂S-0.5P₂S₅-LiI was synthesized by mixing stoichiometric amounts of Li₂S (99.9%, Sigma Aldrich), P₂S₅ (99%, Sigma Aldrich), and LiI (99.99%, Alfa Aesar) in a planetary ball-mill (Fritsch) under an Ar atmosphere for 12 h at 450 rpm using a 70 ml zirconia jar [29]. Li₆PS₅Cl was used as received. Polyisobutene (OPN, OPPANOL N 150, *M*_w = 3.1·10⁶ g mol⁻¹, BASF SE) was used as binder for the study. Super C65 carbon black (TIM-CAL) as an electronically conductive additive was dried at 300 °C in a vacuum overnight prior to use. LiNbO₃-coated NCM was prepared by coating a 1 wt.% sol-gel LiNbO₃ layer onto the pristine CAM [25]. Carbon-coated Li₄Ti₅O₁₂ (LTO, NEI Corp.) was used as AAM. All materials were handled and stored in an Ar-filled glovebox from MBraun ([O₂] < 0.1 ppm, [H₂O] < 0.5 ppm).

4.2. Preparation of pelletized electrode composites

The cathode composite was prepared by planetary mixing LiNbO₃-coated NCM622 with either glassy 1.5Li₂S-0.5P₂S₅-LiI or argyrodite Li₆PS₅Cl SE and Super C65 carbon black (7:3:0.1 weight ratio) under an Ar atmosphere for 30 min at 140 rpm [29]. The anode composite was prepared in a similar fashion by planetary mixing carbon-coated LTO with either glassy 1.5Li₂S-0.5P₂S₅-LiI or argyrodite Li₆PS₅Cl SE and Super C65 carbon black (3:6:1 weight ratio).

4.3. Preparation of cathode sheets

The cathode composite contained LiNbO₃-coated NCM622 (or LiNbO₃-coated NCM851005), Super C65, OPN, and either glassy 1.5Li₂S-0.5P₂S₅-LiI or argyrodite Li₆PS₅Cl SE. Their quantities were calculated to achieve an electrode with 1 wt.% polymer binder. Preparation of the cathode composite sheet involved a series of mixing steps, which are described in detail elsewhere [37]. The slurry was coated onto an Al foil with a mini-tape casting coater from MTI (300 μm doctor-blade slit size). Finally, the electrode was dried at room temperature in a two-step drying process. All chemicals and processing steps were handled in an Ar environment (Jacomex glovebox with [O₂] < 1.0 ppm and [H₂O] < 1.0 ppm).

4.3 Results and Discussion – The interplay between (electro)chemical and (chemo)mechanical effects in the cycling performance of thiophosphate-based solid-state batteries

4.4. Cell assembly and electrochemical testing

A customized setup was used for both the powder and slurry-cast cells. For the pelletized cell, 100 mg of SE was compressed at 125 MPa. Following, ~ 11 mg (~ 1.8 mAh cm $^{-2}$) of cathode composite was placed on top of the separator layer and subsequently compressed at 375 MPa. Lastly, 60 mg of anode composite was pressed onto the other side of the separator layer at 125 MPa (~ 200 μ m thickness). For the slurry-cast cell, both the sequence of assembly steps and the applied pressures were identical. The only difference was the cathode. Cathode sheet was punched out into a circular geometry (9 mm diameter; g-SE cell: ~ 3.5 mAh cm $^{-2}$, c-SE cell: ~ 3.2 mAh cm $^{-2}$) and placed on top of the separator layer. During electrochemical testing, a stack pressure of 80 MPa was maintained. Galvanostatic cycling was done at a rate of C/5 (1 C = 180 mA/g_{NCM622} or 190 mA/g_{NCM851005}) and 45 °C in the voltage range of 1.35–2.85 V vs Li₄Ti₅O₁₂/Li₇Ti₅O₁₂ using a MACCOR battery cycler. All cells were kept at 1 h open-circuit voltage (OCV) prior to cycling.

4.5. EIS

EIS measurements were conducted on cells after 200 cycles (C/5, 45 °C) using a SP-300 potentiostat (BioLogic). Spectra were collected in the frequency range between 100 mHz and 7.0 MHz with an AC voltage amplitude of 10 mV and fitted using the EC-lab software (BioLogic).

4.6. In situ pressure monitoring

After assembling the cell in the same customized setup used for electrochemical testing, it was packed in a pouch bag and removed from the glovebox. The rigid frame that was used to maintain the stack pressure was modified to accommodate an additional force sensor (KM26 10 kN, ME-Meßsysteme GmbH). The sealed cell with the force sensor was sandwiched within the custom frame and an initial pressure of 80 MPa was set. The stack was then placed in a heating chamber at 45 °C. Prior to the beginning of a similar galvanostatic charge/discharge measurement, a 24 h OCV period was maintained. This was done to allow enough time for the temperature-driven mechanical relaxation to occur and achieve a good baseline for the recording of stress response during cycling. The cell was cycled at a rate of C/5 in the voltage range of 1.35–2.85 V vs Li₄Ti₅O₁₂/Li₇Ti₅O₁₂ using a VMP3 multichannel potentiostat (BioLogic).

4.7. CV

CV measurements were conducted using the same setup described in the pressure-monitoring experiment. They were performed in the voltage range of OCV–2.85 V for the first cycle and 0–2.85 V vs Li₄Ti₅O₁₂/Li₇Ti₅O₁₂ for the subsequent cycles at a sweep rate of 0.05 mV s $^{-1}$ using a VMP3 multichannel potentiostat. The positive electrode consisted of either glassy 1.5Li₂S–0.5P₂S₅–LiI or argyrodite Li₆PS₅Cl SE and Super C65 carbon black with the weight ratio of 7.5:2.5.

The anode composite was similar to that used in the electrochemical measurements.

4.8. SEM

Cathode pellets/sheets were recovered from the cells in an Ar-filled glovebox. The samples were then mounted onto a sample holder using conductive carbon tape and probed using cross-sectional SEM at 10 kV.

4.9. DEMS

The cells consisted of a slurry-cast cathode, an SE pellet separator (glassy 1.5Li₂S–0.5P₂S₅–LiI or argyrodite Li₆PS₅Cl), and an In-foil anode. They were assembled in a method described in previous publications [37, 55]. Galvanostatic cycling was done at a rate of C/20 and 45 °C in the voltage range of 2.3–4.4 V vs In/InLi using a VMP3 multichannel potentiostat. A 10 h OCV period was included in the beginning to allow the cell to stabilize at the temperature and establish a proper background for the mass spectrometer. The flow of carrier gas (2.5 ml min $^{-1}$, 6.0 helium) was controlled by a mass flow controller (F-201CV, Bronkhorst). For gas analysis, a mass spectrometer (OmniStar GSD 320 O₂, Pfeiffer Vacuum GmbH) was used. After each measurement, a calibration gas was introduced to convert the measured ion currents into mol/g values.

4.10. XPS

XPS analysis was carried out with a PHI5000 Versa Probe II system (Physical Electronics GmbH). Analogous to previous studies, the samples were attached to the sample holder using nonconducting adhesive tape [27, 60, 61]. During the measurement, a dual-beam charge neutralization was applied. Additionally, depth profiling was done to clean the surface in order to reduce the influence of degradation processes at the current collector/SE interface. For analysis, a monochromatic Al-K α radiation (1486.6 eV) was used. The x-ray source was operated with a power of 50 W and voltage between 15 and 17 kV. The experimental data were evaluated using the software CasaXPS (version 2.3.22, Casa Software Ltd). The energy calibration was performed similarly to previous studies [27, 60, 63]. The XP spectra of all composite cathodes were calibrated in relation to the energetic signal position of the main component of the S 2p signal (PS₄ $^{3-}$) at 161.7 eV in order to avoid detrimental surface effects and misleading energy calibration when using the C 1s signal. The suitability of the energy calibration was verified with other main components of the SE. For signal fitting, Shirley background, GL(30) line shapes, and common fitting restrictions were applied [67].

4.11. ToF-SIMS

ToF-SIMS analysis was performed with a TOF.SIMS 5–100 system (IONTOF GmbH). It is equipped with a 25 keV Bi cluster primary-ion gun for analysis and a dual-source column, enabling depth profiling by using either O₂ $^{+}$ or Cs $^{+}$ (up to 2 keV). In addition, a FIB option can be used to mill craters

4.3 Results and Discussion – The interplay between (electro)chemical and (chemo)mechanical effects in the cycling performance of thiophosphate-based solid-state batteries

with monatomic gallium (30 keV). The samples were attached to the sample holder using nonconductive adhesive tape. The sample surface was flooded with low-energy electrons for charge compensation. All measurements were done in negative ion mode using Bi_3^+ species (25 keV) for analysis and a cycle time of 60 μs . Surface analysis was performed by operating the instrument in spectrometry mode (bunched mode). This mode enables high signal intensities and a high mass resolution [$\text{FWHM } m/\Delta m > 4500$ for $m/z = 31.97$ (S^-)], thereby minimizing effects of signal interferences in the mass spectra. The analysis area was set to $150 \times 150 \mu\text{m}^2$ and rasterized with 256×256 pixels. Every patch was analyzed with one frame and one shot per pixel and frame. For comparable measuring conditions, the analysis was stopped after a primary-ion dose of 1×10^{12} ions cm^{-2} (static conditions). The primary-ion current was ~ 0.5 pA. Ten mass spectra per sample were measured in different areas on the surface to alleviate area-dependent effects and ensure the reproducibility of results (increase statistics). The evaluation of ToF-SIMS data was done with the software SurfaceLab 7.0 (IONTOF GmbH). All secondary ion images were normalized in relation to the total ion signal to mitigate topographic effects. The signal intensities were extracted from the respective normalized secondary ion images.

Acknowledgments

This study was supported by BASF SE. F Strauss acknowledges financial support from the Fonds der Chemischen Industrie through a Liebig fellowship.

ORCID iD

Torsten Brezesinski  <https://orcid.org/0000-0002-4336-263X>

References

- [1] Blomgren G E 2017 *J. Electrochem. Soc.* **164** A5019–25
- [2] Tarascon J-M and Armand M 2001 *Nature* **414** 359–67
- [3] Larcher D and Tarascon J-M 2015 *Nat. Chem.* **7** 19–29
- [4] Wang Q, Ping P, Zhao X, Chu G, Sun J and Chen C 2012 *J. Power Sources* **208** 210–24
- [5] Etacheri V, Marom R, Elazari R, Salitra G and Aurbach D 2011 *Energy Environ. Sci.* **4** 3243–62
- [6] Janek J and Zeier W G 2016 *Nat. Energy* **1** 16141
- [7] Conforto G, Ruess R, Schröder D, Trevisanello E, Fantin R, Richter F H and Janek J 2021 *J. Electrochem. Soc.* **168** 070546
- [8] Ruess R, Schweidler S, Hemmelmann H, Conforto G, Bielefeld A, Weber D A, Sann J, Elm M T and Janek J 2020 *J. Electrochem. Soc.* **167** 100532
- [9] Ma Y, Teo J H, Kitsche D, Diemant T, Strauss F, Ma Y, Goonetilleke D, Janek J, Bianchini M and Brezesinski T 2021 *ACS Energy Lett.* **6** 3020–8
- [10] de Biasi L, Kondrakov A O, Geßwein H, Brezesinski T, Hartmann P and Janek J 2017 *J. Phys. Chem. C* **121** 26163–71
- [11] Jung S H, Kim U-H, Kim J-H, Jun S, Yoon C S, Jung Y S and Sun Y-K 2020 *Adv. Energy Mater.* **10** 1903360
- [12] Li W, Erickson E M and Manthiram A 2020 *Nat. Energy* **5** 26–34
- [13] Deng Z, Wang Z, Chu I-H, Luo J and Ong S P 2016 *J. Electrochem. Soc.* **163** A67–A74
- [14] McGrogan F P, Swamy T, Bishop S R, Eggleton E, Porz L, Chen X, Chiang Y-M and Van Vliet K J 2017 *Adv. Energy Mater.* **7** 1602011
- [15] Kato A, Yamamoto M, Sakuda A, Hayashi A and Tatsumisago M 2018 *ACS Appl. Energy Mater.* **1** 1002–7
- [16] Han F, Yue J, Zhu X and Wang C 2018 *Adv. Energy Mater.* **8** 1703644
- [17] Han Y, Jung S H, Kwak H, Jun S, Kwak H H, Lee J H, Hong S-T and Jung Y S 2021 *Adv. Energy Mater.* **11** 2100126
- [18] Koerver R, Aygün I, Leichtweiß T, Dietrich C, Zhang W, Binder J O, Hartmann P, Zeier W G and Janek J 2017 *Chem. Mater.* **29** 5574–82
- [19] Park K H, Bai Q, Kim D H, Oh D Y, Zhu Y, Mo Y and Jung Y S 2018 *Adv. Energy Mater.* **8** 1800035
- [20] Richards W D, Miara L J, Wang Y, Kim J C and Ceder G 2016 *Chem. Mater.* **28** 266–73
- [21] Wang S, Xu H, Li W, Dolocan A and Manthiram A 2018 *J. Am. Chem. Soc.* **140** 250–7
- [22] Takada K, Ohta N, Zhang L, Fukuda K, Sakaguchi I, Ma R, Osada M and Sasaki T 2008 *Solid State Ion.* **179** 1333–7
- [23] Ohta N, Takada K, Sakaguchi I, Zhang L, Ma R, Fukuda K, Osada M and Sasaki T 2007 *Electrochem. Commun.* **9** 1486–90
- [24] Machida N, Kashiwagi J, Naito M and Shigematsu T 2012 *Solid State Ion.* **225** 354–8
- [25] Kim A-Y, Strauss F, Bartsch T, Teo J H, Hatsukade T, Mazilkin A, Janek J, Hartmann P and Brezesinski T 2019 *Chem. Mater.* **31** 9664–72
- [26] Strauss F, Teo J H, Maibach J, Kim A-Y, Mazilkin A, Janek J and Brezesinski T 2020 *ACS Appl. Mater. Interfaces* **12** 57146–54
- [27] Walther F, Randau S, Schneider Y, Sann J, Rohnke M, Richter F H, Zeier W G and Janek J 2020 *Chem. Mater.* **32** 6123–36
- [28] Wang S et al 2021 *Adv. Energy Mater.* **11** 2100654
- [29] Strauss F, Teo J H, Janek J and Brezesinski T 2020 *Inorg. Chem. Front.* **7** 3953–60
- [30] Koerver R, Zhang W, de Biasi L, Schweidler S, Kondrakov A O, Kolling S, Brezesinski T, Hartmann P, Zeier W G and Janek J 2018 *Energy Environ. Sci.* **11** 2142–58
- [31] Shi T, Zhang Y-Q, Tu Q, Wang Y, Scott M C and Ceder G 2020 *J. Mater. Chem. A* **8** 17399–404
- [32] Strauss F, de Biasi L, Kim A-Y, Hertle J, Schweidler S, Janek J, Hartmann P and Brezesinski T 2020 *ACS Mater. Lett.* **2** 84–88
- [33] Reuter F, Baasner A, Pampel J, Piwko M, Dörfler S, Althues H and Kaskel S 2019 *J. Electrochem. Soc.* **166** A3265–A3271
- [34] Chen S, Zhang J, Nie L, Hu X, Huang Y, Yu Y and Liu W 2021 *Adv. Mater.* **33** 2002325
- [35] Minnmann P, Quillman L, Burkhardt S, Richter F H and Janek J 2021 *J. Electrochem. Soc.* **168** 040537
- [36] Kim M-J, Park J-W, Kim B G, Lee Y-J, Ha Y-C, Lee S-M and Baeg K-J 2020 *Sci. Rep.* **10** 11923
- [37] Teo J H, Strauss F, Tripković Đ, Schweidler S, Ma Y, Bianchini M, Janek J and Brezesinski T 2021 *Cell Rep. Phys. Sci.* **2** 100465
- [38] Zhang W, Schröder D, Arlt T, Manke I, Koerver R, Pinedo R, Weber D A, Sann J, Zeier W G and Janek J 2017 *J. Mater. Chem. A* **5** 9929–36
- [39] Zhang W et al 2017 *ACS Appl. Mater. Interfaces* **9** 17835–45
- [40] Sakuda A, Hayashi A and Tatsumisago M 2010 *Chem. Mater.* **22** 949–56

4.3 Results and Discussion – The interplay between (electro)chemical and (chemo)mechanical effects in the cycling performance of thiophosphate-based solid-state batteries

- [41] Ohzuku T, Ueda A and Yamamoto N 1995 *J. Electrochem. Soc.* **142** 1431–5
- [42] Wagemaker M, Simon D R, Kelder E M, Schoonman J, Ringpfeil C, Haake U, Lützenkirchen-Hecht D, Frahm R and Mulder F M 2006 *Adv. Mater.* **18** 3169–73
- [43] Haetge J, Hartmann P, Brezesinski K, Janek J and Brezesinski T 2011 *Chem. Mater.* **23** 4384–93
- [44] Sun G, Sui T, Song B, Zheng H, Lu L and Korsunsky A M 2016 *Extreme Mech. Lett.* **9** 449–58
- [45] Sakuda A, Hayashi A, Takigawa Y, Higashi K and Tatsumisago M 2013 *J. Ceram. Soc. Japan* **121** 946–9
- [46] Wang S et al 2021 *Adv. Energy Mater.* **11** 2101370
- [47] Ujiie S, Hayashi A and Tatsumisago M 2013 *J. Solid State Electrochem.* **17** 675–80
- [48] Ujiie S, Hayashi A and Tatsumisago M 2012 *Solid State Ion.* **211** 42–45
- [49] Auvergniot J, Cassel A, Ledeuil J-B, Viallet V, Seznec V and Dedryvère R 2017 *Chem. Mater.* **29** 3883–90
- [50] Bernhard R, Meini S and Gasteiger H A 2014 *J. Electrochem. Soc.* **161** A497–A505
- [51] Calpa M, Rosero-Navarro N C, Miura A, Jalem R, Tateyama Y and Tadanaga K 2021 *Appl. Mater. Today* **22** 100918
- [52] Jung R, Metzger M, Maglia F, Stinner C and Gasteiger H A 2017 *J. Electrochem. Soc.* **164** A1361–A1377
- [53] Jung R, Strobl P, Maglia F, Stinner C and Gasteiger H A 2018 *J. Electrochem. Soc.* **165** A2869–A2879
- [54] Bartsch T, Strauss F, Hatsukade T, Schiele A, Kim A-Y, Hartmann P, Janek J and Brezesinski T 2018 *ACS Energy Lett.* **3** 2539–43
- [55] Strauss F, Teo J H, Schiele A, Bartsch T, Hatsukade T, Hartmann P, Janek J and Brezesinski T 2020 *ACS Appl. Mater. Interfaces* **12** 20462–8
- [56] Wandt J, Freiberg A T S, Ogródnik A and Gasteiger H A 2018 *Mater. Today* **21** 825–33
- [57] Jung R, Metzger M, Maglia F, Stinner C and Gasteiger H A 2017 *J. Phys. Chem. Lett.* **8** 4820–5
- [58] Mahne N, Renfrew S E, McCloskey B D and Freunberger S A 2018 *Angew. Chem., Int. Ed.* **57** 5529–33
- [59] Hatsukade T, Schiele A, Hartmann P, Brezesinski T and Janek J 2018 *ACS Appl. Mater. Interfaces* **10** 38892–9
- [60] Walther F, Strauss F, Wu X, Mogwitz B, Hertle J, Sann J, Rohnke M, Brezesinski T and Janek J 2021 *Chem. Mater.* **33** 2110–25
- [61] Auvergniot J, Cassel A, Foix D, Viallet V, Seznec V and Dedryvère R 2017 *Solid State Ion.* **300** 78–85
- [62] Dietrich C, Koerver R, Gaultois M W, Kieslich G, Cibir G, Janek J and Zeier W G 2018 *Phys. Chem. Chem. Phys.* **20** 20088–95
- [63] Walther F, Koerver R, Fuchs T, Ohno S, Sann J, Rohnke M, Zeier W G and Janek J 2019 *Chem. Mater.* **31** 3745–55
- [64] Minami K, Hayashi A and Tatsumisago M 2010 *Solid State Ion.* **181** 1505–9
- [65] Franke R, Chassé T, Streubel P and Meisel A 1991 *J. Electron Spectrosc. Relat. Phenom.* **56** 381–8
- [66] Cronau M, Szabo M, König C, Wassermann T B and Roling B 2021 *ACS Energy Lett.* **6** 3072–7
- [67] Vizintin A, Lozinšek M, Chellappan R K, Foix D, Krajnc A, Mali G, Drazic G, Genorio B, Dedryvère R and Dominko R 2015 *Chem. Mater.* **27** 7070–81

Supporting information

The Interplay between (Electro)chemical and (Chemo)mechanical Effects in the Cycling Performance of Thiophosphate-based Solid-State Batteries

Jun Hao Teo,¹ Florian Strauss,¹ Felix Walther,² Yuan Ma,¹ Seyedhosein Payandeh,¹ Torsten Scherer,³ Matteo Bianchini,^{1,4} Jürgen Janek^{1,2,*} and Torsten Brezesinski^{1,*}

¹Battery and Electrochemistry Laboratory, Institute of Nanotechnology, Karlsruhe Institute of Technology (KIT), Hermann-von-Helmholtz-Platz 1, 76344 Eggenstein-Leopoldshafen, Germany.

²Institute of Physical Chemistry & Center for Materials Research, Justus-Liebig-University Giessen, Heinrich-Buff-Ring 17, 35392 Giessen, Germany.

³KNMF Laboratory for Micro- and Nanostructuring, Institute of Nanotechnology, Karlsruhe Institute of Technology (KIT), Hermann-von-Helmholtz-Platz 1, 76344 Eggenstein-Leopoldshafen, Germany.

⁴BASF SE, Carl-Bosch-Str. 38, 67056 Ludwigshafen, Germany.

*E-mail: juergen.janek@kit.edu, torsten.brezesinski@kit.edu

4.3 Results and Discussion – The interplay between (electro)chemical and (chemo)mechanical effects in the cycling performance of thiophosphate-based solid-state batteries

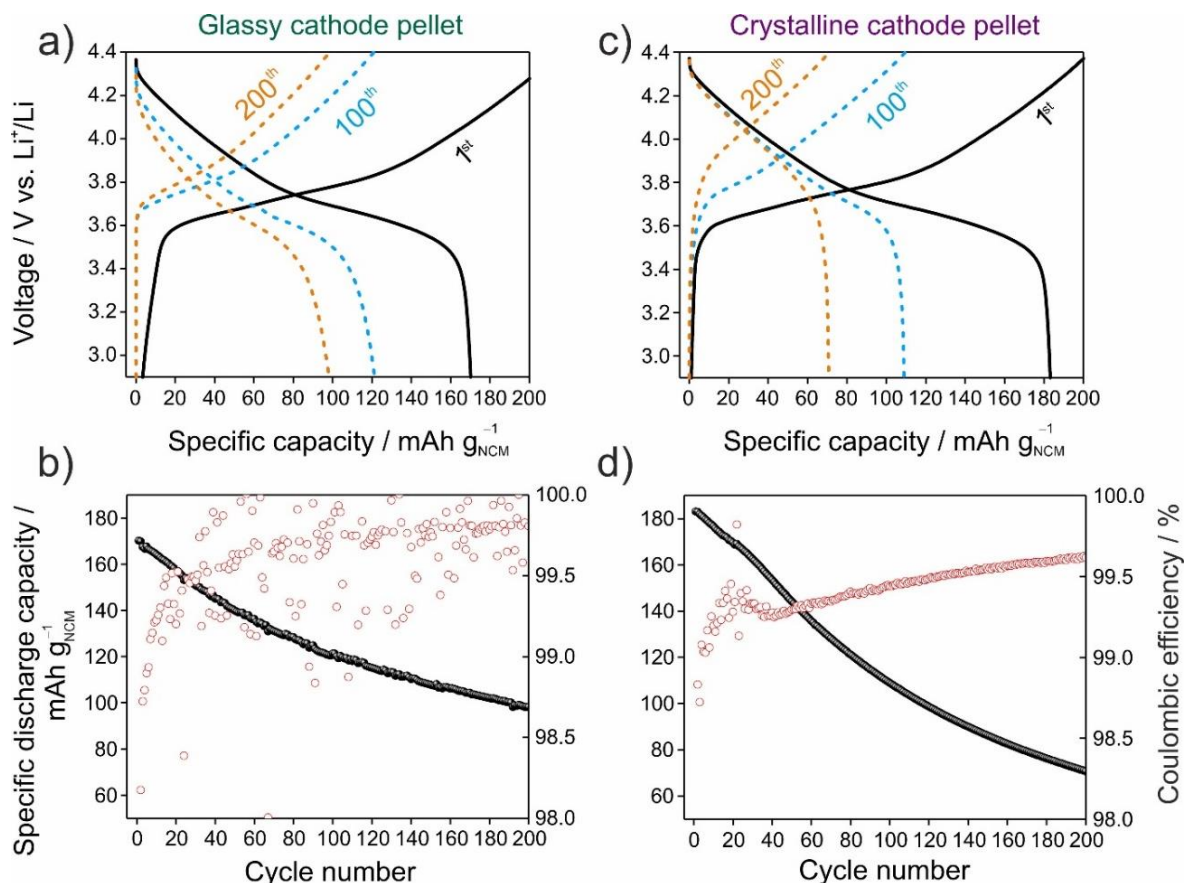


Figure S1. Representative 1st, 100th, and 200th cycle charge/discharge curves at a rate of C/5 and 45 °C of pelletized SSB cells with (a) glassy SE (1.5Li₂S-0.5P₂S₅-LiI) and (c) crystalline SE (Li₆PS₅Cl) and (b, d) corresponding specific discharge capacities and Coulombic efficiencies over 200 cycles.

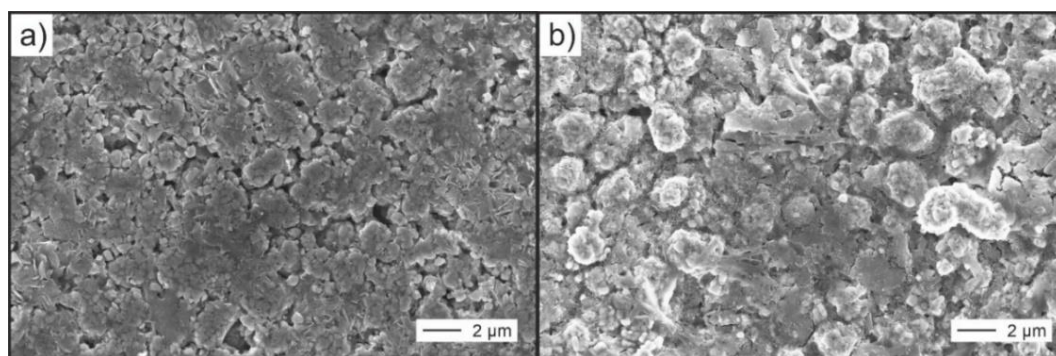


Figure S2. Top-view SEM images of the cathode of SSB cells in (a) pelletized and (b) slurry-cast setups.

4.3 Results and Discussion – The interplay between (electro)chemical and (chemo)mechanical effects in the cycling performance of thiophosphate-based solid-state batteries

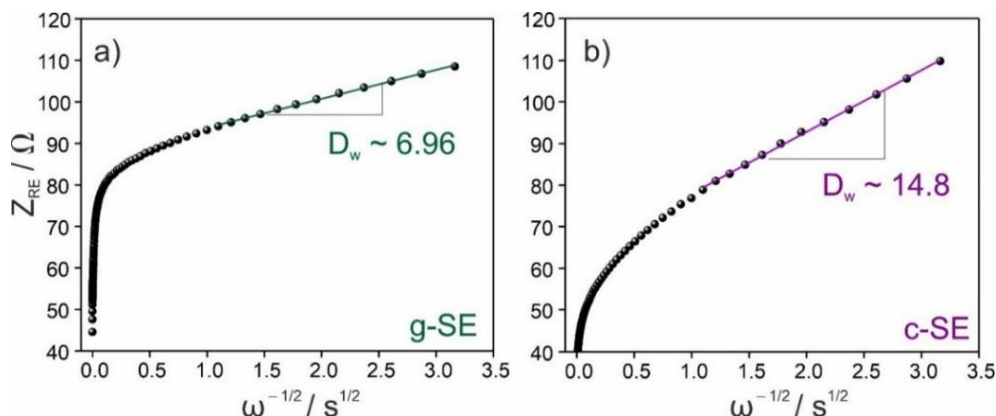


Figure S3. The real part of impedance data plotted versus the $(\text{frequency})^{-1/2}$ and corresponding linear fit at low frequencies for (a) the g-SE cell and (b) the c-SE cell after 200 cycles at a rate of C/5 and 45 °C.

The following equations correlate the Warburg coefficient to the contact area at the CAM/SE interface:^[1-3]

$$Z_{\text{RE}}(\omega) = R_{\text{SE}} + R_{\text{CT}} + D_{\text{W}} \cdot \frac{1}{\sqrt{\omega}} \quad (\text{Eq. S1}),$$

with $Z_{\text{RE}}(\omega)$ being the real part of the impedance, R_{SE} the SE bulk resistance, R_{CT} the charge-transfer resistance, D_{W} the Warburg coefficient, and ω the frequency.

$$D_{\text{W}} = \frac{RT}{n^2 F^2 A \sqrt{2}} \left(\frac{1}{c_i \sqrt{D_i}} \right) \quad (\text{Eq. S2})$$

R is the gas constant, T the absolute temperature, n the number of electrons exchanged in the redox process, F the Faraday constant, A the contact area, D_i the lithium-diffusion coefficient in the bulk electrode material, and c_i represents the concentration of lithium ions in the bulk electrode material.

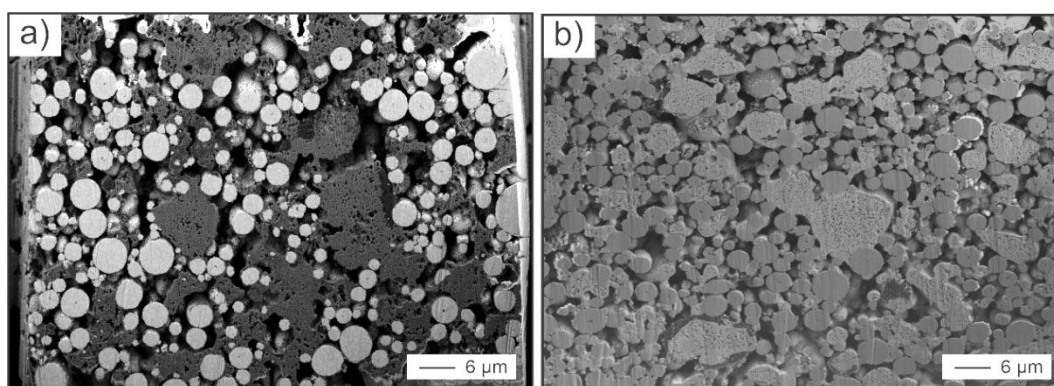


Figure S4. Cross-sectional FIB-SEM slice images of slurry-cast cathodes with (a) glassy SE ($1.5\text{Li}_2\text{S}-0.5\text{P}_2\text{S}_5\text{-LiI}$) and (b) crystalline SE ($\text{Li}_6\text{PS}_5\text{Cl}$). Note that the cathode was not cold-pressed prior to the measurement. More pores within the SE particles are

4.3 Results and Discussion – The interplay between (electro)chemical and (chemo)mechanical effects in the cycling performance of thiophosphate-based solid-state batteries

observed for the c-SE cell than the g-SE cell. Panel (a) shows a backscattered electron image and panel (b) is a secondary electron image.

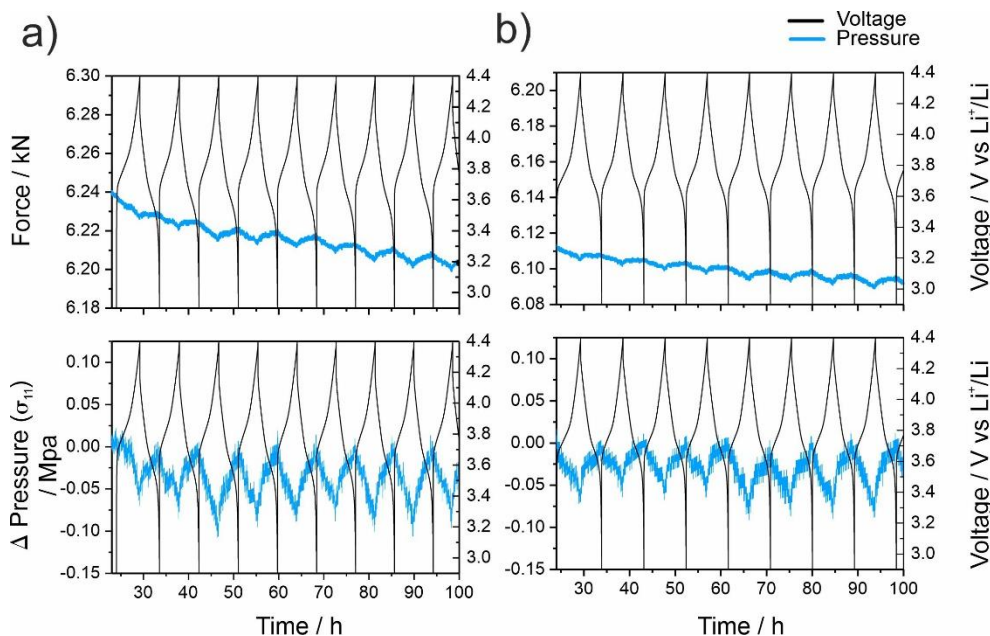
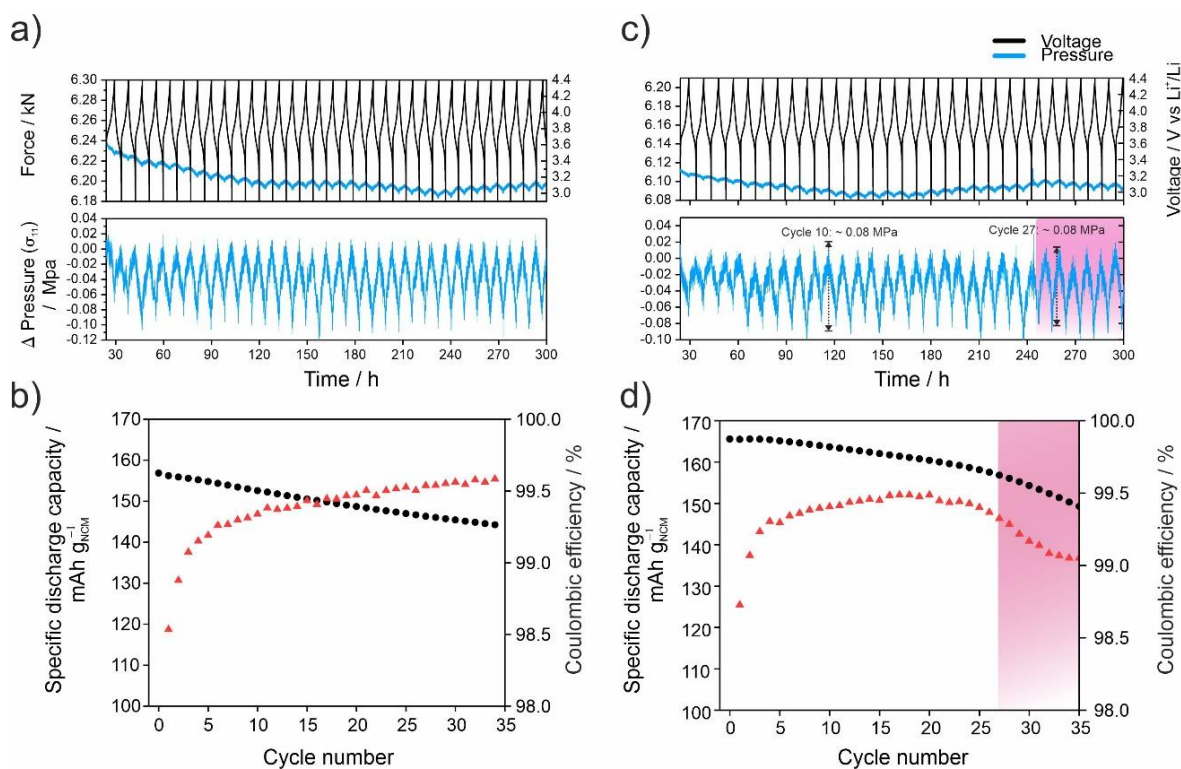


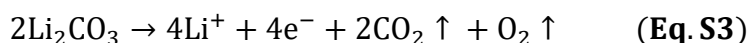
Figure S5. Raw data of the uniaxial force of slurry-cast cathodes with (a) glassy SE (1.5Li₂S-0.5P₂S₅-LiI) and (b) crystalline SE (Li₆PS₅Cl) recorded during cycling and the corresponding change in uniaxial stress (σ_{11}) after baseline correction. SSB cells tested at 45 °C, C/5, 2.9-4.4 V vs Li⁺/Li.



4.3 Results and Discussion – The interplay between (electro)chemical and (chemo)mechanical effects in the cycling performance of thiophosphate-based solid-state batteries

Figure S6. Force and pressure response during cycling of slurry-cast cathodes with (a) glassy SE (1.5Li₂S-0.5P₂S₅-LiI) and (c) crystalline SE (Li₆PS₅Cl) and (b, d) corresponding specific discharge capacities and Coulombic efficiencies over 35 cycles. SSB cells tested at 45 °C, C/5, 2.9-4.4 V vs Li⁺/Li.

Electrochemical decomposition of Li₂CO₃ impurities:



References

- [1] Wang S, Zhang W, Chen X, Das D, Reuss R, Gautam A, Walther F, Ohno S, Koerver R, Zhang Q, Zeier W G, F H Richter, Nan C-W and Janek J. 2021 *Adv. Energy Mater.* **11** 2100654.
- [2] Wang P-P, Xu C-Y, Li W-D, Wang L and Zhen L. 2015 *Electrochim. Acta* **169** 440-446.
- [3] Xiao P, Lv T, Chen X and Chang C. 2017 *Sci. Rep.* **7** 1408.

5. Conclusion and Outlook

The PhD project is centered around the primary use of differential electrochemical mass spectrometry (DEMS) under various unique experimental procedures to investigate SSB cells with a focus on the underlying degradation mechanisms during cycling aiming towards large-scale processing. In our study, we have systematically studied SSB cells from lab scale towards the transition phase towards large scale processing. A focus on coupling the DEMS analysis technique to various standard measurements such as XPS was performed at every stage of the systematic study. Therefore, the conclusion and outlook will be focused on sulfide based SSBs on manufacturability.

Summarizing the previous chapter, we have observed distinct differences in gassing trend between SSB and LIB cells. The cumulative amount of gas evolution from SSB cells are a magnitude of order lower than that of LIB cells largely due to the lack of a liquid electrolyte. It was seen that $^{12}\text{CO}_2$ release contributed to most of the gas evolution in LIB cells, which comes from both the electrochemical decomposition of Li_2CO_3 -passivation layer and the oxidation of the carbonate-based electrolyte with released reactive oxygen ($^1\text{O}_2$) from the NCM. The DEMS data was corroborated with acid titration studies which found a larger fraction of Li_2CO_3 remaining in the SSB cells. Despite low amounts of gas evolution, SSB cells with sulfide-based SE are prone to toxic H_2S and SO_2 gas release when exposed to moisture and reactive oxygen, respectively. However, the release of such gasses typically occurs only during manufacturing and formation cycles. H_2S is mostly never observed on a lab scale, in part because assembly and handling of the cells is performed in a glove box under inert atmosphere (Argon). However, in a series production, dry room environments with moisture levels > 0.1 ppm are common, thus H_2S release is unavoidable and must be removed through proper gas circulation. During battery operation, SO_2 can be suppressed to a certain extent, where the use of suitable coating chemistries are shown to suppress SO_2 evolution.⁹⁰ Furthermore, the amount of SO_2 release depends largely on the amount of released reactive oxygen ($^1\text{O}_2$) from the cathode (Ni-rich layered oxides) during cycling, which decreases rapidly after the formation cycles. Therefore, toxic gas evolution for SSBs can be easily removed during a battery formation process and would not be a problem during operation as long as the cell chemistries are not exposed to ambient conditions. On the topic of toxic gas evolution, this is also observed for LIB cells in the form of HF gas. The release of HF gas is intensified with higher temperatures or with mechanisms leading to cell failures. SSBs do not run the risk of failure-induced gas evolution except when the cell packaging has been subjected to mechanical damage, where moisture is introduced to the sulfur-based cell chemistry. During the initial part of our studies, we established improved safety from a gassing perspective by using DEMS and showed SSB cells possessing comparable electrochemical performance with SOTA LIBs. The next stage of our studies encompasses investigating the viability of transitioning SSB cell assembly from powder-based lab scale towards slurry-cast processing. The study showed that the

slurry-casting processes used to produce SOTA LIBs are viable for SSB production. The wet-chemical process enabled closer particle-particle contact between the solid components in the composite electrode, which was confirmed both by SEM images and improved electrochemical performances. Moreover, XRD analysis showed that wet-chemical processing with an appropriate choice of solvent and binder chemistries do not lead to degradation of both the CAM and the SE chemistries. Screening of parameters for wet-chemical processing is very time intensive, given the large number of variations available. One way of reducing the large amount of data sets required is the use of a simple statistical approach. Design-of-experiments (DoE) was employed to screen conductive carbon additives and different binder chemistries with a goal to optimize both the manufacturability and the electrochemical performance. In the DoE-guided approach, the straight chain alkyl Polyisobutene (Oppanol) was found to be the best performing largely due to its weaker chemical/physical interaction with the solid components in the cathode composite. Both styrene butadiene rubber (SBR) and hydrogenated nitrile butadiene rubber (hNBR) were shown to interact directly/indirectly to certain extents with either the solid electrolyte or the cathode active material, which led to poorer electrochemical performance. These interactions were observable indirectly from gas evolutions via DEMS. In the case of SBR, an enhanced CO_2 evolution indicated a reaction between the binder and singlet O_2 since it was the only investigated binder chemistry with alkene chains (units). For hNBR, an enhanced SO_2 evolution suggested a destabilization of the sulfur-based SE structure, making it more susceptible to chemical reactions with the released singlet O_2 . These observations highlighted the importance of DEMS as an analytical tool in different stages of battery research from an initial investigation on safety and degradation reactions to the screening of parameters needed for production upscaling. The DoE approach allowed us to produce robust electrode sheets and could be further used to further optimize other components in the SSB cells. For example, the choice of SE is intensively studied and there are a variety of chemistries available (polymers, oxides, and sulfides). Through such a statistical approach, SSB cells with Li-anode compatibility or high (chemo)mechanical stability could be realized because of material optimization. Such a chemo-mechanical stable SE was observed in the later part of our studies with a glassy SE. The choice of a glassy SE was an attempt in improving the cycling stability of SSB, which has shown poor capacity retention among crystalline SE in our studies. The cells with a glassy SE exhibited exceptional cycling stability in part due to an improved interfacial formation that possesses both a high (electro)chemical and (chemo)mechanical stability. The use of a DoE approach would eliminate discoveries by chance and promote a more systematical approach towards material discoveries. One of the reasons for the poor cycling stability was the crystalline nature of the SE and its poor mechanical properties to suppress the volume changes of the CAM during cycling. The use of a glassy SE was able to show improved electrochemical performance, in part due to improved interfacial formation and having a low modulus. The improved interfacial formation was verified by a combination of analytical techniques, DEMS included. First cross-sectional SEM images showed lesser void formations. Following which, DEMS showed a larger amount of molecular O_2 evolution

for the crystalline SE, while the glassy SE showed less than half of that. The larger O₂ evolution for crystalline SE was attributed to more distance (voids) between the CAM and the SE, which allowed a higher fraction of singlet oxygen to physically decay to its molecular state. Further corroborations with XPS and ToF-SIMS analysis also showed increased degradation reactions for the glassy SE in the form of oxidized sulfur and phosphor species, which is an indication of closer particle-particle contact between the CAM and the SE. The improvement of cycling stability is an important stage towards commercialization, since according to automotive standards, at least 1000 cycles are required.^{91,92} Even at this stage of SSB research, DEMS has shown its versatility as an analysis technique. In conclusion, further research needs to be conducted on the anode side to achieve a fully casted cell. Attempts have been made with LTO sheets, however due to its low content in the anode composite, balancing with the cathode side required thick LTO sheets. This resulted in poor electrochemical performance. There have been newly published approaches to the anode side for SSB, specifically the use of Si anodes or Li metal anodes. Recently, Meng *et al.* reported the use of Si anodes successfully in sulfide based SSB with excellent electrochemical performance.⁹³ With regards to Li metal anode in SSBs, companies such as QuantumScape (oxide-based) and Solid Power (sulfide-based) have individually reported cycling performance with Li metal anodes.^{16,94} After decades of concentrated research on the cathode side, the anode side is currently the limiting factor to achieve cost- and performance-competitiveness against SOTA LIBs. DEMS could play a role as well in this stage of SSB commercialization and be able to provide new insights and validations to other analysis techniques.

Equations

$$XY + e \rightarrow XY + \bullet + e - \quad (2.2.1) \dots 19$$

$$XY + e \rightarrow XYn + \bullet + (n + 1)e - \quad (2.2.2) \dots 19$$

$$XY + e \rightarrow Xn + Y \bullet + (n + 1)e - \quad (2.2.3) \dots 19$$

$$XY + e \rightarrow X + Y - + e - \quad (2.2.4) \dots 19$$

$$\Phi(x, y) = \frac{(x^2 - y^2)(U - V \cos \omega t)}{r_0^2} \quad (2.2.5) \dots 20$$

$$\vec{F} = m\vec{a} = -ze\vec{\nabla}\Phi \quad (2.2.6) \dots 20$$

$$m\vec{a} = -ze\vec{\nabla}\Phi$$

$$\rightarrow F_x = m \frac{d^2x}{dt^2} = -ze \frac{\partial \Phi}{\partial x} \quad \rightarrow F_y = m \frac{d^2y}{dt^2} = -ze \frac{\partial \Phi}{\partial y} \quad (2.2.7) \dots 21$$

$$\frac{d^2x}{dt^2} + \frac{2ez}{mr_0^2}(U - V \cos \omega t)x = 0 \quad \frac{d^2y}{dt^2} - (a_y - 2q_y \cos 2\tau)y = 0 \quad (2.2.8) \dots 21$$

$$\frac{d^2x}{d\tau^2} + (a_x - 2q_x \cos 2\tau)x = 0 \quad \frac{d^2y}{d\tau^2} - (a_y - 2q_y \cos 2\tau)y = 0 \quad (2.2.9) \dots 21$$

$$a_x = -a_y = \frac{8zeU}{m_i \omega^2 r_0^2} \quad q_x = -q_y = \frac{4zeV}{m_i \omega^2 r_0^2} \quad \tau = \frac{\omega t}{2} \quad (2.2.10) \dots 21$$

$$U = a_x \left(\frac{m_i}{z} \right) \frac{\omega^2 r_0^2}{8e} \quad V = q_x \left(\frac{m_i}{z} \right) \frac{\omega^2 r_0^2}{4e} \quad (2.2.11) \dots 21$$

Figures

Figure 1.1 Graphical representation of a conventional liquid-base LIB (left) and a solid-state LIB (right).	4
Figure 1.2 Representative 1 st cycle voltage profiles for common layered transition metal oxides with LCO represented in black, NCM111 in red, NCM622 in green, NCM851005 in blue and LNO in orange. The cells are cycled in a liquid-based LIB against a Li metal anode at C/10 and 25°C in the voltage range 3.0 – 4.3 V. LP5 was used as the liquid electrolyte.	9
Figure 1.3 Unit cell of the layered transition metal oxide [Li(TM)O ₂] with crystal structure <i>R3m</i> .	10
Figure 1.4 Unit cell of spinel Li ₄ Ti ₅ O ₁₂ with crystal structure <i>Fd3m</i> .	12
Figure 1.5 Voltage profile of Li _{4+x} Ti ₅ O ₁₂ as it transitions from spinel-Li ₄ Ti ₅ O ₁₂ to rock-salt-Li ₇ Ti ₅ O ₁₂ with graphical representation of the transformation (starting at the outermost surface inwards).	13
Figure 2.1 Graphical representation of the DEMS setup. The individual components are labeled accordingly. ⁴⁸	15
Figure 2.2 Modified design of the DEMS cell design for use in SSB-DEMS analysis. Flow of the carrier gas and the evolved gas during cycling is indicated.	17
Figure 2.3 Representative O ₂ , ¹³ CO ₂ and ¹² CO ₂ gas evolution of two thiophosphate-based SSB (Li ₆ PS ₅ Cl and β-Li ₃ PS ₄) in both the old (free-standing) and new (sandwich in PEEK) setup	18
Figure 2.4 Photograph of the ionization chamber (left) and the linear quadrupole/mass filter (right) used in the mass spectrometer Omnistar GSD320	20
Figure 2.5 Photograph of the secondary electron multiplier (SEM) used in the mass spectrometer Omnistar GSD320	22
Figure 3.1 Photographs of Li ₆ PS ₅ Cl SE dissolved in various solvents with decreasing polarity index (from a to f). The degree of degradation and instability of the Li ₆ PS ₅ Cl SE is directly correlated to the intensity of color change of both the suspension and the SE powder. The panels show the dissolution of the SE in (a) methanol, (b) ethanol, (c) pyridine, (d) 2-propanol, (e) o-xylene and (f) heptane. The study was carried out under in a glovebox (Ar-atmosphere, [O ₂] < 0.1 ppm, [H ₂ O] < 0.5 ppm).	28
Figure 3.2 XRD patterns of the Li ₆ PS ₅ Cl SE (black), CAM (NCM851005) (purple), cathode composite before solvent treatment (red) and after treatment (orange).	29
Figure 3.3 Single-blade (left) versus double-blade (right) doctor blades. (a) The height of the reservoir (H ₀) decreases as the slurry gets used up, resulting in an irregular pressure-driven flow. (b) Height H is maintained even as the slurry is depleted, reducing the effect of irregular pressure-driven flow.	32
Figure 3.4 Representative Nyquist plots of Li ₃ PS ₄ powder (BASF) exposed to dry-room conditions for different duration. The measured Li-ion conductivity provided by BASF was 0.13 mS/cm. After exposure to the glovebox environment (0 min), the conductivity was measured at 0.08 mS/cm. Only after 30 min, do we start to see a change in ionic conductivity that cannot be explained by measurement variance. The Li-ion conductivity of the SE powder was performed with a symmetric cell with stainless-steel current collectors under a stack pressure of 226 Pa (Diameter of cell = 10mm).	35

Bibliography

1. International Energy Agency, <https://www.iea.org/countries/germany>.
2. 'Dieselgate' - a timeline of the car emissions fraud scandal in Germany.
3. Uitz, M. *et al.* Aging of Tesla's 18650 Lithium-Ion Cells: Correlating Solid-Electrolyte-Interphase Evolution with Fading in Capacity and Power. *J. Electrochem. Soc.* **164**, A3503–A3510 (2017).
4. Blomgren, G. E. The Development and Future of Lithium Ion Batteries. *J. Electrochem. Soc.* **164**, A5019–A5025 (2017).
5. Myung, S.-T. *et al.* Nickel-Rich Layered Cathode Materials for Automotive Lithium-Ion Batteries: Achievements and Perspectives. *ACS Energy Lett.* **2**, 196–223 (2017).
6. Han, X. *et al.* A review on the key issues of the lithium ion battery degradation among the whole life cycle. *eTransportation* **1**, 100005 (2019).
7. Janek, J. & Zeier, W. G. A solid future for battery development. *Nat. Energy* **1**, 16141 (2016).
8. *Lithium-ion batteries: basics and applications*. (Springer Berlin Heidelberg, 2017).
9. Xu, W. *et al.* Lithium metal anodes for rechargeable batteries. *Energy Env. Sci* **7**, 513–537 (2014).
10. Aurbach, D. A short review of failure mechanisms of lithium metal and lithiated graphite anodes in liquid electrolyte solutions. *Solid State Ion.* **148**, 405–416 (2002).
11. Qian, J. *et al.* High rate and stable cycling of lithium metal anode. *Nat. Commun.* **6**, 6362 (2015).
12. Schnell, J. *et al.* All-solid-state lithium-ion and lithium metal batteries – paving the way to large-scale production. *J. Power Sources* **382**, 160–175 (2018).
13. Richards, W. D., Miara, L. J., Wang, Y., Kim, J. C. & Ceder, G. Interface Stability in Solid-State Batteries. *Chem. Mater.* **28**, 266–273 (2016).
14. Zhu, Y., He, X. & Mo, Y. Origin of Outstanding Stability in the Lithium Solid Electrolyte Materials: Insights from Thermodynamic Analyses Based on First-Principles Calculations. *ACS Appl. Mater. Interfaces* **7**, 23685–23693 (2015).
15. Manuel Stephan, A. & Nahm, K. S. Review on composite polymer electrolytes for lithium batteries. *Polymer* **47**, 5952–5964 (2006).
16. Solid Power Analyst Day Presentation.
17. Hartmann, P. *et al.* Degradation of NASICON-Type Materials in Contact with Lithium Metal: Formation of Mixed Conducting Interphases (MCI) on Solid Electrolytes. *J. Phys. Chem. C* **117**, 21064–21074 (2013).
18. Han, X. *et al.* A review on the key issues of the lithium ion battery degradation among the whole life cycle. *eTransportation* **1**, 100005 (2019).
19. Chen, S. *et al.* Sulfide solid electrolytes for all-solid-state lithium batteries: Structure, conductivity, stability and application. *Energy Storage Mater.* **14**, 58–74 (2018).
20. Sakuda, A., Hayashi, A. & Tatsumisago, M. Sulfide Solid Electrolyte with Favorable Mechanical Property for All-Solid-State Lithium Battery. *Sci. Rep.* **3**, 2261 (2013).
21. Han, Y. *et al.* Single- or Poly-Crystalline Ni-Rich Layered Cathode, Sulfide or Halide Solid Electrolyte: Which Will be the Winners for All-Solid-State Batteries? *Adv. Energy Mater.* **11**, 2100126 (2021).
22. Nitta, N., Wu, F., Lee, J. T. & Yushin, G. Li-ion battery materials: present and future. *Mater. Today* **18**, 252–264 (2015).
23. Glaize, C. *lithium batteries and other electrochemical storage systems*. (ISTE Wiley, 2013).
24. Mizushima, K., Jones, P. C., Wiseman, P. J. & Goodenough, J. B. Li_xCoO_2 ($0 < x < 1$): A new cathode material for batteries of high energy density. *Mater. Res. Bull.* **15**, 783–789 (1980).

25. Chen, Z., Lu, Z. & Dahn, J. R. Staging Phase Transitions in $\text{Li}_{\text{x}}\text{CoO}_2$. *J. Electrochem. Soc.* **149**, A1604 (2002).
26. Lee, K. T., Jeong, S. & Cho, J. Roles of Surface Chemistry on Safety and Electrochemistry in Lithium Ion Batteries. *Acc. Chem. Res.* **46**, 1161–1170 (2013).
27. Bianchini, M., Roca-Ayats, M., Hartmann, P., Brezesinski, T. & Janek, J. There and Back Again—The Journey of LiNiO_2 as a Cathode Active Material. *Angew. Chem. Int. Ed.* **58**, 10434–10458 (2019).
28. Yoon, C. S., Jun, D.-W., Myung, S.-T. & Sun, Y.-K. Structural Stability of LiNiO_2 Cycled above 4.2 V. *ACS Energy Lett.* **2**, 1150–1155 (2017).
29. Li, W., Reimers, J. & Dahn, J. In situ x-ray diffraction and electrochemical studies of $\text{Li}_{1-\text{x}}\text{NiO}_2$. *Solid State Ion.* **67**, 123–130 (1993).
30. Koerver, R. *et al.* Chemo-mechanical expansion of lithium electrode materials – on the route to mechanically optimized all-solid-state batteries. *Energy Environ. Sci.* **11**, 2142–2158 (2018).
31. Dahn, J., Fuller, E., Obrovac, M. & Vonsacken, U. Thermal stability of $\text{Li}_\text{x}\text{CoO}_2$, $\text{Li}_\text{x}\text{NiO}_2$ and $\lambda\text{-MnO}_2$ and consequences for the safety of Li-ion cells. *Solid State Ion.* **69**, 265–270 (1994).
32. Noh, H.-J., Youn, S., Yoon, C. S. & Sun, Y.-K. Comparison of the structural and electrochemical properties of layered $\text{Li}[\text{Ni}_\text{x}\text{Co}_\text{y}\text{Mn}_\text{z}]\text{O}_2$ ($\text{x} = 1/3, 0.5, 0.6, 0.7, 0.8$ and 0.85) cathode material for lithium-ion batteries. *J. Power Sources* **233**, 121–130 (2013).
33. Sun, Y.-K. *et al.* Nanostructured high-energy cathode materials for advanced lithium batteries. *Nat. Mater.* **11**, 942–947 (2012).
34. de Biasi, L. *et al.* Between Scylla and Charybdis: Balancing Among Structural Stability and Energy Density of Layered NCM Cathode Materials for Advanced Lithium-Ion Batteries. *J. Phys. Chem. C* **121**, 26163–26171 (2017).
35. Akimoto, J., Gotoh, Y. & Oosawa, Y. Synthesis and Structure Refinement of LiCoO_2 Single Crystals. *J. Solid State Chem.* **141**, 298–302 (1998).
36. Ohzuku, T., Ueda, A. & Nagayama, M. Electrochemistry and Structural Chemistry of LiNiO_2 (R3m) for 4 Volt Secondary Lithium Cells. *J. Electrochem. Soc.* **140**, 1862–1870 (1993).
37. *Handbuch lithium-ionen-batterien.* (Springer Berlin Heidelberg, 2013).
38. Schiele, A., Sommer, H., Brezesinski, T., Janek, J. & Berkes, B. B. Differential Electrochemical Mass Spectrometry in Lithium Battery Research. in *Encyclopedia of Interfacial Chemistry* 44–53 (Elsevier, 2018). doi:10.1016/B978-0-12-409547-2.13293-7.
39. Bruckenstein, S. & Comeau, J. Electrochemical mass spectrometry. Part 1.—Preliminary studies of propane oxidation on platinum. *Faraday Discuss Chem Soc* **56**, 285–292 (1973).
40. Bruckenstein, S. & Gadde, R. R. Use of a porous electrode for in situ mass spectrometric determination of volatile electrode reaction products. *J. Am. Chem. Soc.* **93**, 793–794 (1971).
41. Wolter, O. & Heitbaum, J. Differential Electrochemical Mass Spectroscopy (DEMS) - a New Method for the Study of Electrode Processes. *Berichte Bunsenges. Für Phys. Chem.* **88**, 2–6 (1984).
42. Novák, P. *et al.* Advanced in situ characterization methods applied to carbonaceous materials. *J. Power Sources* **146**, 15–20 (2005).
43. Peng, Z., Freunberger, S. A., Chen, Y. & Bruce, P. G. A Reversible and Higher-Rate Li-O₂ Battery. *Science* **337**, 563–566 (2012).

44. McCloskey, B. D., Bethune, D. S., Shelby, R. M., Girishkumar, G. & Luntz, A. C. Solvents' Critical Role in Nonaqueous Lithium–Oxygen Battery Electrochemistry. *J. Phys. Chem. Lett.* **2**, 1161–1166 (2011).
45. Tsiouvaras, N., Meini, S., Buchberger, I. & Gasteiger, H. A. A Novel On-Line Mass Spectrometer Design for the Study of Multiple Charging Cycles of a Li-O₂ Battery. *J. Electrochem. Soc.* **160**, A471–A477 (2013).
46. Metzger, M., Marino, C., Sicklinger, J., Haering, D. & Gasteiger, H. A. Anodic Oxidation of Conductive Carbon and Ethylene Carbonate in High-Voltage Li-Ion Batteries Quantified by On-Line Electrochemical Mass Spectrometry. *J. Electrochem. Soc.* **162**, A1123–A1134 (2015).
47. Metzger, M., Strehle, B., Solchenbach, S. & Gasteiger, H. A. Origin of H₂ Evolution in LIBs: H₂O Reduction vs. Electrolyte Oxidation. *J. Electrochem. Soc.* **163**, A798–A809 (2016).
48. Berkes, B. B. *et al.* Online Continuous Flow Differential Electrochemical Mass Spectrometry with a Realistic Battery Setup for High-Precision, Long-Term Cycling Tests. *Anal. Chem.* **87**, 5878–5883 (2015).
49. Gross, J. H. *Mass Spectrometry: A Textbook*. (Springer International Publishing : Imprint: Springer, 2017). doi:10.1007/978-3-319-54398-7.
50. Mark, T. D. Fundamental aspects of electron impact ionization. *Int. J. Mass Spectrom. Ion Phys.* **45**, 125–145 (1982).
51. Lee, K. *et al.* Selection of Binder and Solvent for Solution-Processed All-Solid-State Battery. *J. Electrochem. Soc.* **164**, A2075–A2081 (2017).
52. Gong, K., Fang, Q., Gu, S., Li, S. F. Y. & Yan, Y. Nonaqueous redox-flow batteries: organic solvents, supporting electrolytes, and redox pairs. *Energy Environ. Sci.* **8**, 3515–3530 (2015).
53. Izutsu, K. *Electrochemistry in nonaqueous solutions*. (Wiley-VCH, 2009).
54. Schirmer, R. E. *Modern methods of pharmaceutical analysis*. (CRC Press, 1991).
55. Snyder, L. R. Classification off the Solvent Properties of Common Liquids. *J. Chromatogr. Sci.* **16**, 223–234 (1978).
56. Riphaut, N. *et al.* Slurry-Based Processing of Solid Electrolytes: A Comparative Binder Study. *J. Electrochem. Soc.* **165**, A3993–A3999 (2018).
57. Ruhl, J., Riegger, L. M., Ghidui, M. & Zeier, W. G. Impact of Solvent Treatment of the Superionic Argyrodite Li₆PS₅Cl on Solid-State Battery Performance. *Adv. Energy Sustain. Res.* **2**, 2000077 (2021).
58. Yamamoto, M., Terauchi, Y., Sakuda, A. & Takahashi, M. Binder-free sheet-type all-solid-state batteries with enhanced rate capabilities and high energy densities. *Sci. Rep.* **8**, 1212 (2018).
59. Kun, R. *et al.* Structural and Computational Assessment of the Influence of Wet-Chemical Post-Processing of the Al-Substituted Cubic Li₇La₃Zr₂O₁₂. *ACS Appl. Mater. Interfaces* **10**, 37188–37197 (2018).
60. Ye, R. *et al.* Water-based fabrication of garnet-based solid electrolyte separators for solid-state lithium batteries. *Green Chem.* **22**, 4952–4961 (2020).
61. Yi, E., Wang, W., Kieffer, J. & Laine, R. M. Key parameters governing the densification of cubic-Li₇La₃Zr₂O₁₂ Li⁺ conductors. *J. Power Sources* **352**, 156–164 (2017).
62. Kasinathan, R., Marinaro, M., Axmann, P. & Wohlfahrt-Mehrens, M. Influence of the Molecular Weight of Poly-Acrylic Acid Binder on Performance of Si-Alloy/Graphite Composite Anodes for Lithium-Ion Batteries. *Energy Technol.* **6**, 2256–2263 (2018).
63. Chen, K. *et al.* Morphological Effect on Reaction Distribution Influenced by Binder Materials in Composite Electrodes for Sheet-type All-Solid-State Lithium-Ion

- Batteries with the Sulfide-based Solid Electrolyte. *J. Phys. Chem. C* **123**, 3292–3298 (2019).
64. Wujcik, K. H. *et al.* Lithium Polysulfide Radical Anions in Ether-Based Solvents. *J. Phys. Chem. C* **120**, 18403–18410 (2016).
 65. Haarmann, M., Griebl, D. & Kwade, A. Continuous Processing of Cathode Slurry by Extrusion for Lithium-Ion Batteries. *Energy Technol.* **9**, 2100250 (2021).
 66. Nam, Y. J., Oh, D. Y., Jung, S. H. & Jung, Y. S. Toward practical all-solid-state lithium-ion batteries with high energy density and safety: Comparative study for electrodes fabricated by dry- and slurry-mixing processes. *J. Power Sources* **375**, 93–101 (2018).
 67. Ates, T., Keller, M., Kulisch, J., Adermann, T. & Passerini, S. Development of an all-solid-state lithium battery by slurry-coating procedures using a sulfidic electrolyte. *Energy Storage Mater.* **17**, 204–210 (2019).
 68. Nam, Y. J. *et al.* Bendable and Thin Sulfide Solid Electrolyte Film: A New Electrolyte Opportunity for Free-Standing and Stackable High-Energy All-Solid-State Lithium-Ion Batteries. *Nano Lett.* **15**, 3317–3323 (2015).
 69. Tok, A. I. Y., Boey, F. Y. C. & Lam, Y. C. Non-Newtonian fluid flow model for ceramic tape casting. *Mater. Sci. Eng. A* **280**, 282–288 (2000).
 70. Jabbari, M., Bulatova, R., Hattel, J. H. & Bahl, C. R. H. Quasi-steady state power law model for flow of $(\text{La}_{0.85}\text{Sr}_{0.15})_{0.9}\text{MnO}_3$ ceramic slurry in tape casting. *Mater. Sci. Technol.* **29**, 1080–1087 (2013).
 71. Mistler, R. E. & Twiname, E. R. *Tape casting: theory and practice*. (American Ceramic Society, 2000).
 72. Bulatova, R. *et al.* The effect of tape casting operational parameters on the quality of adjacently graded ceramic film. *Ceram. Int.* **42**, 4663–4671 (2016).
 73. Bulatova, R. *et al.* Thickness control and interface quality as functions of slurry formulation and casting speed in side-by-side tape casting. *J. Eur. Ceram. Soc.* **34**, 4285–4295 (2014).
 74. Zhang, G., Wang, Y. & Ma, J. Bingham plastic fluid flow model for ceramic tape casting. *Mater. Sci. Eng. A* **337**, 274–280 (2002).
 75. Kumberg, J. *et al.* Drying of Lithium-Ion Battery Anodes for Use in High-Energy Cells: Influence of Electrode Thickness on Drying Time, Adhesion, and Crack Formation. *Energy Technol.* **7**, 1900722 (2019).
 76. Font, F., Protas, B., Richardson, G. & Foster, J. M. Binder migration during drying of lithium-ion battery electrodes: Modelling and comparison to experiment. *J. Power Sources* **393**, 177–185 (2018).
 77. Jaiser, S. *et al.* Investigation of film solidification and binder migration during drying of Li-Ion battery anodes. *J. Power Sources* **318**, 210–219 (2016).
 78. Baunach, M. *et al.* Delamination behavior of lithium-ion battery anodes: Influence of drying temperature during electrode processing. *Dry. Technol.* **34**, 462–473 (2016).
 79. Pfaffmann, L. *et al.* New method for binder and carbon black detection at nanometer scale in carbon electrodes for lithium ion batteries. *J. Power Sources* **363**, 460–469 (2017).
 80. Jaiser, S. *et al.* Microstructure formation of lithium-ion battery electrodes during drying – An ex-situ study using cryogenic broad ion beam slope-cutting and scanning electron microscopy (Cryo-BIB-SEM). *J. Power Sources* **345**, 97–107 (2017).
 81. Sim, R., Lee, S., Li, W. & Manthiram, A. Influence of Calendering on the Electrochemical Performance of $\text{LiNi}_{0.9}\text{Mn}_{0.05}\text{Al}_{0.05}\text{O}_2$ Cathodes in Lithium-Ion Cells. *ACS Appl. Mater. Interfaces* **13**, 42898–42908 (2021).

82. Oladimeji, C. F., Moss, P. L. & Weatherspoon, M. H. Analyses of the Calendaring Process for Performance Optimization of Li-Ion Battery Cathode. *Adv. Chem.* **2016**, 1–7 (2016).
83. Stephenson, D. E. *et al.* Modeling 3D Microstructure and Ion Transport in Porous Li-Ion Battery Electrodes. *J. Electrochem. Soc.* **158**, A781 (2011).
84. Ebner, M., Geldmacher, F., Marone, F., Stampanoni, M. & Wood, V. X-Ray Tomography of Porous, Transition Metal Oxide Based Lithium Ion Battery Electrodes. *Adv. Energy Mater.* **3**, 845–850 (2013).
85. Oswald, S., Pritzl, D., Wetjen, M. & Gasteiger, H. A. Novel Method for Monitoring the Electrochemical Capacitance by In Situ Impedance Spectroscopy as Indicator for Particle Cracking of Nickel-Rich NCMs: Part I. Theory and Validation. *J. Electrochem. Soc.* **167**, 100511 (2020).
86. Ebner, M., Chung, D.-W., García, R. E. & Wood, V. Tortuosity Anisotropy in Lithium-Ion Battery Electrodes. *Adv. Energy Mater.* **4**, 1301278 (2014).
87. Daemi, S. R. *et al.* 4D visualisation of *in situ* nano-compression of Li-ion cathode materials to mimic early stage calendaring. *Mater. Horiz.* **6**, 612–617 (2019).
88. Lu, X. *et al.* Microstructural Evolution of Battery Electrodes During Calendaring. *Joule* **4**, 2746–2768 (2020).
89. Günther, T. *et al.* Classification of Calendaring-Induced Electrode Defects and Their Influence on Subsequent Processes of Lithium-Ion Battery Production. *Energy Technol.* **8**, 1900026 (2020).
90. Kim, A.-Y. *et al.* Stabilizing Effect of a Hybrid Surface Coating on a Ni-Rich NCM Cathode Material in All-Solid-State Batteries. *Chem. Mater.* **31**, 9664–9672 (2019).
91. Hoekstra, A. The Underestimated Potential of Battery Electric Vehicles to Reduce Emissions. *Joule* **3**, 1412–1414 (2019).
92. König, A. *et al.* An Overview of Parameter and Cost for Battery Electric Vehicles. *World Electr. Veh. J.* **12**, 21 (2021).
93. Tan, D. H. S. *et al.* Carbon-free high-loading silicon anodes enabled by sulfide solid electrolytes. *Science* **373**, 1494–1499 (2021).
94. QuantumScape Investor Presentation, <https://ir.quantumscape.com/resources/events-and-presentations/default.aspx>

List of Abbreviations

ACN	Acetonitrile
CAM	Cathode active material
CE	Coulombic efficiency
DEMS	Differential electrochemical mass spectrometry
DoE	Design-of-experiments
EDS	Energy-dispersive X-ray spectroscopy
EIS	Electrochemical impedance spectroscopy
EtOH	Ethanol
hNBR	Hydrogenated nitrile butadiene rubber
ICE	Internal combustion engine
LCO	LiCoO ₂
LD ₅₀	Lethal dose
LFP	LiFePO ₄
LIB	Lithium-ion batteries
LiTMO ₂	Lithium transition metal oxides
LNO	LiNiO ₂
LTO	Li ₄ Ti ₅ O ₁₂
MeOH	Methanol
NCA	LiNi _{1-x-y} Co _x Al _y O ₂
NMC/NMC	Li _{1+x} (Ni _{1-y-z} Co _y Mn _z) _{1-x} O ₂
NMP	N-Methyl-2-pyrrolidone
NMF	N-methylformamide
PEEK	Polyether ether keton
PEVA	Poly(ethylene vinyl acetate)
PI	Polarity index
PIB	Polyisobutene
PMMA	Poly(methyl methacrylate)
PVDF	Poly(vinylidene fluoride)
PVP	Polyvinylpyrrolidone
SBR	Styrene butadiene rubber
SE	Solid electrolyte
SEBS	Styrene-(ethylene-butylene)-styrene
SEI	Solid electrolyte interphase
SEM	Secondary electron multiplier
SEM	Secondary electron microscopy
SOC	State of charge
SSB	All-solid-state batteries
THF	Tetrahydrofuran
ToF-SIMS	Time-of-Flight secondary ion mass spectrometry
XPS	X-ray photoelectron spectroscopy
XRD	X-ray diffraction

List of Scientific Contributions

1. Bartsch, T.; Kim, A.-Y.; Strauss, F.; Biasi, L. de; Teo, J. H.; Janek, J.; Hartmann, P.; Brezesinski, T. **2019**. Indirect state-of-charge determination of all-solid-state battery cells by X-ray diffraction. *Chemical communications*, 55 (75), 11223–11226.
2. Kim, A.-Y.; Strauss, F.; Bartsch, T.; Teo, J. H.; Hatsukade, T.; Mazilkin, A.; Janek, J.; Hartmann, P.; Brezesinski, T. **2019**. Stabilizing Effect of a Hybrid Surface Coating on a Ni-Rich NCM Cathode Material in All-Solid-State Batteries. *Chemistry of materials*, 31 (23), 9664–9672.
3. Strauss, F.; Teo, J. H.; Schiele, A.; Bartsch, T.; Hatsukade, T.; Hartmann, P.; Janek, J.; Brezesinski, T. **2020**. Gas Evolution in Lithium-Ion Batteries: Solid versus Liquid Electrolyte. *ACS applied materials & interfaces*, 12 (18), 20462–20468.
4. Strauss, F.; Teo, J. H.; Janek, J.; Brezesinski, T. **2020**. Investigations into the superionic glass phase of Li₄PS₄I for improving the stability of high-loading all-solid-state batteries. *Inorganic chemistry frontiers*, 7 (20), 3953–3960.
5. Strauss, F.; Teo, J. H.; Maibach, J.; Kim, A.-Y.; Mazilkin, A.; Janek, J.; Brezesinski, T. **2020**. Li₂ZrO₃-Coated NCM622 for Application in Inorganic Solid-State Batteries: Role of Surface Carbonates in the Cycling Performance. *ACS applied materials & interfaces*, 12 (51), 57146–57154.
6. Kim, A.-Y.; Strauss, F.; Bartsch, T.; Teo, J. H.; Janek, J.; Brezesinski, T. **2021**. Effect of surface carbonates on the cyclability of LiNbO₃-coated NCM622 in all-solid-state batteries with lithium thiophosphate electrolytes. *Scientific Reports*, 11 (1), Art.-Nr.: 5367.
7. Teo, J. H.; Strauss, F.; Tripković, Đ.; Schweidler, S.; Ma, Y.; Bianchini, M.; Janek, J.; Brezesinski, T. **2021**. Design-of-experiments-guided optimization of slurry-cast cathodes for solid-state batteries. *Cell Reports Physical Science*, 2 (6), Art.-Nr.: 100465.
8. Ma, Y.; Teo, J. H.; Kutsche, D.; Diemant, T.; Strauss, F.; Ma, Y.; Goonetilleke, D.; Janek, J.; Bianchini, M.; Brezesinski, T. Cycling Performance and Limitations of LiNiO₂ in Solid-State Batteries. **2021**. *ACS energy letters*, 6 (9), 3020–3028.
9. Teo, J. H.; Strauss, F.; Walther, F.; Ma, Y.; Payandeh, S.; Scherer, T.; Bianchini, M.; Janek, J.; Brezesinski, T. **2022**. The interplay between (electro)chemical and (chemo)mechanical effects in the cycling performance of thiophosphate-based solid-state batteries. *Materials Futures*, 1 (1), Artk.Nr.: 015102.

Acknowledgements

For the last page of my doctoral thesis, I would like to use this opportunity to thank everyone that has helped me during my three and a half year journey at Karlsruhe Institute of Technology (KIT).

I would like to especially thank my Doktorvater Prof. Dr. Jürgen Janek for giving me the opportunity to engage in high level research on solid-state batteries at the BELLA group in KIT. Furthermore, I am extremely fortunate for his scientific support during the entire duration of my doctoral thesis. Moreover, since Prof. Dr. Jürgen Janek is one of the leading authorities on solid-state batteries, I was given the opportunities to network with leading researchers in various institutes. This has widened my network within the battery industry as well as provided me with essential work experiences.

Next, I would like to thank Prof. Dr. Smarsly for accepting the role of the second xxxxx

The next person I would like to thank is Dr. Torsten Brezesinski. I am extremely grateful for all the support that he has provided me during my doctoral thesis. He was extremely patient and educative not just in the scientific field but also in life/working skills. The support and ideas that he provided for my publications have been a tremendous help in making everything “waterproof”, easy to read and to the point. I have learnt a lot from our interactions during my time at BELLA and will incorporate these learnings to improve my skills both in the professional and personal areas further.

I would also like to thank the lab managers from BASF, specifically Dr. Pascal Hartmann and Prof. Dr. Matteo Bianchini. Both were very supporting of the research work at BELLA. Dr. Pascal Hartmann was the person that initially introduce DoE to the lab and has been the source of inspiration for one of my publications. I would also like to thank Dr. Xiaohan Wu for all the support as a BASF research coordinator for SSB. The interactions and exchanges have always been very educational and engaging. Prof. Dr. Matteo Bianchini has also been extremely helpful by providing extensive knowledge in X-ray analysis. Together with Dr. Torsten Brezesinski and Prof. Dr. Jürgen Janek, they have been very helpful and their inputs have always elevated the publications to a higher level.

Lastly, I would like to thank all my colleagues at BELLA. The work environment at BELLA was truly something special, something I have not experienced before. High level research and professionalism were mixed together with a very friendly work atmosphere, making my time at BELLA an unforgettable life experience. Special thanks to Dr. Timo Bartsch, Dr. Florian Strauss and Dr. A-Young Kim – the three figures within the original all-solid-state group at BELLA. I wish Dr. Florian Strauss all the best and success in building up his own research group within KIT. I have learnt a lot from them throughout their time at BELLA. Among the new group members engaged in SSB research, I would also like to thank Dr. Yuan Ma for all the help and insights he has provided during our work together.